Investigation of degradation at halide perovskite surfaces using near-ambient pressure X-ray photoelectron spectroscopy

A thesis submitted to The University of Manchester

for the degree of Doctor of Philosophy

in the Faculty of Science and Engineering

2019

Chun-Ren Ke

Department of Physics and Astronomy in the School of Natural Sciences

Content

Word Count: 77777

List of Tables

Table 8.4 (Paper 5) Table S2 Quantified atomic concentrations of C–O (BE: 286.3 ± 0.1 eV) from the C 1s NAP-XPS spectra and O–C (BE: 532.1 ± 0.1 eV) from the O 1s NAP-XPS spectra of AACVD (+HI)-grown films. All elements are normalised to Cs (using [Cs] = 2.0), consistent with Tables 1&2. Spectra were measured under UHV conditions before and after exposure to water or O_2……250

List of Figures

Abstract

Perovskite solar cell (PSC) is one of the most promising next-generation photovoltaic technologies that can provide low-cost, alternative renewable energy. The main hindrances to the deployment of PSC panels are instability issues. Deterioration in the power conversion efficiency of PSCs over time greatly originates from perovskite light absorbers. Hence, in this thesis, the stability of lead and tin perovskites is investigated.

Some key factors to improve the stability of perovskite materials are discussed, including processing, materials, and understanding degradation mechanisms in particular. I introduce a state-of-the-art characterisation technique, near-ambient pressure X-ray photoelectron spectroscopy (NAP-XPS), to investigate the surface stability and degradation process of perovskites. We propose the moisture-induced degradation behaviour of a prototypical halide perovskite, methylammonium lead iodide (MAPI): MAPI decomposes into lead iodide and hydrocarbon chains by releasing hydrogen iodide and ammonia gases. For processing, we find that MAPI films made by aerosol-assisted chemical vapour deposition (AACVD) generally have better stability in humid air than their spin-coated counterparts, which can be attributed to larger grain sizes. Moreover, surface passivation plays a crucial role in the improved stability against moisture. This can be achieved using excess CH_3NH_3I (to react with a $Pb(SCN)_2$ precursor) or bulky ammonium iodides for MAPI films.

Formamidinium (FA)-based mixed-cation mixed-halide perovskites and Cs_2SnI_6 double perovskite not only have better water resistance but also undergo different degradation routes compared to MAPI. Upon H_2O vapour exposure, the FA cation transforms into $CH_3NH_3^+$ first, whilst the degraded species of Cs_2SnI_6, CsI, remains at the surface. It will be shown that these insights can pave the way towards stable PSCs.

Declaration

No portion of the work referred to in this thesis has been submitted in support of an application for another degree or qualification of this or any other university or other institute of learning.

Copyright

List of Publications

This thesis is based on the following publications:

[1] (Paper 1) **Chun-Ren Ke**, Alex Walton, David Lewis, Aleksander Tedstone, Paul O'Brien, Andrew Thomas, Wendy Flavell, *In situ* investigation of degradation at organometal halide perovskite surfaces by X-ray photoelectron spectroscopy at realistic water vapour pressure. *Chemical Communications* **2017**, *53*, p. 5231.

[2] (Paper 2) **Chun-Ren Ke**, David Lewis, Alex Walton, Qian Chen, Ben Spencer, Muhamad Mokhtar, Claudia Compean-Gonzalez, Paul O'Brien, Andrew Thomas, Wendy Flavell, Air-stable methylammonium lead iodide perovskite thin films fabricated via aerosol-assisted chemical vapour deposition from a pseudohalide $Pb(SCN)_2$ precursor. *ACS Applied Energy Materials* **2019**, *2*, p. 6012.

[3] (Paper 3) **Chun-Ren Ke**, Tse-Wei Wang, Alex Walton, Andrew Thomas, Wendy Flavell, Investigation of degradation at halide perovskite surfaces passivated by ammonium iodides using *in situ* X-ray photoelectron spectroscopy in a humid environment. *In Preparation*.

[4] (Paper 4) **Chun-Ren Ke**, Tse-Wei Wang, Alex Walton, Gregory Wilson, Andrew Thomas, Wendy Flavell, Thermal degradation behaviour of mixed-cation perovskite surfaces probed by *in situ* X-Ray photoelectron spectroscopy under humid conditions. *In Preparation*.

[5] (Paper 5) **Chun-Ren Ke**, David Lewis, Alex Walton, Qian Chen, Paul O'Brien, Andrew Thomas, Wendy Flavell, Ambient-air-stable inorganic Cs_2SnI_6 double perovskite thin films via aerosol-assisted chemical vapour deposition. *Journal of Materials Chemistry A* **2018**, *6*, p. 11205.

Other publications which I have contributed to, but not included in this thesis: (only list the works associated with the PhD study at UoM)

[6] Pip Clark, Nathan Lewis, **Chun-Ren Ke**, Ruben Ahumada-Lazo, Alex Abelson, Darren Neo, Chao Yi, Kan Fu, Ashley Gaulding, Igor Pis, Silvia Nappini, Federica Bondino, Elena Magnano, Mathieu Silly, Matt Law, Wendy Flavell, Surface band bending and carrier dynamics in colloidal quantum dot solids". *In Preparation*.

[7] Mary Burkitt-Gray, Simon Fairclough, **Chun-Ren Ke**, Wijttra Wichiansee, Pip Clark, Edward Lewis, Wendy Flavell, Sarah Haigh, Mark Green, are InP/ZnS quantum dots always simple core/shells? An analysis of alloyed InZnP, InZnPZnS, and InZnPCdS nanoparticles. *In Preparation*.

[8] Edward Lewis, Lewis Le Fevre, Aleksander Tedstone, **Chun-Ren Ke**, Andrew Forsyth, Andrew Thomas, Robert Dryfe, David Lewis, Paul O'Brien, Sarah Haigh, Direct growth of molybdenum disulfide (MoS_2) nanosheets on graphene oxide: a molecular precursor route to 2D heterostructures for supercapacitor applications. *In Preparation*.

[9] Qian Chen, Muhamad Mokhtar, **Chun-Ren Ke**, Andrew Thomas, Aseel Hadi, Eric Whittaker, Michele Curionia, Zhu Liu, A one-step laser process for rapid manufacture of mesoscopic perovskite solar cells prepared under high relative humidity. *Sustainable Energy & Fuels* **2018**, *2*, p. 1216.

[10] Muhamad Mokhtar, Qian Chen, Qing Lian, David Lewis, Brian Saunders, Alex Walton, **Chun-Ren Ke**, Eric Whittaker, Bruce Hamilton, Decoupling structure and composition of $CH_3NH_3PbI_{3-x}Br_x$ films prepared by combined one-step and two-step deposition. *ACS Applied Energy Materials* **2018**, *1*, p. 5567.

[11] Kane Norton, Jens Kunstmann, Lu Ping, Alexander Rakowski, Chuchen Wang, Alexander Marsden, Ghulam Murtaza, Niting Zeng, Simon McAdams, Mark Bissett, Sarah Haigh, Brian Derby, Gotthard Seifert, **Chun-Ren Ke**, David Lewis, (Correction) Synthetic 2-D lead tin sulfide nanosheets with tuneable optoelectronic properties from a potentially scalable reaction pathway. *Chemical Science* **2019**, *10*, p. 1035.

[12] Chotiros Dokkhana, Muhamad Mokhtara, **Chun-Ren Ke**, Alex Walton, Qian Chen, Nigel Hodson, Qing Lian, Brian Saunders, Modulating crystallization in semi-transparent perovskite films using sub-micrometer sponge-like polymer colloid particles to improve solar cell performance. *ACS Applied Energy Materials* **2019**, *2*, p. 6624.

[13] Hoyeon Choi, **Chun-Ren Ke**, Stefan Skalsky, Christopher Castle, Kexue Li, Katie Moore, Wendy Flavell, Patrick Parkinson, Visualizing the Role of Photoinduced Ion Migration on Optoelectronic Performance in Halide Perovskite Grains. *Submitted*.

[14] Qian Chen, **Chun-Ren Ke**, Dong Wang, Muhamad Mokhtar, Andrew G. Thomas, Zhu Liu, Impact of Halide Additives and Stoichiometry on Ambient-Processed Planar Organometal Halide Perovskite Solar Cells. *Submitted*.

Other manuscripts under early-stage preparation I have contributed to do not be listed here.

Other publications that are not linked to the PhD study can be found in the following link: (Google Scholar):

https://scholar.google.com/citations?user=jbNkEfwAAAAJ&hl=zh-TW

Current indexes:

Citation of 205, H index of 7, and i10 index of 7 (accessed by 19/Dec/2019)

Acknowledgements

First and foremost, I would like to greatly thank Prof Wendy Flavell and Dr Andrew Thomas for attentive supervision. Without their support, I would never secure a PDS award that has enabled my memorable PhD student life. Without their instructions, I would never achieve such an accomplishment and expand my knowledge from materials to surface science. Huge thank my viva examiners, Prof Sven Schroeder and Dr Patrick Parkinson for useful suggestions and kind instructions. Thank Pip for kicking-off my initial learning of XPS data analysis and helping me strengthen engagement with colleagues. I thank all group members, Marina, Atip, Andrew, Ruben, Claudia, Nathan, Stefan, Suresh, Hoyeon, and Chris. I also thank Janet, Mike, Rosie, Khadisha, and Fahad. So many PSI people need to be acknowledged.

Moreover, more talent researchers must be listed and thanked here. Thank you Qian Chen; we are pioneers in making PSCs at the UoM. Without you, I could not set perovskite research up. I am very grateful that Alex and Ben taught me NAP-XPS and XPS a lot. Alex, I might not highly develop interest in NAP-XPS if you did not show such passion in guiding me. Thank David and Paul O'Brien (R.I.P) for offering good opportunities of using AACVD, allowing me to extent my research further into materials chemistry. I also give a massive thank to Hasif and Jacob Wang for leading the way towards a better PSC avenue. I may miss some other important staff here but I definitely thank all the people who ever helped me, much appreciated.

Last but most important, I have to give my deepest appreciation to my dad, my mom, my sister, and my girlfriend. Without any of you, I cannot reach such a great achievement and get an unforgettable PhD life, much appreciated.

Chapter 1 Introduction

1.1 Background and Motivation

Although rapid industrialisation has brought human beings tremendous convenience, it has also given rise to the colossal emission of greenhouse gases, such as carbon dioxide (CO_2), leading to severe global warming. This further causes extreme weather conditions and climate change that significantly impact ecological systems, and could induce the extinction of humanity.[1] To make all life on earth sustainable, it is crucial to halt the course of global warming.

The majority of greenhouse gas production is attributed to the burning of fossil fuels, which supplies the great portion of electricity generation, surpassing 50%.[2] In order to reduce the emission of greenhouse gases, other electricity supply sources urgently need to be developed to replace conventional fossil fuel sources such as coal, oil, and natural gas. Renewable energies are ideal substitutes for fossil fuels since they are sustainable and generally clean and safe to operate. Apart from nuclear energy, they are unlikely to bring catastrophic disasters and in general they do not produce wastes that are difficult to handle. Amongst all the renewables, solar power is the most abundant renewable energy source (*ca.* 120,000 terawatts incident on the earth [3]) and one that can perpetually provide the earth with sunlight. The most efficient way to utilise such energy is through photovoltaic (PV) devices that can directly convert light into electricity. However, since the cost per watt has not been sufficiently competitive, further improvements in power conversion efficiency (PCE) and cost reduction are required without delay to boost the market share of PVs in electricity generation.

Currently, mainstream PV panels are composed of single-junction crystalline silicon solar cells, with a record PCE of 26.1% (non-concentrator).[4] To date, over 95% of market production has been based on these solar cells, mainly due to their rapidly declining manufacturing costs and high efficiencies, which are now typically higher than 20%, if *n*-type monocrystalline wafers are applied.[5] However, the conventional silicon solar cells are quite rigid and fragile and hence do not well adapt to curved surfaces and to building-integrated PV (BIPV). Thin-film PV technologies, such as copper indium gallium selenide (CIGS) and CdTe, are proving to be promising for deployment in the real world due to their light weight, transparency, and flexibility, as they can be fabricated on plastic substrates. However, CIGS and CdTe currently are not competitive compared to silicon-based solar cells, partially owing to the use of expensive (In and Ga), toxic (Cd), or scarce (Te) elements, respectively. Therefore, alternative thin-film technologies urgently need to be commercially developed to compete with or complement silicon-based solar cells in order to promote PVs as the primary electricity source worldwide.

In addition to classical thin film solar cells mentioned above, third-generation PV cells such as dye-sensitised solar cell (DSSC) and quantum dot solar cell (QDSC) have also attracted notable attention partially due to their potentially low cost. However, the PCEs of these emerging PV technologies are lower than 20%, which is uncompetitive with mainstream silicon solar cells.[4] Amongst all newly developed PVs, perovskite solar cells (PSCs) have emerged as one of the most promising solar power technologies in recent years due to the unprecedented PCE enhancements, from 3.8% to 25.2% (single-junction PSC) within just a decade.[4, 6] Perovskite/Si tandem devices have further boosted the efficiency to 28%, where PSC acts as an effective auxiliary on the top of silicon solar cells.[4] Such progress has attracted more and more attention from both academic and

industrial researchers due not only to their high efficiencies but also their potentially low manufacturing costs, *i.e.* low cost per watt. The light absorbers (*e.g.* $CH_3NH_3PbI_3$, methylammonium lead iodide (MAPI), the prototype of halide perovskites) of PSCs are typically composed of inexpensive, abundant elements. If 25-terawatt PSC panels need to be installed, Pb for use in PSCs only consumes around one-day Pb production capacity (Figure 1.1) based on the current production status,[7] which means that key raw material acquisition would not be problematic in large-scale commercial PSC production. Contrarily, Si for use in silicon-based solar cells requires over one-year Si production capacity to meet 25-terawatt solar panel installation, indicating that the annual supply may fail to meet the demand. This suggests if PV market dramatically grows to terawatt-level market in the future, the silicon-based solar cell is less likely to be dominant. More surprisingly, the key elements applied in other PV technologies, such as CIGS, CdTe, and GaAs, would need a thousand years at current production rates to deliver a 25 terawatt PV installation, as shown in Figure 1.1. This is a strong indication that those technologies are unlikely to dominate the major PV market in the future. PSC is therefore expected to play a vital role in the future PV market and any effort that advances the development of PSCs is important. This is why this thesis focuses on the PSC area. However, the key factor impeding PSC commercialisation is the lifetime issue — PSCs currently cannot sustain operation for > 20 years, which is the current market standard. The main cause of instability in PSCs originates from the perovskite layers themselves. Therefore, in this thesis we concentrate the investigation on the stability of halide perovskites for use in PSCs.

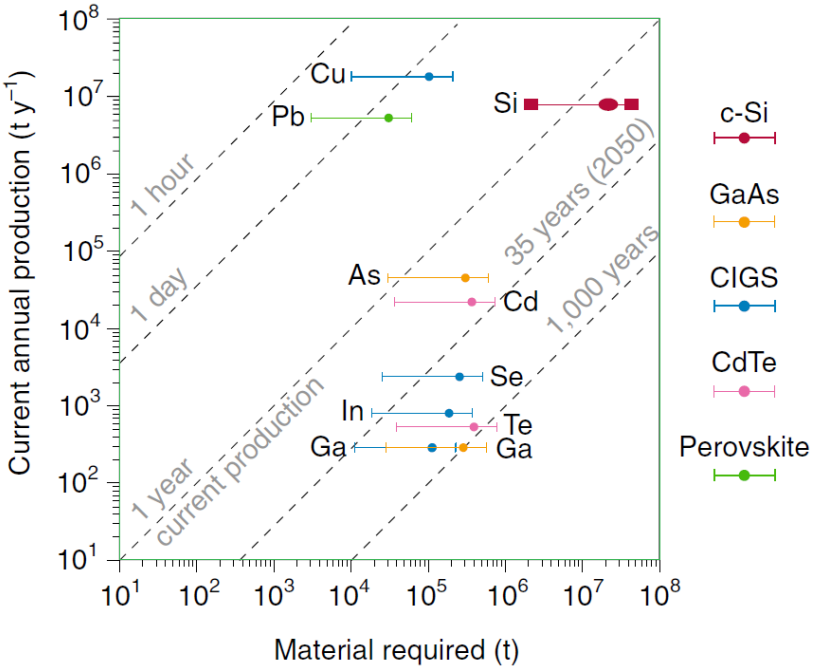

Figure 1.1 Annual material production (in 2015) versus material required to deliver 5% (left end of the bar), 50% (circle), and 100% (right end of the bar) of a potential 25-terawatt PV installation for perovskite, silicon, GaAs, CIGS, and CdTe.[7]

1.2 Aims and Outline of the Thesis

This thesis builds on the investigation of the stability of metal halide perovskites. As the progress of PSCs is primarily constrained by instability that mainly arises from the perovskite light absorbers, improving the stability of these halide perovskites is the top priority for current research in the PSC area. Therefore, the thesis selectively focuses on the stability of perovskite materials instead of concentrating on the PCEs of PSC devices that have already reached competitive standard. This work is expected to pave the way to stable PSCs by discussing some key factors of improving the stability of metal halide perovskites, including materials, processing, and understanding the degradation mechanism. In particular, surface characterisations as a function of degradation are crucial in aiding understanding the degradation mechanism of perovskite materials.

Chapter 2 describes the relevant background of PSCs, including progress in improving efficiency, materials, and processing, with an emphasis on the stability issues highlighted in Section 2.4. Prior to the discussion of PSCs, a fundamental knowledge of semiconductors and the principles of solar cells is required, so this information is presented in the later sections of this chapter. Chapter 3 introduces the techniques and theory used in association with this work, with a stress on the basics of X-ray photoelectron spectroscopy (XPS), since this research involves significant XPS studies. In particular, this thesis pioneers the introduction of near-ambient pressure XPS (NAP-XPS) into the PSC sphere.

From Chapters 4 to 8, we present the results of this thesis, composed of five published, submitted and draft papers. In Chapter 4, the degradation mechanism of MAPI upon exposure to water vapour is investigated by NAP-XPS.[8] The environment provided during the experiment corresponds to relative humidity (RH) of up to *ca.* 30%, which simulates realistic conditions. Chapter 5 focuses on the same material, MAPI, but we apply a different approach, aerosol-assisted chemical vapour deposition (AACVD), to produce MAPI thin films. In this work, lead thiocyanate is utilised as the lead precursor in order to gain better stability in ambient processing and ageing. Various characterisations in conjunction with the NAP-XPS study assist in discovering how to make halide perovskite films more stable. The reasons why AACVD can produce relatively stable films compared to spin coating are discussed in this chapter. Chapter 6 further employs a distinct method to improve the stability of MAPI using bulky ammonium iodides to passivate the surface. The moisture-induced degradation behaviour and stability of MAPI films with and without surface functionalisation are investigated using NAP-XPS.

Chapter 7 contains a discussion of thermal stability and stability against moisture separately, and also of the effect of a combination of thermal stress and water vapour for

mixed-cation perovskites. This chapter compares the stability and degradation mechanisms of dual-cation (Cs and formamidinium (FA)) and triple-cation (plus methylammonium (MA)) perovskite films. Chapter 8 concentrates on lead-free perovskites in order to reduce the toxicity of halide perovskite materials. We employed AACVD to deposit an inorganic tin double perovskite, Cs_2SnI_6.[9] The results reveal a strong dependence of stability on processing method for Cs_2SnI_6 material, by comparing AACVD-grown and spin-coated films. The reasons why AACVD can produce relatively stable films compared to spin coating are also discussed in this chapter. Finally, the key findings and the outlook of this thesis — namely, to achieve stable halide perovskites for use in PSCs — are summarised and presented in Chapter 9.

1.3 Semiconductors

PV devices usually contain semiconductor materials. A semiconductor, as its name suggests, is not as conductive as a metallic conductor but can conduct carriers to a certain extent. Materials can be generally classified into three categories: metal, semiconductor, and insulator. From metal to insulator, the electrical conductivity significantly reduces due to differences in the band structure. The band structure can be simplified in an energy band diagram, as shown in Figure 1.2. In this diagram, it can be seen that metals do not have energy bandgap, so electrons at the Fermi level (E_F) can move into empty states close in energy (within $\pm k_BT$, where k_B and T are Boltzmann constant and temperature, respectively) and do not require being excited under illumination to conduct. Hence, a metal is capable of conducting electricity at low temperature. However, when the temperature of a metal increases, the thermal vibration of metallic atoms enhances resistance to moving electrons, resulting in a decrease in electrical conductivity. In a metal at absolute zero, the Fermi

energy/level is defined as the energy of the highest occupied electronic states. At any given temperatures, the Fermi level can be considered to be a hypothetical energy level of an electron such that at thermodynamic equilibrium this energy level has a 50% probability of being occupied by an electron at any given time.[10]

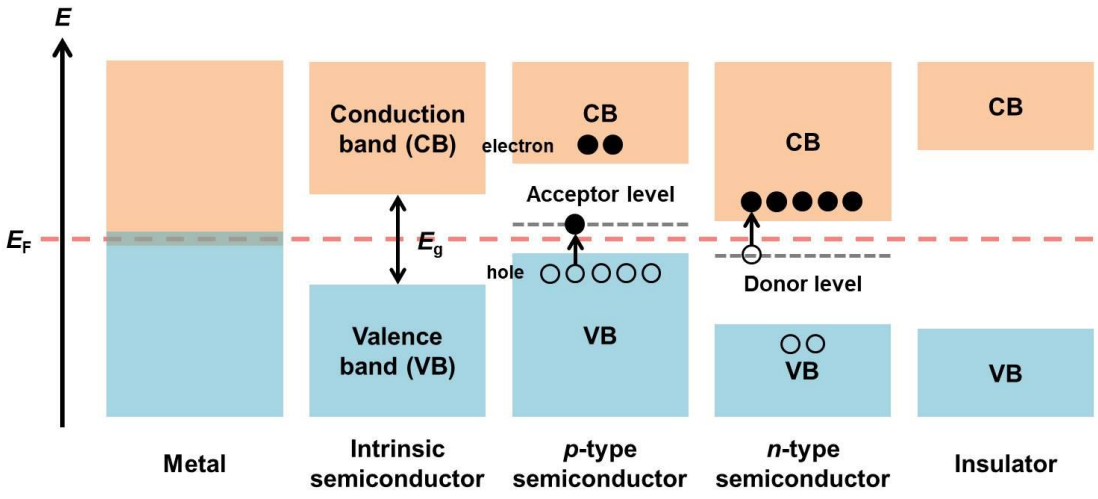

Figure 1.2 Energy band diagrams for metals, semiconductors, and insulators. The blank space between conduction and valence bands depicts the forbidden energy gap.

Semiconductors have a relatively small energy bandgap (typically, 1–3 eV) between valence band (VB) and conduction band (CB) compared to insulators. VB is the highest range of occupied electronic states, where its top is the valence band maximum (VBM). CB is the lowest range of vacant electronic states, where its bottom is called the conduction band minimum (CBM). The properties of semiconductors greatly depend on the position of the Fermi level. If the Fermi level is roughly located at the centre of the bandgap, the material is called an intrinsic semiconductor, such as undoped Si. If the Fermi level is close to the VBM or CBM, the material is a *p*-type or *n*-type semiconductor (both known as an extrinsic semiconductor), respectively, as shown in Figure 1.2. The shift in the Fermi level occurs as a result of the presence of dopants/impurities in an intrinsic semiconductor.

If the dopant provides an extra electron or hole (*e.g.* P or B in Si), an additional donor or acceptor level is generated slightly below or over the Fermi level (Figure 1.2) within the bandgap region, respectively. In a *n*-type material donor level is close to the CBM so that electrons at the donor states can be easily excited to the CB, whereas for a *p*-type material the dopant level accepts electrons excited from the VB, leaving mobile holes in the VB. For organic materials, long-range delocalisation giving continuous bands does not typically exist, and the VBM and CBM are conventionally labelled the highest occupied and lowest unoccupied molecular orbitals (HOMO and LUMO), respectively. When the bandgap is larger (typically, at least 3 eV), the electrons in the VB have a very low probability of being excited to the CB. Therefore, the electrical conductivity is quite low and such a material can be deemed an insulator.

The conductivity (*n*-type or *p*-type) of semiconductors can be tuned by doping impurities to enhance electron or hole conductivities, based on requirements. Taking the intrinsic semiconductor Si for example, if boron (which has one fewer electron than Si) is doped into the Si structure, this can be deemed to increase the hole concentration and is an electron acceptor. The doped extrinsic material is called a *p*-type semiconductor, whereas when phosphorus (an electron donor) is doped into silicon the substance becomes an *n*-type semiconductor. If an *n*-type semiconductor is in contact with a *p*-type one, a *p*-*n* junction can be formed by carrier migration, and the Fermi level reaches an equilibrium position, as shown in Figure 1.3.

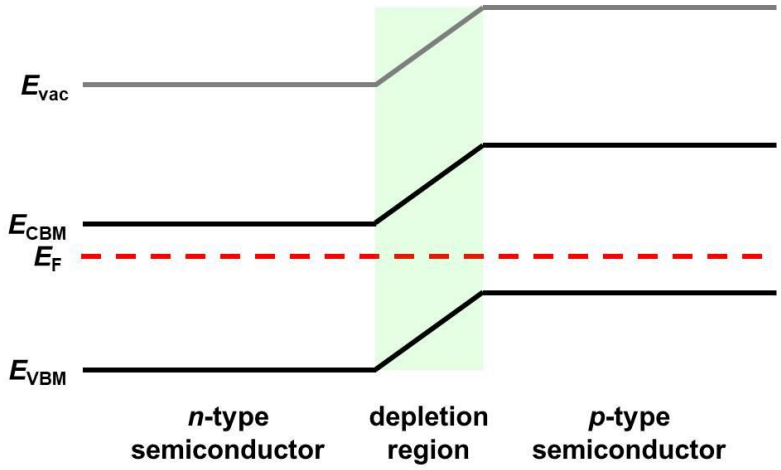

Figure 1.3 Diagram of the formation of a *p*-*n* junction after the Fermi energy reaches equilibrium. The depletion region generated is highlighted. E_{vac} is the vacuum energy level.

In order to reach the equilibrium state, diffusion of the carriers across the *p*-*n* junction occurs; *i.e.* holes diffuse from *p*-type to *n*-type materials, whereas electrons move from the *n*-type to the *p*-type semiconductor at the junction. This leads to opposite charging of the two semiconductors at the junction (namely, positive ions at the *n*-type side and negative ions at the *p*-type edge), generating a depletion region which has a built-in electric field.[11] This electric field stops the further diffusion of the majority carriers in the semiconductors. When photons are absorbed in the depletion region, the electron–hole pairs can be separated by the built-in electric field. In this way, electrons transport to the *n*-type side, whereas holes move to the *p*-type material, generating a drift current in the opposite direction to the diffusion current.

If the electron–hole pairs are produced outside the depletion region, there is no driving force through drift; namely, the transport is dominated by diffusion in the opposite direction of the current produced from a PV device. Hence, increasing the width of the depletion region can produce more effective electron–hole pair separation. This can be realised by

inserting an intrinsic layer between the *p*- and *n*-type semiconductors, forming a *p*-*i*-*n* junction. However, intrinsic semiconductors are typically less conductive, potentially resulting in an increase in the series resistance of a PV device. Therefore, the thickness requires optimisation to prevent a reduction in efficiency in *p*-*i*-*n* solar cells.

1.4 Principles of Solar Cells

The photovoltaic effect can be traced back to the early years of the nineteenth century when it simply described the electrical voltage and current in a material that was generated under light illumination.[12] Such PV materials are typically semiconductors that can produce an electrical potential difference through excitation of electrons across the energy bandgap when the material is radiated. Basically, a solar cell contains a diode or *p*-*n* junction where electrons and holes pass through the *n*- and *p*-type semiconductors respectively to the external circuit. The working principles of a PV device involve several processes, as shown in Figure 1.4. First, light absorbing materials sandwiched between two conducting electrodes (front and back contacts, typically metal) only absorb that portion of the light with photon energies larger than their bandgap energy, whilst other photons with various wavelengths can be transmitted, or reflected by the material or by the metal contacts under irradiation. Subsequently, photon absorption creates an electron–hole pair or a so-called exciton, with a specific exciton binding energy, that depends on the material. An exciton is a bound state of an electron and a hole that attract to each other through the electrostatic Coulomb force, which can be deemed as an electrically neutral quasiparticle. In accordance with the characteristics of excitons, they can be classified into two types, depending on the dielectric constant of the material: Frenkel exciton and Wannier–Mott exciton, as shown in Figure 1.5. In materials with a relatively low

dielectric constant, an electron and a hole are tightly bound with an exciton binding energy on the order of 0.1 to 1 eV. Such an exciton is called Frenkel exciton, which can be typically found in organic semiconductors. In the case of excitons generated in a material with a relatively high dielectric constant (*e.g.* inorganic semiconductors), the exciton has relatively low binding energy on the order of 0.01 eV, which is called Wannier–Mott exciton. The electron and hole of the exciton in such system are relatively easy to separate, which is preferable to photovoltaic devices. Organolead perovskites have exciton binding energies in the range of approximately 0.05 eV, sitting between the values for Frenkel and Wannier–Mott excitons.[13]

Excess energy that surpasses the bandgap energy usually dissipates in the form of thermal energy, a process called thermalisation (Figure 1.6).[14] When the E_g is lower, the material potentially absorbs more photons and may produce a higher electric current. However, the lower bandgap means the electrical voltage is limited. Therefore, there is a bandgap range (*ca.* 1.1 – 1.4 eV) that produces optimised efficiencies for single-junction solar cells by balancing the electric current and voltage, according to the theory of Shockley and Queisser (which assumes a standard solar spectrum (AM 1.5)).[15] The bandgap energies of crystalline Si (1.1 eV) and MAPI (1.55 eV) are roughly located within this range.

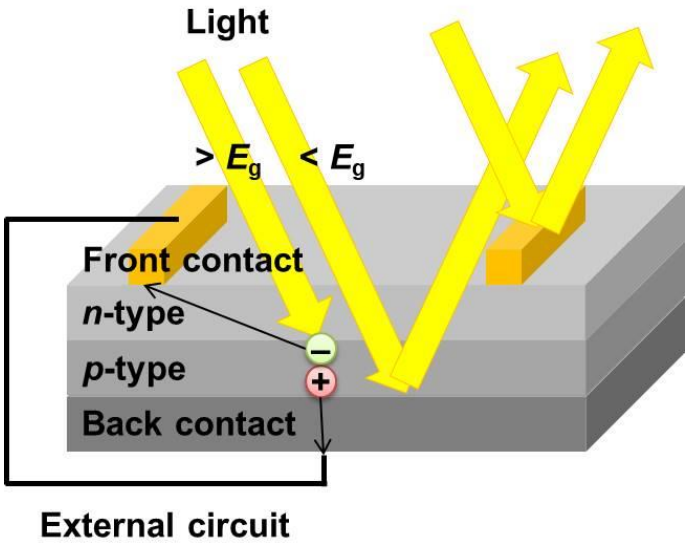

Figure 1.4 Working principles of a typical PV device. The range of *n*- and *p*-type materials is the light absorbing region sandwiched by two electrodes connected to the external circuit.

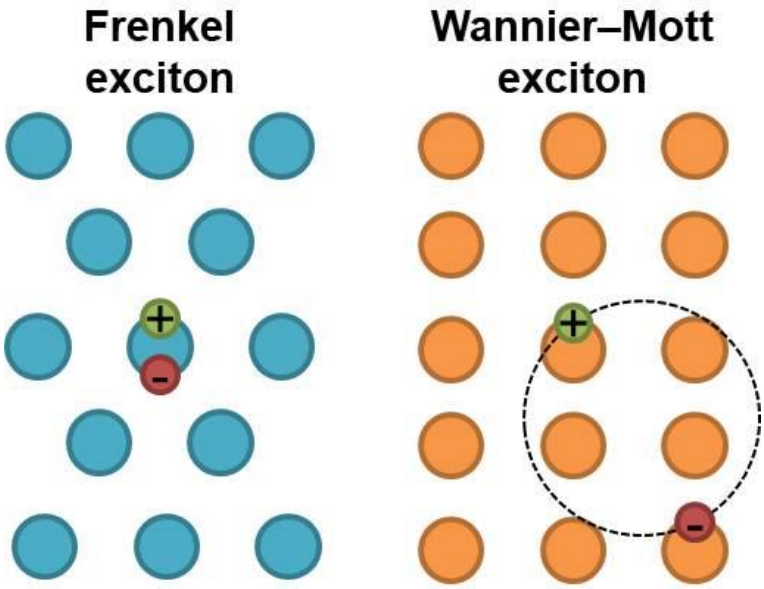

Figure 1.5 Types of excitons (Frenkel and Wannier–Mott exciton) exist in semiconductors. The distance between an electron (red minus) and a hole (green plus) is comparable or larger than the size of a crystal (circles) in the material for Frenkel and Wannier–Mott excitons, respectively.

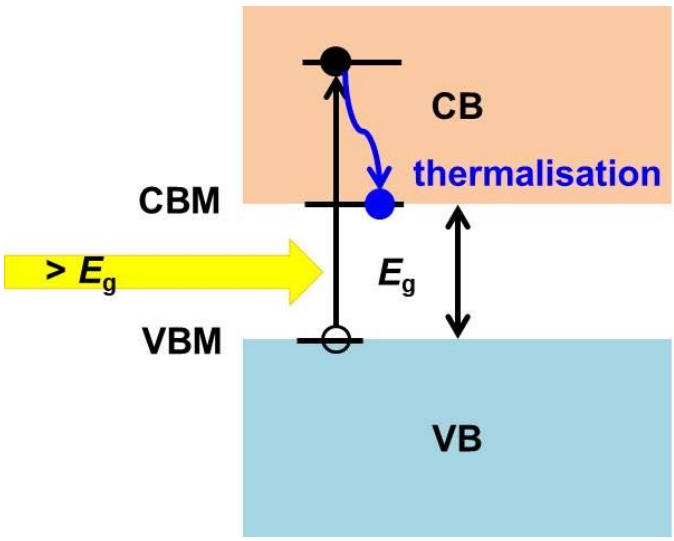

Figure 1.6 A thermalisation process when a semiconductor absorbs light with energy greater its optical bandgap.

The excitons generated must then be separated; otherwise, the electron and hole may recombine. The charge separation mechanism is associated with the *p*-*n* junction, which has been described in Section 1.3. In brief, electrons tend to move towards the *n*-type side, whilst holes move in the *p*-type semiconductor direction, as shown in Figure 1.4. Then both charge carriers with different polarity are possibly collected by the corresponding electrodes. In fact, the charge carriers created do not necessarily deliver electrical output. When an electron travels through the materials and interfaces of the cell, it may still encounter a hole and recombination may occur. The diffusion length (L_D) of a material can evaluate the extent of carrier recombination and be defined as below equation:

$$L_D = \sqrt{D\tau}, \tag{1.1}$$

where D is the diffusion constant or diffusivity (m^2/s) and τ is the lifetime in seconds. The diffusion length is the average distance that a carrier moves between generation and recombination. According to this equation, for fixed D, long diffusion length is associated

with a prolonged lifetime, which means that the carriers can survive for longer in the material. The diffusion constant is a function of several factors, as shown below:

$$D = \frac{\mu k_B T}{q}, \quad (1.2)$$

where μ, T, k_B, and q are carrier mobility, temperature, Boltzmann constant, and elementary charge, respectively. The carrier mobility is also a material-dependent factor, and electron and hole mobility typically have different values. The recombination mechanisms can be classified into two main categories: radiative (photon) and non-radiative (phonon or Auger electron), depending on the form of released energy as a result of the recombination, as shown in Figure 1.7. Compared to non-radiative recombination, radiative recombination is preferred to a photovoltaic device since the emitted light could be reabsorbed by the light absorber (so-called photon recycling effect).[16] Radiative recombination is typically a band-to-band recombination, where electrons in the CB directly recombine with holes in the VB without significant carrier momentum (Figure 1.6). Non-radiative recombination typically involves traps generated within the band gap. The recombination induced by traps is called trap-assisted recombination or the Shockley–Read–Hall process.[17] These localised deep-level traps can absorb momentum differences between electrons and holes, resulting in energy dissipation in the form of phonon excitation. The light emitted through radiative recombination may cause electrons (so called Auger electrons) emitted or excited to higher into the conduction band from the sample. This process is known as Auger recombination, as shown in Figure 1.7.

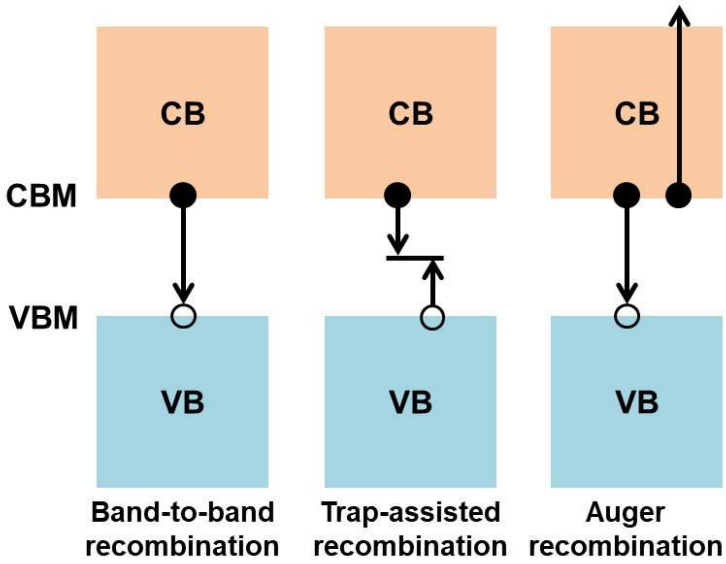

Figure 1.7 Recombination mechanisms in semiconductors, where solid and hollow circles are electron and hole, respectively.

If the carriers successfully avoid recombination to reach the electrodes, the overall current generated under illumination can be expressed as:

$$J_{\text{tot}} = J_{\text{light}} - J_{\text{dark}}. \tag{1.3}$$

Without illumination, a current is still produced (dark current, J_{dark}) due to a built-in field, which is typically in the reverse direction to the photocurrent. When carriers can reach the electrodes, an electric current and voltage can be produced, and the electrical output can be defined *via* the power conversion efficiency (PCE), which can be calculated by the following equation:

$$\text{PCE} = \frac{J_{\text{max}} \times V_{\text{max}}}{P_{\text{in}}}, \tag{1.4}$$

where P_{in} is the input power and PCE is the maximum output power. The maximum power point (MPP, P_{max}) is obtained when the product of the current density (J_{max}) and the voltage

(V_{max}) is maximised, as shown in the purple diamond of Figure 1.8. As revealed in the figure, J_{max} and V_{max} are not the highest current density and voltage, respectively; instead, these are given by the short-circuit current (J_{sc}, when voltage applied is zero) and open-circuit voltage (V_{oc}, when there is no current density detected). The ratio of the P_{max} to the product of J_{sc} and V_{oc} is the so-called fill factor (FF):

$$FF = \frac{J_{max} \times V_{max}}{J_{sc} \times V_{oc}}. \quad (1.5)$$

FF is thus the ratio of the areas of the green and red rectangles as shown in Figure 1.8. Therefore, PCE is conventionally expressed as the following equation:

$$\text{PCE} = \frac{J_{sc} \times V_{oc} \times FF}{P_{in}}. \quad (1.6)$$

Accordingly, it can be seen that higher J_{sc}, V_{oc}, and FF give better PCEs.

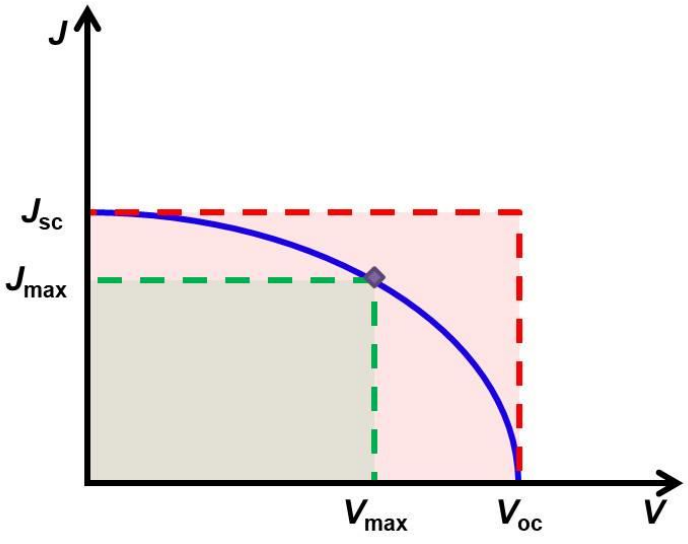

Figure 1.8 A representative graph of current density versus voltage for a typical PV device. The blue curve is the so-called *J-V* curve and the purple diamond is the maximum power point (MPP, P_{max}).

Chapter 2 Perovskite Solar Cells (PSCs)

Perovskite solar cell (PSC) is one of the most promising next-generation PV technologies to compete with or to be in tandem with mainstream crystalline silicon solar cells.[18] The reason PSCs attract tremendous attention is their high power conversion efficiencies (PCEs), surpassing 20% at relatively low costs.[19] At present, two of the three key components of the golden triangle (Figure 2.1), which describes the feasibility of commercialisation of solar panels, have been met by PSCs, namely the efficiency and the cost of manufacturing and raw materials.[19] However, the lifetime of PSCs (*ca.* 1 year) is currently far lower than that of commercialised silicon solar cells (*ca.* 25 years, with at least a 20-year warranty). One of the major causes of the instability of PSCs originates from the poor stability of perovskite materials themselves, which is discussed further in Section 2.4. This issue significantly hinders progress in the real-world deployment of PSC panels. Therefore, it is urgent to put more effort into improving the stability of metal halide perovskites, which is the core theme of this thesis.

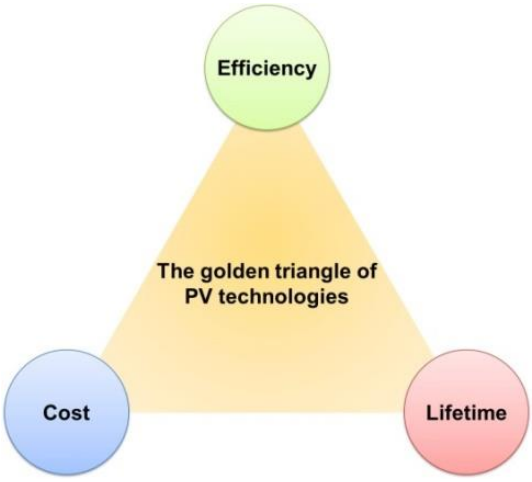

Figure 2.1 Diagram of the golden triangle to gauge the capability for commercialisation of PV technologies (efficiency, cost, and lifetime).[19]

The stability of PSCs is comparatively important compared to other devices in the current research stage because the PCEs are now relatively satisfactory. The unprecedented improvement in PCEs is the key element attracting so much interest from worldwide researchers. Hence, the advances in the PCEs of PSCs are discussed in Section 2.1.

The typical structure of a PSC is shown in Figure 2.2, where the light illuminates on the glass side. On the top of the glass, a transparent conducting oxide (TCO), such as indium tin oxide (ITO) or fluorine-doped tin oxide (FTO) is utilised to conduct electrons to an external circuit. A hole blocking layer (HBL) is located on the TCO film to reduce carrier recombination; compact TiO_2 (c-TiO_2) is often used. Then, an electron transporting material (ETM) like mesoporous TiO_2 (m-TiO_2) sits on the HBL; if a mesoporous layer is absent in the structure, this is the so-called planar architecture. Next, the key component, the perovskite light absorber, infiltrates in the mesoporous layer and a thin perovskite capping layer on the top of the mesoporous scaffold is preferred, as shown in Figure 2.3.[20] The commonly used perovskite, methylammonium lead iodide (MAPI; $CH_3NH_3PbI_3$), is a typical material. (More perovskite materials are introduced in Section 2.2 and the processing of those materials is presented in Section 2.3). Over the perovskite layer, a hole transporting material (HTM) like Spiro-OMeTAD and a metal electrode are deposited. Precious metals are often applied to connect to the external circuit to improve electrical conductivity. If the perovskite layer is deposited on an HTM, this architecture is called an inverted structure. In an inverted device, the HTM used is typically not a mesoporous layer, so an inverted device is often a planar structure.

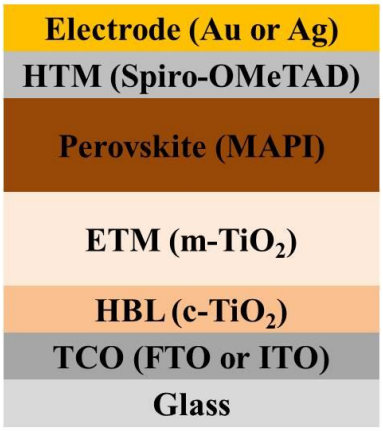

Figure 2.2 Illustration of the conventional architecture of a PSC. Note the height of the blocks does not reflect the real relative thickness of each layer.

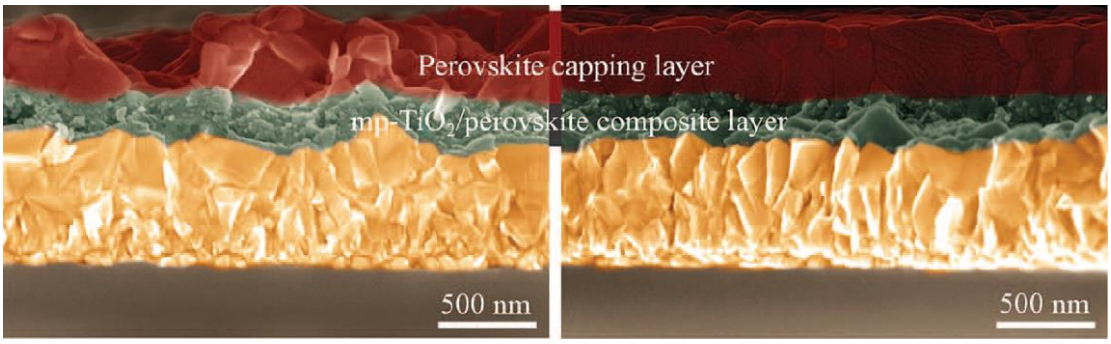

Figure 2.3 Scanning electron microscopy (SEM) images of a perovskite capping layer on a mesoporous (mp) TiO_2/perovskite composite layer.[20]

2.1 Advances in Power Conversion Efficiency

The overall view of advances in the PCE of PSCs can be seen in Figure 2.4; all the associated works in the figure are described in the below text. The first demonstration of PSCs was to employ nanocrystalline MAPI or methylammonium lead bromide (MAPB) as light sensitisers with a liquid electrolyte to deliver PCEs of 3.8% and 3.1%, respectively, back in 2009.[6] The architecture is based on liquid-state dye-sensitised solar cells (DSSCs) by simply replacing the dye molecules with perovskites. Following this, MAPI

has gained more attention than MAPB due not only to the higher beginning efficiency but also the bandgap of MAPI (*ca.* 1.55 eV) which is relatively close to the optimised bandgap (1.1–1.4 eV) according to the Shockley–Queisser treatment.[15] Hence, MAPI is commonly considered the prototype for PSCs and dominates the early stage of the development of the organometal halide perovskites.

PSCs received little attention prior to 2011 due to the low efficiency and extremely short lifetime as a result of the use of liquid electrolytes. Inspired by quantum dot solar cells (QDSCs), the crystalline size of MAPI was reduced to quantum-dot dimensions (less than 10 nm) for use in PSCs to yield a PCE of 6.5%.[21] These cells employed a liquid electrolyte for the redox couple transport and thus the PCE and stability of the PSCs were still limited. However, an important trend in the efficiencies was observed, namely that a thinner mesoporous TiO_2 layer (still in micrometre range) gave better efficiencies.[21] This finding was critical for later studies since researchers became aware that the properties of halide perovskites might be quite different from dye molecules. Important progress was made from 2012.

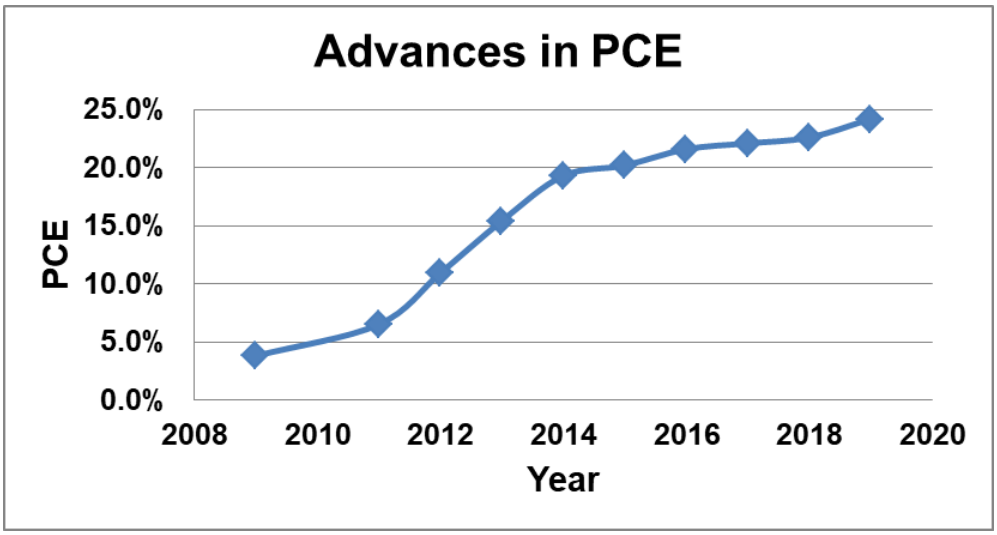

Figure 2.4 Advances in the PCE of PSCs. All concerned works are described in the main text. Note not all the PCEs shown in this figure were certificated.

Just a year later from the quantum-dot perovskite work, the same research group led by Park reported the realisation of solid-state PSCs using as an HTM layer to replace liquid electrolyte, which produced a PCE close to 10%.[22] This also led to a significant improvement in long-term stability because the problem of dissolution of MAPI into the liquid electrolyte was removed. In that work, it was again reported that a PSC containing thinner mesoporous TiO_2 (0.6 μm) generates better PCE due to a reduction in electron transport resistance. HTM-free PSCs were produced by creating a direct contact between MAPI and an Au electrode; however the PCE is lower (5.5%).[23]

Another key breakthrough made in 2012 was presented by Lee *et al.*; they first applied a mixed-halide perovskite ($CH_3NH_3PbI_2Cl$) on an Al_2O_3 scaffold to construct a PSC with a PCE of 10.9%.[24] The work demonstrated that perovskites themselves can conduct electrons well so that the ETM layer, TiO_2, is not essential in the PSC architecture. They also found that chlorine-doped MAPI is more adapted to air processing, focussing attention on mixed-halide perovskites. Building on a similar structure containing a low-temperature-processed Al_2O_3 scaffold (processed at 150 ^oC compared to 500 ^oC in the former work), $CH_3NH_3PbI_{3-x}Cl_x$-based PSCs were produced which achieved better performance with a PCE of up to 12.3%.[25] This low-temperature-annealing process potentially allows meso-superstructured PSCs to be fabricated on flexible substrates.

Heo and co-workers deposited MAPI on mesoporous TiO_2, forming a PSC with a PCE of 12.0% by employing poly-triarylamine (PTAA) as the HTM.[26] They tried various polymer-based HTMs and found that PTAA is the best candidate amongst them. Whilst the aforementioned organolead perovskites were all made *via* a one-step method, a sequential deposition (two-step process) was firstly proposed by Burschka *et al.* to produce high-quality perovskite films to yield a PCE of *ca.* 15%.[27] The advantage of this method

is that PbI_2 is easier to infiltrate into the nanopores of a TiO_2 layer compared to MAPI. Then, the PbI_2 film is converted into MAPI by dipping the film into a CH_3NH_3I solution. This gives an improved pore-filling.

Vapour deposition was then introduced to fabricate pinhole-free $CH_3NH_3PbI_{3-x}Cl_x$ perovskite films, allowing highly efficient (PCE 15.4%) planar PSCs to be made without the introduction of a mesoporous layer.[28] Meanwhile, Stranks *et al.* further verified that using $CH_3NH_3PbI_{3-x}Cl_x$ perovskites can significantly increase the diffusion lengths (to > 1 μm) compared to that in MAPI and thus the film thickness can be thicker (*ca.* 500 nm), which can offer better light absorption.[29] Chiang *et al.* utilised [6,6]-Phenyl C_{71} butyric acid methyl ester ($PC_{71}BM$) in PSCs to extract electrons, boosting the PCE up to 16.3% based on a planar architecture with the use of PEDOT:PSS as the HTM.[30] The architecture of this inverted PSC device is shown in Figure 2.5, where no metal oxides were employed as the electron/hole transporting materials of the cell.

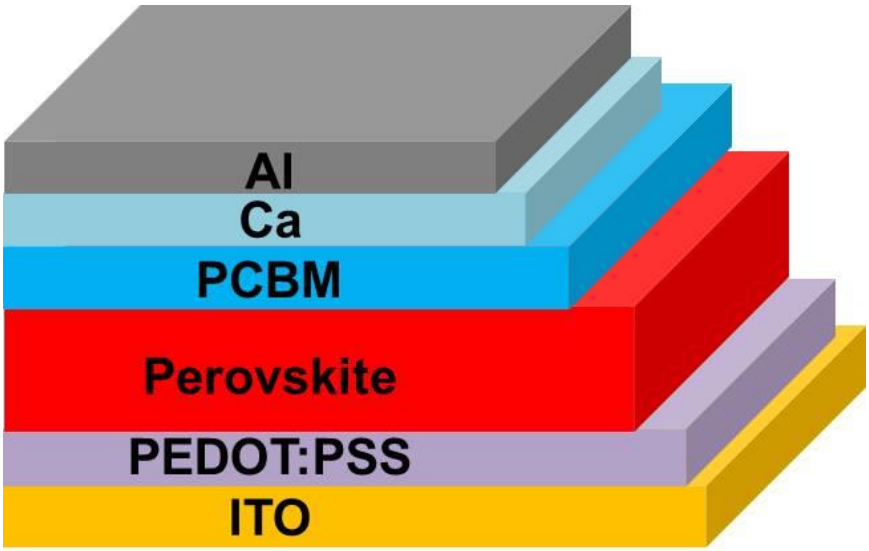

Figure 2.5 The architecture of an inverted PSC device containing PCBM as an electron transporting layer.[30]

In order to decrease the bandgap of MAPI to absorb more light, Eperon *et al.* replaced the MA cation with a larger formamidinium (FA) cation to form FAPI.[31] The resultant PSCs have achieved PCEs of 14.2% and a high short-circuit current (J_{sc}, >23 mA cm^{-2}) due to a reduction in bandgap (from 1.55 to 1.48 eV on exchanging MA for FA). Zhou *et al.* further boosted the PCE of the PSCs to an impressive value of *ca.* 19.3% through interface engineering.[32] They doped yttrium into TiO_2 to form an efficient ETM layer to extract and transport electrons better. The ITO film was also modified to possess a reduced work function to match the conduction band minimum (CBM) of the doped TiO_2. Interestingly, they found that preparing $CH_3NH_3PbI_{3-x}Cl_x$-perovskite films in a controlled relative humidity of *ca.* 30% provided a higher electrical output compared to those fabricated in completely dry conditions. In parallel, Im *et al.* optimised the two-step process to produce a high-quality MAPI film composed of well-defined cuboid perovskite grains, leading to reduction of standard deviations in PCEs, as shown in Figure 2.6.[33] The concentration of MAI solution in the sequential spin-coating step was found to be important to make efficient PSCs with PCE up to *ca.* 17%.

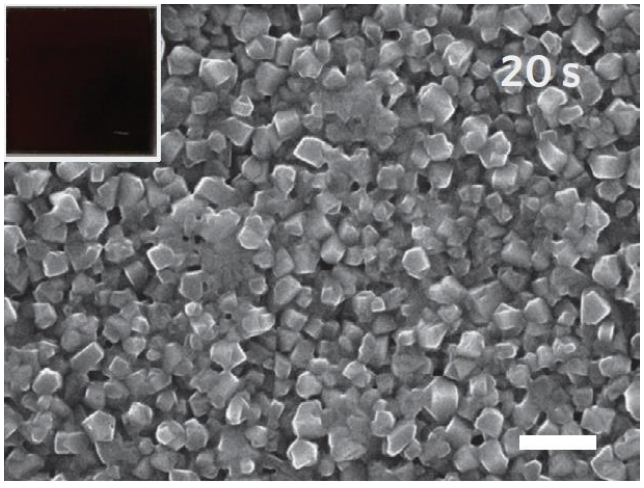

Figure 2.6 SEM image of a MAPI film containing cuboid perovskite grains.[33] Top-left view is the photograph of the sample. The scale bar is 500 nm and the time shown on the image is the loading time in MAI solution in the second step.

Mitigating the phenomenon of the hysteresis of *J-V* curves is also crucial in order to improve the PCEs of perovskite devices. The hysteresis effect is often observed in PSCs and represents the difference in the *J-V* curves of a PV device when measured in forward- (J_{sc} to V_{oc} direction) and reverse-bias (V_{oc} to J_{sc} direction) scans, as shown in Figure 2.7. In the figure, it can be seen that by inserting a PCBM layer between MAPI and TiO_2 the extent of hysteresis was significantly alleviated. Inverted PSC structures, typically with lower hysteresis have also attracted great attention. Heo *et al.* further boosted the PCE of a hysteresis-less inverted-PSC device up to 18.1% using a one-step deposition process to form a MAPI perovskite.[34] The improvement in PCEs can be partially attributed to the addition of hydriodic acid into the perovskite precursor solution, which reduces the number of iodine defects. In 2015 PCEs reached more than 20% (20.2% in [35]), which meant that the power output could compete with mainstream PVs, such as crystalline Si and CdTe solar cells. The work employed an intramolecular exchange method using dimethylsulfoxide (DMSO)-intercalated PbI_2 as the precursor to produce FAPI. Since then, research groups have shifted their attention from MA to FA-based PSCs.

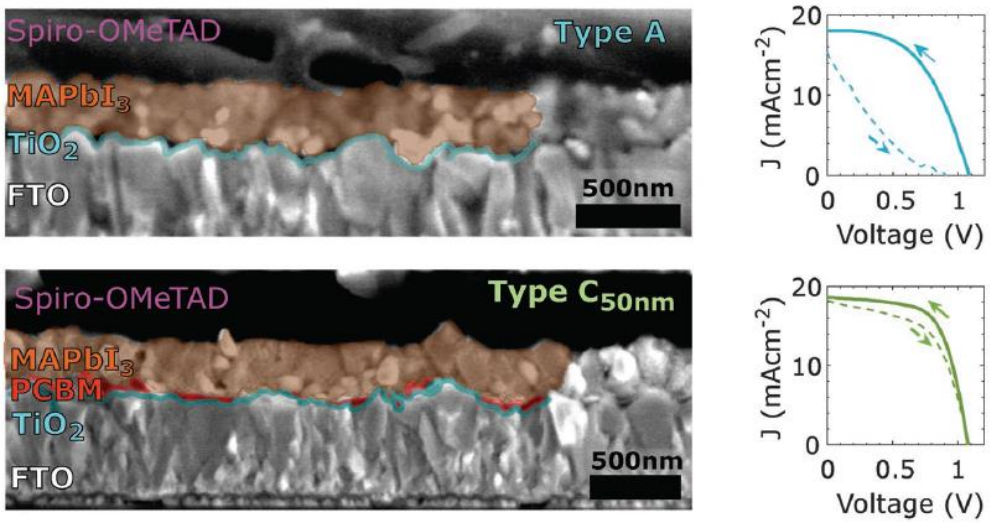

Figure 2.7 *J-V* curves (right) with different degree of hysteresis effect recorded from two architectures (left; SEM cross-section images).[36]

In recent years, mixed-cation perovskites have been used in order to produce more stable and efficient devices (with PCEs > 20%). Saliba *et al.* utilised caesium-containing triple-cation perovskites (FA, MA, and Cs) with mixed halides (I and Br) to achieve a stabilised PCE of 21.1%.[37] The same authors subsequently added one more inorganic cation, Rb, into the perovskite structure to further increase the PCE up to 21.6%.[38] The PCE of FA-based perovskites was then further raised to 22.1% by reducing iodine deficiencies in 2017.[39] Jeon and co-workers developed a new HTM with a fluorine-terminated structure to reach a PCE of 23.2% (certified 22.6%).[40] It is noted that although in the latest National Renewable Energy Laboratory (NREL) efficiency chart there is a record PCE of 25.2% achieved by KRICT/MIT,[4] the corresponding paper has not yet been published to date.

The above-presented content is based on single-junction PSCs; however, multiple-junction PSCs in tandem with various PVs to maximise light absorption have also been produced. Briefly, a PSC can either be combined with other PSCs having different bandgaps,[41] or with other types of solar cells such as silicon (typically PSCs are on the top due to better transparency as a result of larger optical bandgap).[18] The top cell with better transparency allows a portion of sunlight to reach the bottom cell. It was reported that PSCs containing FA and Cs in combination with Si solar cells form two-terminal tandem PV devices with the best PCE (23.6%).[42] Sahli *et al.* further applied the texture technique to give additional light absorption to reach a PCE of 25.2%.[43] Textured coatings are often applied to form an anti-reflective layer in order to prevent light from escaping from light absorbing regions. As shown in Figure 2.8, the bottom silicon cell was pyramidally textured in order to trap more light within the device. Using a PSC/Si architecture, now efficiencies as high as 28% have been achieved by Oxford PV.[4] The

multiple-junction tandem PSC is promising since it can potentially reach PCEs surpassing 30%,[44] overcoming the Shockley–Queisser limit of single-junction devices. Hence, there is still plenty of room to further improve the PCEs of PV devices containing PSCs.

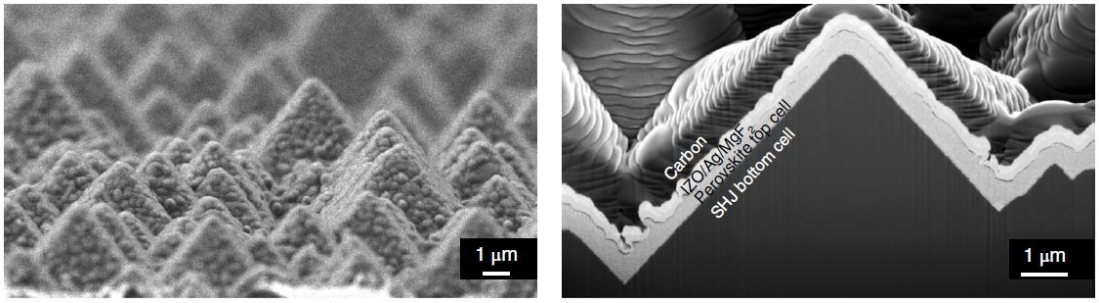

Figure 2.8 Cross-sectional SEM images of a perovskite top coated on a pyramid-textured silicon heterojunction (SHJ) bottom cell.

2.2 Metal Halide Perovskites

The perovskite light absorber is the key component of a PSC and the focus of this thesis, thereby requiring detailed discussion in this section. Generally, metal halide perovskites can be classified into mainstream lead (Section 2.2.1) and lead-free perovskites; in the latter, tin perovskites are dominant (Section 2.2.2) but other lead-free perovskites (Section 2.2.3) have also attracted great attention. A typical perovskite structure, ABX_3 (exemplified by the prototype $CH_3NH_3PbI_3$ or MAPI), is shown in Figure 2.9. Typically, the A site can be occupied by an inorganic metal ion like Cs^+ or an organic cation such as MA ($CH_3NH_3^+$) and FA ($CH(NH_2)_2^+$); B is Pb^{2+} or Sn^{2+} and X denotes halide ions (Cl^-, Br^-, and I^-). Actually, additional elements and molecules could be potentially fitted into the perovskite structure, depending on the tolerance factor.[45] The theory of the tolerance factor was proposed by Goldschmidt to estimate the structural stability of a perovskite compound, as shown in the following equation:[46]

$$t = \frac{r_A + r_X}{\sqrt{2}(r_B + r_X)}, \quad (2.1)$$

where t is the Goldschmidt tolerance factor, and r_A, r_B, and r_X are the ionic radius of the ions at A, B, and X sites in ABX_3 perovskite structure, respectively. For lead iodine perovskites, only Cs, MA, and FA sit at the acceptable tolerance-factor range from 0.8 to 1.0 in turn, as shown in Figure 2.10.[45] $APbI_3$ compounds with Goldschmidt tolerance factor out of the range indicated above are structurally unstable. Alkali metals (*e.g.* K and Rb) are too small to fit the structure well so that they typically act as dopants, which will be discussed later.

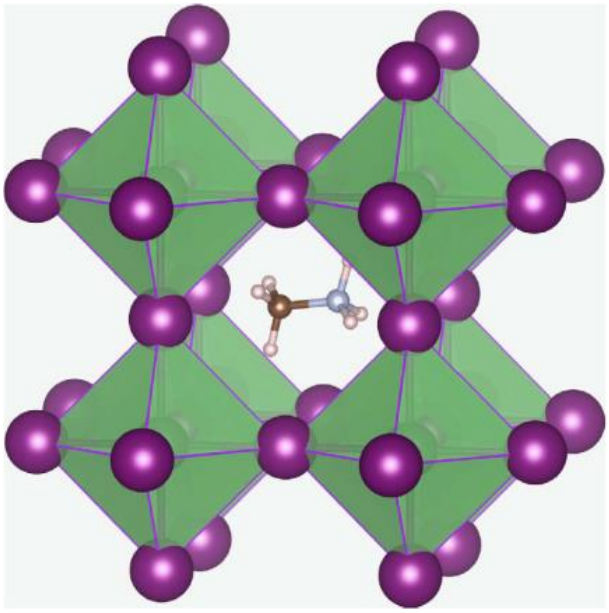

Figure 2.9 The perovskite structure (ABX_3) of MAPI. The methylammonium cation (A) is located at the central site surrounded by eight corner-sharing PbI_6 octahedra (B = Pb and X = I).[47]

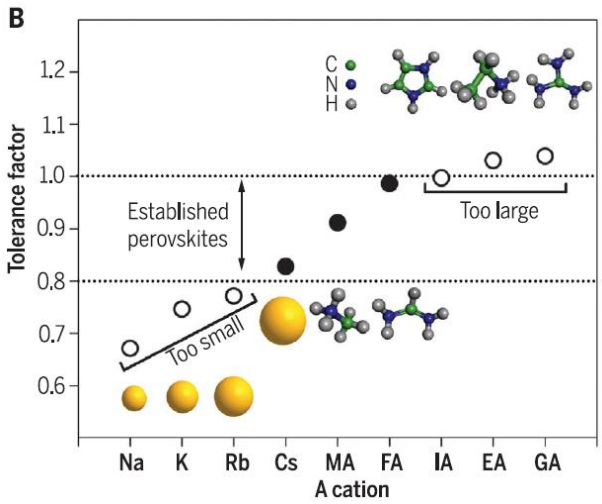

Figure 2.10 Tolerance factor of $APbI_3$ perovskites with A cations that are too small (Na, K, and Rb), applicable (Cs, MA, and FA), or too large (imidazolium (IA), ethylamine (EA), guanidinium (GA)).[45]

2.2.1 Lead Perovskites

Lead perovskites currently dominate PSCs, despite the toxicity of lead, mainly due to apparently higher efficiencies. Lead is a notorious element that can either harm the human body or easily spread into the environment to cause serious environmental issues. However, Snaith, commenting on the perovskite/Si tandem PV manufacturing process, has claimed that lead perovskites only contribute 0.27% or less to the total freshwater ecotoxicity and human toxicity of the total toxicity contribution from all process to produce a perovskite/Si tandem PV device.[7] Therefore, the research and development on lead PSCs should be continued in parallel with the investigation of other less toxic materials.

Lead perovskites have extraordinary properties that make them ideal for optoelectronics applications, such as solar cells as well as light-emitting diodes (LEDs). Taking the prototype MAPI as an example, it has a direct bandgap of *ca.* 1.55 eV, approaching the optimised Shockley–Queisser bandgap (1.1–1.4 eV) only applicable for

single-junction PV devices.[48] For a single-junction PSC, changing the chemical composition of perovskite light absorbers to adjust the optical bandgap to the Shockley–Queisser range is preferred in order to further boost the PCE. However, if halide perovskites are applied to visible-light LEDs (photon energy of 1.8–3.0 eV) or the top cell of a tandem cell, enlarging the optical bandgap of lead perovskites is required in order to well fit the corresponding applications, which can be done by substituting halide atoms. If the iodine is completely replaced by bromine and chlorine, the optical bandgap can be extended to approximately 2.25 and 3.00 eV, respectively.[48]

The substitution of the halide in lead perovskites does not allow the bandgap to be reduced to preferred values for a single-junction PV device. However, the replacement of MA by a larger organic cation (*i.e.* FA) has opened an avenue to realising a lower bandgap. FAPI can deliver not only a bandgap of *ca.* 1.48 eV but also a long diffusion length (6.6 μm for single crystals), higher than that of MAPI (hundreds nm).[49] This suggests that FA is a good choice to replace MA for use in PSCs. However, a phase stability issue impedes the use of pristine FAPI in PV devices. At room temperature, it can convert into either a photoactive black phase (α) or a photoinactive yellow phase (δ).[50] This has become a great concern for the use of pure FAPI films despite numerous approaches proposed to solve this issue.

Compared to FAPI, MAPI has more stability problems, including a structural phase transition at temperatures as low as 55 ^{o}C and degradation when exposed to heat and/or moisture.[8, 51] Consequently, it is still worth pursuing attempts to obtain structurally stable FAPI perovskites in order to achieve relatively stable and efficient FA-based PSCs. The phase instability of FAPI may originate from a high tolerance factor very close to 1 and therefore doping smaller monovalent cations is one of the best ways to structurally stabilise

FA in the perovskite structure.[37] In recent years, FA-based mixed-cation perovskites have been produced, including dual- (FA and Cs [18]), triple- (FA, MA, and Cs [37]), and even quadruple-cation perovskites (KCsFAMA [52]). In most of the mixed-cation cases, the perovskites still contain MA, which potentially degrades under thermal stress. MA-free triple-cation perovskites (RbCsFA) have recently been proposed to solve the MA-containing issue and the poor reproducibility of the CsFA perovskites.[53]

The lead perovskites presented above all have a conventional three-dimensional (3D) perovskite structure. 2D perovskites have also been proposed and investigated since they potentially extend the PSC lifetime.[54] The 2D perovskite is also called a layered perovskite because the typical use of a larger organic cation (*e.g. n*-butylammonium (BA)) can isolate the anionic Pb–I layers, as shown in Figure . The most common layered perovskites for use in PSCs is Ruddlesden–Popper (R-P) phase.[54] In a 3D perovskite structure (Figure 2.9), PbI_6 octahedra are three-dimensionally surrounded by organic cations, whilst in an R-P structure the inorganically anionic layers and organically cationic spacers are alternative to each other (Figure 2.11). Depending on the ratio between organic cations and inorganic anions (*e.g.* lead iodide) in the 2D perovskite structure, the crystal structure can be tuned and the physical properties vary as a result. The fundamental physics of 2D perovskites can be explained by the quantum well model, as shown in Figure 2.12. The thickness of organic-cation layers in 2D perovskites can be deemed as the width of a quantum well.[55] When the thickness increases, the wave function of an electron has lower ground-state energy and is less likely to penetrate the barrier due to quantum confinement. Therefore, the electron movement in the organic-cation layer is relatively constrained in 2D direction.

Due to the promising stability of 2D perovskites, they have gained great attention in

recent years.[56] However, to date, the PCEs are apparently lower than those of their 3D perovskite counterparts. Therefore, more efforts should be placed on developing more efficient 2D-lead-perovskite-based PSCs with enhanced stability. Pure inorganic perovskites are equally important regardless of their low efficiencies since they do not contain relatively vulnerable organic cations.[57] In this category, $CsPbI_3$ shows the greatest potential due to its relatively low optical bandgap of *ca.* 1.75 eV. Nevertheless, like FAPI, its photoactive phase (α-$CsPbI_3$) is not stable at room temperature and it typically requires a high annealing temperature of up to 300 ^{o}C to form, which impedes its deployment in flexible substrates. A breakthrough has been made by reducing the size of $CsPbI_3$ to quantum-dot dimensions (typically $\leq$10 nm) to stabilise the photoactive cubic phase.[58] Not only do $CsPbI_3$ quantum dots significantly improve the PCEs of $CsPbI_3$-based PSCs but a certified PCE record of 13.43% for QDSCs has also been achieved. In has also been observed that organic 2D perovskites can stabilise the α-$CsPbI_3$ phase and allow phase stability at room temperature to be maintained for months.[59]

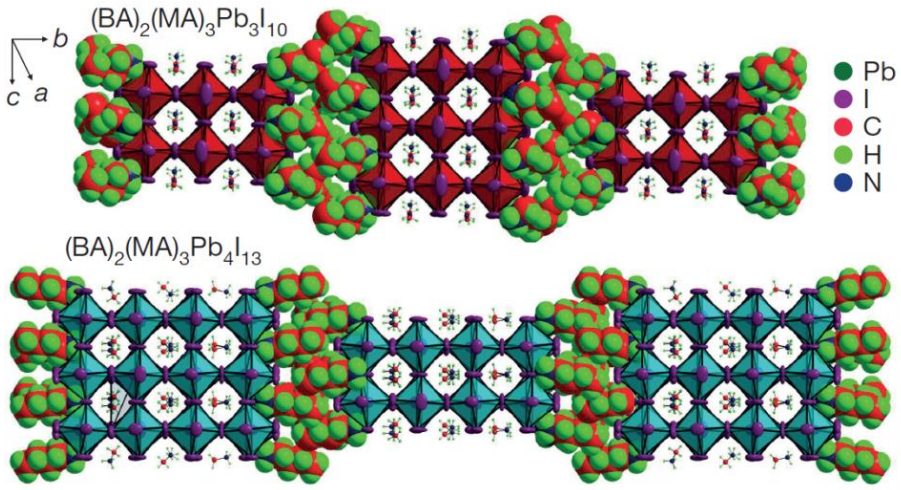

Figure 2.11 Crystal structure of the Ruddlesden–Popper $(BA)_2(MA)_2Pb_3I_{10}$ and $(BA)_2(MA)_3Pb_4I_{13}$ layered perovskites.[54]

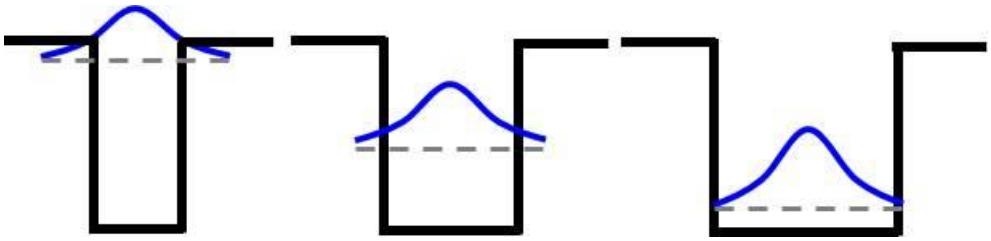

Figure 2.12 Diagram of the quantum confinement effect in 2D perovskites. Various thicknesses of organic-cation layers in 2D perovskites lead to the different widths of quantum wells (black lines; equivalent to CBM energy level in a semiconductor). The (blue) curve is the wave function of an electron and the (grey) dash line indicates the lowest energy (ground state) of the wave function.

2.2.2 Tin Perovskites

In order to replace the toxic lead in halide perovskites, tin perovskites with less toxicity have been investigated due to their similar properties to lead and lower optical bandgaps. The first attempt to make tin-based PSCs, methylammonium tin iodide (MASI, $CH_3NH_3SnI_3$), was reported in 2014.[60] In that work, a $CH_3NH_3SnIBr_2$-based PSC reached a PCE of *ca.* 6%. The preparation requires care because Sn^{2+} is easily oxidised to Sn^{4+}, leading to heavy *p*-type doping. FASI-containing ($FASnI_3$) PSCs were used to generate a PCE of up to 6.22%, based on a planar inverted architecture.[61] Recently, the efficiencies of Sn-based PSCs have been enhanced to values approaching 10%,[62, 63] triggering more on-going research in this area. Shao *et al.* mixed a small amount of 2D tin perovskites into 3D FASI to improve efficiencies.[63] Based on this strategy, Jokar and colleagues further boosted the PCE to 9.6%.[62] As in lead perovskites, FA is found to be more stable than MA (offering a lower oxidation rate) and can offer better efficiencies. Until now, compared to MAPI or FAPI, Sn-based PSCs have comparable short-circuit current density and fill factor but a significantly lower open-circuit voltage. This suggests severe carrier recombination, which must be urgently addressed to reach higher PCEs.

Inorganic tin perovskites, which potentially possess better stability compared to MASI and FASI, have also been widely studied. $CsSnI_3$-based PSCs (using hydrazine to suppress the formation of Sn^{4+}) have reached a PCE of 4.81%.[64] Although many approaches to solving the oxidation issue have been proposed, the formation of Sn^{4+} is still inevitable in tin (Sn^{2+}) perovskites. Based on this fact, the double perovskite structure (Cs_2SnI_6; see Figure 2.13) has gained interest from researchers since this is a Sn^{4+} compound. According to the figure, Cs_2SnI_6 can be deemed as removal of half Sn in the structure of $CsSnI_3$. Cs_2SnI_6 was firstly utilised in DSSCs as a HTM and showed promising physical properties, such as a low optical bandgap of *ca.* 1.3 eV and satisfactory electron mobility (310 $cm^2/V \cdot s$).[65] These properties suggest the potential to apply Cs_2SnI_6 as a light absorber for use in PSCs. However, to date, these materials reveal a range of physical properties, probably depending on the preparation process.[9, 66, 67] It does, however, show excellent air stability both during and after fabrication. Qiu *et al.* applied ageing as a process to transform $CsSnI_3$ to Cs_2SnI_6 and obtained a device with PCEs below 1%.[66] They ascribed the low PCEs to the mismatch of energy level alignment (ELA) between the TiO_2/perovskite/HTM layers. By optimising preparation processes, Lee and co-workers demonstrated a pristine Cs_2SnI_6-based PSC with a PCE of approximately 1.5%, whilst $Cs_2SnI_4Br_2$-based PSCs can reach *ca.* 2%.[68] The use of Sn-doped TiO_2 facilitates the electron extraction from the double perovskite due to better ELA. It is worth noting that the architecture used was not the classic type due to the occurrence of a short-circuit in the classical structure as a result of an incomplete coverage. The light absorber was sandwiched by two substrates rather than deposited on one substrate as the conventional form. A 2018 patent reports the PCE has been further improved to 5.21% (not yet published as a journal paper), which is comparable with that of $CsSnI_3$-based PSCs but with much better stability.[69] Although the promise

of this material is unclear, there is still great room to improve the performance of the devices, making use of its excellent stability.

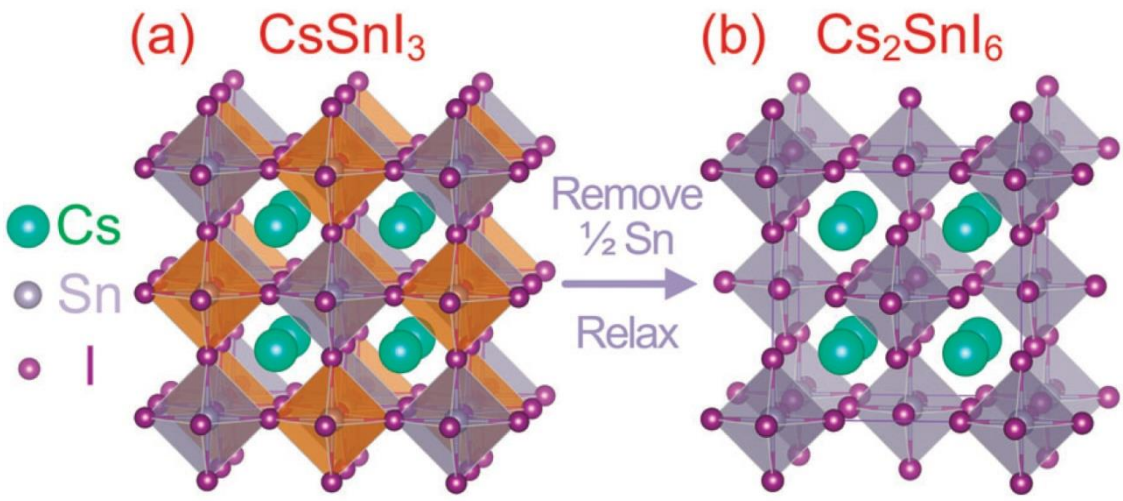

Figure 2.13 Crystal structures of the $CsSnI_3$ perovskite (left) and Cs_2SnI_6 double perovskite (right).[70]

2.2.3 Other Lead-Free Perovskites

Tin perovskites not only suffer oxidation issues, but currently also show low PCE. Therefore, other lead-free materials have been investigated to replace toxic lead. Based on the requirement for stability, most of the studies on non-tin lead-free perovskites relate to materials having the double perovskite structure. Amongst these, bismuth (Bi) has recently emerged as a potential less toxic element compared to Pb for use in PSCs.[71] Unlike Cs_2SnI_6, $Cs_2AgBiBr_6$ possesses different elements in the B site with the same total valence electrons (Bi^{3+} and Ag^{+}) of 4 as Sn^{4+} in Cs_2SnI_6.[71] The bandgap of this material is close to 2 eV, which may make it a good candidate in tandem with silicon solar cells. Encouragingly, $Cs_2AgBiBr_6$ has quite a long carrier recombination lifetime (*ca.* 660 ns), suggesting the potential for use in PSCs. By changing the dimensionality, Bi-based

perovskites can adopt the form of $Cs_3Bi_2I_9$ for example, with a bandgap of 1.9 eV.[72] To date, the PCEs of Bi-based PSCs have reached approximately 1.26% (for $Cs_2AgBiBr_6$).[73] Other major non-tin lead-free perovskites are antimony (Sb)-based materials, such as $Cs_3Sb_2I_9$.[74] Sb has similar properties (less toxic than Pb) and abundance (Figure 2.14) to Bi, and, recently, $Cs_3Sb_2I_9$-based PSCs have reached an efficiency of around 1%.[75]

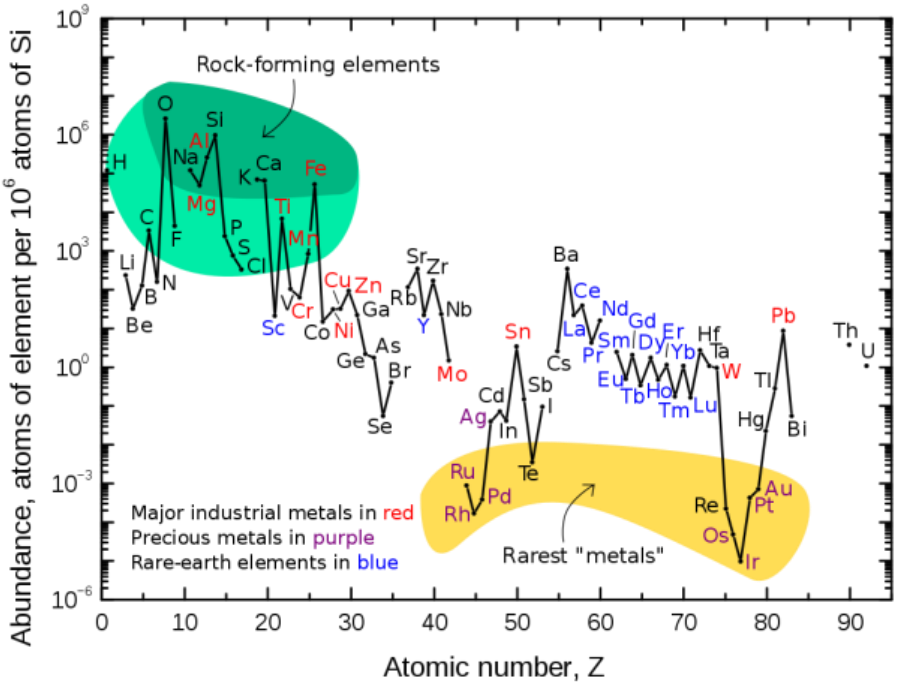

Figure 2.14 Diagram of the abundance of elements in the upper continental crust.[76]

2.3 Processing

Compared to semiconductor manufacturing, the fabrication of PSC devices is relatively simple and facile, so they have a low manufacturing cost. The synthetic details of the preparation of the perovskite light absorber play a vitally important role in achieving highly efficient and stable solar cells. Thus, the processing is discussed below. This thesis focuses on the fabrication of halide perovskite films only.

2.3.1 Solution-Based Methods

Solution-based preparation is predominant in the fabrication of halide perovskites due to its simplicity and low cost. Spin coating is applied in most academic studies and lab-scale preparations. Spin coaters are ubiquitous in chemical labs and their parameters, such as rotational speed, are easy to tune. Typically, spin coating only allows small substrates (less than 3 cm^2) to be uniformly coated.[77] Therefore, the scalability of the spin coating is a great concern but it enables PSCs to be investigated easily in the lab.

Spin coating for halide perovskites is classified into two main routes: one-step (single-step) and two-step (sequential deposition). Taking MAPI as an example, in the single-step process typically PbI_2 and MAI are dissolved into *N*,*N*-dimethylformamide (DMF) to form a 1M (molar concentration) precursor solution. The disadvantage of this method is that perovskite molecules are too big to infiltrate well into the pores of mesoporous TiO_2.[27] Hence, the pore filling may be insufficient to afford efficient PSCs.

In order to solve the pore-filling issue, the Graetzel group developed a sequential process in which PbI_2 is deposited first and subsequently reacted with MAI to form the perovskite structure.[27] The first step is typically spin coating and the second step can be dip coating,[27] spin coating,[78] or vapour deposition [79]. Amongst them, dip coating is the dominant route for this sequential step as a result of simplicity, and the as-formed PbI_2 film is typically immersed into a 2-propanol (IPA) solution containing MAI with suitable concentration (*e.g.* 10 mg ml^{-1}) for a few seconds.[27] The selection of IPA is because it is a poor solvent for PbI_2 and the perovskites. However, the sequential process may lead to incomplete conversion to perovskites. Therefore, adding some MAI into the PbI_2 precursor was proposed to alleviate this problem.[80] The optimised ratio of MAI/PbI_2 is

typically found to be approximately 20%.[81]

Apart from PbI_2, other lead precursors have been utilised to form perovskites, *e.g.* $PbCl_2$:MAI 1:3 in molar concentration.[82] Chlorine incorporation into the film was found to be negligible but it tends to aggregate at the TiO_2 interface.[82] MAPI films prepared from different lead precursors appear to have distinct properties, especially differing in stabilities in air. Generally, the use of other lead precursors (such as $PbCl_2$, [25] lead acetate ($Pb(Ac)_2$), [83] and lead thiocyanate ($Pb(SCN)_2$) [78]) instead of PbI_2 can give better ambient air stability. In particular, $Pb(SCN)_2$ enables ambient-air processing (Figure 2.15) to obtain satisfactory efficiencies, but the current PCEs still remain at *ca.* 15%.

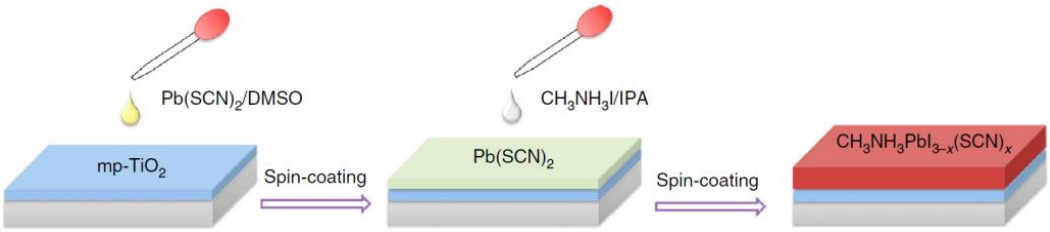

Figure 2.15 Illustration of fabrication of perovskite films from $Pb(SCN)_2$ precursor using a sequential (two-step) process.[78]

The use of DMSO in the solvent mix revolutionises the spin-coating process. Unlike DMF or γ-butyrolactone (GBL), DMSO acts as not only a solvent but also as a functional additive to form a PbI_2–DMSO–MAI intermediate that retards rapid self-assembly crystallisation.[84] This control of the nucleation rate allows the perovskite deposition to be uniform and dense films are produced. These deposition processes are typically carried out in conjunction with the use of an antisolvent to make the films more uniform and dense. The requirement of an antisolvent is that it cannot dissolve the perovskite materials and is miscible with the other solvents used.[84] Generally, the antisolvent used is dripped onto

the surface during spinning (Figure 2.16). The exact dripping timing depends on the type of the antisolvent used and the perovskite system.

To date, a variety of antisolvents have been applied to the preparation of perovskite films, *e.g.* toluene,[84] chlorobenzene[85], ether and acetate associates.[85] Toluene and chlorobenzene are the most common antisolvents integrated into the spin-coating process, typically under low relative humidity conditions. In an ambient atmosphere with high relative humidity (RH) of above 50%, methyl acetate and ethyl acetate (EA) are the preferred antisolvents since they are expected to extract water molecules from the perovskite films as they form.[86, 87] Therefore, the use of EA is selected in this thesis (Chapter 5) to enable air processing of MAPI.

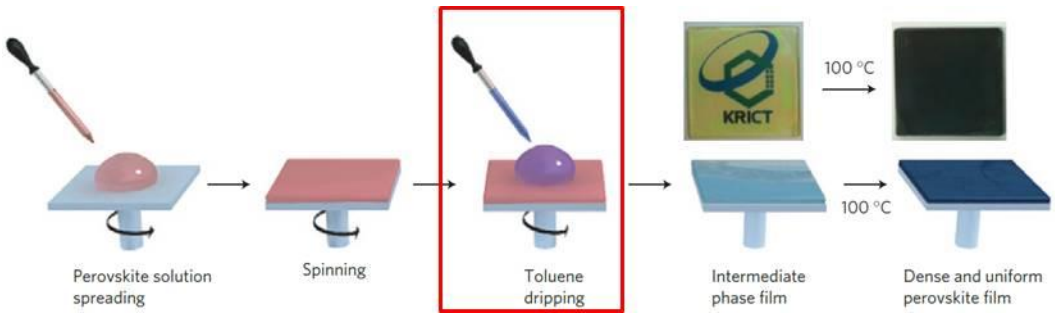

Figure 2.16 Illustration of the spin-coating process involving an antisolvent step highlighted.[84]

2.3.2 Non-Solvent Deposition

Typically, for manufacturing processes requiring high-quality films, a non-solvent method or vapour-based deposition is favoured to produce pinhole-free, homogenous films. The spin-coating method for the fabrication of PSC devices has limited scalability, which hinders progress in the commercialisation of PSC panels. Although vapour deposition, which typically requires the employment of a vacuum system, has a higher cost than

solution-based methods, it possesses numerous advantages over spin coating. For example, vacuum vapour deposition can easily enable multilayer deposition. In contrast, the use of solution-based methods typically leads to the dissolution of the first-layer perovskite film when depositing the second-layer perovskite solution.[88] This confines PSC architectures deposited by this route to those containing single-layer perovskites only, limiting further improvements in PCEs.

Vapour deposition was first utilised in PSCs by Liu *et al*. to produce efficient planar devices with a PCE of 15.4% from dual sources of MAI and $PbCl_2$.[28] Vapour deposition has also been used to fabricate MAPI films from PbI_2 in an inverted architecture, showing excellent smoothness of the films.[89] Although better scalability is expected through vapour deposition, most of the studies using vapour deposition are still based on small-area devices. A first attempt to make a relatively larger active area device (*ca.* 1 cm^2) was carried out by Malinkiewicz *et al*.[90] A PCE of around 11% was obtained, a reduced value compared to the corresponding small-area devices. Until now, perovskite films fabricated *via* vapour deposition have not produced better PCEs than spin-coated films, probably due to reduced flexibility in controlling the morphology of the films.[91]

2.3.3 Hybrid Processes

Hybrid processes that combine the concepts of solution-based and non-solvent methods have also gained attention in order to further improve the efficiency and stability of PSCs. The most typical hybrid process is to use spin coating as the first step and vapour deposition as the sequential step. For instance, Chiang and co-workers used MAI vapour to convert PbI_2 and $Pb(SCN)_2$ to perovskite films.[79] This kind of approach is called a vapour-assisted solution process (VASP) and leads to full surface coverage and small surface

roughness. [92] Whilst the majority of the VASP vapour deposition processes are carried out in a vacuum system, Yin *et al*. conducted the vapour deposition step under ambient pressure to obtain efficient PSCs with PCEs over 18%.[93]

Another related process that combines elements of solution processing with vapour deposition is aerosol-assisted chemical vapour deposition (AACVD). The deployment of the AACVD technique into the PSC area was first achieved by Lewis *et al*. for the fabrication of $CH_3NH_3PbBr_3$.[94] Subsequently, a few studies were dedicated to AACVD-grown perovskite films, through either single-step, [95-98] or sequential step processes.[99, 100] All works cited previously focus on lead perovskites, particularly MAPI films. The first synthesis of a lead-free perovskite by AACVD (Cs_2SnI_6 double perovskite) is presented in Chapter 8.[9] For AACVD-grown MAPI, only PbI_2 had been used as a precursor prior to this work. In this thesis, a pseudohalide lead precursor, $Pb(SCN)_2$, is utilised to enable air annealing and enhance the stability against humid air; the details are presented in Chapter 5. Since AACVD is one of the key components in this report, a detailed introduction is given below and the instrumentation is presented in Section 3.3.3.

2.3.3.1 Aerosol-Assisted Chemical Vapour Deposition (AACVD)

AACVD is a solution-based variant of the conventional CVD process and can be operated under atmospheric pressure. The solution used is typically more dilute than that used for spin coating and the solvent needs to be capable of being nebulised; *i.e.* it must transform into a mist or aerosol. An aerosol is generated from the precursor solution by an ultrasonic humidifier/nebuliser. Then, a carrier gas is input to bring the mist generated to the connected CVD reactor or furnace where substrates are placed and heated. When the

precursor aerosol droplets travel from the solution at room temperature to the heated substrate, the solvent evaporates as a result of experiencing increasing temperature, as shown in Figure 2.17. The temperature set needs to be high enough to evaporate the solvent(s) and enable the desired chemical reaction. However, if the temperature is too high, the solvent of the aerosol droplet could completely evaporate and the aerosols become powders prior to reaching the substrate such that the resulting film may have unsatisfactory adhesion to the substrate and can be porous. Therefore, correct adjustment of the temperature profile along the reactor is extremely important for the AACVD process. Compared to conventional CVD techniques, the deposition rate in AACVD is higher, so in principle it has a greater production capacity. Furthermore, AACVD allows a greater range of precursors to be used; *e.g.* lead thiocyanate cannot be utilised in vacuum deposition due to its relatively low decomposition temperature compared to its vapourisation temperature.

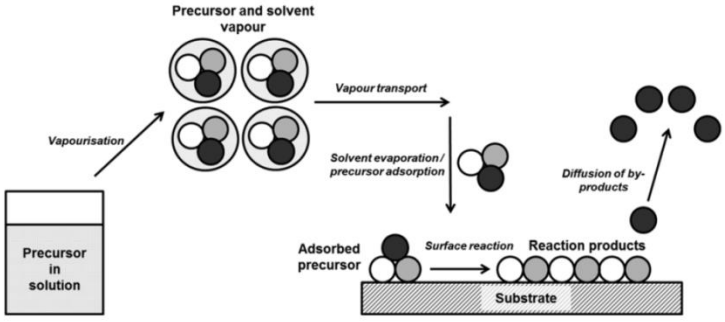

Figure 2.17 Schematic illustration of the mechanism and processes of AACVD.[101]

2.4 Progress in Stability

The instability of PSCs constrains their commercialisation, despite the fact that the efficiencies of the devices have made them competitive with other photovoltaic technologies.

Until now, the best PSCs can only achieve lifetimes (defined as a PCE drop of less than 20% of its original value) of approximately 1 year, far lower than those of commercialised silicon solar cells (*ca.* 25 years).[19] The device with a one year lifetime only has a PCE of *ca.* 11%.[102] The lifetimes of PSCs with efficiencies higher than 20% reach only around one to two months; thus, great effort is required to improve the stability of PSCs.[103]

The instability of PSC devices mainly originates from the perovskite light absorber itself and its interfaces in contact with carrier transporting layers. The sources that induce degradation of perovskites are classified into three types: atmospheric, thermal stress, and light, as detailed below.

2.4.1 Atmosphere-induced Degradation

Typical halide perovskites, such as MAPI, are notorious for their vulnerability to ambient air during or after formation. This is the reason that perovskite materials are typically prepared in a controlled environment, *e.g.* a drybox or glovebox. Two main factors in the air that cause degradation of perovskites are oxygen and moisture. Oxygen-induced degradation can originate from external or internal factors, *i.e.* oxygen gas in the air or oxygen from metal oxides used as electron/hole transporting materials, respectively. The oxygen-induced degradation of perovskite materials generally occurs under light illumination. When light is present, photo-excited electrons are generated in the perovskite absorber, which can transform the oxygen gas contacted with the perovskite surfaces into superoxide (O_2^-).[104] Then the superoxide generated can react with the organic components of the perovskites, *e.g.* MA^+ in MAPI, leading to deprotonation of $CH_3NH_3^+$ to CH_3NH_2, along with the decomposition of MAPI.[104] Aristidou *et al*. found that the degradation rate of MAPI varied as a result of the distinct amounts of superoxide

produced in different metal oxide scaffolds used (with the rate of degradation higher for an Al_2O_3 scaffold than for TiO_2).[104] These authors proposed that in TiO_2, the photo-excited electrons are extracted quickly by TiO_2, resulting in reduced time to form superoxide. In a later study, the same research group found that the smaller the perovskite grain sizes, the more severe the degradation. It was also found that iodine vacancies are the preferred locations to induce this degradation.[105] Although the above-mentioned studies suggest the decomposition of MAPI directly to PbI_2, it was also suggested that superoxide could adsorb at iodine vacancy sites to form Pb−O bonds in the perovskite.[106] Sun *et al*. further suggests oxygen-induced degradation can commence during the fabrication of perovskite films.[107]

Another ubiquitous source to degrade perovskite films is water (vapour). Wang *et al*. found that moisture can infiltrate into the grain boundaries and intergranular films, leading to grain degradation.[108] Interestingly, after placing perovskite films in humid air for a few hours, the PCEs were improved, suggesting that an environment with moderate relative humidity (RH *ca*. 50%) is preferred for the fabrication of perovskite films.[109] It was also found that H_2O molecules can assist the formation of larger grains. This is proposed to occur when moisture located at the grain boundaries acts as an adhesive leading two adjacent grains to merge together.[110]

However, longer ageing times in humid air can lead to the decomposition of the perovskite. Upon H_2O exposure, it is proposed that MAPI turns into hydrates first and then into PbI_2, which has been observed by *in situ* X-ray diffraction.[111] There have been a number of proposals for the degradation mechanism in the presence of water. Niu *et al*. suggested that, unlike oxygen-induced degradation, Al_2O_3 can provide better protection for MAPI compared to TiO_2.[112] They also proposed that moisture induces MAPI to degrade

into MAI and PbI_2 and then CH_3NH_2 may be released from the films. However, there is no clear evidence to show the formation of MAI from MAPI. Yang *et al*. suggested that before forming MAI, hydrated MAPI ($(CH_3NH_3)_4PbI_6 \cdot 2H_2O$) is produced upon exposure to moisture.[111] At this stage, the process is reversible. Leguy and co-workers further suggested that prior to the formation of MAPI dihydrate, MAPI monohydrate ($CH_3NH_3PbI_3 \cdot H_2O$) forms on exposure to moisture.[113] However, once PbI_2 is formed after exposure to sufficient H_2O molecules, the degradation becomes irreversible.[114]

Whilst all reports agree on the eventual formation of PbI_2 upon water exposure, there is still some debate regarding whether the by-product containing nitrogen is MAI, MA, or NH_3. [113-116] However, through XPS study, Li *et al*. found that under H_2O exposure, the carbon atoms of the MAPI surface actually remain following loss of nitrogen, suggesting that the nitrogen is lost as ammonia gas.[116] In this thesis, we further support this inference by using the NAP-XPS technique to probe the reaction of MAPI with water (Chapter 4). The increased amount of hydrocarbon bonds matches the decrease in the nitrogen concentration, suggesting that the loss of nitrogen cannot proceed by the escape of MA.[8]

2.4.2 Thermal Stability

Halide perovskites can degrade and decompose even under gentle thermal stress, particularly the types containing organic cations such as MA. $MAPbCl_3$ can undergo decomposition at around 150 ^oC, whilst MAPI and $MAPbBr_3$ can tolerate higher temperatures of up to *ca.* 240 ^oC, as revealed by *in situ* X-ray diffraction (XRD).[117] However, it was found that when MAPI is annealed at 130–150 ^oC, the efficiency of the PSCs starts to significantly drop due to the formation of PbI_2.[118] In that work, the film

has fully converted into PbI_2 at only 170 ^oC, which may be attributed to different preparation methods. Apart from the heating temperature, the duration of heating also requires consideration; Franeker *et al*. found that at an annealing temperature of 92 ^oC, 5-minutes is the optimum heating time to give the best PCEs.[119] These authors used XPS to determine the surface composition of MAPI films and discovered that after 5 minutes' annealing, the N/Pb ratio is close to 1 (the stoichiometric value).

Although MAPI films are typically stable when heated up to 100 ^oC, the phase transition can de-stabilise the perovskite films. At an increasing temperature exceeding 60 ^oC, the crystal structure of MAPI may transform from a tetragonal to a cubic system.[120] This also raises the concern regarding long-term stability at 85 ℃, since such a temperature is easily achieved on exposure to sunlight. Conings *et al*. performed a detailed study of MAPI heated at 85 ^oC in various atmospheres (N_2, O_2, and ambient air).[121] They discovered that humidity is primarily responsible for the degradation, in conjunction with thermal stress and oxygen.

The carrier transporting material in contact with the perovskite layer also plays an important role in thermal-induced degradation. Several studies have found that ZnO accelerates the degradation under thermal stress due to the presence of hydroxides on the surface of ZnO.[122, 123] The OH^- leads to the dissociation of iodine in MAPI films to form CH_3NH_3OH which easily further degrades into CH_3NH_2 and H_2O under thermal stress. Thus, ZnO may not be a good choice for use in PSCs.

FAPI, which can be heated up to *ca.* 150 ^oC, is relatively thermally stable compared to MAPI.[31] Doping inorganic Cs into FAPI can improve both the phase and thermal stability of FAPI.[18] Long *et al*. conducted a detailed thermal degradation study of

$Cs_{0.17}FA_{0.83}PbI_2Br$.[124] It was found that at temperatures over 160 ^oC, PbI_2 impurities start to form. In addition, FA and Br are congruently lost from 100 ^oC in the form of FABr gas, resulting in decomposition. Therefore, Long *et al.* proposed FABr post-treatment to enhance the stability of the perovskites; this could pave the way towards highly stable PSCs.

Although FA is more stable than MA, FA-based perovskites are still not sufficiently stable to prevent degradation upon heating caused by light soaking. Using Cs to replace organic MA and FA can improve the thermal stability since both $CsPbI_3$ and $CsPbI_2Br$ can tolerate temperatures over 300 ^oC.[57, 125] However, due to their low structural tolerance factor, some approaches are required to stabilise the photoactive phase. For example, Zeng *et al*. found that adding $Pb(Ac)_2$ as an additive into $CsPbI_2Br$ can form PbO that passivates grain boundaries and not only improves the phase stability but also lowers the fabrication temperature from 350 to 150 ^oC.[125] To sum up, improving thermal stability is mainly addressed by composition tuning to increase the decomposition barrier, whilst the atmospheric instability may be solved by encapsulation techniques.[19]

2.4.3 Photostability

Photodegradation of perovskites is a critical issue to be solved as they are the light absorbers in PSCs. Tang *et al*. used many *in situ* techniques to identify the photoinduced degradation of MAPI films; they found that under illumination, MAPI degrades more in the air and in a vacuum than under nitrogen.[126] In a vacuum, MAPI directly decomposes into lead iodide and metallic lead, whilst in the air, MAPI can degrade into $Pb(OH)_2$ and $PbCO_3$, in addition to PbI_2 and Pb^0, due to the presence of oxygen atoms in molecular oxygen and water. Interestingly, in dark and ambient air environments, the MAPI film does not undergo any obvious change, suggesting that light accelerates the deterioration of

MAPI films in the air. Recently, Yang and co-workers performed a comprehensive study of the photostability of various perovskites ($MAPb(I_{0.83}Br_{0.17})_3$, $FA_{0.83}MA_{0.17}Pb(I_{0.83}Br_{0.17})_3$, and $Cs_{0.1}(FA_{0.83}MA_{0.17})0.9Pb(I_{0.83}Br_{0.17})_3$, abbreviated as MA, FAMA, and CsFAMA respectively).[127] According to XRD, under light illumination, CsFAMA has the least PbI_2 impurities and exhibits the best photostability. These authors also found that the degradation is more obvious in UHV than in N_2 environments since the organic components of the perovskite tend to vapourise in vacuum with pressures lower than their vapour pressures.

In sunlight, the UV component has a key role in degradation since UV light easily causes the decomposition of perovskite films if a mesoporous layer, such as TiO_2, is present.[128] Leijtens *et al*. proposed that the prevalent surface defect of TiO_2, Ti^{3+}, acts as an effective electron-donating site to interact with adsorb O_2 from the atmosphere.[128] UV light can photoexcite TiO_2 (E_g ~3.2 eV) and the photoexcited electrons can react with O_2 *via* Ti^{3+} surface states. Therefore, O_2^-/Ti^{4+} coupling complex is formed as a result of charge transfer.[129] Subsequently, the superoxides generated attack neighbouring perovskite materials, especially the organic parts, as mentioned in Section 2.4.1.[104] It is noted that the work by Aristidou *et al*. as described in Section 2.4.1 applied a tungsten halogen lamp (visible light) rather than a UV light source.[104] Therefore, the light degradation of MAPI was contrarily alleviated by applying TiO_2 mesoporous layer, showing some discrepancies in the outcome of these two works.[104, 129] The quality of the TiO_2 film used in PSCs, *i.e.* the concentration of Ti^{3+}, in contact with halide perovskites can also affect the light-induced degradation behaviour of the perovskite films. The UV degradation issue may be solved by introducing a UV filter, but some electrical output is sacrificed.

Chapter 3 Techniques and Theory

3.1 X-ray Photoelectron Spectroscopy (XPS)

3.1.1 Theory of Photoemission

X-ray photoelectron spectroscopy (XPS) is a surface characterisation technique that can provide the quantitative information of a sample with an atomic sensitivity down to 0.1%. The working principles of XPS are based on the photoelectric effect that describes the emission of electrons when light illuminates a material. X-rays are used as the light source in XPS. An incident X-ray of energy ($h\nu$) excites electrons, causing them to be emitted from the surface (mostly within 1 – 2 nm). In an ideal situation, some of the electrons coming from the sample do not undergo kinetic energy (*KE*) loss after being excited by X-rays. As a consequence, the kinetic energy of the electrons measured by an electron energy analyser can be obtained from the equation (3.1):

$$KE = h\nu - BE - \Phi. \quad (3.1)$$

BE is the binding energy of the electron excited in an atom and Φ is the work function that describes the minimum photon energy required to remove an electron from the Fermi level (E_F) of a given material to the vacuum level (E_{vac}) outside the material. The binding energy of an electron can be defined as the energy difference between the initial state and the final state of the atom/ion and the free photoelectron.[130] The value is equal to the negative of the orbital energy, based on the Koopmans' theorem.[130]

An illustration of the photoelectric effect is shown in Figure 3.1; a photo-excited electron (the solid circle) needs to overcome two barriers, *i.e.* the binding energy and the

work function to reach the electron energy analyser, with the remaining kinetic energy to be recorded. Following the electron emission from the atom, the atom is left positively charged. A hole (the hollow circle) then is left in the original energy state. As shown in the diagram, the binding energy of a core-level electron (a discrete energy state) is higher than that of a valence electron (a continuous band associated with bonding between the neighbouring atoms). Therefore, photo-exciting a valence electron requires less energy compared to a core-level electron.

According to Figure 3.1, the work function of the sample is not essential to obtain the binding energy. Since the spectrometer and the sample probed are in electrical contact, their Fermi levels are aligned. Hence, only the kinetic energy (KE_{spec}) measured and the work function of the spectrometer (Φ_{spec}) are required to obtain the *BE* of the sample.

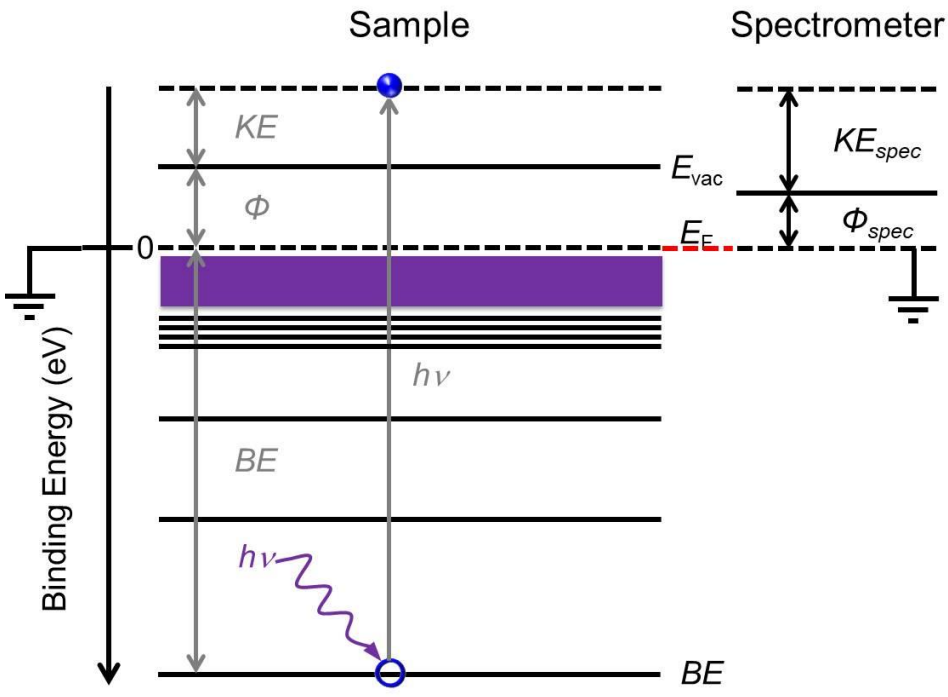

Figure 3.1 Diagram of the principles of the photoelectric effect. The solid ball represents an excited photoelectron, leaving a hole (hollow circle) at its initial state position.

Practically, the binding energy estimated by Koopmans' approximation is typically too large compared to the experimental results since it does not take the other electrons into account. The presence of the other electrons results in screening of the core hole generated. Therefore, the interaction between the emitted electron and core hole changes, leading to the breakdown of Koopmans' theorem.[131] In addition, the processes presented above are actually simplified by assuming that only one atom is present in the sample. In reality, the three-step model can describe a photoemission process in a better way.[132] The first step (excitation): upon X-ray illumination, atoms are ionised by absorption of the photon, so the atom becomes positively charged. The second step (diffusion and energy loss): the electron needs to pass through a number of other atoms in the sample prior to leaving from the surface of a solid. Typically, only the electrons from a depth of less than 10 nm can escape from the surface without loss of energy, if a conventional lab-based XPS is applied due to inelastic collision (see Section 3.1.1.3). The third step of the model is that the electron at the interface between the sample and vacuum escapes from the sample and passes to the vacuum to reach the analyser. In this process, the electron can still lose kinetic energy due to collision with gas molecules.

The kinetic energy of the emitted electron is dependent on the binding energy which is characteristic for a particular element and the atomic orbital from which it is emitted. The binding energy of an element can change with the chemical environment. For example, metallic lead has a binding energy of ~137.0 eV whilst the binding energy of lead iodide sits at ~138.8 eV.[133] Such an effect is called a chemical shift, allowing different chemical bonding to be identified. For example, typically the binding energy of a metallic element in a metal oxide would have a higher binding energy than metal due to screening effects.[134]

The photoelectric effect describes the photoemission processes in association with both core and valence electrons. The latter is typically associated with electrons relatively far from the nucleus and involved in bonding with neighbouring atoms. In general, the energy states of valence electrons are not discrete; instead, they form a continuous band structure at low BEs, typically between 0 and 10 eV. In this thesis, we do not discuss valence band spectra owing to the fact that, typically, lab-based XPS has a low cross-section for photoemission for valence band electrons compared to ultraviolet photoelectron spectroscopy (UPS).[135] Typical lab-based UPS instruments employ a helium lamp to generate He I UV light with a photon energy of 21.2 eV or He II ($h\nu$ = 40.8 eV) to investigate the electronic structure at low binding energy regions. The kinetic energy of photoelectrons generated in UPS is too low to allow them to escape from the deep surface; hence, UPS is even more surface sensitive than XPS.

Core electrons do not generally participate in chemical bonding and are highly localised on an atom. Each element generates a distinct set of core-level peaks in an XPS spectrum. The binding energy of core-level orbitals is highly dependent on the chemical environment such that the shifts in binding energy due to different chemical states are called a chemical shift. In core-level XPS spectra, photoemitted electrons related to *s*, or *p*, *d*, and *f* orbitals give rise to single or doublet peaks, respectively. The origin of doublet peaks or *p*, *d*, and *f* orbitals is discussed in Section 3.1.1.5.

As well as photoemission of core and valence electrons in primary processes, Auger electrons are produced in the sample and appear as distinct spectral features. The emission of Auger electrons is a secondary process in which, following generation of a core hole by primary photoemission, the hole is filled by an outer electron, as shown in Figure 3.2. In this way, the excess energy needs to be released in the form of light or an

electron. If the relaxation process induces the release of a photon, it is called fluorescence; if it induces the release of electrons, the electrons are called Auger electrons. In contrast to core photoelectrons, the kinetic energy of the Auger electrons detected is independent of the photon energy of the incident X-ray. This is because when a core hole generated is filled by a specific electron, the relaxation energy is fixed. In other words, the energy of the Auger electron only depends on the energy difference between the energy levels of the outer core electron and the core hole. Therefore, the spectral features from Auger electrons are easily identified by examining whether or not the kinetic energy is independent of the photon energy.

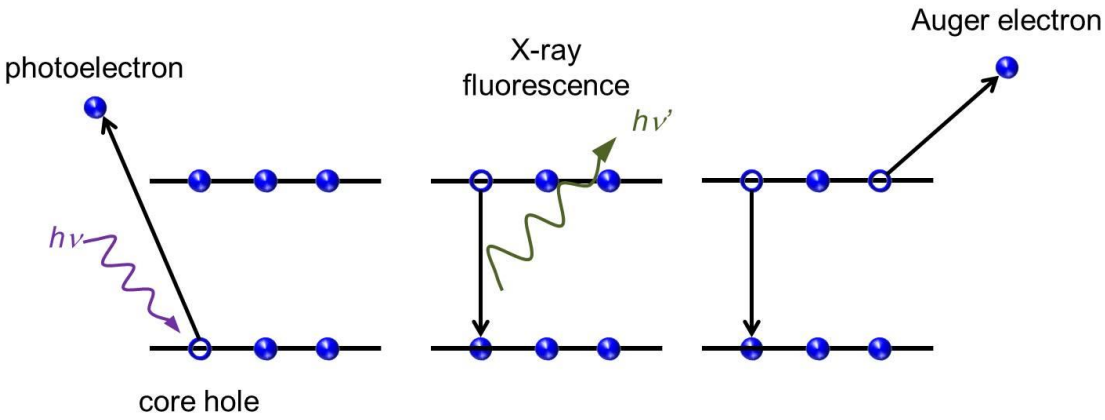

Figure 3.2 Illustration of core hole relaxation processes after a photoelectron is emitted, leaving a core hole at its original core-level states. The core hole can be filled by an electron from the outer shell of the atom. The excess energy is released in the form of either light (so-called X-ray fluorescence) or an electron called Auger electron.

3.1.1.1 Core-level Peak Shape

The full width at half-maximum (FWHM) is used to measure the width of a peak in a sensible way and is influenced by three key factors: the specific core levels being measured, the X-ray source, and the analyser resolution. The core-hole lifetime contributes to peak

broadening due to the Heisenberg energy-time uncertainty, which can be expressed by the following equation:

$$\Gamma = \frac{h}{t}, \tag{3.2}$$

where t (unit: s) is the lifetime of the core hole generated and h (unit: eV·s) is the Planck constant and Γ is the line width of the emitted photoelectrons. According to the equation, a shorter lifetime gives rise to a broader peak. After photoemission, the excited electron experiences the interaction between the core hole and itself. If the hole is re-filled in a short period of time on the order of femtoseconds, the electron undergoes changes in the interaction and hence the width is broader due to variations in kinetic energy. The effects from these changes are final state effects and the inherent phenomenon results in a Lorentzian broadening of the detected peak.

The X-ray source generates X-rays of a desired photon energy with a natural line width; *e.g.* a typical Al Kα X-ray has a line width of 0.85 eV.[136] Additional width broadening (Gaussian broadening) from the X-ray source can be partially attributed to the *Bremsstrahlung* effect, which arises from the deceleration of electrons, and X-ray satellites. These two components can be reduced by applying an X-ray transparent foil and a monochromator. The use of a monochromator can effectively narrows the photon energy distribution and hence decreases the width of the peak measured.

Another key factor in broadening is the contribution from the resolution of the analyser used. Typically, the resolution of the electron energy analyser is adjusted by varying the pass energy. Generally, higher pass energy is used in survey scans and lower pass energy (such as 20 or 30 eV) is utilised in detailed core-level scans to obtain better

spectral resolution. The effect of analyser pass energy on resolution and, therefore, peak width is discussed in Section 3.1.2.4. In general for a high-resolution scan, it is noted that a peak with a wide FWHM (*e.g.* $\geqq$ 2.0 eV) is typically the result of chemical shift; *i.e.* the element exists in various chemical bonding environments or spin-orbit coupling with a small doublet separation is present for the specific core level being probed (*e.g.* P 2p).

3.1.1.2 Final State Effects in XPS Spectra

As discussed above, core holes generated through the photoemission processes can be re-filled by outer electrons and, as a consequence, the electronic structure of the excited and surrounding atoms can rearrange. The state of the atoms after this rearrangement is the so-called final state. Hence, if the emitted electron experiences a change in the interaction between itself and those atoms due to the rearrangement, resulting in a change in kinetic energy, this is called a final state effect. A photoelectron can lose kinetic energy in several ways; *e.g.* it can excite an electron from the valence band into a higher unoccupied state. Depending on the sample, this can change the appearance of the core-level peak. If the specimen is a metal, the density of states around the Fermi level is continuous, resulting in a tail on the high BE side of the peak so that the core levels of metals often exhibit an asymmetric peak shape. For non-metallic samples, excitation across the band gap is between discrete states, giving rise to discrete “energy-loss” peaks just above the main photoemission peak. Such peaks are known as ‘shake-up’ satellites. If the electron is excited to a continuous state, then this contributes to the broadening of the core-level peaks or the inelastic background, resulting in so-called ‘shake-off’ satellites.

3.1.1.3 Inelastic Collisions

A photoelectron can lose kinetic energy due to loss processes such as those discussed above and as a result will not contribute to the intensity of a core level or Auger peak. These inelastic collisions mean that the outgoing electrons involved do not give rise to discrete features, since the loss of energy can be arbitrary values. Instead, these electrons form the background of the XPS spectra. This results in an increasing background with binding energy.

3.1.1.4 Surface Sensitivity

The penetration depth of soft X-rays in a material is typically a few μm [137] so XPS obtains its surface sensitivity due to the small inelastic mean free path (IMFP) of the photoelectrons. The IMFP is the average distance of an electron between two inelastic collisions in a specimen. It is dependent on the kinetic energy of the photoelectron and the material through which the electron is moving. The probability that an electron will escape from the sample surface with a depth of the IMFP (λ), is defined as 1/*e*. From the Beer–Lambert law,[138] the sampling depth is defined as the depth at which only 5% of the electrons escape without undergoing inelastic collisions, which can be expressed as:

$$\frac{I}{I_0} = e^{\frac{-d}{\lambda}}, \tag{3.3}$$

where I_0 and I are the initial and final intensity, respectively, and d is the thickness of the sample probed. A knowledge of the IMFP can be very useful for the estimation of the thickness of an overlayer on a sample. The value can be estimated by theoretical models which require knowledge of some key parameters of the material being measured. There

are a few approaches to obtain IMFPs such as the 'TPP-2M' equation proposed by Tanuma *et al*.[139] It is used for the estimation of the IMFP of MAPI in this work (see Chapter 4) *via* the National Institute of Standards and Testing (NIST) software, called the NIST Electron Effective-Attenuation-Length Database.[8] The TPP-2M equation requires knowledge of: (1) the elemental stoichiometry of the material probed; (2) the density; (3) the number of valence electrons per formula; (4) the bandgap. If the bandgap information of the specimen is unavailable, then the 'Gries G1' formula can be used to predict the IMFP values.[140]

3.1.1.5 Spin-orbit Splitting

As presented, core-level states with an angular momentum $\geqq 1$ (non-*s* orbitals) result in splitting of the photoemission peak, known as spin-orbit or doublet splitting. Such orbitals have two different total angular momenta (j) derived from the combination of the orbital angular momentum (l) and intrinsic angular momentum (s, spin), which can be expressed as the following equation (3.3):

$$j = l + s, \tag{3.3}$$

The values of the orbital angular momentums for *p*, *d*, and *f* are 1, 2, and 3, respectively, and the intrinsic angular momentums can be ±1/2. For instance, *p* orbitals can have j values of 3/2 and 1/2, giving rise to $p_{3/2}$ and $p_{1/2}$ doublets. Each doublet from a specific element and the orbital has a particular separation value, *e.g.* 4.9 eV BE for Pb 4f. The area ratio of a doublet originates from the degeneracy ($2j$+1) of energy levels. The area ratios of various *p*, *d*, and *f* orbitals are summarised in Table 3.1. These values can be used in XPS spectra fitting; *e.g.* the area of the Ti $2p_{1/2}$ peak is equal to a half of the Ti $2p_{3/2}$ area.

Table 3.1 Area ratios of spin-orbit doublets from *p*, *d*, and *f* orbitals.

Orbital	Area ratio
p	2:1 ($p_{3/2}$:$p_{1/2}$)
d	3:2 ($d_{5/2}$:$d_{3/2}$)
f	4:3 ($f_{7/2}$:$f_{5/2}$)

3.1.1.6 Binding Energy Calibration

All XPS spectra acquired in this study were processed using CasaXPS software (Version 2.3.18).[141] Prior to peak fitting, calibration of the BE is required. If a sample is not sufficiently conductive, the surface of the sample becomes positively charged due to the loss of emitted electrons. An electron flood gun (see Section 3.1.2.3) can be applied to compensate for the charging, but under or overcompensation can occur. Therefore, BEs are calibrated by reference to a relevant standard. The spectrometer is normally calibrated to the binding energy of a noble metal core level of known energy, (*e.g.* Au foil, $4f_{7/2}$ = 84.0 eV), which allows a straightforward calibration for conducting samples. However in cases where charge compensation is required, calibrating BE to the C 1s peak at 284.8 eV from adventitious carbon is often applied.

3.1.1.7 Quantification

The quantification of XPS data obtained for a lab-based source of fixed photon energy requires correction of three key factors: the photoionisation cross section, the sampling depth, and the transmission function of the analyser. The photoionisation cross section is simply the probability of ionisation of a particular core level at a particular photon energy. The sampling depth is related to IMFP (see Section 3.1.1.4) and is therefore kinetic-energy

dependent. However, the kinetic energy cannot be fixed using lab-based equipment due to constant photon energy. For many measurements, relative sensitive factor (R.S.F.) databases based on empirical measurements can be applied to the data acquired, allowing the stoichiometric information of a surface to be obtained. In this thesis, CasaXPS sensitivity factors by Kratos are applied to calculate the stoichiometry of perovskite films. Some frequently used R.S.F. values in this study are listed in Table 3.2 for reference. Using a $SrTiO_3$ single crystal, we found that the R.S.F. from the Kratos (F 1s = 1) database is also suitable to be applied for the data from the SPECS instrument. The stoichiometry of a sample in near ambient conditions cannot be derived due to the absence of analyser transmission-function-adapted at the higher gas pressures. The analyser transmission function affects the sensitivity of the analyser for the detection of electrons emitted with a certain kinetic energy.

Table 3.2 A few representative values of the sensitivity factors used for calculating the stoichiometry of MAPI perovskite films.

Core level	Kratos C 1s (C 1s = 1)	Kratos F 1s (F 1s = 1)
C 1s	1	0.278
N 1s	1.8	0.477
Pb $4f_{7/2}$	12.73	4.76
I $3d_{5/2}$	19.87	7.02

3.1.2 Instrumentation

Conventional XPS experiments are usually performed under an ultra-high vacuum (UHV) environment, which encloses the sample, X-ray source and an electron analyser, to ensure the quality of the signals probed. The *in situ* preparation/treatment of the sample can also be conducted in UHV, resulting in the removal of complication due to the presence of adventitious hydrocarbon or other possible atmospheric contaminants. Some essential components of an XPS instrument are introduced in the following sections.

3.1.2.1 Vacuum System

In order to achieve UHV conditions, a pumping system consisting of various types of pumps is required. In brief, roughing pumps (*e.g.* rotary or scroll pumps) take the pressure down to the order of 10^{-3} mbar from atmospheric pressure. Subsequently, UHV pumps can further reduce the pressure down to the UHV range (< 10^{-9} mbar). The different sorts of pumps used in XPS instruments are introduced below.[136]

Rotary Pump

The rotary pump is a mechanical pump composed of a rotor connected to vanes in a cavity, with oil as the lubricant. When the rotor is moving, a volume of gas from the inlet is sucked in and subsequently compressed and released from the outlet into air or vents.

Scroll Pump

The scroll pump uses two interleaving scrolls to pump air out. Typically, one of the scrolls is fixed, whilst the other scroll move eccentrically without rotation to pump air out. Nowadays, oil-free scroll pumps are often used in XPS instruments as roughing pumps,

resulting in a reduced chance of oil contamination of the vacuum.

Turbomolecular pump

The turbomolecular pump, also known as a turbo pump, possesses multiple stages of turbines. The spinning blades propel gas molecules from one session to the next stage to the exhaust which is backed by a roughing pump.

Sputter-ion pump

The sputter ion pump (also known as an ion pump) consists of an anode and a reactive cathode, such as titanium. By applying voltage, residual gas molecules which pass through the region are ionised and transported to the cathode as a result of the electric field. Subsequently, these gas ions are adsorbed on the surface of the cathode and therefore the pressure is reduced. In addition, some of the cathode material is sputtered, forming reactive ions to react with residual gas molecules to further decrease the pressure of the chamber.

Titanium sublimation pump

The titanium sublimation pump (TSP) contains a titanium filament that will sublime when the current is sufficiently high to heat the filament above the sublimation temperature of titanium. The titanium vapour produced traps gas molecules as it condenses on the chamber walls to reduce the pressure of the chamber. It provides a reactive coating on the walls or the chamber to which molecules adsorb. The coating needs to be replenished periodically by repeated heating of the TSP.

3.1.2.2 X-ray Source

A lab-based X-ray source (also known as an X-ray tube) has a fixed photon energy, depending on the target material (anode) used. Common anodes are Al (Al Kα, 1486.6 eV) and Mg (Mg Kα, 1254.6 eV). The X-ray is produced by bombarding the metal target anode with high energy electrons (beam current) accelerated onto the anode by applying high voltage, typically 15 kV. Core-level electrons of the bombarded material are released (~1%) from the atoms and the holes produced are subsequently filled by outer electrons, resulting in the production of an X-ray by fluorescence. It is noted that most of the energy generated by bombardment generates a great deal of heat so that a cooling system (typically cooling water) is essential in an X-ray gun.[142] A typical X-ray spectrum generated consists of characteristic lines and a broad background produced as a result of the deceleration of moving electrons, so-called *Bremsstrahlung* radiation. In addition, secondary lines of lower intensity are produced from different core-hole decay mechanisms. These unfavourable background signals can be reduced by an X-ray transparent metallic foil (such as Al) in order to enhance the quality of the X-ray used as presented. Most modern X-ray sources are monochromated in order to get better quality spectral data. They allow a higher flux and remove X-ray satellites from the spectrum. The monochromator is an optical device that can narrow the window of light wavelength. It incorporates a single crystal (*e.g.* quartz for Al kα) mirror to selectively reflect a desired wavelength in accordance with Bragg's law.

3.1.2.3 Electron Flood Gun

The electron flood gun or electron neutraliser is utilised to compensate for the positive charging of the sample measured by XPS, as discussed in Section 3.1.1.6. Charge

compensation is often applied unless the sample is sufficiently conductive. The gun emits low energy electrons towards the sample surface to counter the positive charge.

3.1.2.4 Electron Energy Analyser

The electron energy analyser probes the kinetic energy of photoelectrons emitted from the sample. The type of analyser used for the work in this thesis is a hemispherical energy analyser. Essentially, such an analyser consists of two concentric hemispheres with radii of R_1 (inner) and R_2 (outer), as shown in Figure 3.3. The average radius of the hemispheres is R_0, which also describes the electron pathway, for an electron at the pass energy, from the entrance slit to the exit slit just before reaching the detector. Briefly, photoelectrons pass through a series of lens system that focus the electron beam in order to precisely enter the entrance slit. In addition, the lens system retards the electrons so electrons with a desired kinetic energy arrive at the entrance slit at the pass energy. Electrons enter the hemispherical analyser and those with kinetic energies different from the pass energy are deviated by electrostatic fields between the inner and outer hemispheres. Electrons with a kinetic energy equal to the pass energy are then transmitted to the detector. The energy resolution (ΔE) of an analyser is related to pass energy (E_{pass}) according to the equation (3.4) shown below:

$$\Delta E = E_{pass}\left(\frac{\omega}{2R_0} + \frac{\alpha^2}{4}\right), \tag{3.4}$$

where ω is the width of entrance and exit slits and α is the maximum acceptance angle of the analyser. Accordingly, lower pass energy gives rise to better energy resolution (namely smaller ΔE), resulting in a reduced FWHM of core-level peaks. However, this reduces the transmission of electrons, leading to a lower intensity of photoelectron signals.

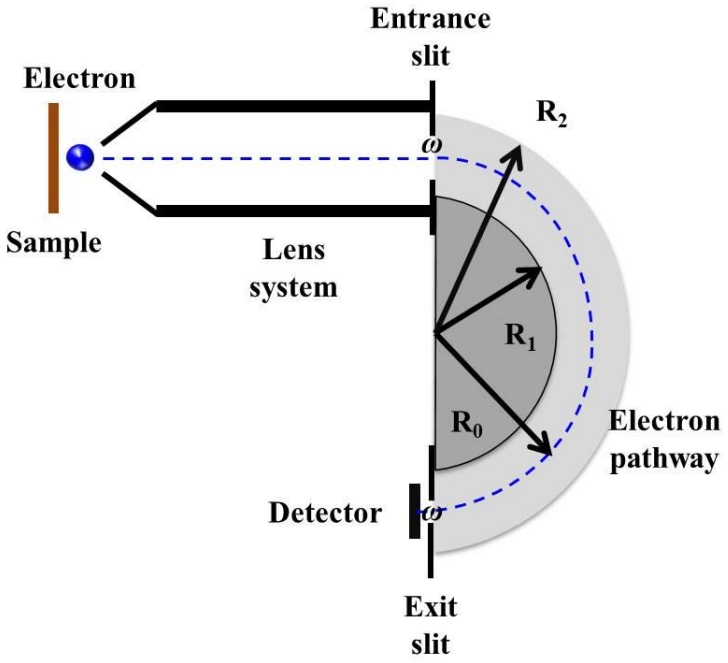

Figure 3.3 Illustration of a hemispherical electron energy analyser composed of two concentric hemispheres with radii of R_1 (inner) and R_2 (outer). The mean radius R_0 and electron pathway are also shown.

3.1.3 Near-ambient pressure X-ray Photoelectron Spectroscopy (NAP-XPS)

Many technologically interesting chemical/physical reactions involve a solid/liquid or a solid/vapour interface, often at elevated pressures. The necessary operation of XPS instruments under high or ultra-high vacuum conditions has led to a "pressure gap" between operational conditions of the instrument and the materials/systems of interest. Near-ambient pressure X-ray photoelectron spectroscopy (NAP-XPS) is a cutting-edge technique in the XPS sphere that has allowed this challenge to be addressed to some extent. Thanks to the development of differential-pumped lens system, samples can be placed in an environment at tens of mbar of pressure, very different from the analyser (10^{-5} – 10^{-7} mbar). In this way, samples exposed to more realistic pressures of gas can be studied *in*

situ. In the SPECS system used in this work, the sample is contained in a specially designed cell which can operate at pressures up to 15 mbar. The NAP cell is enclosed to prevent from the contamination of the UHV chamber and to maintain the cell pressure. The X-ray therefore passes through an X-ray transparent window, typically made of silicon nitride (SiN_x) compounds, as shown in Figure 3.4. Subsequently, the excited photoelectrons enter a lens system with decreasing pressures ($P_1 < P_2 < P_3$) towards the main body of the hemispherical analyser, created by a well-designed differential pumping system. Generally, the pressure at the pre-lens (P_1) is approximately in the order of 10^{-4} mbar.[143] Various gases and mixtures, such as water vapour,[8, 9, 144] O_2,[9] NO_x,[145] CO_x,[146-148] *etc*, can be introduced into the system.

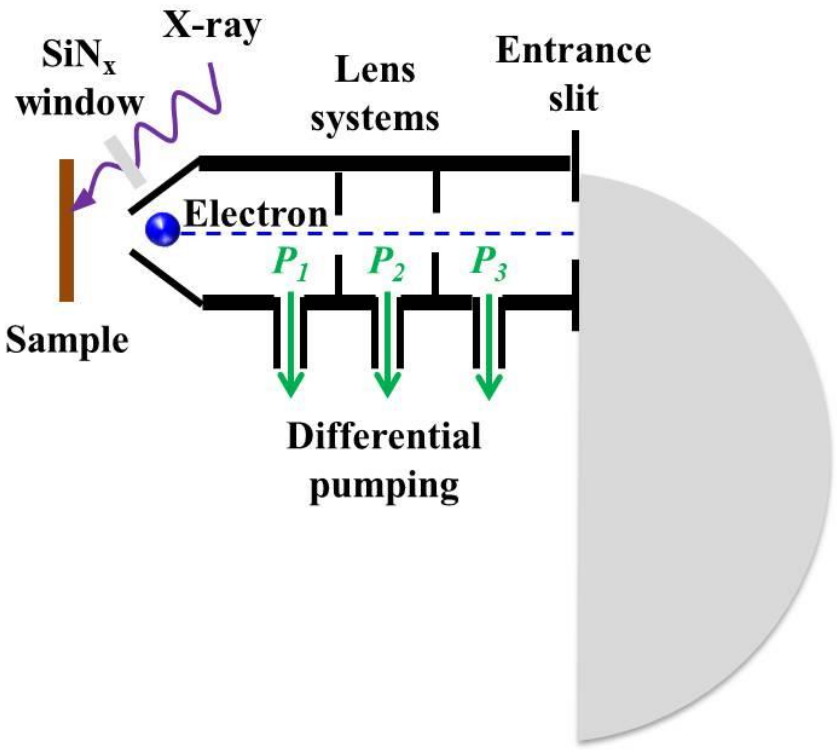

Figure 3.4 Illustration of a NAP-XPS kit containing a SiN_x X-ray transparent window and a differential pumping system.

3.2 Application of Photoemission Spectroscopy to the PSC field

Photoemission spectroscopy (PES) plays an essential role in this thesis since XPS is utilised to investigate halide perovskite surfaces. As discussed in Section 3.1, the usefulness of XPS to probe chemically compositional information to realise the initial (fresh) and final state (following degradation) of the perovskite films detected is well known. An overview of XPS as well as other PES techniques employed to the PSC field will be presented in the following sections.

3.2.1 Energy Level Alignment

Investigation of the energy level alignment (ELA) is important in solar cell areas in order to ensure that carriers can be efficiently extracted and subsequently transported to the electrodes and external circuit. Unlike conventional XPS research for surface compositions, ELA mainly focuses on the VB region of XPS or ultraviolet photoelectron spectroscopy (UPS) spectra, with BE regions typically ranging from 0 to 10 eV with respect to the Fermi level (E_F). The BE probed can be extended to 20 eV to cover the secondary electron cut-off (SECO) region in order to calculate the work function and the ionisation energy. The appearance of the SECO edge arises due to the fact that photoelectrons with lower KEs than the edge cannot overcome the work function to be detected by the analyser. The practical use of these calculations will be discussed.

The majority of the ELA studies involve probing TiO_2/perovskite interfaces since such a junction is often applied in PSC devices.[149-151] Lindblad *et al*. performed hard X-ray photoelectron spectroscopy (HAXPES) to probe TiO_2/MAPI interfaces with a

photon energy of 4000 eV where the MAPI films were fabricated by either a one-step or two-step method.[149] As shown in Figure 3.5, the VBM positions with respect to (w.r.t.) E_F are quite similar for both the MAPI films made by the different preparation approaches. However, it is clear that the TiO_2/PbI_2 interface has a deeper VBM position (0.35 eV downshifted from the Fermi level), which is a similar value observed in its core-level shift (0.3 eV). Such a change in binding energies can be utilised to distinguish MAPI and PbI_2 if the energy resolution is good enough to resolve such a BE difference.

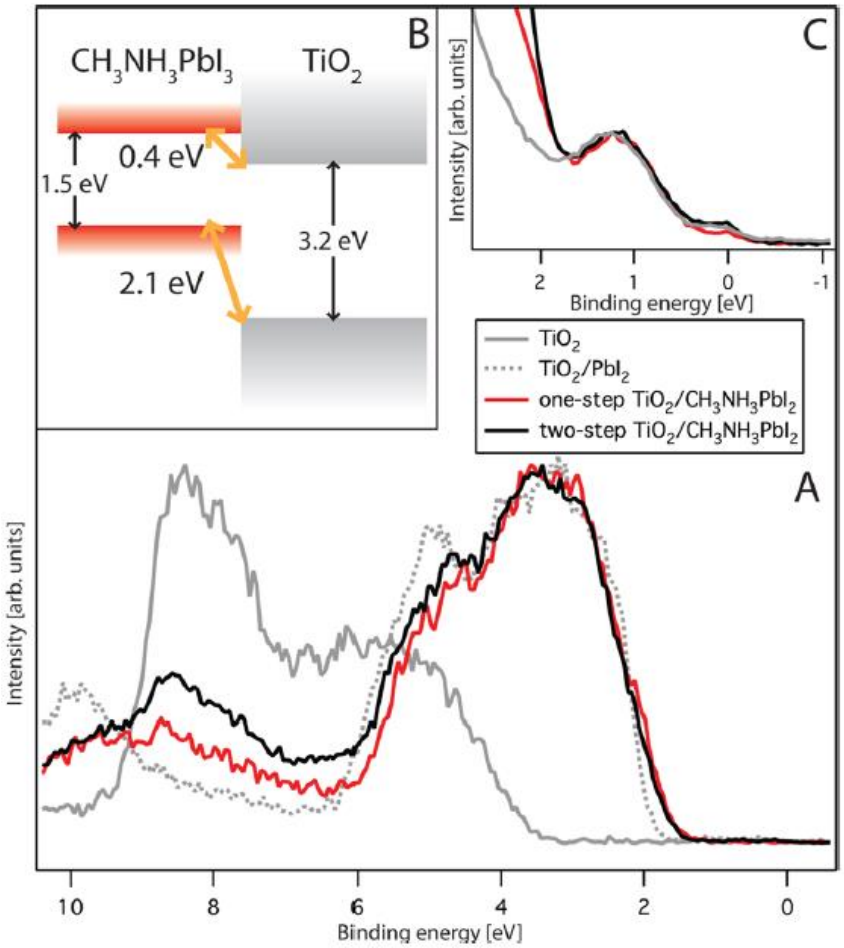

Figure 3.5 (A) VB regions of the TiO_2 film, TiO_2/PbI_2, and TiO_2/MAPI films. (B) ELA diagram of the CBM and VBM of TiO_2 and the MAPI films. (C) Bandgap region for the TiO_2 film and perovskites.[149]

Moreover, this study demonstrates that in the ELA of TiO_2/MAPI, electrons can be extracted by TiO_2 from MAPI and holes can be prevented from moving towards TiO_2 (see Figure 3.5B). They found that the results of CBM and VBM positions obtained by XPS are different from those acquired by UPS.[22] This occurs because UPS is extremely surface sensitive and is therefore influenced by surface-adsorbed species including contamination. The XPS results are in agreement with another study involving density functional theory (DFT) calculations.[152] However, the relative CBM position between TiO_2 and MAPI shows a discrepancy in the work of Kim and co-workers using XPS at varying photon energies.[150] They found the CB edge of TiO_2 is extremely close to that of MAPI (less than 0.1 eV) and their equilibrium Fermi level also approaches both the CBMs, which exhibits strong *n*-type behaviour. The difference is probably due to distinct compositions at the interfaces. In the reference cited, there is an additional peak found (at ~400 eV BE) in the N 1s spectra as well as the MAPI component, which can be attributed to CH_3NH_2.[153] In addition, PbI_2 is present at the TiO_2/MAPI interface in accordance with the Pb $4f_{7/2}$ BE position (138.8 eV). Therefore, the films become even more *n*-type due to the presence of CH_3NH_2 and PbI_2, as interstitial MA (MA_i) and iodine vacancies (V_I) have been demonstrated to be *n*-type dopants through first-principles calculations.[154] The TiO_2/FAPI interface has also been probed by the PES technique. It was seen that the CBM of TiO_2 is also significantly close to that of FAPI, as shown in Figure 3.6.[151] In addition, it was found that CB and VB edges shift upwards (to lower BE) if the FAPI films were deposited on ITO instead of TiO_2, suggesting that substrates used can play an important role in ELA.

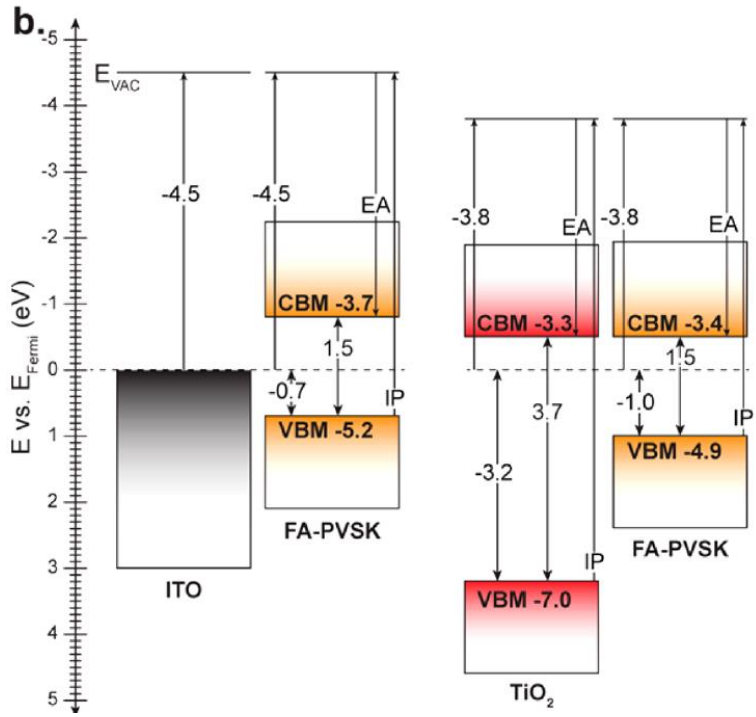

Figure 3.6 ELA diagrams for ITO/FAPI and TiO_2/FAPI perovskite (PVSK) interfaces. EA and IP represent electron affinity and ionisation potential, respectively.[151]

The figure illustrates that IP and EA values can also be obtained by PES techniques. Ionisation potential, more often called ionisation energy (E_i), is the minimum amount of energy required to remove the valence electron of an isolated neutral gaseous atoms or molecules from the surface to the vacuum level. The process can be simply expressed as the below equation (3.4):

$$X + E_i \rightarrow X^+ + e^-, \tag{3.4}$$

where X is any neutral atom or molecule that can be ionised and X^+ is its ionised form by giving out an electron e^-. As in the ELA diagram, the highest occupied level of electrons is the VBM so the value of E_i is approximately the energy difference between the VBM and vacuum level. Therefore, ionisation energy is equal to the sum of the binding energy of VBM (BE_{VBM}) and the gap between the vacuum level and Fermi level, *i.e.* the work

function (Φ), which can be expressed as the following equation (3.5):

$$E_{\mathrm{i}} = \mathrm{BE}_{\mathrm{VBM}} + \Phi. \quad (3.5)$$

The work function of the sample can be obtained by measuring the SECO region, as described later. The electron affinity energy (E_{EA}) of a neutral atom or molecule is defined as the amount of energy released when an electron is added to a gaseous neutral atom or molecule to form a negative ion (X^-), as shown below in equation (3.6):

$$\mathrm{X} + e^- = \mathrm{X}^- + E_{\mathrm{EA}}. \quad (3.6)$$

The electron can only be added into a lowest unoccupied state, namely, the CBM. Therefore, the absolute energy difference between the electron affinity and ionisation potential is the bandgap energy (E_{g}) that can be determined by ultraviolet-visible-near-infrared (UV-VIS-NIR) spectroscopy, photoluminescence (PL) spectroscopy, *etc*. Equation (3.7) can be used to relate these three properties:

$$E_{\mathrm{i}} = E_{\mathrm{EA}} + E_{\mathrm{g}}. \quad (3.7)$$

It is shown in Figure 3.6 that the energy level positions of FAPI can be influenced by the type of substrates used.[151] This is the same for MAPI; Miller and co-workers performed XPS to detect the band positions of MAPI deposited on various substrates.[155]

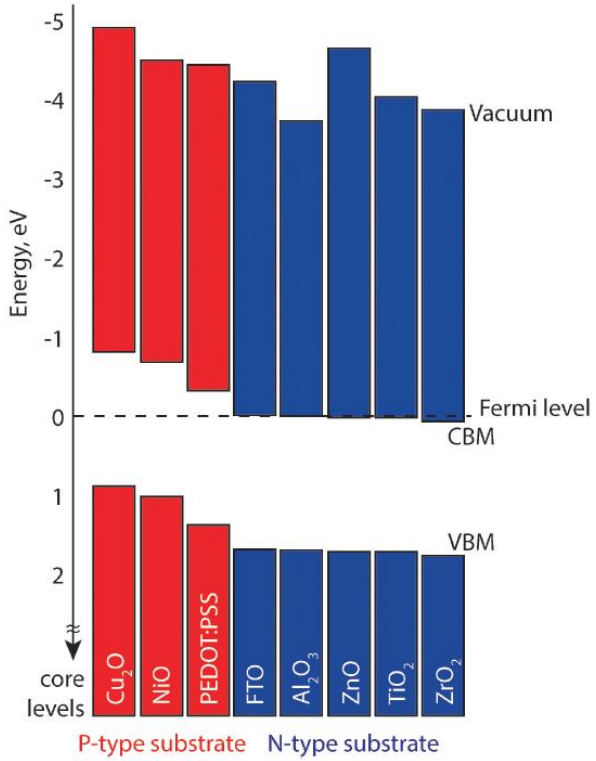

Figure 3.7 Overall ELA results of MAPI films deposited on various substrates from XPS. The energy values refer to the Fermi level.[155]

As shown in Figure 3.7, the vacuum level of MAPI on different substrates varies significantly due to discrepancies in the work function of material surfaces. It is noted that the *p*-type substrates do not convert inherently *n*-type MAPI films into real p-type films but, rather, become 'less *n*-type' in agreement with Fermi-level positions. A detailed work function study of thermally-evaporated MAPI films on different substrates was performed.[156] By observing the cut-off edge of the SECO region, work function information can be obtained, as shown in Figure 3.8. By using kinetic energy as the *x*-axis in a spectroscopic plot, the value of the work function of materials probed can be simply acquired. Secondary electrons have lower kinetic energy due to energy loss compared to primary electrons. In this way, if the remaining kinetic energy of those secondary electrons cannot overcome the work function of the sample to leave the surface,

the electrons cannot reach the analyser and therefore the spectrum shows a clear cut-off region. Hence, the work function of a sample can be expressed as below (3.8):[156]

$$\Phi = h\nu - \mathrm{BE}_{\mathrm{SECO}} = \mathrm{KE}_{\mathrm{SECO}}. \quad (3.8)$$

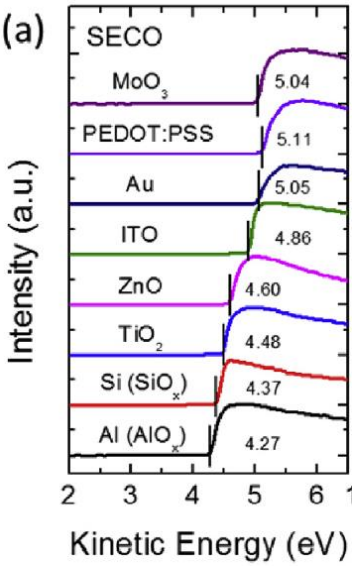

Figure 3.8 Typical SECO region of the UPS spectra of the thermally-evaporated MAPI films on different substrates.[156]

Until now, only iodine perovskites have been discussed but PES studies for other halide perovskites, such as methylammonium lead bromide (MAPB), have been studied.[157, 158] It was found that by fully replacing iodine with bromine, the CB edge shifts upwards for to ~0.25 eV whilst the VBM moves downwards by approximately 0.50 eV.[157] MAPB keeps *n*-type behaviour but is less *n*-type compared to MAPI. The *n*-type nature of the MAPB surface is probably as a result of Pb segregation on the surface.[158] Mixed halide perovskites have also been investigated in order to have a better understanding of bandgap-adjustable halide perovskites.[159-163] Philippe *et al.* utilised synchrotron-based PES techniques (UPS and XPS using soft and hard X-rays) with varying photon energies in order to probe the electronic structure of

$MA_{0.15}FA_{0.85}Pb(I_{0.85}Br_{0.15})_3$ perovskites at various depths.[159] They found that the appearance of the spectra recorded at different depths is quite distinct. Such discrepancies can be ascribed to halide inhomogeneity with sampling depth. They clearly show that the Br/I ratio is higher at the shallow surfaces through core-level observation (Br 3d versus I 3d). This leads to distinct valence band features at different depths, which matches the DFT calculations based on the combined results between MAPI and MAPB.

Partially doping Br into MAPI films gradually moves CBM and VBM upwards and downwards, respectively, by expanding their bandgaps.[160] Similar to the case of pure MAPI and MAPB, the presence of Br has less effect on the position of the CBM compared to VBM, suggesting that halide substitution delivers more impact on the VB electronic structure. It was found that adding Cl into mixed iodine and bromine perovskites using $PbCl_2$ has a similar effect on band structure.[161] Unlike the difference between MAPB and MAPI, methylammonium lead chloride (MAPC), however, has a significant shift in CBM (upwards) when replacing iodine with chlorine.[162] In that study, they also found that the bandgap values obtained by UV-VIS-NIR and PES techniques (UPS and inverse photoemission spectroscopy (IPES)) are different, *i.e.* CBM positions are higher using IPES. The difference between these values is useful to estimate the exciton binding energy, *e.g.* for MAPI it is 0.18 eV. Compared to UV-VIS-NIR, IPES is less often utilised to obtain CBM information. IPES is a technique used to study the unoccupied electronic states of surfaces with mechanism as follows. A low-energy electron beam (< 20 eV) illuminate on the sample probed to couple with the higher unoccupied electronic states. Then, those electrons decay to the lower unoccupied electronic states, resulting in emission of light that will be subsequently detected. Figure 3.9 shows a typically combined spectrum of the UPS and IPES spectra of a MAPI film.[163] The Fermi level of the film

in that work is relatively close to VBM, suggesting *p*-type behaviour, which is different from most of the studies, probably due to the substrate used and the defects present in the film.

The electronic structure of perovskite films can also be tuned by annealing time.[164] By increasing the annealing time of MAPI from 10 to 100 minutes, the film becomes strongly *n*-type due to full conversion to MAPI from intermediate phases,[164] which have distinct electronic properties.[165] The electronic structure and ionisation energy of perovskite films appear to be highly process-dependent.[166] Emara *et al*. performed spin coating and vapour deposition with various parameters and found significant discrepancies in E_i and stoichiometry.[166] Generally, more PbI_2 added (relative to MAI) in the precursor solution resulted in a higher E_i obtained.

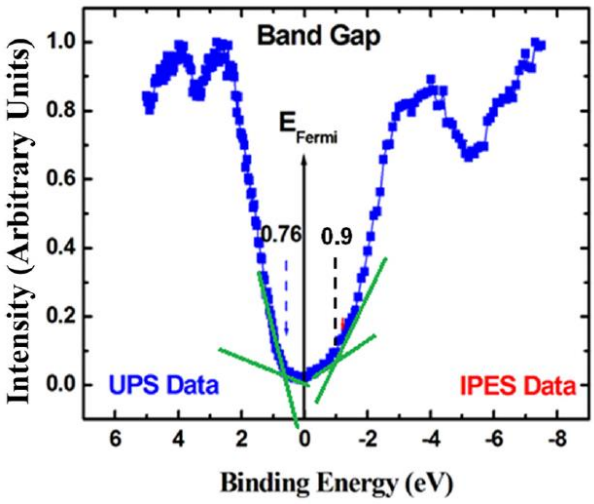

Figure 3.9 A combined UPS and IPES spectrum of the MAPI film, showing an E_g of 1.66 eV.[163]

Ng *et al*. further investigated the formation chemistry of perovskite films by probing the interfacial ELA between methylammonium halide (MAI or MABr) and lead halide (PbI_2, $PbBr_2$, or $PbCl_2$) precursors of lead perovskites.[167] Band bending and a strong

interfacial dipole were observed, particularly for MAI/$PbCl_2$ interfaces. The study suggests MAI/$PbCl_2$ can deliver better charge transfer in the formation of MAPI compared to MAI/PbI_2. It was concluded that this was related to the ionic charge exchange process. Temperature can also affect the VBM position of perovskite films.[168] It was observed that with increasing temperature, the VB edge of MAPI shifts downwards. This suggests that when a PSC device is heated by sunlight or the environment, the ELA in a device may change.

Perovskite films in contact with different carrier transporting materials and electrodes were also investigated.[169-172] Schulz and colleagues investigated the ELA of Spiro-MeOTAD, a commonly used HTM, on different perovskite materials.[169] The results show the band alignments are all suitable to extract holes from the lead perovskites. They also found minor downward band bending of Spiro-MeOTAD with increased thickness. It was found that Au can induce upward band bending of MAPI at the Au/MAPI interface, facilitating the extraction of holes and preventing carrier recombination.[170] CuSCN has been demonstrated as a HTM for MAPI using air photoemission spectroscopy.[171] The band positions of CuSCN are suitable to allow it to be inserted between PEDOT:PSS and MAPI. PEDOT:PSS is a widely used HTM in an inverted-structural PSC. However, the semimetallic nature of PEDOT:PSS cannot efficiently prevent electron flow to the anode, causing a significant efficiency loss. The CBM of CuSCN is far higher that of MAPI, facilitating the blocking of back electron flow. Therefore, CuSCN is also a good choice for use as the HTM of MAPI in PSC devices. Although ZnO has been employed successfully as an ETM for MAPI, it cannot be used with FAPI due to its CBM being higher than that of FAPI by 0.05 eV.[172] The addition of CdSe quantum dots to a PSC device not only increases light absorption but also delivers

better charge extraction.[173] Through ELA studies, it was demonstrated that using CdSe quantum dots with a size of 2 nm, the electrons produced in the quantum dots can transfer to MAPI and the holes generated in MAPI can be extracted by the quantum dots. However, CdSe quantum dots with a size of 4 nm cannot transfer holes to Spiro-MeOTAD due to band misalignment. Hence, the size control of CdSe quantum dots for use in PSCs is crucial.

ELA study of the inorganic perovskite, $CsSnBr_3$, has also been conducted.[174] It was found that by doping SnF_2 into the inorganic perovskite, both the CB and VB edges shift up whilst maintain the bandgap. The CBM of SnF_2-doped $CsSnBr_3$ becomes relatively close to that of TiO_2, resulting in better charge transfer and giving higher efficiencies. However, the CB edge of TiO_2 is still 0.15 eV higher than that of the perovskite layer, leading to inefficient electron injection from $CsSnBr_3$ to TiO_2. This could be the main reason for the low PCEs generated, suggesting that energy level alignment is a key factor for producing highly efficient PSC devices. Nevertheless, modifying the crystal structure can be an effective approach to adjust ELA. Zhang *et al*. investigated FTO/TiO_2 and TiO_2/TiO_2 interfaces with different crystalline phases (rutile and anatase).[175] As shown in Figure 3.10, the ELA of a rutile compact TiO_2 and an anatase mesoporous TiO_2 mismatches, whereas the reverse crystalline phases for these layers can deliver efficient electron transfer. The results suggest that even for the same compound, the crystalline phase should be carefully considered to ensure relevant ELA for a device or an interface.

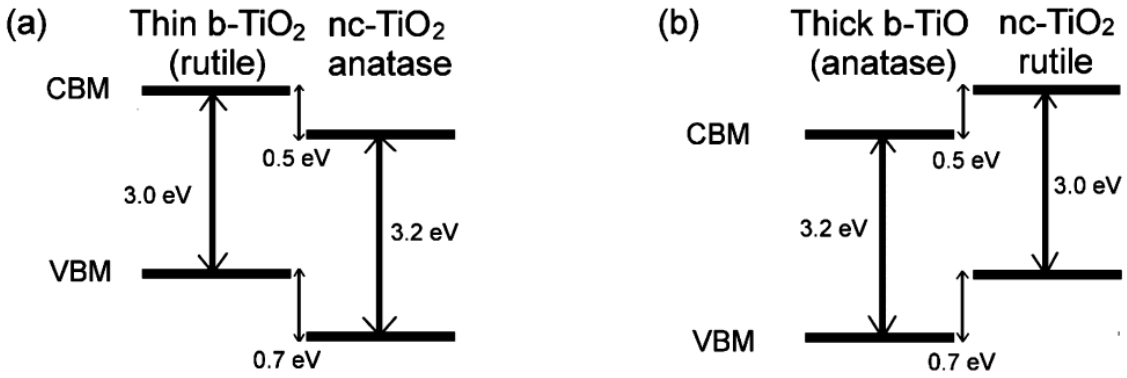

Figure 3.10 (a) The ELA between a blocking TiO_2 (b-TiO_2) layer with rutile polymorph and a mesoporous anatase nanocrystalline TiO_2 (nc-TiO_2) layer. (b) The ELA between a b-TiO_2 layer with anatase polymorph and a mesoporous rutile nc-TiO_2 layer.[175]

3.2.2 Surface Composition

Obtaining compositional information from the surface of an as-deposited film has been the dominant use of XPS in the sphere of PSCs. Not all of the research focuses on the surface composition of halide perovskite films. However, XPS is also often used to probe the surface of the carrier transporting materials, such as TiO_2 [176, 177] and graphene oxide [178, 179]. To date, the most widely-investigated halide perovskites using XPS have been MAPI films where the Pb 4f, I 3d, N 1s, and C 1s spectra are commonly probed to obtain elemental composition information. For the Pb $4f_{7/2}$ spectra of MAPI, the binding energy (BE) is typically located at ~138.6 eV, depending on the BE reference.[133, 157, 180, 181] This value is generally lower than the BE of the lead precursors of MAPI, such as PbI_2 (~138.8 eV [8]) and $PbCl_2$ (~139.5 eV [8]). This allows researchers to determine whether MAPI perovskite formation at the surface is complete. However, the BE of PbI_2 is so close to that of MAPI. It is difficult to distinguish these two chemical components if the resolution of the instrument is insufficient. Therefore, stoichiometry measurements are essential to complement the BE data as the I/Pb ratios of MAPI and PbI_2 should be 3 and 2, respectively. It has been found, however, most

as-deposited MAPI films are imperfect; *i.e.*, they have defects. Iodine vacancies are fairly easily formed in MAPI films.[8] As a result, the I/Pb ratio of MAPI films can be lower than 3, particularly for films prepared by a 'two-step' method.[149] This may be related to the incomplete conversion of MAPI from PbI_2 during the sequential step. Another feature often seen in the Pb 4f spectra is metallic lead with a BE of ~137 eV, as shown in the representative spectra in Figure 3.11.[157] The appearance of atomic lead represents the loss of the halide moiety,[149] which could be due to X-ray damage.[133] Therefore, high photon flux may be a problem in measuring halide perovskite materials.

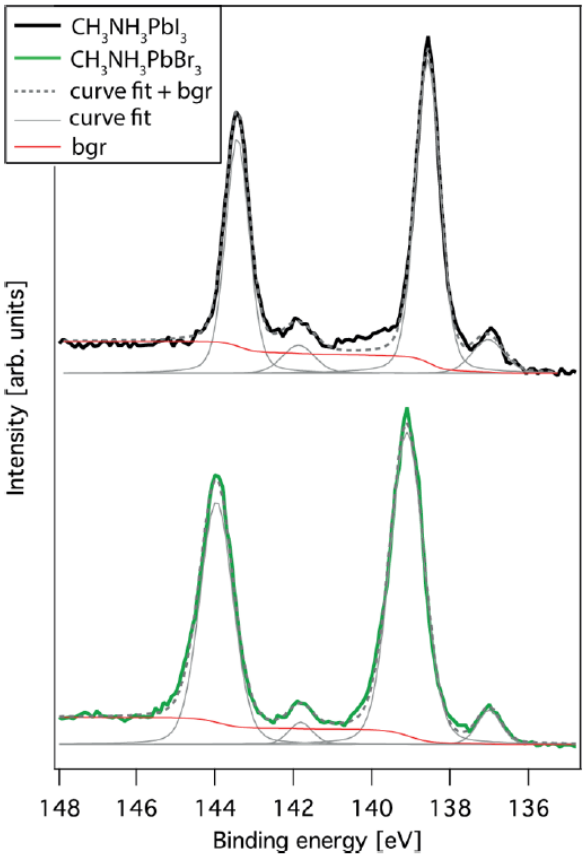

Figure 3.11 A representative Pb 4f core-level spectra of MAPI and MAPB films with metallic lead signals fitted.[157]

XPS is also widely used to investigate the role of chlorine in MAPI films prepared from a $PbCl_2$ precursor (or denoted as $CH_3NH_3PbI_{3-x}Cl_x$). Starr *et al*. found that after

annealing the amount of chlorine is negligible,[82] and suggested Cl is possibly lost in the form of MACI or Cl_2 gases.[182] Yu *et al*. used a polymer layer on the top of $CH_3NH_3PbI_{3-x}Cl_x$ films to block the release of gaseous Cl-containing compound(s) and found that the chlorine content in the films significantly increased.[182] Using angle-resolved XPS (AR-XPS), chlorine was detected deeper into the surface of $CH_3NH_3PbI_{3-x}Cl_x$ films, close to the perovskite/TiO_2 interface.[183, 184]

A significant issue with the use of XPS in the perovskite literature is that not all spectra recorded from MAPI, for example, prepared by similar processes show consistency. There are discrepancies in the binding energies and assignments of specific photoemission peaks even when calibrated to identical references. For instance, typically, only a single N 1s component (~402.5 eV BE) is observed in MAPI films.[8] However, in a few cases, a low-BE shoulder located at a BE of ~400.5 eV can be seen, as shown in Figure 3.12.[185] Some studies have suggested that, a component could arise from CH_3NH_2, a deprotonated form of the MA cation ($CH_3NH_3^+$) in MAPI films.[185, 186] However, the reason for the formation of this component is unclear. One suggestion is that it is due to the dissociation of the gaseous by-product, MACl, where Cl is lost in the form of HCl gas.[185] Such a neutral species, CH_3NH_2, is then trapped within the perovskite crystal lattice and can be removed by applying a higher annealing temperature and longer heating time. However, these actions could lead to the loss of the MA cation of perovskite and the escape of iodine.[185] Jung *et al*. applied density functional theory (DFT) calculation to find that CH_3NH_2 should be mainly located at grain boundaries or surfaces rather than the crystal lattice.[186] The grain boundary region would allow moisture to penetrate, further leading to grain degradation.[108]

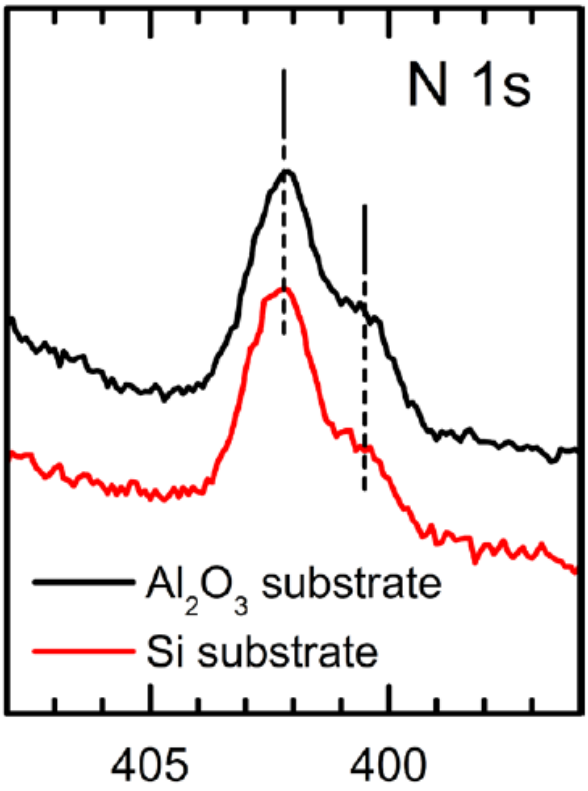

Figure 3.12 XPS N 1s spectra of fresh MAPI films deposited on Al_2O_3 and Si substrates. A right shoulder (CH_3NH_2) is observed in addition to the main MAPI peak.[185]

Another discrepancy amongst the existing literature is BE values. The Pb $4f_{7/2}$ peak of a MAPI film, for example, can have a value of ~137.7 eV, 0.9 eV lower than the most common values, as presented when the BE is calibrated to the adventitious carbon (285.0 eV BE).[184] Such a difference can be attributed to defect chemistry that can influence the position of the Fermi level.[185] Most MAPI films exhibit strong *n*-type behaviour (iodine vacancies and/or interstitial MA). However, if many lead vacancies are present, MAPI can become a *p*-type material that has lower BE due to the downward shift of the Fermi level.[154] Materials deposited on the top of perovskite films can also change the surface properties of the halide perovskites. Depositing MoO_3 on a MAPI film induces a BE shift towards the low BE side, making the MAPI film relatively *p*-type.[187]

Chiang *et al*. utilised XPS to measure whether or not sulphur is present in the MAPI films prepared from a $Pb(SCN)_2$ precursor by two-step deposition.[79] It was found that the S 2p signal is negligible, suggesting most of the sulphur is lost as some gaseous sulphur-containing compounds. In recent years, surface composition studies have also been applied to probe mixed cation perovskites. Philippe *et al*. measured various types of mixed-cation perovskite films, such as a RbCsMAFA quadruple-cation perovskite, using two different photon energies, 2100 and 4000 eV, to probe different depths.[188] Interestingly, it was found that iodine is relatively rich at the topmost surface compared to the deeper region, suggesting inhomogeneity of halides throughout perovskite films. FA and MA can be simply distinguished in the C 1s and N 1s XPS spectra, as shown in Figure 3.13.[189] FA (N—C—N, ~288.5 eV BE) has a higher BE in the C 1s spectra compared to MA (C—N, ~286.8 eV BE). In the N 1s spectra, the measured BEs are approximately 400.8 eV for FA and 402.5 eV for MA, respectively.

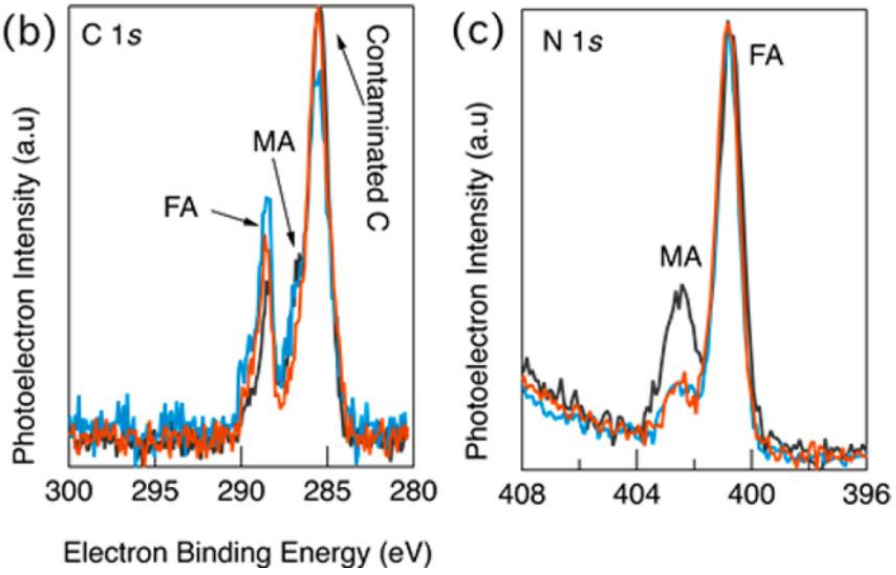

Figure 3.13 XPS C 1s and N 1s core-level spectra of mixed-cation perovskite films.[189] Black, red, and blue correspond to AZO, ITO, and IZO, respectively.

The formation chemistry of perovskite films has also been investigated using XPS.[180, 190] Liu *et al.* gradually deposited MAI on PbI_2 and found that prior to the formation of the C—N perovskite peak located at a BE of ~286.6 eV in C 1s spectra, a peak appears at a BE of approximately 285.3 eV.[190] This component has slightly higher BE than adventitious carbon and can be assigned to CH_3I following the loss of NH_3 from the MAI precursor. Depositing $PbCl_2$ on MAI to form MAPI was also studied. The BEs of the MAPI peaks shift towards a high BE side with the increasing thickness of $PbCl_2$.[180] The results suggest a charge transfer mechanism during the chemical interaction between the two precursors, as shown in Figure 3.14. The lead reacts with iodine ions to form Pb—I bonds in the perovskite structure and chlorine atoms are lost from the perovskite film when MAI is sufficient.

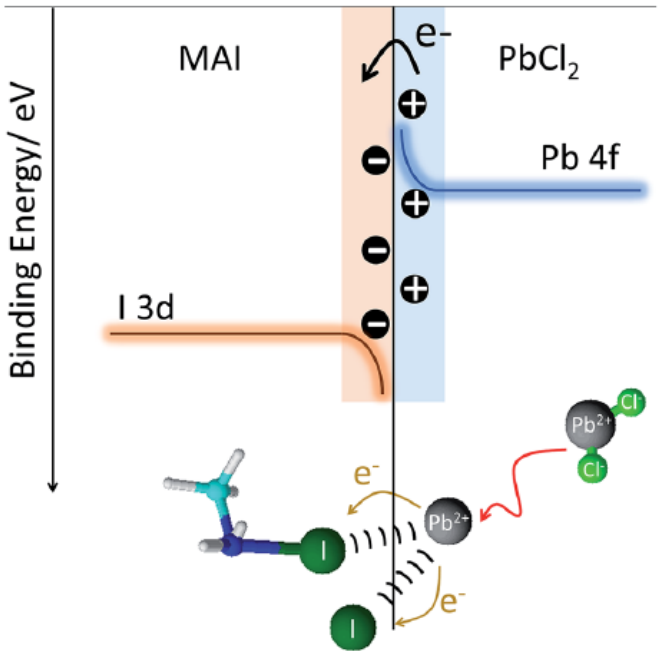

Figure 3.14 A schematic diagram illustrating the charge transfer and chemical interaction at the MAI/$PbCl_2$ interface.[180]

It was found that using excess MAI in a precursor solution for the formation of MAPI, the dissociation of MAI into smaller molecules, such as CH_3I, can occur.[153] Jian *et al.* utilised a sequential MAI vapour to convert PbI_2 to MAPI and found that the I/Pb ratio gradually increases from ~2.0 to 3.0 after 60 minutes, indicating the formation of the perovskite.[191] Furthermore, thermal evaporation is often used to deposit perovskite films for use in the measurements of XPS since it can be simply integrated into PES equipment. In this way, as-deposited films are not exposed to ambient air, ensuring fresh surfaces can be studied.[8, 192, 193] Zhou and co-workers performed *in situ* co-evaporation of PbI_2 and MAI to form MAPI on a ZnO(0001) single crystal.[193] It was found that the film is PbI_2-rich when the thickness was only 1.5 nm. They applied equation (3.9) to calculate the thickness of MAPI films by considering the attenuation of signals caused by an overlayer:[194]

$$I = I_0 \exp(-d/\lambda), \tag{3.9}$$

where I and I_0 are the attenuated and original photoelectron intensity after and before deposition, respectively. d is the thickness of a perovskite film and λ is the IMFP. Another study reveals a similar result with the presence of PbI_2 at the early growth stage, even in an MAI-rich environment.[195] They suggest that the reason can be the extremely low binding energy of adsorbed MAI molecules on the substrates, such as ITO. The ratio of precursors can also affect the surface composition of perovskite films. Compared to a precursor solution containing less PbI_2, perovskite films fabricated from an equimolar mixtures of MAI and PbI_2 have 0.2 eV higher BE in various core levels.[196] They also found by annealing MAPI films at 150 ^{o}C, the MAPI converted from weakly *p*-type to strong *n*-doped film (+0.5 eV BE). In summary, despite some difficulties, using

XPS to investigate the formation chemistry of perovskite films provides a lot of useful information.

Ar ion sputtering can be utilised in XPS to clean the perovskite surfaces [197] and/or study depth profiling [198]. However, due to the difference in mass of the elemental components of typical perovskite films, some side effects were found as a result of Ar^+ sputtering, *i.e.* the preferential loss of nitrogen and halide, and an increase in the metallic lead signal.[197] Therefore, the uniformity of the stoichiometry of etched perovskite films by sputtering would be a concern. Nonetheless, the relative concentrations of various elements throughout a PSC device can still be understood. For instance, the diffusion of iodine ion from MAPI to an Au electrode can be observed, suggesting the iodine component of MAPI passes through the hole transporting material to form a contact with the Au electrode.[198]

XPS can also be utilised to understand the surface coverage of deposited films in a qualitative way.[177, 199] If there are fewer signals from the substrate, such as In 3d from ITO, it means the surface coverage of films on the top of the substrate is better. This would be useful when SEM images are insufficiently clear to show whether or not pinholes penetrate through the film, or if the substrate is amorphous, which cannot be detected by XRD. The study of surface compositions by XPS is also applied to inorganic lead [200, 201] and tin perovskites [9, 202], despite very limited reports. It was found that the total amount of halide in $CsPbX_3$ (X is halide) quantum dot surfaces significantly surpasses the normal stoichiometry of 3, suggesting the halide-rich surface of the quantum dots.[200, 201] Kumar *et al*. found that Sn^{4+} is present at the surface of $CsSnI_3$, indicating the occurrence of Sn^{2+} oxidation.[202]

3.2.3 Surface Stability

The surface stability studies of halide perovskites can be studied by comparing fresh and aged perovskite films. PES techniques are powerful tools to detect the early stages of degradation since the decomposition of a perovskite film typically occurs at the surface first. This is because the outermost surface would be in direct contact with sources that can initiate degradation, such as H_2O vapour, before those species penetrate into the bulk. Many drivers of degradation of perovskite films have been investigated by XPS, *i.e.* heat [121, 123, 203, 204], ambient air [116, 205-209], H_2O vapour [116, 210], oxygen [116, 210], light [211-214]. In this section, PES studies of the various degradation models are summarised.

3.2.3.1 Heat

XPS measurements on MAPI films heated *ex situ* at 85 ^oC in different atmospheres (air, N_2, and O_2) were performed by Conings and co-workers.[121] In all cases, the nitrogen moiety of the MAPI films was gradually lost along with the formation of metallic lead with heating time. This suggests that MAPI is intrinsically unstable at these temperatures. However, heating in N_2 and O_2 for a day leads to mild degradation, compared to the severe decomposition of MAPI heated in air. The results clearly suggest that moisture is, therefore, a key atmospheric component involved in dissociation of MAPI perovskite films. It was also found that the presence of ZnO accelerated the degradation of MAPI.[123] This can be attributed to a large amount of OH^- present at the surface of ZnO that dissociates the iodine part of MAPI by ion exchange. However, this study did not provide direct evidence by probing MAPI *via* XPS. It is worth investigating the reaction between perovskites and transporting materials to ensure stable interfaces.

Huang *et al.* further investigated the thermal degradation behaviour (up to 300 ^{o}C) of MAPI films using XPS and NAP-XPS.[203] In *vacuo*, the nitrogen component of MAPI is completely lost between temperatures of 100 and 150 ^{o}C, with formation of metallic lead above 150 ^{o}C. The former suggests the conversion from MAPI to PbI_2 and the further transformation of PbI_2 into metallic lead by loss of iodine when heated at higher temperatures. They further studied the *in situ* thermal degradation of MAPI under 1 mbar pressure of O_2 and H_2O vapour using NAP-XPS, as shown in Figure 3.15. Unlike the in UHV study, the lead of MAPI films becomes oxidised at 250 ^{o}C and above in both the H_2O and O_2 environments. It can be also seen that the Pb 4f BEs of Pb^{2+}—O and Pb^{4+}—O are lower than that of Pb—I bonding from either MAPI or PbI_2. Most of the metallic lead appears to transform to lead oxides under heating in the presence of oxygen. In addition, hot H_2O vapour facilitates the formation of OH^- bonding to $Pb(OH)_2$ when the film is heated above 250 ^{o}C.

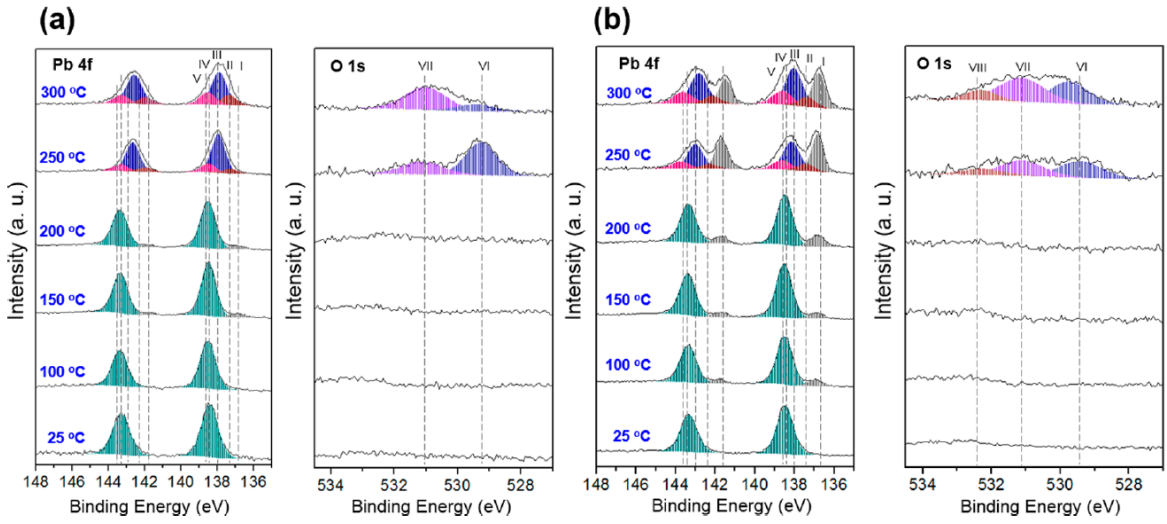

Figure 3.15 Pb 4f and O 1s spectra of the MAPI films annealed under 1 mbar pressure of (a) O_2 and (b) H_2O. Peak assignments: (I) Pb^0; (II) Pb^{2+}—O; (III) Pb^{4+}—O; (IV) Pb^{2+}—I; (V) Pb^{4+}—O satellite and Pb^{2+}—OH; (VI) α-Pb^{2+}—O/Pb^{4+}—O; (VII) β-Pb^{2+}—O/Pb^{4+}—O satellite, and (VIII) Pb^{2+}—OH.[203]

3.2.3.2 Ambient Air

MAPI films stored under ambient atmospheric conditions with a relative humidity (RH) of ~40% for 10 days were found not to have significant changes in surface compositions.[205] However, the films become more *n*-type, which was ascribed to H_2O doping. In contrast, other MAPI films placed in a less humid environment show more degradation for a comparable ageing length in air,[206] probably due to different preparation routes. An apparent decrease in iodine and nitrogen relative to lead was observed. Following 21 days ageing, the width of the Pb $4f_{7/2}$ peak broadens and can be fitted into three components, assigned to $PbCO_3$, $Pb(OH)_2$, and PbO at BEs of 139.3, 138.5, and 137.8 eV, respectively. The key sources that cause this degradation/oxidation would not be distinguished in this study owing to the presence of both H_2O and O_2 in ambient air.

By exposing MAPI films to air, it was seen that the hydrocarbon C 1s peak substantially increases, which can be attributed to contamination from the atmosphere as well as decomposition MAPI.[116] However, after the film is exposed to air for > 1 hr, the nitrogen moiety of MAPI is found to be almost completely lost from the MAPI film. This is possibly due to the co-evaporated films being very thin (~10 nm) compared to spin-coated films, which have a typical thickness of approximately 200 nm. It was found that for aged MAPI films deposited on TiO_2 in the air for 1000 days, the relative Ti and metal oxide concentrations obtained from Ti 2p and O 1s spectra increase, indicating that the degraded film became less dense.[209] The influence from HTM such as Li-doped Spiro-MeOTAD on MAPI films was also investigated.[207] It was found that with ageing time in ambient air, the Li 1s signals of the MAPI film increase, indicating the occurrence of chemical reactions between the HTM and the perovskite layer.

3.2.3.3 H_2O Vapour

A detailed XPS study of MAPI films exposed to water vapour was conducted by Li *et al*.[116] They performed the exposure process (up to 20 mbar) in the preparation chamber in the XPS apparatus without exposing the samples to ambient air. It was found again that H_2O molecules act as *n*-type dopants for MAPI films prior to the occurrence of severe degradation. Upon exposure to higher pressures of H_2O, the iodine was partially and nitrogen completely lost from the MAPI film, whilst the overall carbon concentrations seemed to be maintained by transformation from C—N to C—H. They therefore proposed the decomposition route of MAPI upon exposure to sufficient H_2O vapour as the following equation (3.10):

$$CH_3NH_3PbI_3\ (s) \xrightarrow{H_2O} (-CH_2-)\ (s) + NH_3\ (g) + HI\ (g) + PbI_2\ (s), \qquad (3.10)$$

where (—CH_2—) represents the residual hydrocarbon complex converted from MAPI, which has a BE of ~285.4 eV. However, this observation is not completely consistent with the widely recognised reaction as expressed below (3.11):[133]

$$CH_3NH_3PbI_3\ (s) \xrightarrow{H_2O} CH_3NH_3I\ (aq) + PbI_2\ (s). \qquad (3.11)$$

The difference between the hydrolysis of MAPI films is probably due to different exposure methods. In the work of Philippe and co-workers, they directly added a water droplet to the surface of perovskite films rather than exposing water vapour.[133] The disappearance of C—N, as well as a decrease in the hydrocarbon peak, confirms the loss of the carbon and nitrogen moieties of MAPI films. The proposed formation of MAI is eventually washed away by liquid water. Nevertheless, the *ex situ* exposure of MAPI

involves many external factors in the reaction which may therefore influence the interpretation of results obtained.

The effect of water vapour was also investigated using UPS to focus on the SECO and VB regions in order to understand the changes in the electronic structure of MAPI.[210] Under low partial pressure water vapour exposure (10^{-6} mbar), they found reversible water adsorption on the MAPI surface and suggested that the oxygen of H_2O molecules points towards the perovskite surface. At this stage, MAPI films were neither degraded nor showing evidence of significant hydrated species. When the pressure of H_2O vapour increased to 4 mbar, it was found that the film became more *n*-type by observing an increase in the BE of the VB edge.

3.2.3.4 Oxygen

Unlike H_2O, oxygen acts as a *p*-type dopant for MAPI films.[116] However, oxygen adsorption is too low to be seen in the O 1s spectra. Compared to H_2O vapour exposure, less impact on the decomposition of MAPI films exposed to oxygen was observed. The decrease in C, N, and I suggest that the leaving species could be MAI. However, the majority of effects may come from the measurement in *vacuo* rather than the O_2. Therefore, it is suggested that H_2O plays a more important role than O_2 in the decomposition reaction of MAPI.

The results above, which were obtained by XPS, are generally consistent with the outcome of a UPS study.[210] Here exposure to O_2 appears to shift the Fermi level closer to the VBM, indicating a change to a more *p*-type material. They ascribe this phenomenon to two possible reasons. First, oxygen, as an electron acceptor, can capture the photogenerated electrons from MAPI film, leading to the formation of superoxide (O_2^-)

species.[104] Subsequently, deprotonation of $CH_3NH_3^+$ occurs to generate CH_3NH_2 that can be released from the surface of MAPI films. Second, oxygen can react with metallic lead and the concentration of Pb^0, which corresponds to *n*-doping, is reduced.

3.2.3.5 Light

Light-induced compositional changes at the surface of perovskite films are of great interest, as perovskite light absorption is inevitable and essential for use in PV devices. Under laser irradiation (wavelength: 408 nm and power: 20 mW), signals from the substrate and metallic lead gradually appear.[211] Since the film surface becomes Pb rich, the MAPI surface becomes more *n*-doped behaviour, resulting in an increase in BEs. The formation of elemental lead is due to degradation of PbI_2 upon exposure to light *via* the reaction below (3.12):

$$PbI_2\ (s) \xrightarrow{\text{light}} Pb\ (s)\ + I_2\ (g). \qquad (3.12)$$

X-ray exposure was also used to investigate the photodegradation of perovskite surfaces.[212] Using a low-flux X-ray (below 10^9 photons/second) to illuminate perovskite films, it was found that the film does not exhibits changes in the surface composition. However, when the film is irradiated by a visible-light laser, it was observed that the BE of the Pb 5d spectrum and the relative concentration of metallic lead increase. Interestingly, when the laser is turned off, not only does the BE shift back to the original value before laser illumination but the amount of metallic lead also reduces. The former can be attributed to the surface photovoltage effect and the latter is possibly due to the partially recovering reaction of the degradation process (3.13):

$$Pb\ (s) + I_2\ (g) + FAI\ (s) \rightarrow FAPbI_3\ \ (s). \qquad (3.13)$$

At the outermost surface, I_2 is expected to leave the film. The authors therefore proposed that iodine molecules diffuse from bulk of the film, and then reacts with residual metallic lead and FAI. Furthermore, after laser irradiation, the concentration of Br in $(FAPbI_3)_{0.85}(MAPbBr_3)_{0.15}$ perovskites significantly increases, whilst that of iodine remains roughly constant.

If an X-ray without flux control illuminates a perovskite surface, the decomposition of MAPI films can occur, as shown in Figure 3.16.[213] Following 14-hour irradiation by a lab-based X-ray source, the N 1s signal from MAPI underwent significant changes; *i.e.* two extra components were generated and the main peak ($CH_3NH_3^+$), attributed to MAPI, decreased. The N 1s peak located at ~401 eV can be assigned to CH_3NH_2. However, the origin of the feature at a BE of ~399.7 eV in N 1s spectra is not discussed. With longer exposure time, the iodine and nitrogen concentrations drop relative to lead significantly, indicating light-induced degradation. The decrease in both nitrogen and iodine is consistent with the data obtained from another report using a similar X-ray source.[214] Here the VB region in the XPS spectra of MAPI showed after X-ray exposure for 200 hours, the VB structure of the degraded film is almost identical to that of PbI_2.[214]

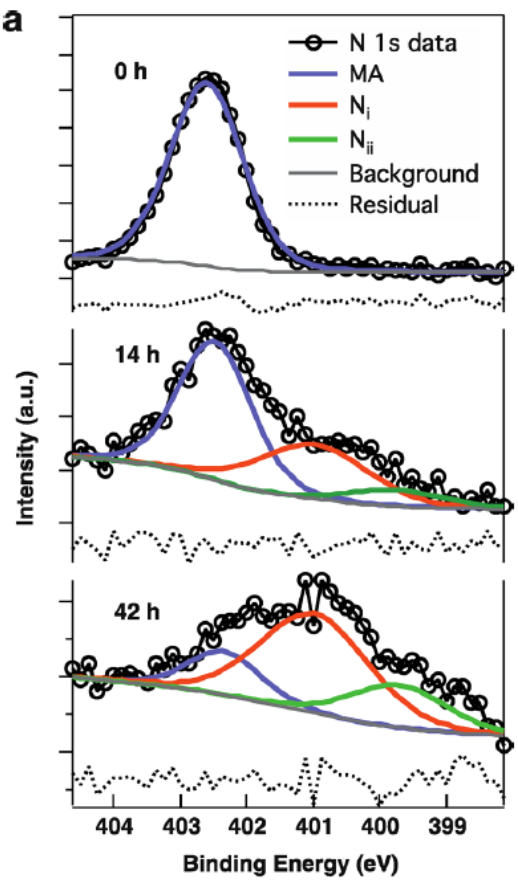

Figure 3.16 N 1s XPS spectra of MAPI on exposure to X-ray.[213]

3.2.3.6 Others

The sections above have introduced the influence of commonly discussed degradation sources on perovskite films using PES techniques. Other potential factors that could induce the surface degradation of halide perovskites are discussed here. Low-energy electrons were also used to study the impact on the surface of MAPI films.[215] It was found that by increasing the incident electron fluence, the nitrogen and iodine concentrations of the film significantly decrease relative to the lead, from ~1.0 and 3.0 to 0.0 and 2.0, respectively. This indicates the complete conversion from MAPI to PbI_2. They also noticed that following degradation, the hydrocarbon component observed in C 1s spectra increases, consistent with the degradation route caused by water vapour.[8]

There is also some evidence suggusting that the electrode can cause the degradation of PSCs.[216] By observing Ag 3d and I 3d XPS spectra of a MAPI device before and after the device was aged in air for 3 weeks, it was seen that the BE shifts in both Ag and I 3d spectra, suggesting the formation of AgI.[216] The authors proposed that the moisture-induced degradation mechanism of MAPI is further promoted by the Ag electrode, as shown in Figure 3.17. In brief, H_2O molecules penetrate the hygroscopic HTM to be in contact with MAPI. Subsequently, the degraded iodine-containing species of MAPI induced by water can migrate through the HTM to contact with the Ag electrode to form AgI. The presence of Ag accelerates the escape of the iodine-containing compounds from MAPI. The device performance is therefore deteriorated due to degradation of MAPI and formation of AgI (increased electrical resistance).

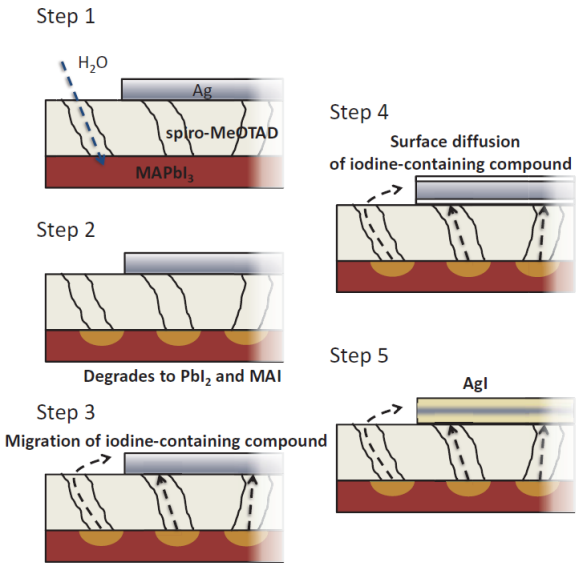

Figure 3.17 Step-by-step illustration of the proposed degradation mechanism of AgI formation in MAPI-based PSC devices: (1) H_2O molecules in air enter pinholes of the spiro-MeOTAD layer; (2) decomposition of MAPI gives rise to iodine-containing volatile compounds; (3) migration of the iodine-containing compounds from the MAPI layer that corrode the Ag electrode ; (4) surface diffusion of the iodine-containing volatile compounds; (5) the formation of AgI.[216]

3.3 Sample Processing

In this thesis, we apply various deposition methods to deposit perovskite films, mainly including spin coating, vapour deposition, and AACVD. The theory, instrumentation, and general experimental information of these techniques will be introduced respectively in this section.

3.3.1 Spin Coating

Spin coating is a thin-film deposition technique that can deposit a small amount of precursor material onto a flat substrate by rotation of the substrate at high speed. The homogeneity of deposited films can be achieved through centrifugal force induced by spinning the substrate. There are a few processing parameters that can be adjusted to meet the required standards of a film. Amongst them, spin speed is of great importance and can determine the uniformity and thickness of deposited films. For perovskite films, these two properties are crucial to the final performance of PSC devices. A higher spin speed gives rise to thinner films deposited with better uniformity.[217] This means simply reducing spin speed will not give uniform thicker films. To obtain thicker films, the concentration of the precursor solution needs to be adjusted, in conjunction with the spin speed. Typically, for perovskite film deposition, the molar concentration of a perovskite precursor solution used is approximately 1.0 M, depending on the requirements.[218] The spin speed is generally set to 4000 or 5000 rpm to ensure a thin and uniform perovskite film. In addition, the acceleration rate can also determine the film quality as well as the thickness of the deposited film. A high acceleration rate would fling off more solution after spinning begins.

The scheme of a typical spin coating process for perovskite film deposition is shown in Figure 3.18. First, some precursor solution is dropped onto the substrate placed in the spin coater. The volume of perovskite precursor solutions used is typically around 100 μl to cover the whole surface of an ITO-glass substrate with a size of 2.0 x 1.5 cm. Then a pre-set spin-coating programme starts immediately to spread the solution uniformly. The excess solution is flung off during rotating. Typically, after spin coating, the originally light-yellow-coloured precursor solution becomes a translucent light-brown-coloured thin film. The coated substrate is then transferred to a hot plate to further evaporate the solvent(s) and form a crystalline perovskite film.

In some cases, so-called ‘dynamic-dispense spin coating’ technique may be applied to achieve even better uniformity. Unlike conventional spin coating, the solution is not dropped on the substrate before spinning; instead, the solution is placed once the spin speed reaches the set speed. Furthermore, some perovskite films are treated with antisolvent in order to obtain better film quality. Typically, the antisolvent used is added to the substrate precusor after the start of the spinning. The amount and time at which it is added depends on the antisolvent used and perovskite system applied. Relative humidity condition can also affect the parameters used for spin coating. If a spin coater is in a dry place, toluene or chlorobenzene is typically used for perovskite film deposition.[219] However, if the environment is more humid (such as the conditions explored in this thesis), acetate-based antisolvents are preferable.[86] The reason for this is that this kind of solvent can absorb moisture and this prevents perovskite films from initial degradation during preparation of the films.

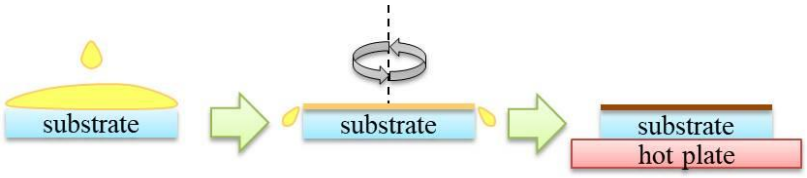

Figure 3.18 Scheme of a typical spin coating process for perovskite film formation.

3.3.2 Vapour Deposition

Vapour deposition is often applied in the manufacture of semiconductors and includes two key techniques chemical vapour deposition (CVD) and physical vapour deposition (PVD). The key difference between CVD and PVD is the involvement of chemical reactions. In other words, if MAPI is used as a single-source precursor to be evaporated, the MAPI film is deposited through a PVD process.[220] On the other hand, using a dual-source of MAI and $PbCl_2$, for example, to form perovskite films, then a chemical reaction is involved so this process is deemed as a CVD method.[8, 28] Only CVD processes were performed in this thesis, including conventional CVD and AACVD. A typical CVD process requires volatile precursors that can be thermally evaporated and a vacuum system which can pump gas by-products away. Depending on the quality of the film needed, the different vacuum levels of CVD can be introduced. In this thesis, (ultra)high vacuum CVD was performed to deposit ultrathin perovskite films (Chapter 4), as shown in Figure 3.19. The thermal evaporation was conducted in a Knudsen cell directly connected to the XPS apparatus, which means the samples are not exposed to ambient air. The heating of two precursor sources was performed using an electric current provided by a power supply. The temperatures were controlled to just above the occurrence of sublimation monitored by thermocouples directly attached to the precursor containers. We generally follow the procedures reported in the literature,[28] which will be presented in detail in Chapter 4.

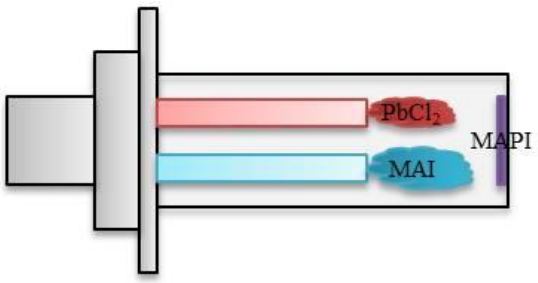

Figure 3.19 Illustration of the Knudsen-cell-type evaporator for MAPI deposition.

3.3.3 AACVD

Chapter 2 introduces the mechanism and application of AACVD in PSCs. In this section, we concentrate on the instrumentation. As illustrated in Figure 3.20, an ultrasonic humidifier is required in order to transform the precursor solution into mist or so-called aerosol. The humidification intensity is typically set at the maximum power that can be provided by the apparatus to ensure sufficient aerosol is generated.

Precursor solutions are poured in a two-necked round-bottom flask that enables a carrier gas to go in and out. It is worth noting that the solution used in AACVD is typically more dilute than that applied in spin coating since the mist of a concentrated solution is extremely difficult to generate. The carrier gas used needs to be an inert gas to prevent perovskite films from degrading. The flow rate of the carrier gas can influence the lateral film-to-film homogeneity and the uniformity of a film. An AACVD glass tube placed in a furnace is connected with the outlet of the flask *via* a plastic tube. The deposition temperature depends on the type of halide perovskites, normally lower than 200 ^{o}C. Variation in deposition time and the amount of the precursor solution can be utilised to control the thickness of films. However, the latter is not useful as a control measure to deposit films with thicknesses of a few hundred nm since the aerosol cannot be produced when the volume of the solution is insufficient.

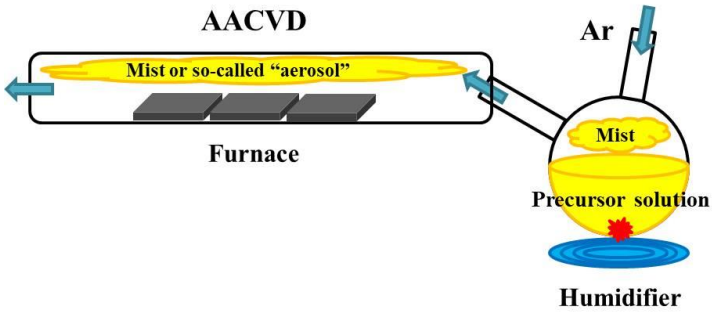

Figure 3.20 Illustration of the whole AACVD apparatus in this research.

3.4 Characterisation Techniques

This section lists and briefly describes the rest of the important characterisation techniques used in this thesis apart from XPS, including scanning electron microscopy (SEM), X-ray diffraction (XRD), ultraviolet-visible-near-infrared (UV-VIS-NIR) spectroscopy, *etc*.

3.4.1 Scanning Electron Microscopy (SEM)

Scanning electron microscopy (SEM) is one of the most commonly used analytical techniques to observe the surface morphology of a sample on micrometre and nanometre scales. Whilst a conventional optical microscope uses visible light to form images, an SEM microscope uses electrons to produce images. SEM has therefore become an essential workhorse in the areas of science and engineering.

In an SEM instrument, an electron beam is emitted from an electron gun, typically fitted with a tungsten filament cathode. When the cathode is electrically heated, a stream of electrons (called primary electrons) is thermionically generated and then is focused by a series of lens and aperture components to hit a specimen. When the primary electrons interact with the sample being studied, the electrons lose kinetic energy due to scattering and

absorption by the specimen. The maximum penetration depth into the sample is typically ~5 μm and the interaction leads to the emission of electrons and photons. The most common mode of operation to collect images in SEM is to detect secondary electrons (so-called SE mode), typically with an energy of below 50 eV. These electrons ejected from the k-shell (the closest shell to the nucleus) of the atoms in the sample are produced by the inelastic scattering interaction between the specimen atoms and primary beam electrons in a similar way to those produced in XPS. The secondary electrons detected only come from a few nanometres from the outermost surface of the sample as a result of their low kinetic energy. The images acquired in this research all used SE signals.

Another commonly used detection mode is to detect backscattered electrons (so-called BSE mode) reflected by the atoms of the sample. This technique is mainly used for distinguishing between chemical compositions at the surface by contrast since heavy elements give stronger backscattering of electrons compared to light atoms, thereby a brighter image is produced. However, using this technique to obtain elemental composition information is limited by the requirement of a large difference in the atomic numbers of the sample atoms. In order to obtain true chemical information, X-ray microanalysis is used and is available in SEM instruments equipped with an X-ray detector.

In SEM, the X-ray microanalysis technique is called energy-dispersive X-ray spectroscopy (EDX or EDS). X-rays are produced from samples measured by SEM, because when a secondary electron is generated, there is a vacancy left in the inner core state which will be filled by an electron from lower binding energy core levels. This transition results in the emission of energy in the form of an X-ray flourescence. A specific transition releases an X-ray with particular energy, allowing the bulk compositional information to be determined, as shown in Figure 3.21.

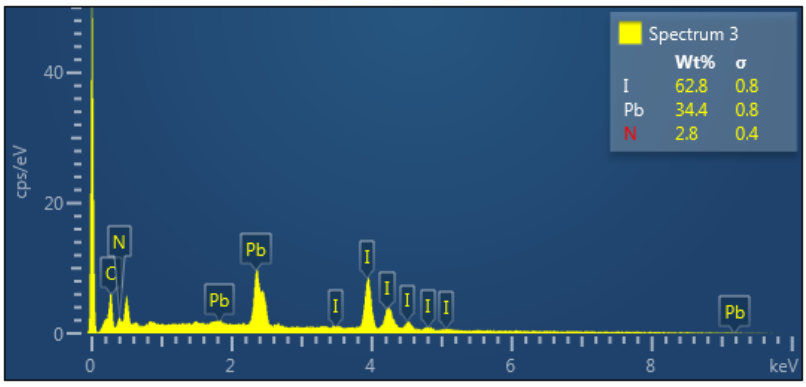

Figure 3.21 A representative EDX spectrum of an MAPI film acquired in SEM.

3.4.2 X-Ray Diffraction (XRD)

XRD is an analytical technique mainly used in phase identification of a crystalline material and it is based on constructive interference of monochromatic X-rays by a crystalline sample. The apparatus used for XRD is called an X-ray diffractometer and consists of three essential elements: an X-ray tube, a sample holder, and an X-ray detector. Like in XPS, X-rays are generated by creating a high voltage across a cathode and anode. Upon the bombardment of the anode material by electrons, characteristic X-ray spectra are produced. Cu is the typical target material used in XRD and it is the one used in this thesis. The X-ray spectrum contains K_α and K_β lines superimposed on the *Bremsstrahlung* background. Cu K_α is used in an X-ray diffractometer, whilst the Cu K_β line is usually filtered. Cu K_α possesses a wavelength of 1.5406 Å which matches well to the interatomic distance of crystalline solids. In addition, copper has excellent thermal conductivity to release the heat produced as a result of electron bombardment, thus preventing the anode melting.

The determination of the lattice parameters of a crystal is primarily in accordance with Bragg's law,[221] as shown below (3.13):

$$n\lambda = 2d \sin\theta, \tag{3.13}$$

where λ is the wavelength of an incident X-ray and n is a positive integer to describe constructive interference by the crystal measured. d is the interplanar distance of the crystalline solid, as shown in Figure 3.22. θ is the scattering angle between the incident X-ray and the crystalline planes. According to as shown in Figure 3.22, the X-ray reflected by the second layer of the crystalline plane lags behind the one that hits the first layer by a distance of $2d\sin\theta$. In order for constructive interference to occur and produce a maximum, this distance must be equal to an integer number of $n\lambda$.

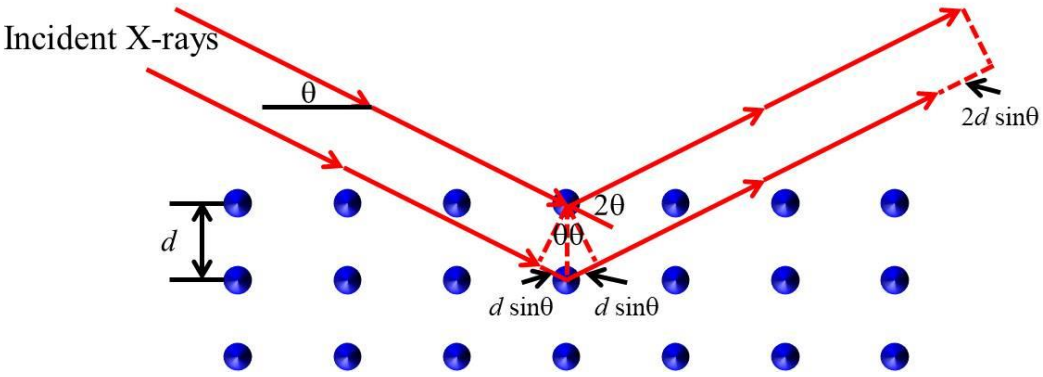

Figure 3.22 Schematic illustration of the diffraction process by a crystal in XRD measurements in accordance with Bragg's law.

After diffraction, the angle difference between the incident X-ray and diffracted X-ray collected by a detector is 2θ. Hence, 2θ is typically expressed as the x-axis of an XRD pattern. In most of the cases, angles ranging from 5^{o} to 80^{o} (2θ) are detected. It is noted that in this research, the thickness of perovskite films are normally less than 1 μm so the sampling depth must remain shallow in order to prevent signals from substrates overlapping that of the film. Hence, grazing incidence XRD (GIXRD) is utilised in this thesis, with a fixed grazing angle at 3^{o}. The grazing incidence function is applied in the

apparatus (Bruker D8 Advance) used. In order to improve the quality of the data collected, the rotational function of the sample stage is enabled. Generally, longer data acquisition time gives XRD patterns with better quality. However, due to the unstable nature of some perovskite films in humid air, the optimised acquisition time in this thesis was set to around 2 hours for each sample. The theta step and dwell time are typically set as 0.05^{o} and 4.5 seconds, respectively. A typical XRD pattern of perovskite films can be seen in Figure 3.23. It shows that primary peaks with Miller indices of (110), (220), and (330), indicating the tetragonal structure of MAPI films. It is noted that the vapour-deposited MAPI film has a minor peak at 12.65^{o}, which can be assigned to PbI_2.[28]

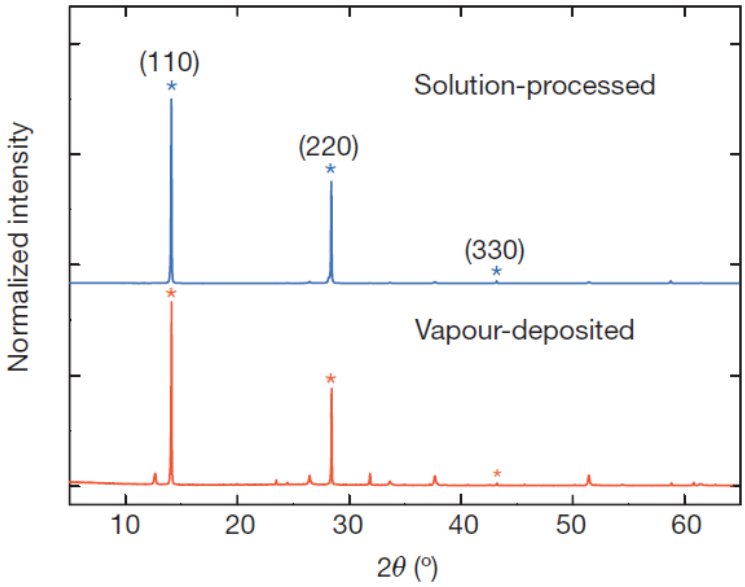

Figure 3.23 A representative XRD spectra of two MAPI films.[28]

3.4.3 Ultraviolet-Visible-Near-Infrared (UV-VIS-NIR) Spectroscopy

The optical properties of perovskite films can be examined using ultraviolet-visible-near-infrared (UV-VIS-NIR) spectroscopy. The NIR region (780 to

2500 nm) is needed to study halide perovskites, since the absorption edge of a typical MAPI film is located at around 800 nm.[111] A material with a narrow optical band gap (E_g) energy, such as Cs_2SnI_6, which can extend its absorption edge to ~950 nm, will absorb light from the NIR region,.[9] In this thesis, UV-VIS-NIR spectroscopy is mainly utilised to determine the E_g of perovskite films deposited. Generally, in a UV-VIS-NIR spectrometer, many modes of operation can be selected, *e.g.* transmission, absorbance, and reflection modes. The fundamental principle of UV-VIS-NIR spectroscopy is based on the equation (3.14) below:

$$A = -\log \frac{I}{I_0}, \tag{3.14}$$

where A is absorbance, and I and I_0 is the intensity of the detected light and the incident light, respectively. The I/I_0 ratio is called transmittance (T) if the light passes through the sample or reflectance (R) if the detected light is reflected from the sample. It is noted that absorbance is different from absorption and is equivalent to -log$T$ in transmission mode. A typical UV-VIS-NIR spectrometer is equipped with multiple radiation sources, such as a tungsten lamp (300 – 2500 nm) and a deuterium lamp (190 – 400 nm), where the latter provides a continuous UV spectrum with better quality when the wavelength is less than 320 nm.

For a solid sample with a fixed thickness, the absorbance depends on the absorption coefficient (α) of the material measured. Absorption coefficient is also called attenuation or extinction coefficient and characterises how easily a volume of material can be penetrated by light. Typical halide perovskites have high absorption coefficients at an order of 10^5 cm^{-1} in the visible-light range.[222] Hence, perovskite films only require

very thin films (< 1 μm) to deliver sufficient light absorption for use in PV devices. For a solution, absorbance can be expressed as below equation, in accordance with Beer–Lambert law:

$$A = \alpha lc, \tag{3.15}$$

where l and c are the thickness and concentration of a medium, respectively. If the sample being measured is a solid, the density of the solid, ρ, is used.

In order to obtain the precise E_g information and absorption spectra of perovskite films, the integrating sphere module is required since the diffuse scattering of light is significant in a typical perovskite sample.[65] Therefore, optical diffuse reflectance using integrating sphere mode is applied to obtain the precise absorption spectra by converting reflectance to absorption data in accordance with the Kubelka−Munk equation (3.15):[223]

$$\alpha/S = (1 - R)^2/2R, \tag{3.15}$$

where S is the scattering factor. The absorption values are directly calculated by the software of the apparatus (Perkin Elmer Lambda-1050) used. Then the E_g of perovskite films can be obtained by a Tauc plot, as shown in Figure 3.24. In a Tauc plot, the power $(1/r)$ of the $(\alpha h\nu)^{1/r}$ is associated with the bandgap energy transition type of the sample measured, where r depends upon the nature of transition. If r is equal to 1/2, 3/2, 2, or 3, the transition is direct allowed, direct forbidden, indirect allowed, or indirect forbidden, respectively. In the case of Figure 3.24, it can be known that Cs_2SnI_6 is assumed as a direct bandgap material in the literature.[65]

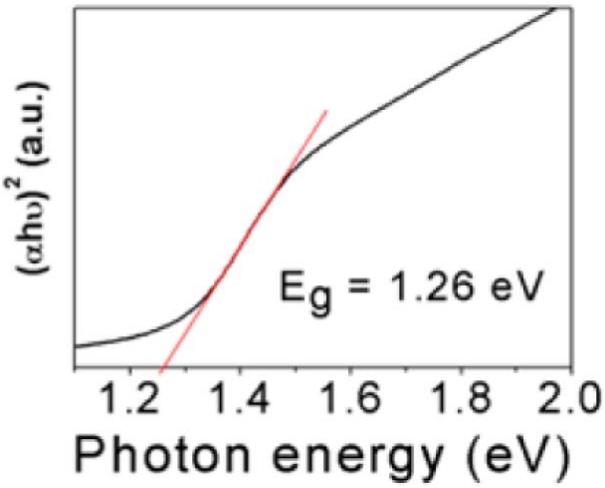

Figure 3.24 A representative Tauc plot of a direct E_g Cs_2SnI_6 film.[65]

3.4.4 Other Characterisation Methods

The previous sections have introduced primary characterisations in this thesis. Here, some other analytical tools are also briefly presented.

3.4.4.1 Surface Profilometer

A surface profilometer is a piece of practical and facile equipment to determine the thickness and roughness of perovskite films. In this thesis, a Veeco Dektak 8 Surface Profilometer is performed to quickly obtain thickness information. A profilometer is a contact-type tool that uses a stylus for specified contact force.

3.4.4.2 Solar Simulator

Current density-voltage (*J-V*) characteristics were obtained using a solar simulator (Oriel SOL3A) consisting of a Keithley 2420 Sourcemeter and 100 mW/cm^2 illumination (AM 1.5G) with a calibrated NREL certified Oriel Si-reference. Some of the selected results are presented in the Appendix, as a side project in this thesis.

Chapter 4 Investigation of Moisture-Induced Degradation at Halide Perovskite Surfaces Using NAP-XPS

This work has been first published in Chemical Communications on 19/04/2017

Cite this: *Chem. Commun.*, 2017, **53**, 5231

4.1 Introduction

This chapter contains a paper that has been published in Chemical Communications.[8] As presented in Section 3.2, photoemission spectroscopy has been widely used to probe the surface of halide perovskites to obtain elemental compositions and/or valence band structure. However, to date, only a few studies apply NAP-XPS to monitor the atmospheric degradation process of halide perovskites.[8, 203] This paper (Paper 1) describes the introduction of NAP-XPS study into the field of PSCs to investigate the surface stability and degradation mechanisms of halide perovskites for the first time. This work purely involves a fundamental surface science study and focuses on a prototypical halide perovskite, MAPI. We employed thermal evaporation to deposit an ultrathin MAPI film using a lead chloride precursor to react with MAI in a vacuum chamber (Knudsen cell) directly connected to the NAP-XPS instrument at the University of Manchester. This prevents the film from exposure to ambient air prior to XPS measurements in order to acquire accurate results for the degradation study. The film was then exposed to water vapour with pressures of up to 9 mbar, which is equivalent to a relative humidity of 30%, to simulate an atmospheric environment. NAP-XPS enables

photoemission signals associated with the degradation process during atmospheric exposure to be probed. This allows researchers to identify the moisture-induced degradation route of MAPI surfaces. We found that upon water vapour exposure, MAPI degraded into lead iodide and hydrocarbon chains through the release of hydrogen iodide and ammonia gases. The lead iodide formed at the surface can further convert into metallic lead and iodine gas in the presence of light and moisture. We believe that this paper opens an avenue of performing an *in situ* investigation of the degradation of halide perovskite surfaces using NAP-XPS. This work acts as the fundamental part of all resulting chapters in this thesis and all following papers adopt the experimental design of NAP-XPS for water exposure experiments.

Contribution

Prof Wendy Flavell and Dr Andrew Thomas inspired me to investigate the degradation process of MAPI surfaces using NAP-XPS. The author played a major role in this work to plan and perform the experiment (including XRD) and to analyse the data obtained, with useful advice from Prof Wendy Flavell and Dr Andrew Thomas. Dr Alex Walton greatly supported the NAP-XPS experiment and taught me the standard operating procedures to use the instrument and provided valuable suggestions for the experimental execution and data analysis. Dr David Lewis and Prof Paul O'Brien (deceased) offered some initial resources for perovskite research, including supplying homemade high-quality MAI powders for use in this work. Dr Aleksander Tedstone provided some advice for the manuscript prior to the submission to the journal. The author wrote this paper with Prof Wendy Flavell and Dr Andrew Thomas, with suggestions from the co-authors.

4.2 Paper 1

4.2.1 Main Text

ChemComm

COMMUNICATION

View Article Online
View Journal | View Issue

Cite this: *Chem. Commun.*, 2017, **53**, 5231

Received 27th February 2017,
Accepted 19th April 2017

DOI: 10.1039/c7cc01538k

rsc.li/chemcomm

In situ investigation of degradation at organometal halide perovskite surfaces by X-ray photoelectron spectroscopy at realistic water vapour pressure†

Jack Chun-Ren Ke, [ab] Alex S. Walton, [bc] David J. Lewis, [d] Aleksander Tedstone, [c] Paul O'Brien, [c] Andrew G. Thomas *[bd] and Wendy R. Flavell *[ab]

Near-ambient-pressure X-ray photoelectron spectroscopy enables the study of the reaction of *in situ*-prepared methylammonium lead iodide (MAPI) perovskite at realistic water vapour pressures for the first time. We show that MAPI decomposes directly to PbI_2, HI and NH_3 without formation of methylammonium iodide, allowing us to distinguish between alternative mechanisms for the atmospheric degradation reaction.

Organometal halide perovskite (OHP) absorbers have rapidly emerged as one of the most promising photovoltaic materials for use in solar cells due to their high visible to near-infrared light absorptivity,[1–4] remarkably low exciton binding energy,[5] and extraordinarily long diffusion length for electrons and holes.[6,7] As a result, perovskite solar cells (PSCs) have achieved certified power conversion efficiencies of more than 20%,[8] in just over 7 years from the initial discovery of the photovoltaic effect in TiO_2 coated with nanocrystalline perovskite.[9] These efficiencies are now comparable to those of commercial polycrystalline silicon solar cells. However, OHPs show poor long-term stability, particularly when exposed to humid atmospheres which means that there are questions about the commercial exploitation of PSCs in solar panels.[10] Improving the stability of OHP absorbers is of paramount importance, but only with insight into the degradation mechanisms at the atomic level can solutions thus be realised.

Numerous characterisation techniques have been applied to investigate the degradation mechanism, such as ultraviolet-visible (UV-Vis) spectroscopy,[11–13] X-ray diffraction (XRD),[11,13,14] Raman spectroscopy,[15] and X-ray photoelectron spectroscopy (XPS).[16–18] This latter technique is useful since it allows *in situ* deposition of the films in an ultrahigh vacuum (UHV) environment,[17,19–21] so that degradation of the films before measurement is ruled out. Several XPS studies have been carried out to determine the surface composition or film growth mechanism,[19–27] and band alignment.[28–30]

Despite these studies, the mechanism of degradation of pristine films at the atomic and nanometre scale remains imprecisely defined. Currently, two models of OHP degradation have been proposed. The first involves the water-catalysed loss of nitrogen, in the form of ammonia, and hydrogen iodide *via* the reaction (eqn (1)):[17]

$$CH_3NH_3PbI_3(s) \xrightarrow{H_2O} (-CH_2-)(s) + NH_3(g) + HI(g) + PbI_2(s) \quad (1)$$

Thermogravimetric analysis of bulk MAPI by Grätzel and co-workers suggests that the organic component of the perovskite material is lost *via* volatilisation of HI and CH_3NH_2 with the latter species lost at higher temperatures.[31] The second proposal involves decomposition to methyl ammonium iodide (MAI) and lead iodide in the presence of liquid water (eqn (2)):[16]

$$CH_3NH_3PbI_3(s) \xrightarrow{H_2O} CH_3NH_3I(aq) + PbI_2(s) \quad (2)$$

Key difficulties in understanding the degradation mechanism of MAPI are the difficulty in determining the surface chemistry of the first few atomic layers of the pristine material without any exposure to ambient atmospheric conditions, and, conversely, the difficulty in measuring this same surface chemistry in real time under exposure to realistic environments. In this work we address both problems simultaneously by utilising Near-Ambient Pressure XPS (NAPXPS) to investigate the real-time degradation of an *in situ*-deposited MAPI film, exposed to water vapour pressures equivalent to atmospheric relative humidity (RH) of *ca.* 30% at a standard temperature of 25 °C, conditions which could be realistically be observed under ambient atmospheric environments. This yields an unparalleled mechanistic insight. The data unambiguously indicate a degradation pathway

[a] *School of Physics and Astronomy, The University of Manchester, Oxford Road, Manchester, M13 9PL, UK. E-mail: wendy.flavell@manchester.ac.uk*
[b] *Photon Science Institute, The University of Manchester, Oxford Road, Manchester, M13 9PL, UK. E-mail: andrew.g.thomas@manchester.ac.uk*
[c] *School of Chemistry, The University of Manchester, Oxford Road, Manchester, M13 9PL, UK*
[d] *School of Materials, The University of Manchester, Oxford Road, Manchester, M13 9PL, UK*

† Electronic supplementary information (ESI) available: Experimental details and supporting results. See DOI: 10.1039/c7cc01538k

by reaction with water which involves complete loss of nitrogen from the film without the formation of MAI.

The MAPI film was prepared in UHV by vacuum deposition of $PbCl_2$ and MAI onto a $SrTiO_3(100)$ single crystal substrate, using the two-step route of Liu *et al.* (see ESI† for details of preparation and characterisation).[32] Fig. 1a shows high-resolution NAPXPS spectra of the Sr 3d and Pb 4f core levels recorded from the MAPI film before water exposure, during water exposure at H_2O vapour pressures of 3 mbar (RH 10%) and 9 mbar (RH 30%), and after the water vapour has been removed and the system returned to UHV conditions. The intensity is normalised to the integrated area of the Sr $3d_{5/2}$ peak from the $SrTiO_3$ substrate, which allows comparison of the intensity of the Pb 4f peaks as a function of water exposure. All photoelectron binding energies are quoted to a precision of ±0.05 eV. Prior to exposure to H_2O vapour and under UHV, the Pb $4f_{7/2}$ peak of the perovskite film is located at a binding energy (BE) of 138.60 eV, which is in excellent agreement with previous reports for the Pb in MAPI perovskite materials (denoted 'Pb-I' in Fig. 1).[16,22,30,33] We note that there is a weaker Pb $4f_{7/2}$ peak at 136.80 eV, which is attributed to metallic lead.[16,22,30,33] This has been observed for several perovskite materials, such as MAPI,[16,22,27,33] $MAPbI_2Cl$,[34] $MAPbBr_3$.[33] Metallic lead is often observed in MAPI perovskite films, both for the standard solution-processed films[35,36] and CVD-deposited films.[22] In the study presented here the metallic Pb probably arises due to

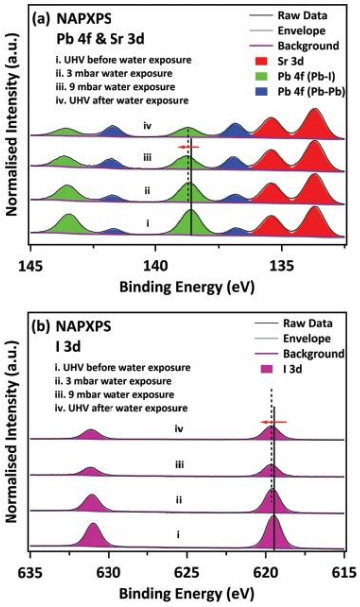

Fig. 1 NAPXPS spectra of (a) Pb 4f & Sr 3d, and (b) I 3d core levels under various conditions as noted (before/during/after water exposure). All the spectra are normalised to the corresponding integrated area of the Sr $3d_{5/2}$ peak.

Table 1 Stoichiometries of the film determined from UHV XPS at different stages, before and after water exposure. The metallic lead content is excluded from these quantifications. A full description of the quantification is given in the ESI

Status ID	I/Pb	N/Pb
UHV before water exposure	2.7 ± 0.1	0.9 ± 0.2
UHV after water exposure	2.4 ± 0.1	0.0 ± 0.2

decomposition of the $PbCl_2$ precursor vapour during the initial deposition step;[21] some beam-induced decomposition cannot be ruled out, but is not the major source of elemental Pb (as we discuss further below). No Cl was observed in survey scans (see Fig. S1, ESI†). The Pb : I : N stoichiometry of the film determined from XPS, excluding the metallic Pb component, was found to be 1.0 ± 0.1 : 2.7 ± 0.1 : 0.9 ± 0.2 (Table 1), in good agreement with the nominal stoichiometry of MAPI. Quantification of the XPS signals is discussed further below and in the ESI† (Tables S1–S3).

Fig. 1(a) shows Pb 4f and Sr 3d spectra recorded during exposure to H_2O vapour. The Pb–I features decrease in intensity, whilst the metallic Pb features increase in intensity. The BE of the Pb $4f_{7/2}$ Pb–I feature shifts upwards slightly to 138.70 eV on exposure to 3 mbar H_2O and to 138.80 eV when the water exposure is increased to 9 mbar. This may be due to the formation of lead iodide (Pb $4f_{7/2}$ BE = 138.90 eV);[16] however the peak cannot be resolved into individual components arising from MAPI and PbI_2. The BE of the MAPI/PbI_2 peak recorded after water exposure, when the water vapour is pumped away and the sample returned to ultra-high vacuum conditions (Fig. 1(a)-iv), is not shifted relative to the spectrum recorded at a water vapour pressure of 9 mbar (Fig. 1(a)-iii). This suggests that the presence of water vapour is not responsible for the observed binding energy shifts, *i.e.* the shifts are due to changes in the nature of the material. The data recorded following removal of the water vapour indicate that the changes induced by exposure to water vapour are not reversible. We observe an additional increase in the intensity of the metallic-lead-derived peak in the UHV spectrum taken following water exposure. In synchrotron studies this was attributed to beam damage,[16] and it is well known that PbI_2 slowly decomposes to Pb and I_2 under illumination with visible light.[37] However, spectra taken at this stage from fresh points on the sample surface (see ESI,† Fig. S3) show a similar surface stoichiometry to that in Fig. 1(a)-iv, and in particular, similar amounts of metallic Pb. We conclude that the decomposition of PbI_2 into Pb and I_2 cannot be attributed solely to beam damage.

Fig. 1b shows I 3d core-level spectra, also normalised to the integrated area of the Sr $3d_{5/2}$ peak. The BE of the I $3d_{5/2}$ shifts towards higher BE, from 619.50 eV (UHV before) to 619.60 eV at 3 mbar water exposure and reaches 619.65 eV at 9 mbar water exposure. The change in BE matches the changes in the Pb 4f spectra. The I signal decreases significantly upon water exposure, suggesting it is lost from the surface, which is not consistent with a degradation mechanism resulting in the formation of MAI. We note that the intensity increases slightly when the water vapour is removed. This is a consequence of the lower kinetic energy of the I 3d electrons relative to Pb 4f. Lower kinetic energy electrons are

less likely to be detected by the analyser than high energy ones as the gas pressure in the NAPXPS cell is increased.

Fig. 2 shows the C 1s and Sr 3p spectra. The C 1s spectrum allows us to investigate the behaviour of the organic part of the perovskite under water vapour exposure. The Sr $3p_{3/2}$ peaks are located at 269.20 eV, consistent with Sr–O bonding.[38] The clean $SrTiO_3$ spectrum shows a very weak signal associated with a small amount of residual adventitious carbon. In the freshly-prepared MAPI film we observe two C species in the C 1s spectrum. The larger C 1s peak is located at a BE of 285.35 eV. This peak has been assigned both to CH_3I,[21] and to C–C bonds (hydrocarbon).[21] Ng *et al.* linked the formation of the C–C species to reaction with PbI_2,[22] but it is perhaps more likely to occur due to decomposition of the precursors or simply due to outgassing of the sources during evaporation of the films. A shoulder is also observed at 286.85 eV, 1.5 eV higher than the main peak, corresponding to C–N bonding in the MAPI perovskite.[16,17,21,34] However, as discussed below, we believe this feature also contains contributions from C=O/C–OH groups in the hydrocarbon contamination. We do not believe the MAI precursor contributes significantly to the higher binding energy feature here, since the core level shift in the C 1s feature between C–C/CH_3I and C–N in MAI is larger at 1.9 eV,[22] than the 1.5 eV measured here. Upon exposure to water vapour, the relative intensities of the C 1s peaks change substantially. The higher energy peak, which contains contributions from C–N in the MAPI, is seen to decrease in intensity. During and after exposure to 9 mbar water vapour there is an increase in the relative intensity of the lower binding energy feature as C–N is converted to CH, consistent with the mechanism proposed in eqn (1).

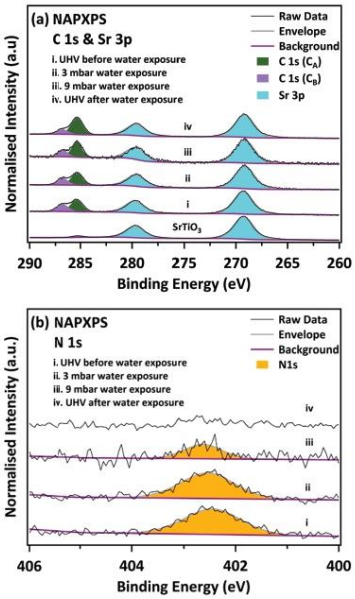

Fig. 2 NAPXPS spectra of (a) C 1s & Sr 3p, and (b) N 1s core levels before/during/after water exposure. All spectra are normalised to the corresponding integrated area of the Sr $3d_{5/2}$ peak.

Stronger evidence for the cleavage of the C–N bond is seen in the corresponding N 1s spectra in Fig. 2. Before exposure to water vapour, the N 1s spectrum of the pristine sample lies at a binding energy of 402.45 eV, in good agreement with the methylammonium group in MAPI.[16,21] During and after exposure to water the N 1s peak is seen to dramatically decrease in intensity during water exposure, and after water exposure the N 1s signal cannot be reliably distinguished from the spectral noise. This confirms that at least some of the intensity in the C 1s peak at 286.75 eV arises from other carbon species (such as C=O/C–OH), since there is some remnant intensity, even after all of the N 1s signal is removed. During and after exposure to 9 mbar water vapour there is an increase in the relative intensity of the lower binding energy feature which may be due to conversion of C–N to C–H/C–C, consistent with the mechanism proposed in eqn (1).

The stoichiometry of the film before and after water exposure is calculated from the integrated peak areas, using CASAXPS sensitivity factors (Table 1).[39] These calculations are only performed for the sample under UHV conditions, since RSFs are not available for the analyser under near-ambient conditions. As noted above, the Pb : I : N: ratio of the as-deposited film is close to the expected stoichiometry. Following H_2O vapour exposure the Pb/I ratio decreases and N is completely lost from the surface. Although obtaining information on the stoichiometry of the C part of the material is difficult because of the hydrocarbon contamination, there are some observations which support the decomposition of MAPI to form NH_3. The decrease in intensity of the higher binding energy component of the C 1s spectrum is consistent with the overall loss of N (see ESI,† Table S2). In addition, we find that the total amount C at the surface remains constant, suggesting that C–N is converted to $-CH_2-$ in accordance with eqn (1).

The evidence from NAPXPS strongly supports a decomposition mechanism similar to that suggested by Li *et al.* (eqn (1)),[17] where nitrogen is lost from the perovskite *via* reaction with water to give NH_3(g). The results are consistent with conversion of lead in the MAPI film to PbI_2 (I/Pb is significantly reduced, Table 1), some of which is then further decomposed as shown in eqn (3).

$$PbI_2(s) \xrightarrow{H_2O,h\nu} Pb(s) + I_2(g) \quad (3)$$

The observed changes in the C 1s spectra induced by water exposure are in agreement with the work of Li *et al.* suggesting that the formation of MAI (*via* eqn (2)) is not involved in the decomposition mechanism in the presence of water vapour.[17] This is further confirmed by the complete loss of the N 1s feature, and a commensurate decrease in the intensity of the feature assigned to C–N in the C 1s spectrum. If MAI were formed we would expect simply to observe a shift to lower BE relative to the MAPI N 1s signal.[21] The release of nitrogen must therefore occur directly from the MAPI film as stated in eqn (1), probably in the form of ammonia gas. We cannot rule out the formation of some CH_3PbI_3 by loss of ammonia during the

degradation process, as its C 1s binding energy cannot be distinguished from that of MAPI.[21] Indeed, this is suggested by the final Pb/I ratio of 2.4 ± 0.1, higher than the 2.0 expected if only PbI_2 is produced.

In conclusion, XPS analysis suggests a stoichiometric MAPI thin film was successfully fabricated *via* vapour deposition, in good agreement with previous studies.[40,41] The data clearly demonstrate the pathway of water-induced degradation of the MAPI film at relative humidity similar to those found in ambient air, using NAPXPS. It is shown that MAI is not formed during decomposition of MAPI during water exposure. The data suggest that at 9 mbar water vapour exposure, MAPI is almost completely transformed into a mixture of Pb, PbI_2 and hydrocarbon species, with a complete loss of nitrogen from the surface. The work further demonstrates the potential for NAPXPS in understanding the surface degradation of materials under atmospheric conditions. In this case it allows us to distinguish unambiguously between the proposed mechanistic pathways,[16,17] potentially allowing methodologies for mitigating the degradation to be developed.

The authors thank the University of Manchester and EPSRC (UK) (grant number EP/K009710) for funding. C. R. Ke thanks the University of Manchester for the award of a President's Doctoral Scholarship.

Notes and references

1 F. Hao, C. C. Stoumpos, D. H. Cao, R. P. Chang and M. G. Kanatzidis, *Nat. Photonics*, 2014, **8**, 489–494.
2 N. J. Jeon, J. H. Noh, W. S. Yang, Y. C. Kim, S. Ryu, J. Seo and S. I. Seok, *Nature*, 2015, **517**, 476–480.
3 M. M. Lee, J. Teuscher, T. Miyasaka, T. N. Murakami and H. J. Snaith, *Science*, 2012, **338**, 643–647.
4 P. Qin, H. Kast, M. K. Nazeeruddin, S. M. Zakeeruddin, A. Mishra, P. Bäuerle and M. Grätzel, *Energy Environ. Sci.*, 2014, **7**, 2981–2985.
5 A. Miyata, A. Mitioglu, P. Plochocka, O. Portugall, J. T.-W. Wang, S. D. Stranks, H. J. Snaith and R. J. Nicholas, *Nat. Phys.*, 2015, **11**, 582–587.
6 S. D. Stranks, G. E. Eperon, G. Grancini, C. Menelaou, M. J. Alcocer, T. Leijtens, L. M. Herz, A. Petrozza and H. J. Snaith, *Science*, 2013, **342**, 341–344.
7 A. A. Zhumekenov, M. I. Saidaminov, M. A. Haque, E. Alarousu, S. P. Sarmah, B. Murali, I. Dursun, X.-H. Miao, A. L. Abdelhady and T. Wu, *ACS Energy Lett.*, 2016, **1**, 32–37.
8 M. A. Green, K. Emery, Y. Hishikawa, W. Warta and E. D. Dunlop, *Prog. Photovoltaics: Res. Appl.*, 2016, **24**, 905–913.
9 A. Kojima, K. Teshima, Y. Shirai and T. Miyasaka, *J. Am. Chem. Soc.*, 2009, **131**, 6050–6051.
10 T. A. Berhe, W.-N. Su, C.-H. Chen, C.-J. Pan, J.-H. Cheng, H.-M. Chen, M.-C. Tsai, L.-Y. Chen, A. A. Dubale and B.-J. Hwang, *Energy Environ. Sci.*, 2016, **9**, 323–356.
11 G. Niu, W. Li, F. Meng, L. Wang, H. Dong and Y. Qiu, *J. Mater. Chem. A*, 2014, **2**, 705–710.
12 F. Matsumoto, S. M. Vorpahl, J. Q. Banks, E. Sengupta and D. S. Ginger, *J. Phys. Chem. C*, 2015, **119**, 20810–20816.
13 J. Yang, B. D. Siempelkamp, D. Liu and T. L. Kelly, *ACS Nano*, 2015, **9**, 1955–1963.
14 Y. Han, S. Meyer, Y. Dkhissi, K. Weber, J. M. Pringle, U. Bach, L. Spiccia and Y.-B. Cheng, *J. Mater. Chem. A*, 2015, **3**, 8139–8147.
15 M. Ledinsky, P. Löper, B. Niesen, J. Holovsky, S.-J. Moon, J.-H. Yum, S. De Wolf, A. Fejfar and C. Ballif, *J. Phys. Chem. Lett.*, 2015, **6**, 401–406.
16 B. Philippe, B.-W. Park, R. Lindblad, J. Oscarsson, S. Ahmadi, E. M. Johansson and H. K. Rensmo, *Chem. Mater.*, 2015, **27**, 1720–1731.
17 Y. Li, X. Xu, C. Wang, C. Wang, F. Xie, J. Yang and Y. Gao, *J. Phys. Chem. C*, 2015, **119**, 23996–24002.
18 W. Huang, J. S. Manser, P. V. Kamat and S. Ptasinska, *Chem. Mater.*, 2015, **28**, 303–311.
19 Y. Li, X. Xu, C. Wang, C. Wang, F. Xie, J. Yang and Y. Gao, *AIP Adv.*, 2015, **5**, 097111.
20 X. Zhou, X. Li, Y. Liu, F. Huang and D. Zhong, *Appl. Phys. Lett.*, 2016, **108**, 121601.
21 L. Liu, J. A. McLeod, R. Wang, P. Shen and S. Duhm, *Appl. Phys. Lett.*, 2015, **107**, 061904.
22 T.-W. Ng, C.-Y. Chan, M.-F. Lo, Z. Q. Guan and C.-S. Lee, *J. Mater. Chem. A*, 2015, **3**, 9081–9085.
23 G. R. Kumar, A. D. Savariraj, S. Karthick, S. Selvam, B. Balamuralitharan, H.-J. Kim, K. Viswanathan, M. Vijaykumar and K. Prabakar, *Phys. Chem. Chem. Phys.*, 2016, **18**, 7284–7292.
24 J. Emara, T. Schnier, N. Pourdavoud, T. Riedl, K. Meerholz and S. Olthof, *Adv. Mater.*, 2016, **28**, 553–559.
25 M.-C. Jung, Y. M. Lee, H.-K. Lee, J. Park, S. R. Raga, L. K. Ono, S. Wang, M. R. Leyden, B. D. Yu and S. Hong, *Appl. Phys. Lett.*, 2016, **108**, 073901.
26 H. Yu, F. Wang, F. Xie, W. Li, J. Chen and N. Zhao, *Adv. Funct. Mater.*, 2014, **24**, 7102–7108.
27 H. Xie, X. Liu, L. Lyu, D. Niu, Q. Wang, J. Huang and Y. Gao, *J. Phys. Chem. C*, 2015, **120**, 215–220.
28 T. Ding, R. Li, W. Kong, B. Zhang and H. Wu, *Appl. Surf. Sci.*, 2015, **357**, 1743–1746.
29 E. M. Miller, Y. Zhao, C. C. Mercado, S. K. Saha, J. M. Luther, K. Zhu, V. Stevanović, C. L. Perkins and J. van de Lagemaat, *Phys. Chem. Chem. Phys.*, 2014, **16**, 22122–22130.
30 R. Lindblad, D. Bi, B.-W. Park, J. Oscarsson, M. Gorgoi, H. Siegbahn, M. Odelius, E. M. Johansson and H. K. Rensmo, *J. Phys. Chem. Lett.*, 2014, **5**, 648–653.
31 A. Dualeh, P. Gao, S. I. Seok, M. K. Nazeeruddin and M. Grätzel, *Chem. Mater.*, 2014, **26**, 6160–6164.
32 M. Liu, M. B. Johnston and H. J. Snaith, *Nature*, 2013, **501**, 395–398.
33 R. Lindblad, N. K. Jena, B. Philippe, J. Oscarsson, D. Bi, A. Lindblad, S. Mandal, B. Pal, D. D. Sarma and O. Karis, *J. Phys. Chem. C*, 2015, **119**, 1818–1825.
34 B. Conings, L. Baeten, C. De Dobbelaere, J. D'Haen, J. Manca and H. G. Boyen, *Adv. Mater.*, 2014, **26**, 2041–2046.
35 W. Zhang, S. Pathak, N. Sakai, T. Stergiopoulos, P. K. Nayak, N. K. Noel, A. A. Haghighirad, V. M. Burlakov, A. Sadhanala and W. Li, *Nat. Commun.*, 2015, **6**, 10030.
36 D. Bi, C. Yi, J. Luo, J.-D. Décoppet, F. Zhang, S. M. Zakeeruddin, X. Li, A. Hagfeldt and M. Grätzel, *Nat. Energy*, 2016, **1**, 16142.
37 R. Dawood, A. Forty and M. Tubbs, *Proc. R. Soc. A*, 1965, **284**, 272–288.
38 H. Seyama and M. Soma, *J. Chem. Soc., Faraday Trans. 1*, 1984, **80**, 237–248.
39 N. Fairley, *CasaXPS manual 2.3. 15*, Acolyte Science, 2009.
40 O. Malinkiewicz, A. Yella, Y. H. Lee, G. M. Espallargas, M. Graetzel, M. K. Nazeeruddin and H. J. Bolink, *Nat. Photonics*, 2014, **8**, 128–132.
41 O. Malinkiewicz, C. Roldán-Carmona, A. Soriano, E. Bandiello, L. Camacho, M. K. Nazeeruddin and H. J. Bolink, *Adv. Energy Mater.*, 2014, **4**, 1400345.

4.2.2 Supporting Information

Electronic Supplementary Material (ESI) for ChemComm.

In Situ Investigation of Degradation at Organometal Halide Perovskite Surfaces by X-ray Photoelectron Spectroscopy in Realistic Water Atmospheres

Chun-Ren Ke, Alex S. Walton, David J. Lewis, Aleksander Tedstone, Paul O'Brien, Andrew G. Thomas,* and Wendy R. Flavell*

Electronic Supplementary Information†

Experimental details

Preparation of methylammonium iodide (MAI)

MAI was prepared as follows: 38 mL methylamine (CH_3NH_2, MA) solution (Aldrich, 33 wt% in absolute ethanol) was added dropwise to 40 mL hydroiodic (HI) acid solution (Sigma-Aldrich, 57 wt% in H_2O). The solution was stirred for 1 hour whilst maintaining the reaction temperature at ~0 - 10 °C by use of an ice bath. The solution was subsequently allowed to warm to room temperature. Solvent was removed by a rotary evaporator in a water bath at 60 to 90 °C. Approximately 45 g of white, crystalline methylammonium iodide (CH_3NH_3I, MAI) powder was obtained after drying in a vacuum oven overnight.

Perovskite thin film preparation

Perovskite thin films were deposited *via* an *in situ* thermal evaporator integrated into the NAPXPS system. $PbCl_2$ (Aldrich, 98%) and the synthesised MAI were placed in a simple dual source Knudsen cell, each with a thermocouple attached in order to measure the evaporation temperatures. $PbCl_2$ and MAI were evaporated at temperatures of 400 °C and 160 °C, respectively onto a $SrTiO_3$ (100) single crystal substrate (MTI Corp.) held at a distance of around 2 cm from the Knudsen cell. Prior to the deposition, the $SrTiO_3$ substrate was heated to approximately 600 °C to remove the surface contaminants and to increase the conductivity.[1]

$PbCl_2$ and MAI were simultaneously evaporated onto the substrate for the first 10 minutes. After 10 minutes, the current to the $PbCl_2$ was shut off, whilst continuing to heat the MAI for a further 20 minutes until chlorine was no longer observed in the XPS spectrum as shown in Fig. S1 below. Prior to XPS measurements, the deposited film was post-annealed at 50 °C for 10 minutes in *vacuo* to ensure formation of the perovskite structure; however we note that several reports have indicated that post-annealing is not necessary for samples fabricated *via* vapour deposition.[2-4] Use of higher annealing temperatures led to thermal decomposition/desorption of the film under UHV conditions. This procedure led to growth of a film of composition consistent with the expected stoichiometry of the methylammonium lead iodide (MAPI) film (see main text). These film growth conditions were optimised to produce a few-nm-thick film, sufficiently thin to be entirely probed by the XPS experiment, as described further below. This was necessary to add confidence to the quantification of sample stoichiometry from XPS. The stoichiometry of the film, together with the absence of signals from $PbCl_2$ in XPS (see below) were taken to indicate complete reaction of the $PbCl_2$ with the MAI to form a methylammonium lead iodide film. This material was then transferred in UHV into the near ambient pressure (NAP) cell.

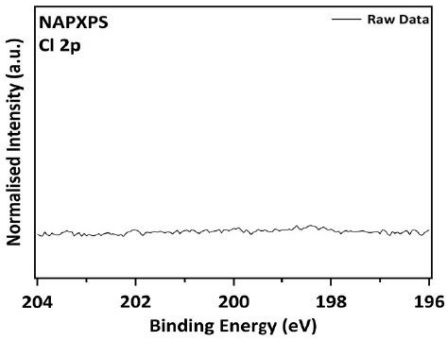

Fig. S1 XPS spectrum of the Cl 2p core level region of the MAPI perovskite film (UHV before water exposure). The intensity is normalised to the Sr $3d_{5/2}$ signal of the substrate (*i.e.* the data are normalised in the same way as in Fig. 1 of the main text). It is clear that no detectable chlorine remains on the surface of the film following reaction of $PbCl_2$ with MAI to form the MAPI film.

X-ray Diffraction

X-ray diffraction (XRD) was carried out on a separate thin film grown in UHV by the same method as that studied by Near-Ambient Pressure X-Ray Photoelectron Spectroscopy (NAPXPS) in order to confirm that the vacuum-deposited films did indeed have the perovskite structure. It was necessary to carry out this measurement on a separate film, as the aim of our experiment was to study the degradation of a pristine film (which had not been exposed to air) by NAPXPS; the film at the end of the experiment is no longer MAPI.

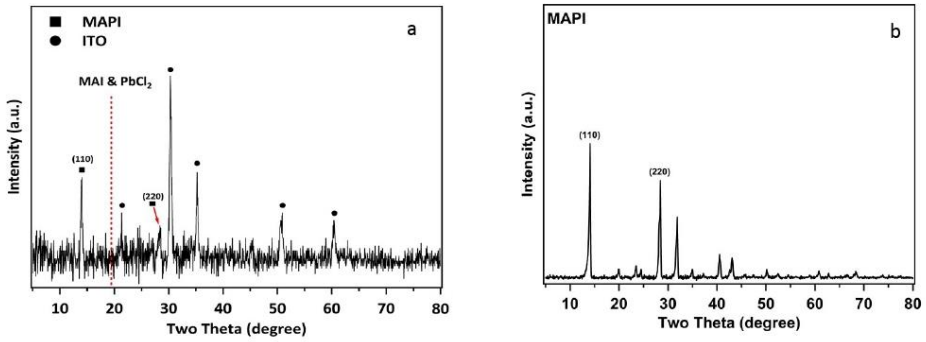

Fig. S2 **a)** X-Ray diffraction pattern of the vacuum-deposited perovskite thin film on an ITO-coated glass slide. Squares mark diffraction peaks associated with the MAPI film and the circles the reflections due to the underlying ITO. b) XRD from bulk MAPI perovskite film grown by aerosol-assisted chemical vapour deposition. The dashed line in a) indicates the position of the primary diffraction peaks of MAI and $PbCl_2$ at 19.5° and 19.6° respectively, demonstrating no precursor-phase remnants in the MAPI film.[5, 6]

XRD was carried out using a Bruker D8 Advance instrument, with the capability for grazing incidence measurements, necessary for the acquisition of diffraction information from the few-nm-thick film. An X-ray grazing incidence angle of 3º was used to detect the signals from the thin films over a range (2θ) of 5º to 80º with a step size of 0.05º and dwell time of 4.5 seconds per point. The diffractogram of the as-deposited film is shown in Fig. S2a), and clearly shows diffraction peaks due to MAPI. The preferred orientation of the (110) planes is in agreement with XRD from a bulk MAPI film grown *ex situ* by a vapour-deposition route (aerosol-assisted chemical vapour deposition) (Figure S2b) and with previous work using solution based deposition techniques[7]. The thin film was grown on tin-doped indium oxide (ITO) glass using a total deposition time of three times that used for the NAPXPS film described below, giving an estimated film thickness of *ca.* 6 nm. From the X-ray absorption coefficient of MAPI (25.884 mm^{-1} [8]), and the incidence angle of 3 degrees, we calculate the X-ray penetration depth to be ~2 μm. Thus as expected the XRD pattern is dominated by reflections from the ITO substrate. We also note that no intensity is observed at a 2θ value corresponding to the primary reflections of the $PbCl_2$ and MAI precursors (shown by the red dashed line in figure S2a).

NAPXPS measurements

The NAPXPS apparatus used in this work is equipped with a SPECS Focus 500 monochromated Al Kα source with photon energy of 1486.6 eV. The analyser for NAP is a SPEC 150 mm Phoibos 150 NAP fitted with a three-stage, differentially pumped electrostatic lens. XPS measurements can be carried out under the conventional conditions in the UHV chamber as well in a near ambient pressure cell which couples to the entrance cone of the analyser lens system. For the NAP measurements, the cell was backfilled with H_2O vapour to reach pressures of 3 mbar and 9 mbar, which roughly corresponds to relative humidity (RH) of 10% and 30%, respectively, under a standard atmospheric temperature of 25 ºC. The water was purified by repeated freeze-thaw cycles.

The binding energy (BE) was calibrated to well-defined Sr $3d_{5/2}$ peak at 133.70 eV, which arises from the $SrTiO_3$ substrate.[9-11] This gives a Ti $2p_{3/2}$ binding energy of 459.20 eV, in good agreement with the value for Ti^{4+} measured by the same equipment previously.[12] BE values are quoted to an accuracy of ±0.05 eV, and thus a binding energy shift of 0.2 eV can be clearly observed. A Shirley background was subtracted from the data presented in the manuscript and supporting information.[13] GL(30) function (70% Gaussian and 30% Lorentzian) curves were used to fit the core level spectra using CasaXPS software.[14] The built in CASAXPS sensitivity factors are used for calculating the stoichiometry of the sample before and after water exposure from UHV measurements only, since transmission-function-adapted data do not currently exist for near-ambient pressure conditions. These sensitivity factors include a correction for the escape depth of the photoelectrons.

In order to add confidence to the quantification of the XPS data, a very thin (few-nm-thick) film was grown for the experiment, where the core level signals due to the underlying substrate remained visible in XPS after film deposition. These were used in the quantification as described below. A calculation of the film thickness using a two-layer model based on a MAPI film grown on the $SrTiO_3$ substrate can be made using equation S1:

$$\frac{I_{Pb}}{I_{Sr}} = \frac{N_{Pb}\sigma_{Pb}\lambda_{Pb}}{N_{Sr}\sigma_{Sr}\lambda_{Sr}}\left(\frac{1 - exp\{-d/\lambda_{Pb}\}}{exp\{-d/\lambda_{Sr}\}}\right). \quad \text{equation S1}$$

Using the intensities (I_{Pb} and I_{Sr}) from the Pb 4f and Sr 3d peaks, with photoionisation cross sections σ_{Pb} *and* σ_{Sr}, number densities N_{Pb} *and* N_{Sr} and calculated inelastic mean free path lengths (from the NIST electron mean free path database[15]) $\lambda_{Pb} = \lambda_{Sr}$, we obtain a value for the MAPI film of 1.9 ± 1 nm. This calculation assumes that the film is of a uniform thickness with no gaps, but measurements at different points on the film revealed a uniform stoichiometry, suggesting that this is the case (see Figure S3).

With regards to the stoichiometry calculation, the use of Sr 3d and 3p peaks allows a self-check of the stoichiometry calculations, since the Pb 4f peaks appear close in binding energy to Sr 3d and the C 1s signal is close to Sr 3p, so any residual effects associated with different probe depths can be confidently accounted for. In addition, the observation of the Sr peaks through the thin film confirms we probe the whole film, thus it is unlikely that (for example) unreacted $PbCl_2$ is present beneath the MAI film, as no Cl 2p signal is present (figure S1). XPS was performed on standard samples of the $PbCl_2$ precursor. We were able to clearly resolve a binding energy shift of 0.3 eV between the Pb 4f features of MAPI and $PbCl_2$ (figure S4), adding confidence to our conclusion that a complete reaction of $PbCl_2$ with MAI to form a methylammonium lead iodide film was achieved. The stoichiometry of the resulting film was in good agreement with the nominal stoichiometry of MAPI (see main manuscript text).

Table S1 Elemental (Sr, Pb, I, N, C, and Cl) quantification of the film determined from UHV XPS at different stages, before and after water exposure. All values are normalised to the area of the Sr 3d peak in the substrate. Only the Pb^{2+} components in the film are shown in the Pb column (the Pb(0) component (main text Fig. 1, and SI Fig. S3) is excluded). We note that metallic lead is always present in the MAPI film, which is also a common phenomenon for solution-grown films processed through sequential steps as reported in the literature.[16, 17] The excess C is assumed to arise from hydrocarbon contamination, most likely outgassing from the hot Knudsen cells, but possibly also due to a small amount of dissociation of MAI in the Knudsen cell.

Sample status	Sr	Pb(II)	I	N	C	Cl
UHV before water exposure	1.00 ± 0.05	0.30 ± 0.05	0.80 ± 0.05	0.27 ± 0.1	2.40 ± 0.1	0.00 ± 0.05
UHV after water exposure	1.00 ± 0.05	0.08 ± 0.05	0.20 ± 0.05	0.00 ± 0.1	2.50 ± 0.1	0.00 ± 0.05

Table S2 Detailed quantification of the C 1s and N 1s spectra where C_A is attributed to C-H, C-I or C-C and C_B is ascribed to C-N and 'C-O' (species such as C=O/C-OH). Areas here are normalised to Sr $3d_{5/2}$ peak areas. It is clear the total C content of the film is unchanged by water exposure and that the peak corresponding to C-N and C-O species decreases in intensity by an amount consistent with the loss of N from the film. At the same time, there is a matching increase in the intensity of the C_A feature, suggesting an increase in hydrocarbon content, consistent with equation 1 of the main manuscript. The high vapour pressure of CH_3NH_3I means that a decomposition mechanism such as that shown in equation 2 of the main manuscript would result in

evaporation of this molecule under vacuum conditions. This would lead to a reduction in intensity of *both* C_A and the C-N related peak (C_B). The increase in the intensity of the C-C related peak observed here is inconsistent with this.

Sample Status	Total C	C_A (CC,CI,CH)	C_B (CN,CO)	N
UHV before water exposure	2.4 ± 0.1	1.5 ± 0.05	0.9 ± 0.1	0.27 ± 0.1
UHV after water exposure	2.5 ± 0.1	1.9 ± 0.05	0.6 ± 0.1	0.0 ± 0.1

Table S3 Quantification of Pb peak area normalised to Sr $3d_{5/2}$ peak area

Sample Status	Total Pb	Pb(II)	Pb(0)
UHV before water exposure	0.35 ± 0.05	0.30 ± 0.05	0.05 ± 0.02
UHV after water exposure	0.18 ± 0.05	0.08 ± 0.05	0.1 ± 0.05

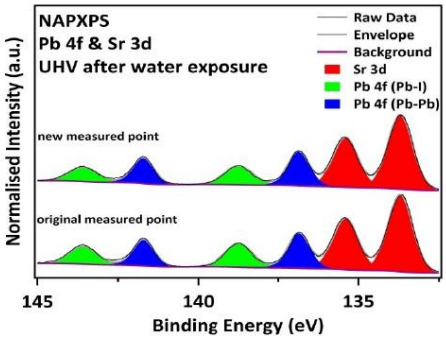

Fig. S3 XPS spectra of Pb 4f & Sr 3d core levels of the film (in UHV after water exposure) taken at two different positions (one exposed to the X-ray beam during data taking for the whole experiment, and a fresh sample position). Both points show a similar Pb(0)/Pb(II) ratio of approximately 1.2. This suggests that changes observed in the spectra are predominantly associated with water exposure rather than beam damage.

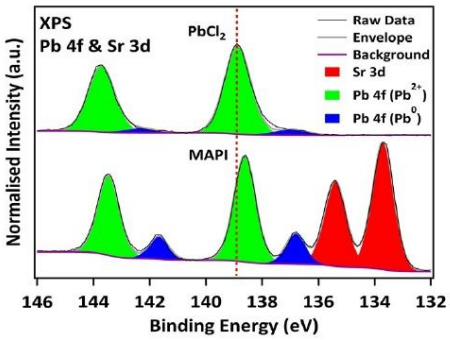

Fig. S4 a) Comparison of the Pb 4f-core-level XPS spectra of $PbCl_2$ and MAPI film showing a shift in Pb $4f_{7/2}$ BE of 0.3 eV between Pb-Cl (138.90 eV[18]) and Pb-I in MAPI (138.60 eV). The $PbCl_2$ film also contains a trace amount of metallic lead, indicating partial decomposition of vapourised $PbCl_2$.

References

1. K. Szot, W. Speier, G. Bihlmayer and R. Waser, *Nature materials*, 2006, **5**, 312-320.
2. O. Malinkiewicz, A. Yella, Y. H. Lee, G. M. Espallargas, M. Graetzel, M. K. Nazeeruddin and H. J. Bolink, *Nature Photonics*, 2014, **8**, 128-132.
3. D. Zhao, W. Ke, C. R. Grice, A. J. Cimaroli, X. Tan, M. Yang, R. W. Collins, H. Zhang, K. Zhu and Y. Yan, *Nano Energy*, 2016, **19**, 88-97.
4. J. B. Patel, J. Wong-Leung, S. Van Reenen, N. Sakai, J. T. W. Wang, E. S. Parrott, M. Liu, H. J. Snaith, L. M. Herz and M. B. Johnston, *Advanced Electronic Materials*, 2016.
5. C. Gao, J. Liu, C. Liao, Q. Ye, Y. Zhang, X. He, X. Guo, J. Mei and W. Lau, *RSC Advances*, 2015, **5**, 26175-26180.
6. N. J. Jeon, J. H. Noh, Y. C. Kim, W. S. Yang, S. Ryu and S. I. Seok, *Nature materials*, 2014, **13**, 897-903.
7. L. J. Phillips, A. M. Rashed, R. E. Treharne, J. Kay, P. Yates, I. Z. Mitrovic, A. Weerakkody, S. Hall and K. Durose, *Solar Energy Materials and Solar Cells*, 2016, **147**, 327-333.
8. C. C. Stoumpos, C. D. Malliakas and M. G. Kanatzidis, *Inorganic chemistry*, 2013, **52**, 9019-9038.
9. Y.-F. Zhu, L. Xu, J. Hu, J. Zhang, R.-G. Du and C.-J. Lin, *Electrochimica Acta*, 2014, **121**, 361-368.
10. D. M. Hill, H. Meyer III and J. Weaver, *Journal of Applied Physics*, 1989, **65**, 4943-4950.
11. W.-D. Yang, *Journal of materials science*, 1999, **34**, 3533-3544.
12. M. J. Jackman, A. G. Thomas and C. Muryn, *The Journal of Physical Chemistry C*, 2015, **119**, 13682-13690.
13. D. A. Shirley, *Physical Review B*, 1972, **5**, 4709.
14. N. Fairley, *CasaXPS manual 2.3. 15*, Acolyte Science, 2009.
15. C. Powell and A. Jablonski, *Electron Effective-Attenuation-Length, Version*, 2011, **1**.
16. W. Zhang, S. Pathak, N. Sakai, T. Stergiopoulos, P. K. Nayak, N. K. Noel, A. A. Haghighirad, V. M. Burlakov, A. Sadhanala and W. Li, *Nature communications*, 2015, **6**.
17. D. Bi, C. Yi, J. Luo, J.-D. Décoppet, F. Zhang, S. M. Zakeeruddin, X. Li, A. Hagfeldt and M. Grätzel, *Nature Energy*, 2016, **1**, 16142.

18. J.-K. Jung and W.-J. Lee, *Japanese Journal of Applied Physics*, 2001, **40**, 1408.

Chapter 5 Methylammonium Lead Iodide Films Fabricated *via* AACVD from a $Pb(SCN)_2$ Precursor

This work has been first published in ACS Applied Energy Materials on 31/07/2019

Cite this: *ACS Appl. Energy Mater.*, 2019, **2**, 6012

5.1 Introduction

This chapter contains a paper that has been published in *ACS Applied Energy Materials*.[224] As presented in Chapter 4, the thermally evaporated MAPI surface completely decomposed at RH of only 30%. Approaches to improvement in the stability of halide perovskites against moisture are the urge to be developed. In this paper (Paper 2), we used AACVD to deposit MAPI films using a pseudohalide $Pb(SCN)_2$ precursor to react with MAI. The use of $Pb(SCN)_2$ as the precursor is expected to have a positive effect on the fabrication process of MAPI in ambient air.[78] We compared AACVD-grown MAPI films with their counterparts that had been fabricated by common spin coating. The spin coating process in ambient air without antisolvent (ethyl acetate) treatment cannot form opaque MAPI films. It was found that the AACVD-grown films were more stable than the spin-coated ones (with antisolvent treatment) through ageing in air, which were examined by numerous bulk and surface characterisation techniques, such as XRD and XPS, respectively. The improved stability in ambient air can be attributed to larger grain sizes observed in SEM. In addition, the use of excess MAI (10% in molar concentration) in the precursor solution resulted in less PbI_2 impurities and other defects in the bulk and surface of the MAPI films. XPS results reveal an additional CH_3NH_2

compound at the MAPI surface as a result of using excess MAI, which may passivate the surfaces/grain boundaries. NAP-XPS outcomes show the AACVD-grown samples from $Pb(SCN)_2$ have much better stability than the thermally evaporated MAPI film from $PbCl_2$ (Chapter 4) on exposure to 9 mbar water exposure. This research paves the way towards stable halide perovskites for use in PSCs and the full details can be found in Section 5.2.

Contribution

Qian Chen inspired the author to use $Pb(SCN)_2$ as the lead precursor to fabricate MAPI films *via* ambient air processing. The author planned and performed most of the experiments of this project including sample preparation and characterisation and analysed all data obtained under the supervision of Prof Wendy Flavell and Dr Andrew Thomas. Dr David Lewis and Prof Paul O'Brien (deceased) provided AACVD apparatuses and related facilities for the author to carry out AACVD experiments. Dr David Lewis also gave me some useful ideas and advice in the initial stage of this research. Dr Alex Walton significantly supported the NAP-XPS experiments including trails for thermally evaporated $Pb(SCN)_2$ (failed due to precursor decomposition) and Qian Chen helped to develop and optimise the antisolvent spin-coating technique for use in this work. Dr Ben Spencer and Claudia Compean-Gonzalez helped to acquire some conventional XPS spectra for the author to use and analyse. Dr Muhamad Mokhtar assisted in PL measurements during the paper revision of the journal in order to address the comments of one reviewer. The author wrote this paper with Prof Wendy Flavell and Dr Andrew Thomas, with suggestions from the co-authors.

5.2 Paper 2

5.2.1 Main Text

ACS APPLIED ENERGY MATERIALS
Cite This: ACS Appl. Energy Mater. 2019, 2, 6012−6022
Article
www.acsaem.org

Air-Stable Methylammonium Lead Iodide Perovskite Thin Films Fabricated via Aerosol-Assisted Chemical Vapor Deposition from a Pseudohalide $Pb(SCN)_2$ Precursor

Chun-Ren Ke,[†,‡] David J. Lewis,[§] Alex S. Walton,[‡,∥] Qian Chen,[§] Ben F. Spencer,[§] Muhamad Z. Mokhtar,[§] Claudia L. Compean-Gonzalez,[‡,§] Paul O'Brien,[⊥,§,∥] Andrew G. Thomas,*[,‡,§] and Wendy R. Flavell*[,†,‡]

[†]School of Physics and Astronomy, The University of Manchester, Oxford Road, Manchester M13 9PL, United Kingdom
[‡]Photon Science Institute, The University of Manchester, Oxford Road, Manchester M13 9PL, United Kingdom
[§]School of Materials, The University of Manchester, Oxford Road, Manchester M13 9PL, United Kingdom
[∥]School of Chemistry, The University of Manchester, Oxford Road, Manchester M13 9PL, United Kingdom

Supporting Information

ABSTRACT: Ambient-air-stable methylammonium lead iodide (MAPI) perovskite thin films have been fabricated via one-step aerosol-assisted chemical vapor deposition (AACVD) from a pseudohalide $Pb(SCN)_2$ precursor. We compare both the bulk and surface properties of the perovskite films grown using AACVD with those made by the widely used spin-coating method. Films with larger grain sizes and much better stability in ambient air can be obtained by AACVD. By addition of excess MAI to the precursor solution, MAPI films with negligible PbI_2 impurities, as determined by X-ray diffraction, are obtained. The AACVD-grown MAPI films retain high phase purity with limited PbI_2 formation after aging in air for approximately one month. The films exhibit an optical bandgap energy of ca. 1.55 eV and the expected nominal bulk stoichiometry (within error). In addition to probing bulk properties, we utilize X-ray photoelectron spectroscopy (XPS) to scrutinize the surface characteristics in detail. We find that the use of excess MAI results in formation of neutral CH_3NH_2 molecules at the surface. With aging time in air, the concentrations of iodine and nitrogen drop with respect to that of lead, but these changes are less severe in the AACVD-grown films compared to the counterparts made by spin-coating. Near-ambient pressure XPS is utilized to examine the surface stability of AACVD-grown films on exposure to 9 mbar H_2O vapor. The formation of CH_3NH_2 molecules at the surface is observed, and the MAPI phase remains largely intact. The CH_3NH_2 molecules may passivate the surfaces and protect MAPI from degradation, providing a rationale for the observed stability of MAPI films fabricated from $Pb(SCN)_2$ with excess MAI.

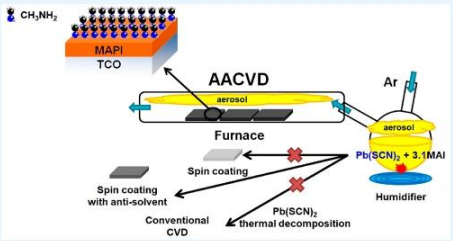

KEYWORDS: *perovskite solar cell, methylammonium lead iodide, AACVD, vapor deposition, lead thiocyanate, XPS, NAP-XPS, antisolvent*

1. INTRODUCTION

The power conversion efficiencies (PCEs) of organometal halide perovskite solar cells (PSCs) have already surpassed 20%,[1] from an initial efficiency of approximately 4% in 2009.[2] Such an increase in PCE is unprecedented in other types of solar cells, giving rise to considerable attention from the scientific community. The power generation capability of PSCs is sufficiently competitive at a relatively low cost to potentially compete with mainstream polycrystalline silicon solar cells. The main reason for the failure to commercialize PSCs is that the lifetime of PSCs currently cannot meet the general market requirement (degradation in PCE of less than 10% in at least 20 years).[3] Perovskite light-absorber materials are typically vulnerable to moisture and thermal stress, and, in some circumstances, to oxygen and ultraviolet (UV) light.[4,5] For example, methylammonium lead (tri)iodide ($CH_3NH_3PbI_3$, MAPI) coverts into lead iodide with hydrocarbon chains through the loss of ammonia and hydrogen iodide (HI), on exposure to moisture.[5,6] Many approaches have been proposed to improve the resistance to moisture of halide perovskite materials.[7−9] One simple way is to change the lead precursors from a lead iodide (PbI_2) to lead chloride ($PbCl_2$),[10] or to a so-called "pseudohalide", lead acetate ($Pb(Ac)_2$),[11] or lead thiocyanate ($Pb(SCN)_2$).[12,13] $Pb(SCN)_2$, in particular, can

Received: June 6, 2019
Accepted: July 30, 2019
Published: July 30, 2019

DOI: 10.1021/acsaem.9b01124
ACS Appl. Energy Mater. 2019, 2, 6012−6022

produce an ambient-air-stable MAPI perovskite material entirely fabricated in ambient air, via a two-step spin-coating method.[12] However, there has been very limited success in achieving one-pot synthesis from $Pb(SCN)_2$ and ammonium iodides alone (i.e., without other types of lead precursors).[14] To date, films prepared by this route show insufficient light absorption to deliver good PCEs for PSC devices, due to an islandic microstructure (with film coverage of ca. 30%). Most studies report that $Pb(SCN)_2$ is used as an additive in a solution of more than one lead precursor to assist the formation of the organometal halide perovskite.[13,15,16] However, sequential methods are less efficient compared to one-pot manufacture, especially when scalability is required. Therefore, a facile one-pot process for organolead halide perovskites fabricated from $Pb(SCN)_2$ alone is of particular interest.

The deposition process is another concern with regard to scale-up of halide perovskite layers. Typically, for small device fabrication, spin-coating from a small amount of perovskite solution is utilized and is a dominant route for the fabrication of PSCs for academic research. However, spin-coating is difficult to apply to large-scale processing or roll-to-roll manufacture for flexible substrates. In addition, most of the available processes for producing ambient-air-stable perovskite layers require an antisolvent step during spin-coating,[17−20] which is particularly difficult to achieve for large-scale processes. Therefore, developing a scalable way to fabricate ambient-air-stable halide perovskites is of great importance for PSC research. Conventional vapor deposition is a scalable process and can produce high-quality and pinhole-free perovskite films.[21−23] However, the cost is far higher compared to that for solution-based methods due to the requirement for vacuum conditions, which may outweigh the advantages of PSCs. Moreover, $Pb(SCN)_2$ has been found to be an inappropriate source for thermal evaporation owing to the fact that thermal decomposition of $Pb(SCN)_2$ occurs prior to sublimation. Therefore, for this kind of lead precursor, utilizing thermal evaporation is not possible, which constrains the opportunities to apply $Pb(SCN)_2$ to fabricate perovskite films with improved stability.

Aerosol-assisted chemical vapor deposition (AACVD) is a fusion of solution-based and vapor-deposition processes, making it a possible solution for those precursors that easily undergo thermal decomposition.[24−26] The AACVD technique has been successfully applied to grow high-quality perovskite thin films, by either one-step[27−30] or two-step (sequential) processes.[31] The most widely used halide perovskite, MAPI, has been grown by efficient one-step AACVD in only one study (Bhachu et al.[28]). In that study, PbI_2 was used in the synthesis of MAPI, which is expected to make the films less stable in ambient air compared to films fabricated from $Pb(SCN)_2$.[12,28] Additionally, the small grain sizes observed (less than 1 μm) have a detrimental effect on carrier nonradiative recombination.[28,32] The stability in humid air of organometal halide perovskite films fabricated by AACVD has not been well-studied but is of paramount importance. To date, the only detailed study pertains to the inorganic Cs_2SnI_6 double perovskite.[30]

In this article, we utilize a one-step AACVD process to fabricate high-quality MAPI films from a $Pb(SCN)_2$ precursor (with at least 3 mol equiv of MAI) for the first time. A detailed study of the fabrication and characterization of the MAPI material produced is carried out. Upon application of this simple, scalable process, films with high uniformity (relatively high coverage of over 90%) and high phase purity can be obtained. The growth of films from $Pb(SCN)_2$ utilizes a relatively low temperature of 130 °C that is well-adapted to plastic substrates,[33] as compared to vacuum deposition (>300 °C)[21] and AACVD from PbI_2 (~200 °C).[28] We also find that applying excess MAI improves the phase purity of the MAPI films by reducing the production of PbI_2 impurities. Moreover, the AACVD-grown films generate a low level of PbI_2 impurities through degradation when placed in humid ambient air (relative humidity (RH) > 70%) for up to ~1 month, far better than counterparts fabricated by spin-coating. We employ near-ambient pressure X-ray photoelectron spectroscopy (NAP-XPS) to uncover the degradation mechanisms of AACVD-grown films prepared with excess MAI (an excess of 10% by molar concentration) under exposure to 9 mbar H_2O vapor. The results unambiguously show that the surface stability of MAPI films prepared from $Pb(SCN)_2$ with excess MAI is much better than those made from $PbCl_2$ using thermal evaporation under identical exposure conditions.[5] In addition, by combining XPS data from a set of experiments, we show that excess nitrogen moieties, most probably neutral CH_3NH_2 molecules, passivate the surfaces, imparting the enhanced stability of the MAPI films. This may be one of the major reasons films prepared from $Pb(SCN)_2$ using excess MAI have superior stability in humid ambient air. This is consistent with findings that report the use of methylamine gas to heal defects in MAPI films and hence obtain enhanced device performance.[34] In addition, excess MAI has been shown to passivate the grain boundaries and thus suppress nonradiative carrier recombination.[35] We believe these insights will help the future development of air-stable organometal halide perovskites for use in photovoltaic devices.

2. RESULTS AND DISCUSSION

The AACVD deposition was carried out under an Ar flow using a 0.2 M MAPI solution, for 1 h. Subsequently, the films were annealed in air at 110 °C for 30 min in order to remove the residual solvent. More details can be found in the Experimental Section. Following annealing in ambient air at 110 °C (RH > 70%) in the AACVD furnace, macroscopically homogeneous and dark gray AACVD-grown MAPI films were made. Stoichiometric films, and films having molar excesses of 10% or 20% MAI (denoted as "MAI+10%" and "MAI+20%", respectively) were produced. An example of an MAI+10% film is shown in Figure 1A. The photograph shows that the film is

Figure 1. Photographs of an AACVD-grown (MAI+10%) MAPI film on ITO-glass substrate: (A) as-prepared, (B) after aging in ambient air for ~1 week, and (C) after aging in ambient air for ~1 month.

opaque. The appearance of stoichiometric and MAI+20% AACVD-processed films (not shown) is similar. After the film was exposed to ambient air (average RH > 70%) for around a week and a month, the appearance of the film (Figure 1B,C, respectively) is not changed significantly compared to the fresh film (Figure 1A). This suggests that the visible-light absorption

DOI: 10.1021/acsaem.9b01124
ACS Appl. Energy Mater. 2019, 2, 6012−6022

capability of the films is unaffected following aging in a humid environment for this period. The photos of the evolution of spin-coated films in ambient air can be seen in Figure S1A, showing much apparent degradation with aging time compared to the AACVD-grown films.

The physical properties of the films were evaluated by peeling and scratching tests, as shown in Figure S1 in the Supporting Information (SI). The outcome suggests the AACVD-grown films (Figure S1B,C) possess better adhesion to the substrates than the films fabricated by spin-coating (Figure S1D,E). It is worth noting that, without applying the antisolvent step (the use of ethyl acetate[17,20]) to the spin-coated (SC) films, the as-grown films are quite transparent, as shown in Figure S1F. This finding is consistent with a previous report in which MAPI films fabricated from pure $Pb(SCN)_2$ with MAI exhibit semitransparent properties due to limited film coverage and an island structure.[14] In addition, we also tried another commonly used antisolvent, chlorobenzene. However, it produced an even more transparent film compared to the samples made without the antisolvent step, indicating the limited formation of perovskite.

In order to examine the crystalline phases, GIXRD patterns of the films were obtained, and examples are shown in Figure 2. Figure 2A shows XRD reflections of the fresh AACVD-processed films with various amounts of MAI added to the precursor solution. For the stoichiometric film (MAI:$Pb(SCN)_2$ = 3:1), all of the peaks can be indexed to the MAPI perovskite,[36] except for minor peaks at 12.65° and 25.95° which can be assigned to the (001) and (101) reflections of a hexagonal PbI_2 impurity.[37] The appearance of the (211) reflection of MAPI in the pattern suggests the formation of the tetragonal perovskite phase, which is the most common crystal structure of MAPI at room temperature, rather than the cubic phase, which is stable at above 60 °C.[38−40] The intensity of the PbI_2(001) peak is approximately 2% of the primary MAPI(110) diffraction peak at 14.10°. There has been some discussion in the literature regarding the benefits from residual PbI_2, which may passivate the grain boundaries of MAPI perovskites.[41] However, in this article, we offer a facile way to prepare pure MAPI films without PbI_2 impurities, using $Pb(SCN)_2$ precursor. When an MAI excess of 10% is added into the precursor solution (MAI+10%; MAI:$Pb(SCN)_2$ = 3.1:1), the PbI_2 impurity is eliminated in the perovskite film, as shown in Figure 2A. On adding further MAI to the AACVD synthesis (MAI+20%; MAI:$Pb(SCN)_2$ = 3.2:1), a peak at 11.45° emerges (Figure 2A), indicating the formation of a two-dimensional (2D) perovskite (or other complexes) in conditions with an excess of MAI.[42−44] This is a known phenomenon; if the concentration of MA cations is too high, they can intercalate between perovskite layers.[42] In addition, we found that the intensity ratio between the (110) and (220) reflections is higher in the MAI+10% film than in the stoichiometric sample, suggesting a stronger preferred (110) orientation for the MAI+10% film. The use of 10% excess MAI results in the purest MAPI with negligible PbI_2, and the stoichiometric sample degraded much more quickly. We chose this composition to conduct stability studies. We note that the presence of initial PbI_2 impurities in the MAPI films may affect their behavior on aging. In what follows, the films under study are MAI+10% samples unless specified otherwise.

Figure 2B shows the effect of aging for up to a month in ambient air on an AACVD-grown MAPI sample. The AACVD-grown films exhibit a superior stability compared to MAPI

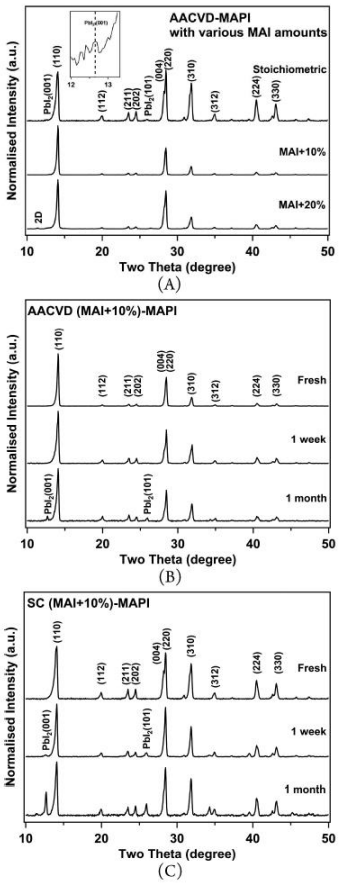

Figure 2. GIXRD patterns of MAPI films showing (A) the effect of different amounts of MAI (stoichiometric, MAI+10%, and MAI +20%) in the precursor solution on AACVD-grown films (the inset shows an enlarged view of the (001) reflection from PbI_2 in the stoichiometric film), (B) the effect of aging in air (RH > 70%) on an AACVD (MAI+10%)-grown film, and (C) the effect of aging in air on a spin-coated (SC) sample.

films synthesized from the identical precursor solution (MAI +10%) by spin-coating (SC, Figure 2C). After aging for a week, no PbI_2 peaks can be observed in the XRD pattern of the AACVD-grown film. Even following aging for a month, the intensity of the PbI_2(001) reflection is only 9% of that of the MAPI(110), much better than the outcome reported for aged MAPI films prepared by thermal evaporation.[45] In contrast to the aged AACVD-grown film, a one-month-aged SC film (Figure 2C) exhibits a substantial amount of PbI_2 (0.44 rising from 0.03 for a week-aged sample), indicating much more severe degradation in air compared to AACVD-grown films. This is consistent with our previous work for Cs_2SnI_6 double

DOI: 10.1021/acsaem.9b01124
ACS Appl. Energy Mater. 2019, 2, 6012−6022

Table 1. Summary of the Results from Characterization of Samples Prepared from MAI+10% Precursor Solution as a Function of Aging[a]

sample ID	$I_{PbI_2(100)}/I_{MAPI(110)}$ (XRD)	$I_{MAPI(110)}/I_{MAPI(220)}$ (XRD)	I/Pb (EDX)	N/Pb (EDX)	E_g
AACVD fresh	0.000 ± 0.002	1.8 ± 0.1	3.0 ± 0.1	1.1 ± 0.1	1.55 ± 0.05
AACVD 1 week	0.000 ± 0.002	1.6 ± 0.1	2.9 ± 0.1	1.0 ± 0.1	1.55 ± 0.05
AACVD 1 month	0.090 ± 0.009	1.7 ± 0.1	2.8 ± 0.1	0.9 ± 0.1	1.55 ± 0.05
SC fresh	0.000 ± 0.002	1.1 ± 0.1	3.0 ± 0.1	1.0 ± 0.1	1.55 ± 0.05
SC 1 week	0.030 ± 0.003	1.1 ± 0.1	2.8 ± 0.1	0.9 ± 0.1	1.55 ± 0.05
SC 1 month	0.440 ± 0.044	1.1 ± 0.1	2.4 ± 0.1	0.5 ± 0.1	>2.00

[a] $I_{PbI2(100)}/I_{MAPI(110)}$ and $I_{MAPI(110)}/I_{MAPI(220)}$ indicate the ratio of the intensities of the PbI_2(001) and MAPI(110) reflections and that of the MAPI(110) and MAPI(220) reflections, respectively, from the XRD patterns. Elemental bulk stoichiometries I/Pb and N/Pb are obtained from EDX. The optical bandgaps (E_g) are acquired from Tauc plots of the absorption spectra shown in Figure 4.

perovskite films, where we find that AACVD-prepared films are more stable than spin-coated samples.[30] It is also consistent with the work in ref 45, where after exposure of the MAPI film to air at 40% relative humidity (RH) for only 24 h, the intensity of the PbI_2(001) was higher than that of the MAPI(110) reflection. In addition, we found in Table 1 that the fresh SC film reveals a MAPI crystalline structure with a reduced preferred (110) orientation compared to AACVD-grown films. Interestingly, during preparation, we found that, on annealing SC samples at the same temperature as used during AACVD deposition (i.e., 130 °C), the films turned yellow instead of dark gray within 10 min, suggesting that AACVD-grown films also have better thermal stability. Therefore, the annealing temperature for SC films was set at around 110 °C, as stated in the Experimental Section. The ratios of the XRD reflections, $I_{PbI_2(100)}/I_{MAPI(110)}$, for MAI+10% samples prepared by AACVD and spin-coating are summarized in Table 1.

In order to understand whether the film quality could affect the stability of the deposited films, the morphologies of various fresh and aged films were examined using SEM, as shown in Figure 3. The as-deposited films prepared by AACVD and spin-coating are shown in Figure 3A,D, respectively. The fresh AACVD-grown film shows a slightly better coverage (ca. 95%), as determined from use of ImageJ software,[46] compared to the as-prepared SC sample (ca. 87%). Both samples consist primarily of micrometer-sized grains and numerous smaller secondary grains between the larger grains. The incomplete coverage may be due to annealing under ambient air.[47] It is worth noting that the step of annealing in ambient air in the AACVD tube is necessary in this case, as we found that annealing in an Ar flow does not completely remove all the residual DMF in a viable time. However, at similar magnification, the coverage of our AACVD-grown and spin-coated (with antisolvent) MAPI films appears to be better than those of films spin-coated from a $PbCl_2$ precursor,[11] or from a $Pb(SCN)_2$ precursor without the antisolvent treatment (ethyl acetate) as well as those prepared without excess MAI.[14]

In general, the appearance of fresh films produced by the two different methods is quite similar. However, the average size of the larger grains in AACVD-grown and SC films is ca. 20 and 15 μm, respectively. This could contribute to the better atmospheric stability of the AACVD-processed films as they have a lower overall surface-to-volume ratio, which is consistent with a previous study for Cs_2SnI_6.[30] The average grain sizes of one-step-prepared MAPI, deposited by either AACVD or spin-coating, are much larger than those made via two-step spin-coating.[12] It is noted that the grain size of the fresh SC film is much larger than films made from a PbI_2 precursor with equimolar MAI using a similar antisolvent process.[17] This suggests that $Pb(SCN)_2$ partially contributes the greater grain sizes observed. A larger grain size is expected to result in a reduction in overall carrier recombination due to a reduced number of grain boundaries which can act as nonradiative recombination centers.[32] The crystal features of the small grains between large grains can be seen in more detail by using higher magnification, as shown in Figure S2C,D. After 1 week, the morphologies of the AACVD-grown and SC films do not show significant changes (Figure 3 B,E), consistent with the XRD results (insignificant PbI_2 impurities). The coverage of both films appears relatively unchanged, with estimated values of approximately 94% and 85% for AACVD-grown and spin-coated films, respectively. However, after one month, the SC sample reveals an obvious alteration in appearance (Figure 3F). Numerous separated islands formed by enlarging the gaps between original large grains have appeared, suggesting that some material has been lost from the grain boundaries. This suggests the occurrence of degradation induced by ambient air, corresponding to the formation of the large amount of PbI_2

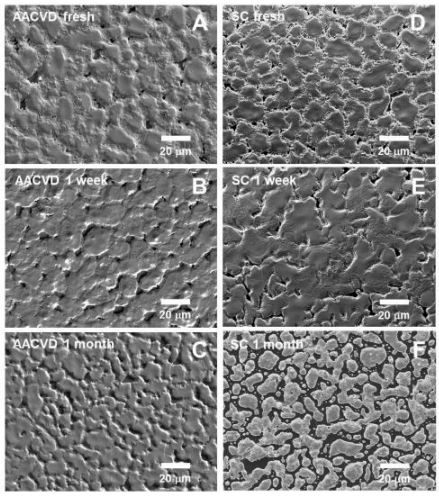

Figure 3. SEM images of MAI+10% films deposited by AACVD (A–C) or spin-coating (D–F) as a function of aging: (A, D) fresh, (B, E) 1 week aging, and (C, F) one month aging in ambient air (average RH > 70%).

DOI: 10.1021/acsaem.9b01124
ACS Appl. Energy Mater. 2019, 2, 6012–6022

found in the corresponding XRD patterns (Figure 2C). According to previous studies, upon exposure to moisture, the nitrogen and iodine constituents are lost from MAPI films in the form of gas, ammonia, and hydrogen iodide (HI), respectively.[5,6] Therefore, the large grains shrink at the grain boundaries by loss of material from the film.[48] It can be seen that the degradation process is much less severe for the sample made by AACVD (Figure 3C, coverage ca. 93%) compared to the SC film (Figure 3F, coverage ca. 55%).

The bulk stoichiometries of the MAI+10% films examined by energy-dispersive X-ray (EDX) spectroscopy are also shown in Table 1. The as-deposited AACVD film has the elemental stoichiometry expected for MAPI with 10% excess MAI within experimental error (i.e., I:Pb:N = 3:1:1.1). The fresh SC film (Table 1) also reveals the expected ideal MAPI stoichiometry within error; however, following aging, the stoichiometries diverge. In general, as expected, iodine and nitrogen are lost with aging time in ambient air, but the loss is much more significant in the SC film, in good agreement with the XRD outcomes (Figure 2). The 1-month-aged AACVD-prepared film has a similar stoichiometry to that of the 1-week-aged SC sample, suggesting less severe degradation in AACVD films. The nitrogen content of the 1-month-aged SC film is approximately half the original value, indicating that around a half of the MAPI is converted to PbI_2.[5]

The optical bandgap energy (E_g) of the films was determined using ultraviolet−visible−near-infrared (UV−vis−NIR) spectroscopy. Tauc plots (Figure 4) were acquired from

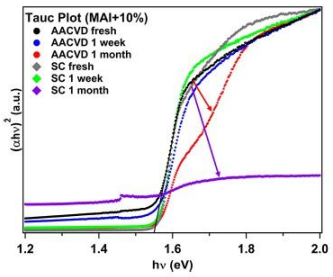

Figure 4. Tauc plots from the UV−vis−NIR spectra of fresh and aged (for 1 week or 1 month) MAI+10% films prepared by AACVD and spin-coating (SC), obtained via the Kubelka−Munk equation by taking MAPI as a direct-bandgap semiconductor. The black straight line is the fitting line of the AACVD fresh curve, showing the onset point of ca. 1.55 eV.

the absorption spectra automatically transformed from the diffuse reflection spectra via the Kubelka−Munk equation.[49] Figure 4 includes data for fresh and aged films deposited by both AACVD and spin-coating. By determining the onset of each spectrum obtained, E_g was acquired for all samples, and the values are summarized in Table 1. All fresh films regardless of preparation method have an E_g of ca. 1.55 eV, in good agreement with the values reported (1.50−1.60 eV).[10,39,50] After aging for 1 week, the E_g values of films prepared by both AACVD and spin-coating are still ca. 1.55 eV, indicating no significant degradation in the optical properties. This is consistent with the results obtained from XRD and SEM, which also show insignificant degradation of films prepared by AACVD or spin-coating following 1 week of aging. This outcome is better than those for MAPI films spin-coated from the PbI_2 precursor in a nitrogen-filled glovebox, which show severe degradation within 4 days in a similar humid environment (RH > 70%).[51]

After a month in ambient air, there is a noticeable shape change in the absorption edge (Figure 4) of the AACVD-grown film in the range 1.6−1.8 eV. However, in this case, the E_g remains similar to the initial value, which implies that degradation has occurred, but MAPI is still the primary phase in the film. By contrast, the SC film after aging for one month shows almost no light absorption in the range shown, which indicates the occurrence of significant degradation. Comparison with the corresponding XRD suggests the transformation from MAPI into PbI_2 with an E_g of ca. 2.3 eV.[52]

The results above demonstrate the influence of degradation on the bulk characteristics of the films prepared via different approaches. The surface properties are of equal importance because degradation first takes place at surfaces and grain boundaries where the surfaces are exposed to atmospheric gases. The surface chemistry and compositions of the fresh and aged films can be probed through X-ray photoelectron spectroscopy (XPS), as shown in Figure 5. Figure 5A,B shows the Pb 4f and I 3d core-level XPS signals recorded from the MAPI films. The Pb $4f_{7/2,5/2}$ doublets show 1 or 2 components, depending on the sample. We observe Pb $4f_{7/2}$ core-level peaks located at binding energies (BEs) of 138.6 ± 0.1 eV for both the fresh AACVD-grown and SC films, which can be attributed to Pb−I bonding in MAPI.[5,53−56] A trace amount of metallic lead (ca. 0.03 relative to MAPI), at a BE of 137.0 eV, is seen in both the fresh AACVD-prepared and SC films. After 1 week of aging, the binding energy of the Pb−I component remains constant (138.6 ± 0.1 eV) in the AACVD-prepared film, indicating no significant changes in the chemical environment of the surface. For the 1-week-aged SC film, on the other hand, the BE of the Pb−I component moves to 138.8 ± 0.1 eV, a 0.2 eV shift in BE compared to that of the fresh sample. This could be due to the partial formation of PbI_2,[5,53] or due to charging because the film becomes more insulating. This latter explanation is supported by the fact that an equivalent shift is observed in the I 3d spectra as discussed below. In addition, the Pb peaks do not exhibit any broadening, which would be expected if a mixture of MAPI and PbI_2 is present.

For 1-month-aged samples prepared by both AACVD and spin-coating, a broad component appears at higher BE in the Pb 4f spectra (Figure 5A, purple features), in addition to the primary Pb $4f_{7/2}$ Pb−I peaks located at 138.9 ± 0.1 eV. The broad, higher-BE feature (centered at 140.8 ± 0.1 eV BE) is not easily assigned on the basis of its BE, as the shift to higher binding energy is very large and the peak is rather broad. On the basis of its similarity to changes in the corresponding I 3d, N 1s, and C 1s spectra (discussed below), we believe it can be assigned to differential charging of the film. This differential charging occurs when different parts of the film are in varying degrees of electrical contact with the spectrometer earth.[57] The presence of a charged component may be attributed to the formation of insulating species at the grain boundaries, coupled with the poor connectivity of the grains that develops on aging, as shown in Figure 3.

The I 3d spectra (Figure 5B) for the as presented AACVD and SC films consist of a single doublet, with the I $3d_{5/2}$ peak at a BE of 619.5 ± 0.1 eV, consistent with that seen in MAPI by others.[8,64−67] After aging for 1 week in ambient air, the

DOI: 10.1021/acsaem.9b01124
ACS Appl. Energy Mater. 2019, 2, 6012−6022

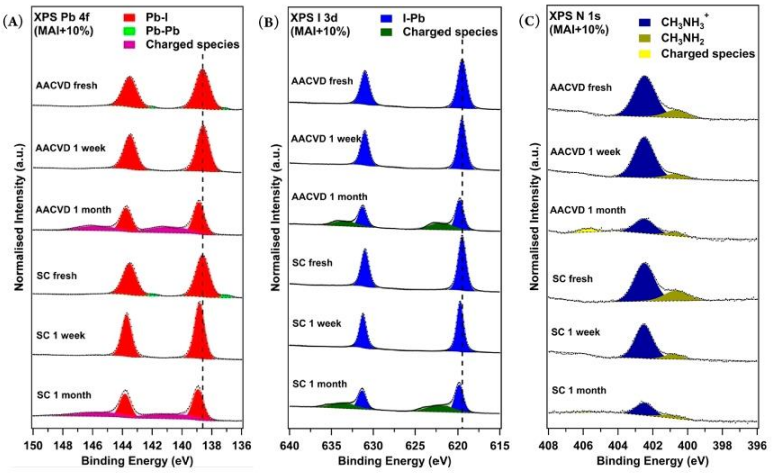

Figure 5. XPS spectra of the (A) Pb 4f, (B) I 3d, and (C) N 1s regions for MAPI (MAI+10%) samples as a function of aging. All spectra are normalized to the total Pb $4f_{7/2}$ area.

spectrum of the AACVD film is unchanged, in agreement with the Pb 4f spectrum. The I 3d spectrum of the SC film, however, is shifted to higher binding energy by 0.3 eV BE to 619.8 ± 0.1 eV (I $3d_{5/2}$) in agreement with the Pb 4f peaks and again consistent with charging of the sample. After 1 month the I 3d spectra exhibit an additional peak, with the I $3d_{5/2}$ peak occurring at 622.1 ± 0.1 eV BE. This is again attributed to differential charging caused by degradation of the film and mirrors the effects seen in the Pb 4f, C 1s (Figure S3), and N 1s (Figure 5C) spectra for these aged films.

In order to gain further insight into the degradation process, the stoichiometries (I/Pb and N/Pb) of the films obtained from the XPS measurements are presented in Table 2. The nitrogen concentration is obtained from Figure 5C, which will be discussed later. For both the fresh AACVD-grown and SC samples, the I/Pb ratio is 3.0 ± 0.1, consistent with stoichiometric MAPI with negligible iodine vacancies. However, after 1 week of aging, the I/Pb ratios diverge (2.8 ± 0.1 for AACVD and 2.6 ± 0.1 for SC). This, in conjunction with the shift in the Pb 4f binding energy, suggests PbI_2 is formed and there is a loss of iodine from the top-most surface, particularly in the 1-week-aged SC film (Figure 5A,B). This is also consistent with the appearance of PbI_2 in the bulk as observed in the XRD results (Figure 2). In the 1-month-aged films, the total I/Pb ratios for both films can be obtained by analyzing the total area for all Pb and I peaks, both charged and uncharged (Table 2). It is found that the overall I/Pb ratio shows a further decrease to 2.6 ± 0.1 for the AACVD-grown film and to 2.5 ± 0.1 for the SC-prepared sample after one month of aging, indicating a further loss of iodine. However, the results here show that the loss of iodine is slower than for films fabricated using PbI_2 as the lead precursor,[58] suggesting that the use of $Pb(SCN)_2$ produces MAPI films with higher stability in humid air.[12] Interestingly, similar values are obtained when the calculation is performed using the "uncharged-only" (indicated by # in the table) or "charged-only" (^) components of the Pb 4f and I 3d spectra. This suggests that iodine deficiency is not the main reason for poor electrical conductivity.

Table 2. Elemental Surface Stoichiometries from XPS[a]

film	I/Pb	N/Pb
AACVD fresh	3.0 ± 0.1	1.2 ± 0.2
AACVD 1 week	2.8 ± 0.1	1.0 ± 0.2
AACVD 1 month	2.6 ± 0.1*	0.6 ± 0.2*
	2.6 ± 0.1#	0.8 ± 0.2#
	2.6 ± 0.1^ (69%)	0.3 ± 0.2^ (23%)
SC fresh	3.0 ± 0.1	1.2 ± 0.2
SC 1 week	2.6 ± 0.1	0.8 ± 0.2
SC 1 month	2.5 ± 0.1*	0.4 ± 0.2*
	2.5 ± 0.1#	0.7 ± 0.2#
	2.5 ± 0.1^ (79%)	0.1 ± 0.2^ (13%)

[a]I/Pb and N/Pb, normalized to to the total Pb $4f_{7/2}$ area (with [Pb] = 1.0) of the AACVD-grown and SC-grown MAI+10% MAPI films as a function of aging (fresh, and aged for a week and for one month). The concentration of nitrogen is calculated from the MAPI N 1s signal at 402.5 eV BE without taking the extra component at 400.8 eV BE into account. For the samples aged for 1 month, * denotes the stoichiometry obtained by including all components (including charged species), while # and ^ denote the calculations for the "uncharged-only" and "charged-only" components, respectively. The percentages in the brackets indicate the relative concentrations of the charged species with respect to the uncharged species.

The MAPI N 1s peak (due to $CH_3NH_3^+$ ions) appears at a binding energy of 402.5 ± 0.1 eV. For this peak the N/Pb ratios for both of the fresh films (Table 2) are roughly at the expected value for stoichiometric MAPI (N/Pb ≈ 1.0). After aging for one month, the N/Pb ratio of the AACVD-grown film is 0.6 ± 0.2 and that for the SC film is 0.4 ± 0.2, suggesting more degradation of the SC sample. While this is consistent with the data obtained from XRD and EDX for the bulk composition, comparison between the surface (XPS) and bulk (EDX) compositions (Table 1) shows more significant N loss from the surface than the bulk. This loss of nitrogen from

DOI: 10.1021/acsaem.9b01124
ACS Appl. Energy Mater. 2019, 2, 6012−6022

the surface is in agreement with previous work on the degradation of a thermally evaporated MAPI film exposed to water vapor, but the reaction here appears to be much slower.[5] However, for the charged component (in Table 2), significantly more loss of nitrogen is observed, indicating that nitrogen deficiencies lead to charging.

The N 1s spectra (Figure 5C) show an additional feature at a binding energy of 400.8 ± 0.1 eV. The origin of this peak is unclear, and it is not typically observed during degradation of MAPI.[5,53,59] In order to understand whether or not this peak is associated with the use of excess MAI, the N 1s spectrum of a stoichiometric MAPI film prepared from $Pb(SCN)_2$ was also examined, as shown in Figure S4A. It is apparent that only a single perovskite ($CH_3NH_3^+$) component is found in the spectrum of the stoichiometric film at a BE of 402.5 ± 0.1 eV, suggesting that the additional peak in Figure 5C may originate in some way from MAI. The binding energy of 400.8 eV is consistent with the presence of surface-adsorbed CH_3NH_2,[60,61] or adsorbed ammonia.[62] Although ammonia has been identified as being lost from the material during degradation,[5] it is unlikely that ammonia would remain adsorbed on the surface, particularly under the ultra-high-vacuum (UHV) conditions employed in the XPS measurements here. Therefore, we assign this feature to CH_3NH_2 associated with the facile dissociation of MAI.[63] This would give rise to HI which can heal the iodine vacancies and/or be lost as HI gas, and CH_3NH_2 species which can remain at grain boundaries, and/or be trapped in the crystal lattice.[60,61]

The CH_3NH_2 to $CH_3NH_3^+$ ratios for the as-deposited AACVD and SC films are ca. 0.20 and 0.30, respectively. The relatively lower value observed for the AACVD-grown films may be ascribed to the larger grain sizes (Figure 3), i.e., to fewer grain boundaries, since CH_3NH_2 molecules tend to aggregate at the grain boundaries of perovskite films.[61] For both films the CH_3NH_2 to $CH_3NH_3^+$ ratio decreases with aging, suggesting loss of CH_3NH_2 molecules from the surface with time. In addition, it is noted that no S 2s XPS signals can be detected in the perovskite film, as shown in Figure S4B, indicating that the sulfur atoms from $Pb(SCN)_2$ are completely lost following formation of MAPI.

In order to gain insight into the changes in surface chemistry during reaction with water vapor, NAP-XPS measurements were carried out. This allows us to control the gas exposure at the surface of the film and, effectively, to monitor the earliest stages of degradation.[30] Figure 6 shows XPS obtained before, during, and after *in situ* exposure to 9 mbar H_2O vapor (equivalent to RH 30% at 20 °C) for a fresh AACVD-grown sample. We observe that the Pb 4f NAP-XPS spectra (Figure 6A) are unchanged on exposure to water, and the Pb $4f_{7/2}$ peaks are all located at a BE of 138.6 ± 0.1 eV. Similarly, the BE of the I 3d core-level NAP-XPS spectra (Figure 6B) does not shift after exposure to water vapor, remaining constant at 619.5 eV ± 0.1 eV BE. This result is very different from previous reports for MAPI films deposited via a $PbCl_2$ precursor.[5] In that case, a ca. 0.2 eV BE shift to high binding energy in the Pb 4f and I 3d signals following exposure to an identical amount of water vapor was reported, suggesting decomposition to form PbI_2.[5] We note that, in that work (albeit using a thinner film), both I and N were lost from the surface upon exposure to water. This led to an increase in the proportion of Pb at the surface. The results here suggest much less decomposition has occurred in the MAPI films deposited from a $Pb(SCN)_2$ precursor. This is reinforced by examining

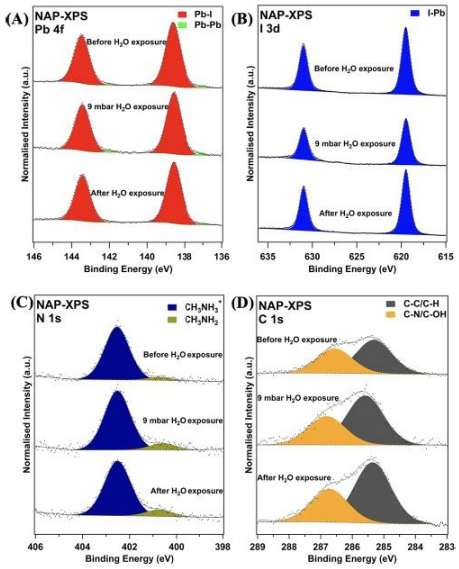

Figure 6. NAP-XPS spectra of (A) Pb 4f, (B) I 3d, (C) N 1s, and (D) C 1s core-level spectra of a fresh MAI+10% AACVD-grown film before, during, and after exposure to 9 mbar H_2O vapor (equivalent to RH 30%). All spectra are normalized to the total Pb $4f_{7/2}$ area for comparison.

the elemental stoichiometries (Table 3), which show only a small reduction in iodine content. The I/Pb ratio decreases from 3.0 ± 0.1 to 2.7 ± 0.1 following H_2O vapor exposure. These ratios are consistent with a previous XPS study of as-deposited MAPI films where an I/Pb ratio of 2.7 ± 0.1 was measured.[56] Therefore, we believe that, after exposure, the perovskite structure is maintained, consistent with the finding that there is no shift in binding energy of the Pb 4f or I 3d peaks associated with the formation of PbI_2. In addition, it is noted that the initial I/Pb ratio is not only stoichiometric but also consistent with the fresh samples studied using UHV XPS (Table 2), suggesting good reproducibility with regards to the surface composition.

The N 1s NAP-XPS spectra of the AACVD-grown film is displayed in Figure 6C, showing that the primary $CH_3NH_3^+$ peak from MAPI (402.50 eV BE) does not change significantly in BE or intensity (relative to Pb). Interestingly, the component at 400.80 eV BE almost doubles in intensity after H_2O vapor exposure. As for the UHV measurements the binding energy is consistent with the presence of CH_3NH_2 species. This suggests that some partial degradation of MAPI takes place on exposure to water, leading to the formation of MAI,[53] which further decomposes to CH_3NH_2 and HI.[53] This is consistent with the observed loss of iodine (Table 3).

This is a significantly different result from the outcome for thermally evaporated thin films deposited from $PbCl_2$ onto $SrTiO_3$ single crystal substrates.[5] Under the same exposure conditions, the nitrogen moiety of these films was shown to be completely lost as ammonia.[5] Here, we note that the intensity

DOI: 10.1021/acsaem.9b01124
ACS Appl. Energy Mater. 2019, 2, 6012−6022

Table 3. Ratios of the Concentrations of Different Components in a Fresh MAI+10% AACVD-Grown Film Determined from NAP-XPS before and after Exposure to 9 mbar H_2O Vapor[a]

	I	N	C−N/C−OH	C−C/C−H	OH−C
UHV before	3.0 ± 0.1	1.2 ± 0.2	2.4 ± 0.2	3.3 ± 0.2	1.0 ± 0.2
UHV after	2.7 ± 0.1	1.0 ± 0.2	3.3 ± 0.2	6.1 ± 0.2	2.1 ± 0.2

[a]All stoichiometries are normalized to the total Pb $4f_{7/2}$ area (with [Pb] = 1.0). The concentration of nitrogen is calculated from the MAPI N 1s signal at 402.5 eV BE excluding the extra component at 400.8 eV BE. OH−C is obtained from the O 1s spectra shown in Figure S6.

of the N 1s signal recorded from the AACVD-grown MAPI remains stable within error, relative to Pb (see Table 3). One possibility is that, rather than forming ammonia,[5] the surface-adsorbed CH_3NH_2 associated with the use of excess MAI may passivate the surfaces and improve their stability. Passivation strategies via various ammonium additives have been proposed and demonstrated;[8,64,65] for example, Yang et al. functionalized MAPI films to be more "water resistant" by attaching alkyl ammonium iodides (of the MA type).[8] MAI has also been demonstrated to passivate the defects at grain boundaries giving better PCEs.[35] To confirm this passivaton effect, photoluminescence (PL) measurements were carried out. The measurements of the MAI+10% MAPI film deposited on glass give rise to much stronger luminescence than the MAPI film without MAI, as shown in Figure S5. This indicates greater radiative recombination in MAI+10% MAPI compared to that in the stoichiometric sample. This suggests the number of surface defects is reduced by adding excess MAI+10%, resulting in the suppression of nonradiative recombination.[1,35] Introducing excess organic cations during post-treatment has also been shown to passivate the organic cation deficiencies induced by aging in air.[66] In addition, CH_3NH_2 gas applied to heal the morphological defects in MAPI has been shown to enhance PSC device performance.[34]

The C 1s NAP-XPS spectra (Figure 6) show two main components that can be assigned to C−N/C−OH (at 286.8 ± 0.1 eV BE) and C−C/C−H (285.3 ± 0.1 eV BE), respectively.[31,34] In addition to C−N contributions from the MAPI film and surface ammonium groups, other carbon species are very common in ex situ prepared samples, particularly those originating from organic solvents. Table 3 shows that both C 1s signals (C−OH/C−N and C−C/C−H) increase in intensity following H_2O exposure. This is consistent with the increase of OH−C in the O 1s spectra after exposure to H_2O vapor (Figure S6 and Table 3). This can be attributed to the contamination introduced into the NAP cell with the water vapor as the increased pressure in the cell tends to displace gas, such as CO, CO_2, and small organics from the chamber walls.[67]

To summarize, we propose that, for MAPI films prepared from $Pb(SCN)_2$ using excess MAI, surface-adsorbed CH_3NH_2 molecules are present at the surface which appear to offer some protection from H_2O vapor in air. This work reveals the first direct observation of how these surface-adsorbed CH_3NH_2 molecules are formed through reaction with ambient air and pure H_2O vapor (by conventional XPS and NAP-XPS, respectively). CH_3NH_2 molecules on the surface impart the stability of MAPI, which confirms literature studies that report that excess organic cations and CH_3NH_2 gas can passivate the defects of perovskite films.[34,66] We do however observe some loss of iodine from the surface to form I-deficient MAPI and then PbI_2 by loss of NH_3 and HI in vacuum, in agreement with previous work.[5,6]

3. CONCLUSIONS

To conclude, we have successfully grown air-stable MAPI perovskite thin films from a $Pb(SCN)_2$ precursor via a one-pot AACVD process for the first time. By applying excess MAI (10% by molar concentration) in the precursor solution, MAPI samples free of a detectable PbI_2 impurity phase can be obtained, as shown by XRD. We found that the AACVD-grown films are more stable than samples prepared by spin-coating when exposed to humid ambient air (RH > 70%) for up to ca. 1 month. The results show that the AACVD-prepared films have somewhat larger grain sizes, contributing to the improved stability in air, consistent with previous results from Cs_2SnI_6.[30] In addition, XPS results also show that the AACVD-prepared films have better surface stability against aging in air than their counterparts prepared by spin-coating. Neutral CH_3NH_2 molecules are found to be present at the surface of the films made from both AACVD and spin-coating as a result of the use of excess MAI in the synthesis. Differential sample charging was observed in XPS after aging for one month, which we ascribe to the degradation of the films into poorly connected islands. NAP-XPS was utilized to examine the surface stability of AACVD-grown films on exposure to 9 mbar H_2O vapor. In marked contrast with MAPI films made from $PbCl_2$,[5] the concentration of $CH_3NH_3^+$ does not significantly decrease on water exposure, indicating much better stability to decomposition. The surface CH_3NH_2 molecules may passivate the surfaces and protect MAPI from degradation, providing a rationale for the observed stability of MAPI films fabricated from $Pb(SCN)_2$ with excess MAI. Ultimately, the study provides insights into the fabrication of novel stable organo-metal halide perovskites and the enhanced stability of MAPI films made by this route.

4. EXPERIMENTAL SECTION

4.1. Sample Preparation. First, 0.194 g of lead(II) thiocyanate ($Pb(SCN)_2$, 99.5%, Aldrich) was added to 3 mL of warm (ca. 70 °C) anhydrous *N,N*-dimethylformamide (DMF, 99.8%, Sigma-Aldrich) solvent with gentle stirring for 30 min to generate a clear greyish-white solution (0.2 M). A stoichiometric aliquot (0.286 g, 0.6 M according to the chemical reaction for non-iodide lead precursors, $Pb(SCN)_2(s) + 3MAI(s) \rightarrow MAPbI_3(s) + 2MA(SCN)(g)$)[12] or an excess (10% or 20% excess in molar concentration) of methyl-ammonium iodide (MAI, CH_3NH_3I, 98%, Aldrich), used for provision of iodine for MAPI, was then poured into the warm solution under continuous stirring. The color of the precursor solution immediately became muddy yellow, and under continued stirring for 30 min at 70 °C, a clear and translucent light-yellow solution was obtained. The excess MAI solutions are denoted as "MAI +10%" and "MAI+20%" for 10% and 20% excess samples, respectively. The resulting solutions were then used for the AACVD process.

The prepared solution was directly used as the supply for AACVD without further steps. The apparatus used for AACVD has been previously described in detail by Ramasamy et al.[68] and used in the synthesis of the inorganic Cs_2SnI_6 double perovskite.[30] First, 3 mL of the DMF solution was poured into a two-necked 100 mL round-

DOI: 10.1021/acsaem.9b01124
ACS Appl. Energy Mater. 2019, 2, 6012−6022

bottom flask with a gas inlet. This allows Ar carrier gas (flow rate ca. 300 sccm) to travel into the solution to support the transport of mist produced by a humidifier. Prior to deposition, the solution was prehumidified for 10 min to ensure a homogeneous solution before use. This flask was connected to a glass tube in a furnace where the temperature during deposition was set to 130 °C. Indium tin oxide (ITO)-coated glass (Ossila) with dimensions of 2.0 × 1.5 cm^2 or gold-coated silicon (Au−Si) was used as substrate. The deposition rate was ca. 10 nm per minute as evaluated by a Veeco Dektak 8 Surface Profilometer, and the deposition time was fixed for an hour. Hence, a film thickness of ca. 600 nm was obtained on the substrates. After the deposition, the samples were annealed at 110 °C in ambient air for 30 min to completely remove residual solvent from both the samples and the AACVD tube. The sample was then cooled to a temperature below 100 °C before removal from the AACVD tube. The prepared samples were immediately placed into plastic tubes filled with dry Ar and then stored in a desiccator to minimize degradation, for no longer than 2 days (denoted as fresh samples in this work). For the investigation of aging, the films were aged in ambient air at an average relative humidity (RH) of >70% for duration up to ∼1 month. All fresh samples were exposed to ambient air for no longer than 10 min when they were transferred from the plastic storage tubes to various characterization chambers.

A small volume (200 μL) of the more concentrated precursor solutions (∼46 wt %) with a molar concentration of 1 M was applied to deposit spin-coated (SC) films in order to obtain films with similar thickness (ca. 600 nm) for comparison with the AACVD-grown films. The films were deposited at 2000 rpm for 30 s. During spin-coating, 200 μL of ethyl acetate as the antisolvent was poured onto the spinning substrate 10 s after starting the program. Subsequently, the as-deposited samples were transferred to a hot plate and annealed at 110 °C in ambient air for 30 min. The resultant samples were then stored or aged in the same way as the AACVD-grown films.

4.2. Characterization. Powder X-ray diffraction (XRD) patterns were measured using a Bruker D8 Advance with a grazing incidence (GI) angle of 3° to collect the signals from the thin films without interference from the signals due to the substrates. The scanning range (2θ) was 10−50° with a theta step of 0.05° and dwell time of 4.5 s.

The morphology of the MAPI films was probed using Philips XL30 and Zeiss Sigma scanning electron microscopes (SEMs). Bulk elemental analysis was performed using an energy-dispersive X-ray spectrometer (EDX, DX4, and AZtec for Philips XL30 and Zeiss Sigma, respectively). EDX was carried out in the SEM chambers.

Optical diffuse reflectance measurements were performed using an ultraviolet−visible−near-infrared (UV−vis−NIR) spectrometer (PerkinElmer Lambda-1050) with an integrated sphere (IS) module to collect the scattered light. Spectra were recorded over a wavelength range 600−1200 nm. The reflectance (R) acquired was automatically converted to absorption (α) according to the Kubelka−Munk equation. The optical energy bandgap (E_g) was obtained using a Tauc plot by finding the onset point. Photoluminescence (PL) spectra were obtained using an Edinburgh Instruments FLS980 spectrometer using an excitation wavelength of 480 nm.[69]

X-ray photoelectron spectroscopy (XPS) measurements were conducted with Kratos Axis Ultra and SPECS XPS instruments. Both spectrometers were equipped with monochromated Al Kα X-ray sources (photon energy $h\nu$ = 1486.6 eV). Emitted photoelectrons were collected using a 165 mm hemispherical energy analyzer (Kratos) and a 150 mm hemispherical energy analyzer (Phoibos 150 SPECS), respectively. Binding energies (BEs) were calibrated to Au $4f_{7/2}$ at 84.0 eV.

The SPECS instrument also enables NAP-XPS measurements to be carried out; the details can be found elsewhere.[5,30] The NAP cell is equipped with differential pumps to allow gas pressures of up to ∼15 mbar to be applied during measurement. In this study, 9 mbar H_2O vapor (RH = ca. 30%, compared with RH = ca. 70% in the ambient air of the laboratory) was applied to maximize the RH obtained while achieving a viable signal-to-noise level in the in situ spectra. All XPS data were analyzed using CasaXPS software, in which a Shirley background and pseudo-Voigt peaks (30% Lorentzian and 70% Gaussian) were fitted to the spectra acquired.[70] BE values are quoted to an accuracy of ±0.1 eV for both UHV and in situ XPS studies, respectively, due to instrumental precision. To obtain quantified surface compositional information, the built-in CasaXPS sensitivity factors (Kratos) were applied for calculating the surface stoichiometries. Note that this is not possible in the case of spectra acquired at near-ambient pressure (NAP) conditions due to the absence of transmission-function-adapted data in such environments.

■ ASSOCIATED CONTENT

Supporting Information

The Supporting Information is available free of charge on the ACS Publications website at DOI: 10.1021/acsaem.9b01124.

Additional SEM micrographs, photoelectron spectroscopy measurements of $Pb(SCN)_2$ powder, scratch test results, and photoluminescence measurements of the stoichiometric and +10% MAI films (PDF)

■ AUTHOR INFORMATION

Corresponding Authors

*E-mail: wendy.flavell@manchester.ac.uk (W.R.F.).
*E-mail: andrew.g.thomas@manchester.ac.uk (A.G.T.).

ORCID

Chun-Ren Ke: 0000-0002-6398-1753
David J. Lewis: 0000-0001-5950-1350
Alex S. Walton: 0000-0002-3207-8406
Ben F. Spencer: 0000-0002-1453-5327
Paul O'Brien: 0000-0001-8744-9174
Andrew G. Thomas: 0000-0002-1900-6686
Wendy R. Flavell: 0000-0002-2457-3669

Notes

The authors declare no competing financial interest.
⊥Deceased October 16, 2018.
The data associated with this paper are openly available from http://dx.doi.org/10.17632/x3ybbsrvpv.1.

■ ACKNOWLEDGMENTS

This article is dedicated with affection and respect to the memory of Prof. Paul O'Brien, FRS: world-class scientist, mentor, and friend. The authors thank the University of Manchester and EPSRC (UK) (grant EP/K009710) for funding. C.-R.K. thanks the University of Manchester for the award of a President's Doctoral Scholarship.

■ REFERENCES

(1) Yang, W. S.; Park, B.-W.; Jung, E. H.; Jeon, N. J.; Kim, Y. C.; Lee, D. U.; Shin, S. S.; Seo, J.; Kim, E. K.; Noh, J. H.; Seok, S. I. Iodide management in formamidinium-lead-halide−based perovskite layers for efficient solar cells. *Science* **2017**, *356*, 1376−1379.
(2) Kojima, A.; Teshima, K.; Shirai, Y.; Miyasaka, T. Organometal halide perovskites as visible-light sensitizers for photovoltaic cells. *J. Am. Chem. Soc.* **2009**, *131*, 6050−6051.
(3) Grancini, G.; Roldán-Carmona, C.; Zimmermann, I.; Mosconi, E.; Lee, X.; Martineau, D.; Narbey, S.; Oswald, F.; De Angelis, F.; Graetzel, M.; NAzeeruddin, M. K. One-Year stable perovskite solar cells by 2D/3D interface engineering. *Nat. Commun.* **2017**, *8*, 15684.
(4) Berhe, T. A.; Su, W.-N.; Chen, C.-H.; Pan, C.-J.; Cheng, J.-H.; Chen, H.-M.; Tsai, M.-C.; Chen, L.-Y.; Dubale, A. A.; Hwang, B.-J. Organometal halide perovskite solar cells: degradation and stability. *Energy Environ. Sci.* **2016**, *9*, 323−356.
(5) Ke, J. C.-R.; Walton, A. S.; Lewis, D. J.; Tedstone, A.; O'Brien, P.; Thomas, A. G.; Flavell, W. R. In situ investigation of degradation

at organometal halide perovskite surfaces by X-ray photoelectron spectroscopy at realistic water vapour pressure. *Chem. Commun.* **2017**, *53*, 5231−5234.
(6) Li, Y.; Xu, X.; Wang, C.; Wang, C.; Xie, F.; Yang, J.; Gao, Y. Degradation by exposure of coevaporated CH3NH3PbI3 thin films. *J. Phys. Chem. C* **2015**, *119*, 23996−24002.
(7) Leijtens, T.; Giovenzana, T.; Habisreutinger, S. N.; Tinkham, J. S.; Noel, N. K.; Kamino, B. A.; Sadoughi, G.; Sellinger, A.; Snaith, H. J. Hydrophobic organic hole transporters for improved moisture resistance in metal halide perovskite solar cells. *ACS Appl. Mater. Interfaces* **2016**, *8*, 5981−5989.
(8) Yang, S.; Wang, Y.; Liu, P.; Cheng, Y.-B.; Zhao, H. J.; Yang, H. G. Functionalization of perovskite thin films with moisture-tolerant molecules. *Nature Energy* **2016**, *1*, 15016.
(9) Smith, I. C.; Hoke, E. T.; Solis-Ibarra, D.; McGehee, M. D.; Karunadasa, H. I. A Layered Hybrid Perovskite Solar-Cell Absorber with Enhanced Moisture Stability. *Angew. Chem.* **2014**, *126*, 11414−11417.
(10) Lee, M. M.; Teuscher, J.; Miyasaka, T.; Murakami, T. N.; Snaith, H. J. Efficient hybrid solar cells based on meso-superstructured organometal halide perovskites. *Science* **2012**, *338*, 643−647.
(11) Zhang, W.; Saliba, M.; Moore, D. T.; Pathak, S. K.; Hörantner, M. T.; Stergiopoulos, T.; Stranks, S. D.; Eperon, G. E.; Alexander-Webber, J. A.; Abate, A.; et al. Ultrasmooth organic−inorganic perovskite thin-film formation and crystallization for efficient planar heterojunction solar cells. *Nat. Commun.* **2015**, *6*, 6142.
(12) Tai, Q.; You, P.; Sang, H.; Liu, Z.; Hu, C.; Chan, H. L.; Yan, F. Efficient and stable perovskite solar cells prepared in ambient air irrespective of the humidity. *Nat. Commun.* **2016**, *7*, 11105.
(13) Chiang, Y.-H.; Li, M.-H.; Cheng, H.-M.; Shen, P.-S.; Chen, P. Mixed Cation Thiocyanate-Based Pseudohalide Perovskite Solar Cells with High Efficiency and Stability. *ACS Appl. Mater. Interfaces* **2017**, *9*, 2403−2409.
(14) Chen, S.; Chen, B.; Gao, X.; Dong, B.; Hu, H.; Yan, K.; Wen, W.; Zou, D. Neutral-colored semitransparent solar cells based on pseudohalide (SCN-)-doped perovskite. *Sustainable Energy & Fuels* **2017**, *1*, 1034−1040.
(15) Yang, S.; Liu, W.; Zuo, L.; Zhang, X.; Ye, T.; Chen, J.; Li, C.-Z.; Wu, G.; Chen, H. Thiocyanate assisted performance enhancement of formamidinium based planar perovskite solar cells through a single one-step solution process. *J. Mater. Chem. A* **2016**, *4*, 9430−9436.
(16) Chiang, Y. H.; Cheng, H. M.; Li, M. H.; Guo, T. F.; Chen, P. Low-Pressure Vapor-Assisted Solution Process for Thiocyanate-Based Pseudohalide Perovskite Solar Cells. *ChemSusChem* **2016**, *9*, 2620−2627.
(17) Troughton, J.; Hooper, K.; Watson, T. M. Humidity resistant fabrication of CH3NH3PbI3 perovskite solar cells and modules. *Nano Energy* **2017**, *39*, 60−68.
(18) Sveinbjörnsson, K.; Aitola, K.; Zhang, J.; Johansson, M. B.; Zhang, X.; Correa-Baena, J.-P.; Hagfeldt, A.; Boschloo, G.; Johansson, E. M. Ambient air-processed mixed-ion perovskites for high-efficiency solar cells. *J. Mater. Chem. A* **2016**, *4*, 16536−16545.
(19) Yang, F.; Kapil, G.; Zhang, P.; Hu, Z.; Kamarudin, M. A.; Ma, T.; Hayase, S. Dependence of acetate-based antisolvents for high humidity fabrication of CH3NH3PbI3 perovskite devices in ambient atmosphere. *ACS Appl. Mater. Interfaces* **2018**, *10*, 16482−16489.
(20) Chen, Q.; Mokhtar, M. Z.; Ke, J. C.-R.; Thomas, A. G.; Hadi, A.; Whittaker, E.; Curioni, M.; Liu, Z. A one-step laser process for rapid manufacture of mesoscopic perovskite solar cells prepared under high relative humidity. *Sustainable Energy & Fuels* **2018**, *2*, 1216−1224.
(21) Liu, M.; Johnston, M. B.; Snaith, H. J. Efficient planar heterojunction perovskite solar cells by vapour deposition. *Nature* **2013**, *501*, 395−398.
(22) Ono, L. K.; Wang, S.; Kato, Y.; Raga, S. R.; Qi, Y. Fabrication of semi-transparent perovskite films with centimeter-scale superior uniformity by the hybrid deposition method. *Energy Environ. Sci.* **2014**, *7*, 3989−3993.
(23) Hsiao, S. Y.; Lin, H. L.; Lee, W. H.; Tsai, W. L.; Chiang, K. M.; Liao, W. Y.; Ren-Wu, C.-Z.; Chen, C. Y.; Lin, H. W. Efficient All-Vacuum Deposited Perovskite Solar Cells by Controlling Reagent Partial Pressure in High Vacuum. *Adv. Mater.* **2016**, *28*, 7013−7019.
(24) Knapp, C. E.; Carmalt, C. J. Solution based CVD of main group materials. *Chem. Soc. Rev.* **2016**, *45*, 1036−1064.
(25) Lewis, D. J.; Tedstone, A. A.; Zhong, X. L.; Lewis, E. A.; Rooney, A.; Savjani, N.; Brent, J. R.; Haigh, S. J.; Burke, M. G.; Muryn, C. A.; et al. Thin Films of Molybdenum Disulfide Doped with Chromium by Aerosol-Assisted Chemical Vapor Deposition (AACVD). *Chem. Mater.* **2015**, *27*, 1367−1374.
(26) Ashraf, S.; Blackman, C. S.; Palgrave, R. G.; Naisbitt, S. C.; Parkin, I. P. Aerosol assisted chemical vapour deposition of WO3 thin films from tungsten hexacarbonyl and their gas sensing properties. *J. Mater. Chem.* **2007**, *17*, 3708−3713.
(27) Lewis, D. J.; O'Brien, P. Ambient pressure aerosol-assisted chemical vapour deposition of (CH 3 NH 3) PbBr 3, an inorganic−organic perovskite important in photovoltaics. *Chem. Commun.* **2014**, *50*, 6319−6321.
(28) Bhachu, D.; Scanlon, D.; Saban, E.; Bronstein, H.; Parkin, I.; Carmalt, C.; Palgrave, R. Scalable route to CH3NH3PbI3 perovskite thin films by aerosol assisted chemical vapour deposition. *J. Mater. Chem. A* **2015**, *3*, 9071−9073.
(29) Aamir, M.; Sher, M.; Khan, M. D.; Malik, M. A.; Akhtar, J.; Revaprasadu, N. Controlled synthesis of all inorganic CsPbBr 2 I perovskite by non-template and aerosol assisted chemical vapour deposition. *Mater. Lett.* **2017**, *190*, 244−247.
(30) Ke, J. C.-R.; Lewis, D. J.; Walton, A. S.; Spencer, B. F.; O'Brien, P.; Thomas, A. G.; Flavell, W. R. Ambient-air-stable inorganic Cs2SnI6 double perovskite thin films via aerosol-assisted chemical vapour deposition. *J. Mater. Chem. A* **2018**, *6*, 11205−11214.
(31) Chen, S.; Briscoe, J.; Shi, Y.; Chen, K.; Wilson, R. M.; Dunn, S.; Binions, R. A simple, low-cost CVD route to high-quality CH3NH3PbI3 perovskite thin films. *CrystEngComm* **2015**, *17*, 7486−7489.
(32) Nie, W.; Tsai, H.; Asadpour, R.; Blancon, J.-C.; Neukirch, A. J.; Gupta, G.; Crochet, J. J.; Chhowalla, M.; Tretiak, S.; Alam, M. A.; et al. High-efficiency solution-processed perovskite solar cells with millimeter-scale grains. *Science* **2015**, *347*, 522−525.
(33) Roldán-Carmona, C.; Malinkiewicz, O.; Soriano, A.; Espallargas, G. M.; Garcia, A.; Reinecke, P.; Kroyer, T.; Dar, M. I.; Nazeeruddin, M. K.; Bolink, H. J. Flexible high efficiency perovskite solar cells. *Energy Environ. Sci.* **2014**, *7*, 994−997.
(34) Zhou, Z.; Wang, Z.; Zhou, Y.; Pang, S.; Wang, D.; Xu, H.; Liu, Z.; Padture, N. P.; Cui, G. Methylamine-Gas-Induced Defect-Healing Behavior of CH3NH3PbI3 Thin Films for Perovskite Solar Cells. *Angew. Chem., Int. Ed.* **2015**, *54*, 9705−9709.
(35) Son, D.-Y.; Lee, J.-W.; Choi, Y. J.; Jang, I.-H.; Lee, S.; Yoo, P. J.; Shin, H.; Ahn, N.; Choi, M.; Kim, D.; Park, N.-G. Self-formed grain boundary healing layer for highly efficient CH3 NH3 PbI3 perovskite solar cells. *Nature Energy* **2016**, *1*, 16081.
(36) Zhang, Y.; Kim, S. G.; Lee, D. K.; Park, N. G. CH3NH3PbI3 and HC (NH2) 2PbI3 Powders Synthesized from Low-Grade PbI2: Single Precursor for High-Efficiency Perovskite Solar Cells. *ChemSusChem* **2018**, *11*, 1813.
(37) Jain, S. M.; Philippe, B.; Johansson, E. M.; Park, B.-w.; Rensmo, H.; Edvinsson, T.; Boschloo, G. Vapor phase conversion of PbI 2 to CH3NH3PbI3: spectroscopic evidence for formation of an intermediate phase. *J. Mater. Chem. A* **2016**, *4*, 2630−2642.
(38) Baikie, T.; Fang, Y.; Kadro, J. M.; Schreyer, M.; Wei, F.; Mhaisalkar, S. G.; Graetzel, M.; White, T. J. Synthesis and crystal chemistry of the hybrid perovskite (CH3NH3)PbI3 for solid-state sensitised solar cell applications. *J. Mater. Chem. A* **2013**, *1*, 5628−5641.
(39) Stoumpos, C. C.; Malliakas, C. D.; Kanatzidis, M. G. Semiconducting tin and lead iodide perovskites with organic cations: phase transitions, high mobilities, and near-infrared photoluminescent properties. *Inorg. Chem.* **2013**, *52*, 9019−9038.

DOI: 10.1021/acsaem.9b01124
ACS Appl. Energy Mater. 2019, 2, 6012−6022

(40) Burschka, J.; Pellet, N.; Moon, S.-J.; Humphry-Baker, R.; Gao, P.; Nazeeruddin, M. K.; Grätzel, M. Sequential deposition as a route to high-performance perovskite-sensitized solar cells. *Nature* **2013**, *499*, 316−319.
(41) Bi, D.; Tress, W.; Dar, M. I.; Gao, P.; Luo, J.; Renevier, C.; Schenk, K.; Abate, A.; Giordano, F.; Baena, J.-P. C.; et al. Efficient luminescent solar cells based on tailored mixed-cation perovskites. *Science advances* **2016**, *2*, No. e1501170.
(42) Song, Z.; Watthage, S. C.; Phillips, A. B.; Tompkins, B. L.; Ellingson, R. J.; Heben, M. J. Impact of processing temperature and composition on the formation of methylammonium lead iodide perovskites. *Chem. Mater.* **2015**, *27*, 4612−4619.
(43) Chen, Y.; Chen, T.; Dai, L. Layer-by-Layer Growth of CH3NH3PbI3- xClx for Highly Efficient Planar Heterojunction Perovskite Solar Cells. *Adv. Mater.* **2015**, *27*, 1053−1059.
(44) Arabpour Roghabadi, F.; Ahmadi, V.; Oniy Aghmiuni, K. Organic-Inorganic Halide Perovskite Formation: In Situ Dissociation of Cation Halide and Metal Halide Complexes During Crystal Formation. *J. Phys. Chem. C* **2017**, *121*, 13532−13538.
(45) Shirayama, M.; Kato, M.; Miyadera, T.; Sugita, T.; Fujiseki, T.; Hara, S.; Kadowaki, H.; Murata, D.; Chikamatsu, M.; Fujiwara, H. Degradation mechanism of CH3NH3PbI3 perovskite materials upon exposure to humid air. *J. Appl. Phys.* **2016**, *119*, 115501.
(46) Eperon, G. E.; Burlakov, V. M.; Docampo, P.; Goriely, A.; Snaith, H. J. Morphological Control for High Performance, Solution-Processed Planar Heterojunction Perovskite Solar Cells. *Adv. Funct. Mater.* **2014**, *24*, 151−157.
(47) Eperon, G. E.; Habisreutinger, S. N.; Leijtens, T.; Bruijnaers, B. J.; van Franeker, J. J.; deQuilettes, D. W.; Pathak, S.; Sutton, R. J.; Grancini, G.; Ginger, D. S.; et al. The importance of moisture in hybrid lead halide perovskite thin film fabrication. *ACS Nano* **2015**, *9*, 9380−9393.
(48) Ahn, N.; Kwak, K.; Jang, M. S.; Yoon, H.; Lee, B. Y.; Lee, J.-K.; Pikhitsa, P. V.; Byun, J.; Choi, M. Trapped charge-driven degradation of perovskite solar cells. *Nat. Commun.* **2016**, *7*, 13422.
(49) Kubelka, P.; Munk, F. An article on optics of paint layers. *Z. Technol. Phys.* **1931**, *12*, 1−16.
(50) Choi, J. J.; Yang, X.; Norman, Z. M.; Billinge, S. J.; Owen, J. S. Structure of methylammonium lead iodide within mesoporous titanium dioxide: active material in high-performance perovskite solar cells. *Nano Lett.* **2014**, *14*, 127−133.
(51) Yang, J.; Siempelkamp, B. D.; Liu, D.; Kelly, T. L. Investigation of CH3NH3PbI3 degradation rates and mechanisms in controlled humidity environments using in situ techniques. *ACS Nano* **2015**, *9*, 1955−1963.
(52) Ahuja, R.; Arwin, H.; Ferreira da Silva, A.; Persson, C.; Osorio-Guillén, J.; Souza de Almeida, J.; Moyses Araujo, C.; Veje, E.; Veissid, N.; An, C.; et al. Electronic and optical properties of lead iodide. *J. Appl. Phys.* **2002**, *92*, 7219−7224.
(53) Philippe, B.; Park, B.-W.; Lindblad, R.; Oscarsson, J.; Ahmadi, S.; Johansson, E. M.; Rensmo, H. k. Chemical and electronic structure characterization of lead halide perovskites and stability behavior under different exposures. A photoelectron spectroscopy investigation. *Chem. Mater.* **2015**, *27*, 1720−1731.
(54) Ng, T.-W.; Chan, C.-Y.; Lo, M.-F.; Guan, Z. Q.; Lee, C.-S. Formation chemistry of perovskites with mixed iodide/chloride content and the implications on charge transport properties. *J. Mater. Chem. A* **2015**, *3*, 9081−9085.
(55) Lindblad, R.; Jena, N. K.; Philippe, B.; Oscarsson, J.; Bi, D.; Lindblad, A.; Mandal, S.; Pal, B.; Sarma, D. D.; Karis, O.; et al. Electronic structure of CH3NH3PbX3 perovskites: dependence on the halide moiety. *J. Phys. Chem. C* **2015**, *119*, 1818−1825.
(56) Lindblad, R.; Bi, D.; Park, B.-w.; Oscarsson, J.; Gorgoi, M.; Siegbahn, H.; Odelius, M.; Johansson, E. M.; Rensmo, H. k. Electronic structure of TiO2/CH3NH3PbI3 perovskite solar cell interfaces. *J. Phys. Chem. Lett.* **2014**, *5*, 648−653.
(57) Suzer, S. Differential charging in X-ray photoelectron spectroscopy: A nuisance or a useful tool? *Anal. Chem.* **2003**, *75*, 7026−7029.
(58) Huang, W.; Manser, J. S.; Kamat, P. V.; Ptasinska, S. Evolution of chemical composition, morphology, and photovoltaic efficiency of CH3NH3PbI3 perovskite under ambient conditions. *Chem. Mater.* **2016**, *28*, 303−311.
(59) Liu, L.; McLeod, J. A.; Wang, R.; Shen, P.; Duhm, S. Tracking the formation of methylammonium lead triiodide perovskite. *Appl. Phys. Lett.* **2015**, *107*, 061904.
(60) Calloni, A.; Abate, A.; Bussetti, G.; Berti, G.; Yivlialin, R.; Ciccacci, F.; Duo, L. Stability of organic cations in solution-processed CH3NH3PbI3 perovskites: formation of modified surface layers. *J. Phys. Chem. C* **2015**, *119*, 21329−21335.
(61) Jung, M.-C.; Lee, Y. M.; Lee, H.-K.; Park, J.; Raga, S. R.; Ono, L. K.; Wang, S.; Leyden, M. R.; Yu, B. D.; Hong, S.; Q, Y. The presence of CH3NH2 neutral species in organometal halide perovskite films. *Appl. Phys. Lett.* **2016**, *108*, 073901.
(62) Farfan-Arribas, E.; Madix, R. J. Characterization of the acid-base properties of the TiO2 (110) surface by adsorption of amines. *J. Phys. Chem. B* **2003**, *107*, 3225−3233.
(63) Arabpour Roghabadi, F.; Ahmadi, V.; Oniy Aghmiuni, K. Organic-inorganic halide perovskite formation: in situ dissociation of cation halide and metal halide complexes during crystal formation. *J. Phys. Chem. C* **2017**, *121*, 13532−13538.
(64) Palazon, F.; Pérez-Del-Rey, D.; Marras, S.; Prato, M.; Sessolo, M.; Bolink, H. J.; Manna, L. Coating Evaporated MAPI Thin Films with Organic Molecules: Improved Stability at High Temperature and Implementation in High-Efficiency Solar Cells. *ACS Energy Letters* **2018**, *3*, 835−839.
(65) Wu, Z.; Raga, S. R.; Juarez-Perez, E. J.; Yao, X.; Jiang, Y.; Ono, L. K.; Ning, Z.; Tian, H.; Qi, Y. Improved Efficiency and Stability of Perovskite Solar Cells Induced by C□O Functionalized Hydrophobic Ammonium□Based Additives. *Adv. Mater.* **2018**, *30*, 1703670.
(66) Long, M.; Zhang, T.; Liu, M.; Chen, Z.; Wang, C.; Xie, W.; Xie, F.; Chen, J.; Li, G.; Xu, J. Abnormal synergetic effect of organic and halide ions on the stability and optoelectronic properties of a mixed perovskite via in situ characterizations. *Adv. Mater.* **2018**, *30*, 1801562.
(67) Booth, S.; Tripathi, A.; Strashnov, I.; Dryfe, R.; Walton, A. The offset droplet: a new methodology for studying the solid/water interface using x-ray photoelectron spectroscopy. *J. Phys.: Condens. Matter* **2017**, *29*, 454001.
(68) Ramasamy, K.; Kuznetsov, V. L.; Gopal, K.; Malik, M. A.; Raftery, J.; Edwards, P. P.; O'Brien, P. Organotin dithiocarbamates: Single-source precursors for tin sulfide thin films by aerosol-assisted chemical vapor deposition (AACVD). *Chem. Mater.* **2013**, *25*, 266−276.
(69) Mokhtar, M. Z.; Chen, Q.; Lian, Q.; Lewis, D. J.; Saunders, B. R.; Walton, A. S.; Ke, C.-R.; Whittaker, E.; Hamilton, B.; Haque, S. Decoupling Structure and Composition of CH3NH3PbI3−xBrx Films Prepared by Combined One-Step and Two-Step Deposition. *ACS Applied Energy Materials* **2018**, *1*, 5567−5578.
(70) Fairley, N. *Casa XPS manual 2.3. 15*; Acolyte Science, 2009.

DOI: 10.1021/acsaem.9b01124
ACS Appl. Energy Mater. 2019, 2, 6012−6022

5.2.2 Supporting Information

Supporting Information

Air-Stable Methylammonium Lead Iodide Perovskite Thin Films Fabricated *via* Aerosol-Assisted Chemical Vapor Deposition from a Pseudohalide $Pb(SCN)_2$ Precursor

Chun-Ren Ke,[a,b] David J. Lewis,[c] Alex S. Walton,[b,d] Qian Chen,[c] Ben F. Spencer,[c] Muhamad Z. Mokhtar,[c] Claudia L. Compean-Gonzalez,[b,c] Paul O'Brien,†[,c,d] Andrew G. Thomas*[,b,c,] and Wendy R. Flavell*[,a,b]

a. School of Physics and Astronomy, The University of Manchester, Oxford Road, Manchester M13 9PL, United Kingdom

b. Photon Science Institute, The University of Manchester, Oxford Road, Manchester M13 9PL, United Kingdom

c. School of Materials, The University of Manchester, Oxford Road, Manchester M13 9PL, United Kingdom

d. School of Chemistry, The University of Manchester, Oxford Road, Manchester M13 9PL, United Kingdom

† Deceased 10/19.

This article is dedicated with affection and respect to the memory of Prof Paul O'Brien, FRS; world-class scientist, mentor, and friend.

* Corresponding Authors

Email: wendy.flavell@manchester.ac.uk (Prof W. R. Flavell)

Email: andrew.g.thomas@manchester.ac.uk (Dr A. G. Thomas)

Supporting Information

Method for peeling and scratching tests

In order to evaluate adherence between MAPI film and ITO-glass substrate, we performed sticking and scratching tests for films fabricated by AACVD and spin coating. The sticking test was conducted using transparent adhesive tape with width of 1 cm. This was attached to the films and then peeled off rapidly. For the scratching test, a needle was used to scratch the films manually, using moderate force.

(A)

(B)

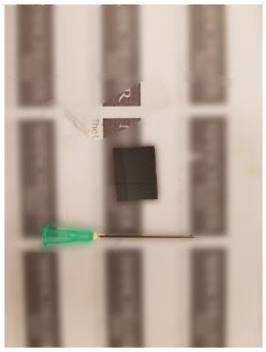

(C)

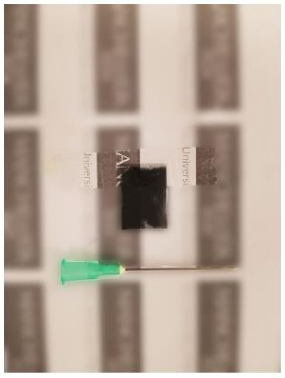

(D)

(E)

S-3

(F)

Figure S1 Photographs of MAPI films fabricated *via* AACVD (B&C) and spin coating (A & D~E). The photos in (A) exhibit the degradation of spin-coated MAPI films in air with aging time up to over one month. (B) shows the as-grown AACVD film and (C) following the peeling and scratching tests. (D) and (E) are equivalents for the spin-coated sample. The film in (F) was fabricated without the antisolvent step.

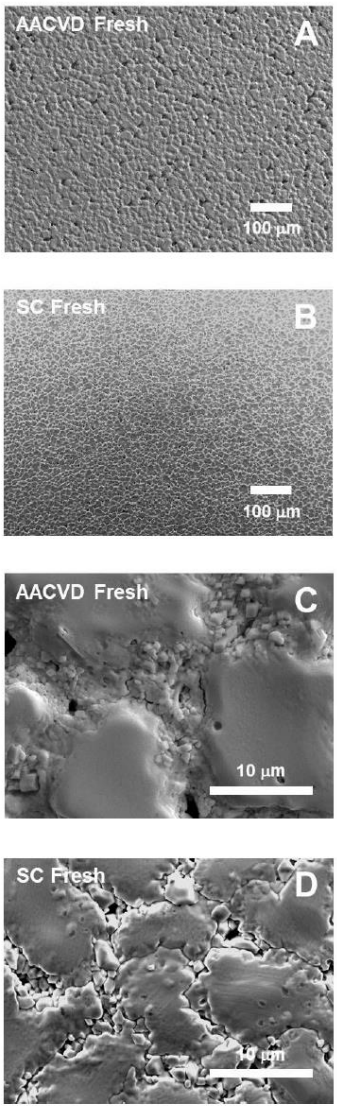

Figure S2 SEM images of fresh MAI+10% films prepared *via* AACVD (A&C) or spin coating (B&D) at lower (A&B) and higher (C&D) magnifications, relative to the SEM images in Figure 3.

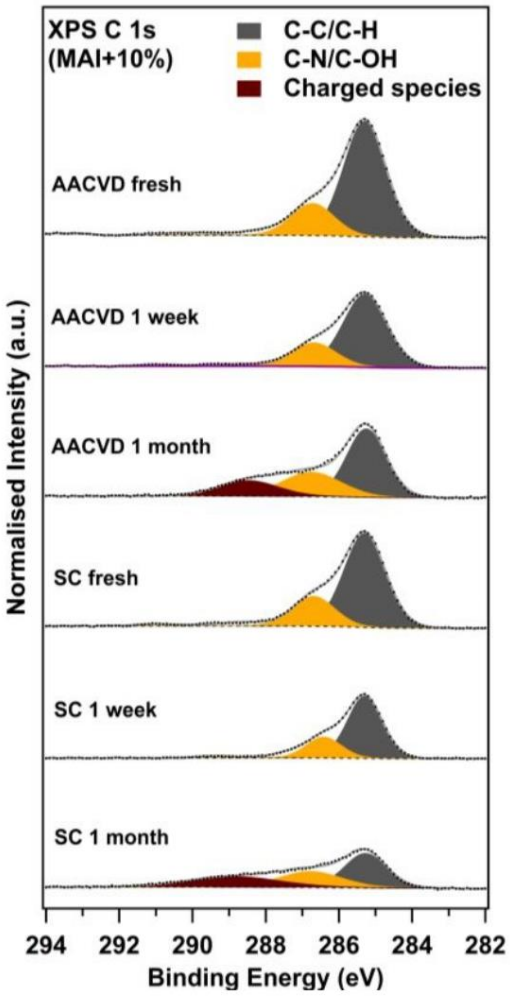

Figure S3 XPS spectra of the C 1s region for MAPI (MAI+10%) samples as a function of aging.

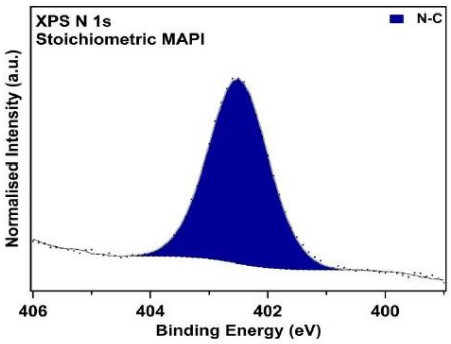

(A)

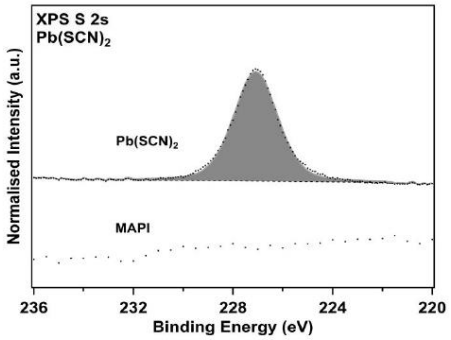

(B)

Figure S4 (A) A N 1s XPS spectrum of a spin-coated MAPI film, fabricated without the use excess MAI, and (B) S 2s core-level XPS spectra of $Pb(SCN)_2$ and MAPI films for comparison.

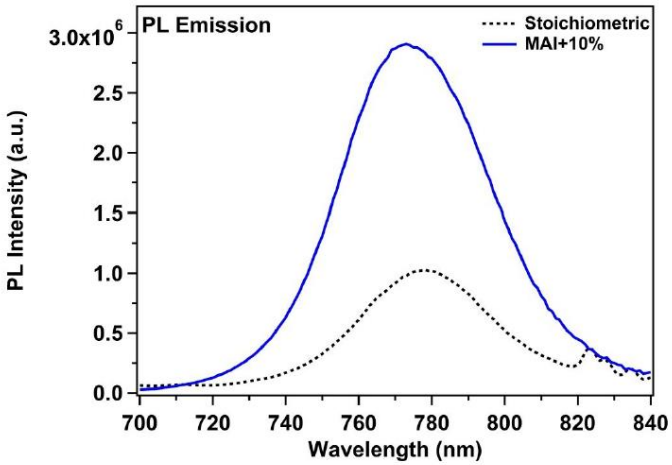

Figure S5 Steady-state PL spectra of the stoichiometric and MAI+10% MAPI films deposited on glass slides.

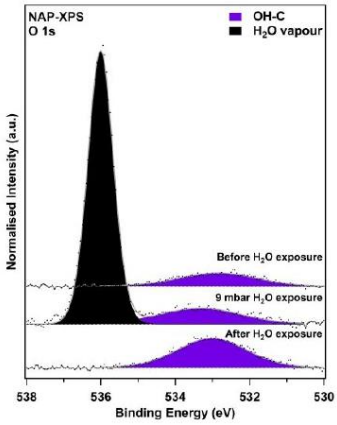

Figure S6 O 1s NAP-XPS spectra of a fresh MAI+10% AACVD-grown film before, during, and after exposure to 9 mbar H_2O vapour (equivalent to RH 30%). All spectra are normalised to the total Pb $4f_{7/2}$ area (in Figure 6A) for comparison. During exposure, an intense water-vapour peak appears at a BE of *ca.* 536 eV.[1-3]

References

(1) Jackman, M. J.; Thomas, A. G.; Muryn, C., Photoelectron spectroscopy study of stoichiometric and reduced anatase TiO2 (101) surfaces: the effect of subsurface defects on water adsorption at near-ambient pressures. *The Journal of Physical Chemistry C* **2015,** *119*, 13682-13690.

(2) Ke, J. C.-R.; Walton, A. S.; Lewis, D. J.; Tedstone, A.; O'Brien, P.; Thomas, A. G.; Flavell, W. R., In situ investigation of degradation at organometal halide perovskite surfaces by X-ray photoelectron spectroscopy at realistic water vapour pressure. *Chemical Communications* **2017,** *53*, 5231-5234.

(3) Ke, J. C.-R.; Lewis, D. J.; Walton, A. S.; Spencer, B. F.; O'Brien, P.; Thomas, A. G.; Flavell, W. R., Ambient-Air-Stable Inorganic Cs2SnI6 Double Perovskite Thin Films via Aerosol-Assisted Chemical Vapour Deposition. *Journal of Materials Chemistry A* **2018,** *6*, 11205-11214.

Chapter 6 Degradation at Halide Perovskite Surfaces Passivated by Ammonium Iodides

6.1 Introduction

This chapter contains a paper resulting from an external collaboration initiated by the author. The collaborator (Dr Jacob Tse-Wei Wang (CSIRO Energy)) provided high-quality methylammonium lead iodide (MAPI) films for near-ambient pressure X-ray photoelectron spectroscopy (NAP-XPS) measurements. It is well known that MAPI is unstable in a moist environment (see Chapter 4). However, *via* surface functionalisation strategies, the degradation of MAPI films in a humid environment may be alleviated. In this chapter, the use of two kinds of bulky ammonium iodides to passivate the surface of MAPI is explored. This was achieved by thermal evaporation in a vacuum. Subsequently, the samples were transferred to an XPS chamber for NAP-XPS measurements without exposure to ambient air. The films were then exposed to 9 mbar water vapour during acquisition of XPS spectra. The degradation process and the surface passivation effect of the ammonium iodides are investigated and are presented in the following draft paper (Paper 3).

Contributions

The high-quality MAPI films were fabricated by Dr Jacob Tse-Wei Wang (CSIRO Energy). The *in situ* surface functionalisation (using ammonium iodides), the NAP-XPS experiment, and the other characterisations, such as SEM were performed by the author. Dr Alex Walton supported the NAP-XPS measurements and (nitrogen bag) sample transfer. The author planned the experiment, analysed the data obtained and wrote the paper with Prof Wendy Flavell and Dr Andrew Thomas, with suggestions from the co-authors.

6.2 Paper 3

6.2.1 Main Text

Investigation of degradation at halide perovskite surfaces passivated by ammonium iodides using *in situ* X-ray photoelectron spectroscopy in a humid environment†

Jack Chun-Ren Ke,[abcf] Jacob Tse-Wei Wang,[d] Alex S. Walton,[bce] Andrew G. Thomas,*[bcf] and Wendy R. Flavell*[abc]

a. Department of Physics and Astronomy, The University of Manchester, Oxford Road, Manchester, M13 9PL, United Kingdom

b. Photon Science Institute, The University of Manchester, Oxford Road, Manchester, M13 9PL, United Kingdom

c. Henry Royce Institute, The University of Manchester, Oxford Road, Manchester, M13 9PL, United Kingdom

d. CSIRO Energy, Mayfield West, NSW, 2304, Australia

e. Department of Chemistry, The University of Manchester, Oxford Road, Manchester, M13 9PL, United Kingdom

f. Department of Materials, The University of Manchester, Oxford Road, Manchester, M13 9PL, United Kingdom

Corresponding authors (emails)

Prof W.R. Flavell: wendy.flavell@manchester.ac.uk

Dr A.G. Thomas: andrew.g.thomas@manchester.ac.uk

Abstract

Near-ambient pressure X-ray photoelectron spectroscopy is used to enable investigation of the degradation process of surface-functionalised methylammonium lead iodide (MAPI) at a realistic water vapour pressure (equivalent to relative humidity of 30%). We show that, through surface passivation by bulky ammonium iodides, *i.e.* tetraethylammonium iodide (TEAI) and tetramethylammonium iodide (TMAI), the stability of the MAPI surfaces can be significantly enhanced. Metallic lead defects at the MAPI surfaces are healed by the ammonium iodides, giving rise to better stability against moisture. Following the deposition of these ammonium iodides, the pristine under-stoichiometric MAPI surfaces (with I/Pb and N/Pb less than 3 and 1 respectively) become nominally stoichiometric, indicating reduction in iodine and nitrogen deficiencies/vacancies. The degradation mechanism in all cases proceeds *via* the loss of equal amounts of nitrogen and iodine, assumed to be in the form of hydrogen iodide and ammonia gases. This suggests that the surface functionalisation does not change the moisture-induced degradation process of MAPI but significantly reduces the rate of decomposition.

Introduction

Metal halide perovskites have attracted immense attention as photovoltaics due to their outstanding physical properties, which include strong solar absorption and low non-radiative carrier recombination rates.[1] These advantages have enabled the power conversion efficiencies (PCEs) of perovskite solar cells (PSCs) to reach above 24%, which is an unprecedented improvement on the initial PCE of *ca.* 4% that was recorded in 2009.[2] Such progress in PCEs makes PSCs one of the most promising photovoltaic technologies to substitute for, or to employ in tandem with, silicon-based solar cells.[3] However, one major concern is that typical halide perovskite materials are unstable in a humid environment, limiting their practical uses.[4] Therefore, many approaches have been proposed to enhance the stability of halide perovskites against moisture, including the use of novel perovskite materials, such as two-dimensional (2D) perovskites[5, 6] as well as double perovskites[7, 8].

Generally, 2D and double perovskites can offer better stability in humid air; however, their typical increased energy bandgaps (E_g) give rise to relatively low electricity output.[5, 9] Hence, until now, perovskite layers that constitute high-efficiency devices have mainly been based on conventional 3D structures, such as the often investigated methylammonium lead iodide (MAPI).[10] MAPI is a prototypical halide perovskite that has been intensively investigated in the past few years, and yields PSC devices with PCEs over 20% .[11]

Pure MAPI films show poor stability against moisture.[12, 13] Approaches to improving the stability of MAPI against moisture have been developed.[14-17] For example, the use of $Pb(SCN)_2$ precursor can not only enable ambient air processing but also enhance the stability of MAPI in humid air.[14, 18] In addition, the selection of acetate-based antisolvents for use in the spin-coating process can reduce the moisture-induced degradation of MAPI during

preparation.[15, 16, 18] The incorporation of a small amount of 2D perovskites into a 3D perovskite can also improve the stability of PSCs.[17] Nonetheless, these methods, in general, do not achieve high PCEs probably because the bulk properties of MAPI are influenced by these processing methods. Therefore, seeking a facile way to improve the water resistance of halide perovskite materials and simultaneously maintain satisfactory PCEs is of paramount importance.

Surface functionalisation has been identified as one of the best approaches to achieving better water resistance, since this step generally only modifies the surface properties rather than the bulk characteristics.[19-22] In this way, the PCEs of PSCs may be maintained at similar levels to those containing unmodified perovskite films. One example is functionalisation of the surface of MAPI films through large substituted ammonium iodide groups.[19-21] Amongst these groups, the tetraethylammonium cation (TEA) and the tetramethylammonium cation (TMA) have been demonstrated to effectively modify the surface of MAPI films, offering better water resistance.[21] Yang *et al*. proposed the improved hydrophobicity of the modified MAPI films is ascribed to the steric hindrance between water molecules and active adsorption sites, *i.e*. lead atoms at the surface.[21] Using density functional theory (DFT) calculations, it was found that the Pb—I angle of a TEA-terminated surface is different to the original MA-terminated structure, preventing water from reacting with active Pb sites. Nevertheless, how these bulky ammonium iodides replace MA to chemically adsorb on the surface is not known. The effect of the surface iodides on subsequent water adsorption has also not been investigated at the molecular level. Hence, the use of surface techniques to investigate the surface passivation of perovskite materials is of great interest as it can complement the results of theoretical calculations and device performance measurements.[21]

In this work, we employ X-ray photoelectron spectroscopy (XPS) to investigate the surface of tetraethylammonium iodide (TEAI)- and tetramethylammonium iodide (TMAI) -modified MAPI films in order to gain a better understanding of the reason for their improved stability against moisture. The disappearance of metallic lead in the XPS spectra after depositing these bulky molecules shows that these molecules may passivate defects. The deposition of the ammonium iodides was performed in a vacuum, thereby removing other factors that originate from the *ex situ* post-treatment, which could otherwise influence the interpretation of the results obtained. We also study the degradation of the surface-modified MAPI films on exposure to 9 mbar water vapour (corresponding to an environment with a relative humidity (RH) of *ca.* 30%) through the use of near-ambient pressure XPS (NAP-XPS). Through the observation of the resulting compositional changes, we can correlate the results of this experiment with the degradation of the PCEs of PSCs in a humid environment.[21] The work gives insights into the surface functionalisation necessary for enhanced stability of halide perovskites against moisture, and paves the way towards more reliable PSC devices.

Experimental Section

Preparation of MAPI films

All MAPI films were directly deposited on a fluorine-doped tin oxide (FTO) glass (7 ohm/square cm, Pilkington, TEC7) to ensure sufficient electrical conductivity for subsequent XPS measurements. The FTO substrates were cleaned in an ultrasonic bath with diluted Hellmanex (2 vol% in deionised water), acetone, and propan-2-ol in succession as the bath solution for 15 minutes each. The substrates were dried using flowing nitrogen, and the clean substrates were then treated with O_2 plasma for 10 minutes, and then

transferred to a nitrogen-filled glovebox prior to perovskite deposition.

The perovskite solution was also prepared in a nitrogen-filled glovebox by mixing methylammonium iodide (MAI, Dyesol) and lead iodide (TCI Chemicals) at a stoichiometric 1:1 molar ratio in a 4:1 (volume-to-volume) solvent mixture of *N*,*N*-dimethylformamide (DMF) and dimethyl sulfoxide (DMSO), respectively, with a final concentration of *ca.* 45 wt%. Then, the perovskite precursor solution was spun onto the treated FTO substrates *via* a two-step programme in a nitrogen-filled glovebox: 10 seconds at 1000 rpm for the first step and subsequently 6000 rpm for 20 seconds. During the second step, 300 μl of chlorobenzene was dripped onto the substrate five seconds before the end of the programme. Following the spin coating, the films were transferred to a hot plate immediately and heated at 100 ^{o}C for 10 minutes. The resulting MAPI films were a dark-brown colour with metallic lustre.

Storage and transfer of the MAPI films

The MAPI films obtained were stored in a nitrogen-filled plastic box with Al-foil cover to prevent illumination and then vacuum-sealed for shipping from Australia to the UK. Following arrival at Manchester, the bag containing the samples was immediately stored in a nitrogen-filled glovebox prior to further procedures. Just before the samples were transferred into the XPS system, the samples were mounted on Ta sample plates in the glovebox. Two Ta strips were attached on the surface of the perovskite films to enhance electrical conductivity in order to prevent possible sample charging during acquisition of spectra. The sample plate was then transferred to an Ar-filled glovebag connected to the entrance of the XPS apparatus, *via* a vacuum desiccator that was then put into the glovebag. As a result, the MAPI films were not exposed to ambient air before XPS characterisation.

Ammonium iodide deposition

Surface modification of the MAPI films by iodide adsorption was performed *in situ via* a thermal evaporator integrated to the NAP-XPS system. TEAI or TMAI (purchased from Sigma-Aldrich) was put into a Knudsen evaporator, with a thermocouple attached to measure the evaporation temperatures. Both ammonium iodides were evaporated at a temperature of 200 ^{o}C for 10 minutes in *vacuo* at a base pressure of approximately 1 x 10^{-6} mbar, directly onto the MAPI surfaces. The distance between the sample surface and the source was roughly 2 cm. The samples did not undergo further vacuum annealing procedures and were directly transferred to the analysis chamber for XPS measurements.

NAP-XPS measurements

The NAP-XPS apparatus used in this research is equipped with a SPECS Focus 500 monochromated Al Kα source with photon energy of 1486.6 eV. The analyser of the NAP-XPS kit is a SPECS 150 mm Phoibos 150 NAP, with three-stage, differentially pumped electrostatic lens. XPS measurements can be performed under conventional ultrahigh vacuum conditions in a UHV chamber or in a near-ambient pressure (NAP) cell that couples to the entrance cone of the analyser lens system. For the NAP-XPS measurements, the NAP cell was backfilled with H_2O vapour to reach a stabilised pressure of *ca.* 9 mbar, which corresponds to relative humidity (RH) of *ca.* 30%, under a standard atmospheric temperature of 25 ^{o}C.

XPS data processing and analysis

The binding energy (BE) was calibrated to the C 1s peak at 285.3 eV, which arises from hydrocarbon species on the MAPI surfaces.[18, 23-25] This BE alignment gives a metallic lead Pb $4f_{7/2}$ peak located at a BE of 137.0 eV recorded from the fresh MAPI films, in good

agreement with the value measured by the identical equipment previously.[23] BE values are quoted to an accuracy of ±0.1 eV, and thus a BE shift of 0.2 eV can be clearly observed. A Shirley background was subtracted from the data presented in this paper.[26] A GL(30) function (70% Gaussian and 30% Lorentzian) was applied to fit the core-level spectra using CasaXPS software.[27] The built-in CasaXPS sensitivity factors (Kratos) are only used for calculating the stoichiometry of the sample before and after water exposure from UHV measurements, since the sensitivity factors for NAP conditions are not currently available.

Results and Discussion

The morphology of the pristine spin-coated MAPI films without surface modification was examined using scanning electron microscopy (SEM), as shown in Figure S1 (see Electronic Supplementary Information, ESI†). The SEM sample was exposed to ambient air for one minute, which is not expected to produce significant impact on the morphology. As described above, the rest of the MAPI films used in surface functionalisation and/or XPS measurements were not exposed to ambient air at any point in the preparation and transfer processes, in order to minimise surface degradation of the films prior to XPS characterisation. In addition, before XPS measurements were performed, the containers of all the films were masked with Al foil to prevent photodegradation.[28] Surface functionalisation of the films with ammonium iodides was carried out *in situ*. The films were transferred under UHV to a preparation chamber with a base pressure of approximately 1×10^{-6} mbar, and an evaporation source containing TEAI or TMAI was then heated to 200 ^{o}C for 10 minutes, resulting in deposition of the ammonium iodides. At evaporation temperatures of 200 ^{o}C for both samples, significant changes in the I 3d and N 1s XPS spectra were observed. Deposition temperatures > 200 ^{o}C and longer evaporation times led

to the underlying signals from MAPI being obscured. The thickness of the iodide layer was estimated as described in the ESI†.

Figure 1 shows the XPS core-level spectra of the primary elements (Pb, I, and N) recorded from the MAPI films before (without) and after (with) the deposition of TEAI (A~C) and TMAI (D~F) molecules using a source temperature of 200 ^{o}C for 10 minutes in vacuum. The Pb 4f XPS spectra in Figures 1A&D show that the films modified by both TEAI and TMAI exhibit a reduction in the concentration of metallic lead (Pb^0) relative to Pb^{2+} in MAPI following the deposition of the ammonium iodides, particularly in the case of TEAI. Metallic lead is often found in MAPI films fabricated either by solution-based methods,[29-31] or by vapour deposition processes.[23, 32] The formation of Pb^0 can be attributed to the loss of iodine, and therefore it is usually accompanied by iodine deficiencies in MAPI films.[23, 30, 31] This phenomenon (that is, a reduction in the amount of surface Pb^0) has also be found in other cases of ammonium ion treatment, such as after treatment of MAPI surfaces with diethylenetriamine[33] and the use of more/excess MAI to complete MAPI formation[18, 32]. A decrease in the amount of metallic lead has been shown to reduce the number of non-radiative recombination centres and therefore is expected to improve the PCEs of PSCs.[34] This observation also suggests that TEAI and TMAI react chemically with the surface of the MAPI films rather than physically adsorbing on the surfaces. The better healing ability of TEAI compared to that of TMAI may be due to the relatively bulky structure of TEAI molecules. The longer hydrocarbon chains of TEAI result in weaker ionic bonds between N^+ and I^-, and therefore the I^- in TEAI is relatively easily donated to react with metallic lead at the MAPI surfaces compared to TMAI.[35, 36]

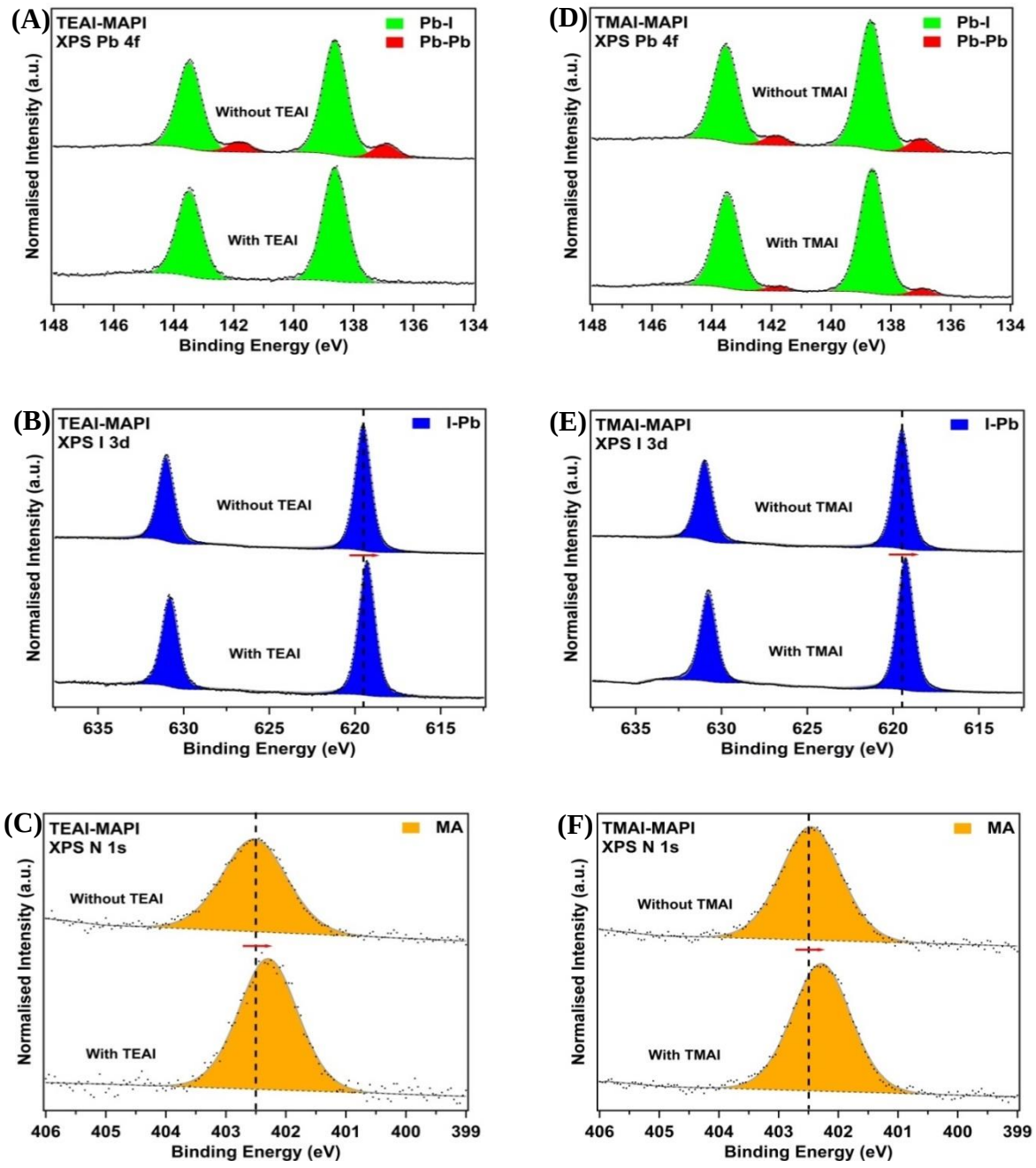

Figure 1 XPS spectra of (A)&(D) Pb 4f, (B)&(E) I 3d, and (C)&(F) N 1s core levels recorded from the MAPI films before and after (A~C) TEAI or (D~F) TMAI molecules were deposited in a vacuum. All the spectra are normalised to the total Pb $4f_{7/2}$ peak area for comparison.

As observed in the Pb 4f XPS spectra (Figures 1A&D), the binding energy (BE) of the (Pb $4f_{7/2}$) MAPI components for all films before and after surface functionalisation by ammonium iodides is 138.6 ± 0.1 eV. This is in agreement with the common values shown in the literature for MAPI surfaces.[23, 37] However, it is interesting that, following the deposition of the ammonium iodides, for both iodides the BEs of I 3d and N1s shift to low BE by approximately 0.2 and 0.1 eV for TEAI-MAPI and TMAI-MAPI films, as shown in Figures 1B&C and Figures 1E&F, respectively. This shift indicates the change in chemical environment and the interaction between the ammonium iodides and the pristine MAPI films. As expected, the I and N concentrations relative to Pb increase after the deposition of TEAI or TMAI, as suggested by Figure 1; the values of the I/Pb and N/Pb ratios before and after surface modification are summarised in Table 1. As shown, the pristine MAPI films are slightly sub-stoichiometric in iodine and nitrogen (MA) compared to the nominal composition. However, the surface stoichiometry is typical of that observed for fresh MAPI,[23, 31] and the BE of Pb $4f_{7/2}$ (138.6 eV ± 0.1 eV) is consistently different from the expected value for PbI_2 at *ca*. 138.9 eV, indicating that there is no significant degradation prior to the XPS measurements.[23, 37] After the surface functionalisation, both films present the nominal stoichiometry containing a substantially reduced amount of metallic lead. This is a clear indication that these ammonium iodides heal most of the defects formed, allowing the MAPI films to attain nearly perfect surfaces. We note that the attenuation of the Pb 4f signals of the Pb—I component recorded from both functionalised MAPI films is minimal following the deposition, so we believe that only a very thin layer of the ammonium iodides chemisorbs on the surface of the perovskite films. Using the process given in the ESI†, we estimate this thickness to be 0.6 ± 0.2 nm, corresponding to a monolayer.

Table 1 Stoichiometries of the MAPI films determined by XPS at different stages, both before and after depositing ammonium iodide molecules. The metallic lead content is excluded from the quantifications of I/Pb and N/Pb (*i.e.* only Pb^{2+} is considered).

Sample ID	**I/Pb**	**N/Pb**	**Pb^0/Pb^{2+}**
Stoichiometric MAPI	3.0 ± 0.1	1.0 ± 0.1	-
MAPI (1)	2.8 ± 0.1	0.8 ± 0.1	12±2%
TEAI-MAPI	3.0 ± 0.1	1.0 ± 0.1	0±2%
MAPI (2)	2.8 ± 0.1	0.8 ± 0.1	10±2%
TMAI-MAPI	3.0 ± 0.1	1.0 ± 0.1	4±2%

Following XPS of the pristine MAPI films with and without modification, the samples were transferred under ultrahigh vacuum (UHV) to the NAP chamber and exposed to 9 mbar water vapour (equivalent to relative humidity of 30% at 25 ^oC) to determine the stability of the films in water. The resulting spectra are shown in Figure 2 for pristine MAPI, TEAI-MAPI, and TMAI-MAPI films, respectively.

As shown in Figure 2A for MAPI, following water exposure, the BE of the primary Pb $4f_{7/2}$ component (Pb^{2+} in MAPI) shifts *ca.* 0.3 eV towards higher BE, to 138.9 ± 0.1 eV. This indicates the formation of lead iodide, consistent with previous work, where it has been demonstrated to form predominantly at the film surface after water exposure.[23, 37] Interestingly, after the film was exposed to water vapour, the amount of metallic lead decreased to a negligible level. The result is significantly different from an ultrathin MAPI film in which the amount of metallic lead increases under the identical exposure condition.[23]

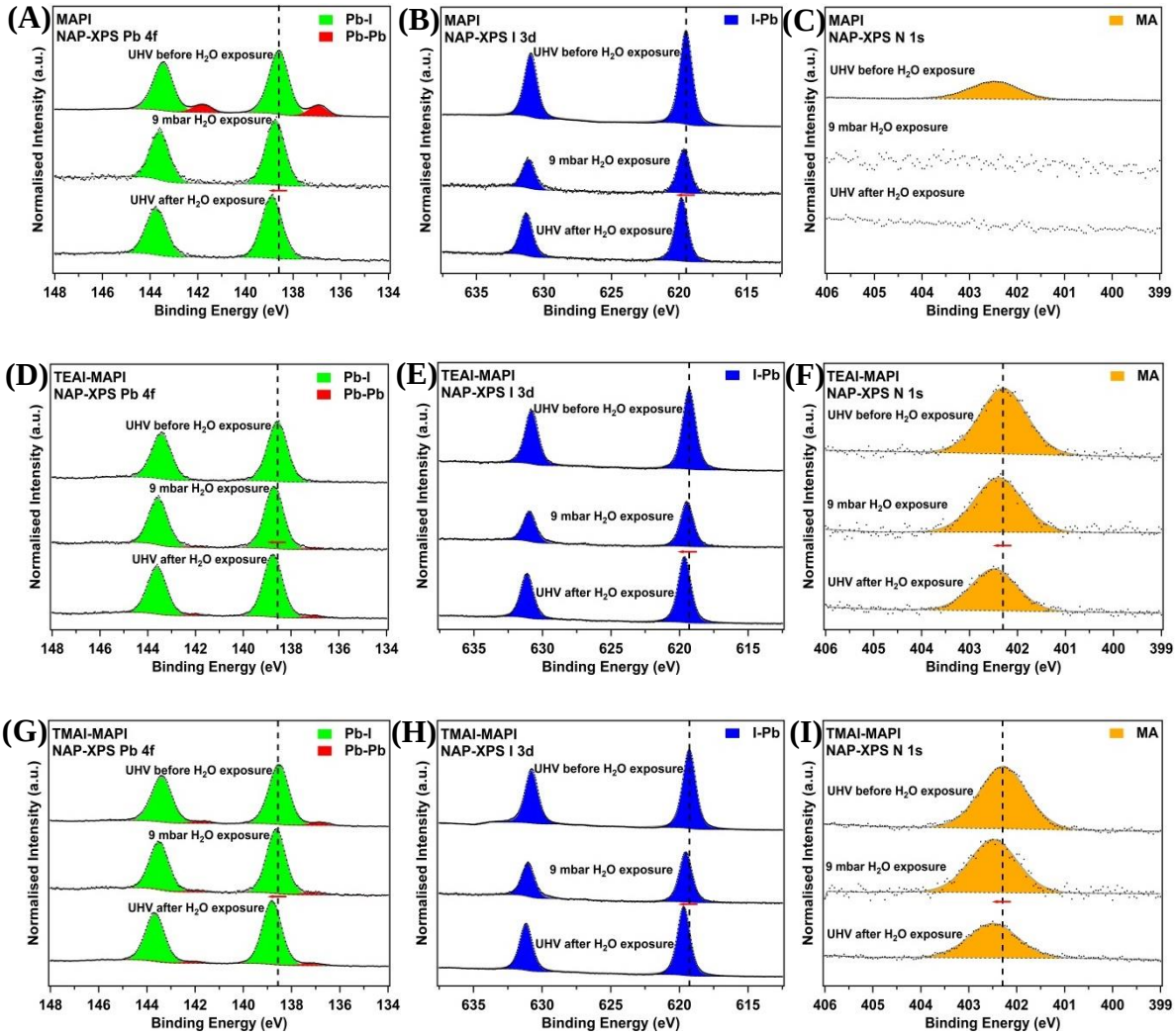

Figure 2 NAP-XPS spectra of (A, D, G) Pb 4f, (B, E, H) I 3d, and (C, F, I) N 1s core levels recorded from the pristine MAPI (A~C), TEAI-MAPI (D~F), and TMAI-MAPI (G~I) films before, during, and after 9 mbar water vapour exposure. All the spectra are normalised to the total Pb $4f_{7/2}$ peak area for comparison.

Figure 2B shows the change in the I 3d XPS spectra induced by water vapour for the pristine MAPI film. It is quite obvious that, following exposure, the iodine concentration compared to lead decreases, and the I $3d_{5/2,3/2}$ doublet also shifts 0.3 eV towards higher BE, suggesting the formation of lead iodide.[23, 37] It can be seen that the intensity of the I 3d peaks (relative to Pb 4f) recorded during water vapour exposure is lower than that recorded in UHV after exposure. This is due to the fact that in a high-pressure environment the attenuation of photoelectrons is much stronger than in UHV, and is stronger for lower the kinetic energy electrons. Thus, in order to quantify the surface composition after exposure, a further spectrum must be obtained in UHV, as shown in Figure 2. The stoichiometries of all films obtained in UHV before and after water exposure are summarised in Table 2. The I/Pb ratio of the pristine MAPI films decreases from 2.8 to 2.0 following 9 mbar water vapour exposure. The residual amount of iodine relative to lead is in good agreement with the stoichiometry of PbI_2, indicating that the MAPI surface is completely converted into PbI_2 on reaction with water vapour. The N 1s spectra in Figure 2C show complete loss of the nitrogen moiety from the surface of the MAPI film after water vapour exposure. This is consistent with the finding for an *in situ* vapour-deposited MAPI film under the identical exposure condition.[34] This suggests that the unmodified MAPI films are vulnerable to moisture regardless of the preparation method.

Turning now to the ammonium-iodide modified films, Figure 2D shows the Pb 4f core-level XPS spectra of the TEAI-MAPI films before, during, and after 9 mbar water vapour exposure. The BE of the Pb $4f_{7/2}$ peak shifts 0.1 eV to *ca.* 138.7 eV. The intensity of the I 3d XPS spectra (Figure 2E) is now only slightly reduced following water exposure. The I/Pb ratios of the TEAI-MAPI films after exposure to water vapour decrease from 3.0 to 2.7 (Table 2), similar to the value (2.8) of the pristine MAPI film, indicating (nearly) no

occurrence of degradation. In addition, the BE of the I $3d_{5/2}$ peak recorded from the TEAI-MAPI film shifts to *ca.* 619.5 eV, identical to that of the pristine MAPI film. These outcomes suggest that the TEAI "capping" layer reacts with water vapour and protects the underlying MAPI surface from moisture-induced degradation.

Table 2 Stoichiometries of MAPI, TEAI-MAPI, and TMAI-MAPI films determined by XPS at different stages, both before and after 9 mbar water vapour exposure. The metallic lead content is excluded from the quantifications of I/Pb and N/Pb (*i.e.* only Pb^{2+} is considered).

Status ID	I/Pb	N/Pb	Pb^0/Pb^{2+}
MAPI before water exposure	2.8 ± 0.1	0.8 ± 0.1	14%±2%
MAPI after water exposure	2.0 ± 0.1	0.0 ± 0.1	0±2%
TEAI-MAPI before water exposure	3.0 ± 0.1	1.0 ± 0.1	0±2%
TEAI-MAPI after water exposure	2.7 ± 0.1	0.7 ± 0.1	4±2%
TMAI-MAPI before water exposure	3.0 ± 0.1	1.0 ± 0.1	4±2%
TMAI-MAPI after water exposure	2.4 ± 0.1	0.4 ± 0.1	4±2%

Figure 2F reveals the effect of water exposure on the N 1s XPS spectrum of the TEAI-MAPI film. The nitrogen concentration is slightly reduced, in sharp contrast with the 'uncapped' MAPI film where the complete loss of nitrogen is observed (Figure 2C), following exposure. As shown in Table 2, the N:Pb ratio is reduced from 1.0 to 0.7. It is noted that the BE of the N 1s peak also shifts back to *ca.* 402.5 eV, which can be assigned to the MA cation of MAPI.[18, 23] The synchronous loss of similar amounts of iodine and nitrogen (*i.e.* I/Pb and N/Pb both reduced by 0.3) also suggests that the MAPI degradation mechanism involves the escape of equal amounts of ammonia and hydrogen iodide on exposure to water vapour.[23, 38]

The other ammonium iodide, TMAI, has been reported to have less effect in improving device stability in humid air compared to TEAI.[225] It is therefore of interest to compare the surface stability on exposure to water with those of TEAI-MAPI and MAPI. The Pb 4f XPS spectra of the TMAI-MAPI film shown in Figure 2G reveal a BE shift following water exposure of 0.2 eV. This shift lies between those observed for the pristine MAPI and TEAI-MAPI films and there is no change in the amount of metallic lead with respect to MAPI. The I/Pb ratio is 2.4 following exposure, as shown in Table , also lying between the values observed for the other two films. The I 3d spectrum in Figure 2H upon exposure to water shows a BE shift to *ca.* 619.7 eV, *i.e.* a shift of 0.3 or 0.2 eV relative to the MAPI films with (*ca.* 619.4 eV) and without (*ca.* 619.5 eV) the TMAI surface functionalisation, suggesting the partial formation of lead iodide and the escape of TMAI molecules due to moisture. We can see the nitrogen concentration compared to lead decreases after water vapour exposure as shown in Figure 2I, again by an amount intermediate between those observed in MAPI and TEAI-MAPI. The N/Pb ratio following exposure is *ca.* 0.4, indicating that some of the MAPI surface degrades into lead iodide as a result of water

vapour exposure. Again, taking TMAI into consideration, extra nitrogen (adding ~0.2 to the N/Pb ratio) is contributed from TMAI (Table 1) and thereby the N/Pb from the original MAPI surface decreases from 0.8 to 0.4 following the exposure. This suggests around half of the MAPI surface is converted into PbI_2 by water vapour. Furthermore, similar drops in the I/Pb and N/Pb ratios on water exposure (both by *ca.* 0.6) demonstrate again that the degradation process is consistent with the equation proposed in previous research, expressed below (Equation 1):[23, 38]

$$CH_3NH_3PbI_3\ (s) \xrightarrow{H_2O} (-CH_2-)\ (s) + NH_3\ (g) + HI\ (g) + PbI_2\ (s) \qquad \text{Equation 1}$$

Overall, the surface compositions of the three MAPI films without surface modification (Table 1 & Table 2) show high consistency and have close- to-ideal stoichiometry, suggesting high reproducibility and high quality, respectively. In comparison with ammonium-iodide-treated samples, the pristine MAPI films have the highest concentration of metallic lead, and iodine and nitrogen vacancies at the surface, giving rise to the worst surface stability, determined by NAP-XPS. This suggests that those defects play important roles in the water-induced degradation processes, in which the iodine vacancies can easily interact with oxygen ions.[39] Following the exposure, the TEAI-MAPI film has fewer iodine and nitrogen vacancies compared to the TEAI-MAPI sample, in good agreement with the device stability reported.[21] Furthermore, we found that for all the films after H_2O vapour exposure, the reduction in I/Pb and N/Pb occurs in similar amounts, consistent with our previous finding that upon exposure to water vapour, MAPI films lose hydrogen iodide and ammonia gases simultaneously.[18, 23]

Conclusions

In conclusion, we have demonstrated an *in situ* method to investigate the effect of surface passivation on perovskite films using NAP-XPS. The ammonium-iodide adsorption improves the surface stability of MAPI against moisture. TEAI is more effective in enhancing the water resistance of the MAPI surfaces compared to TMAI, consistent with the device stability in humid air.[21] We have also observed that ammonium iodide passivation can heal the surface defects in the MAPI films, such as metallic lead, and iodine and nitrogen deficiencies. The reduction of elemental lead also suggests the occurrence of chemical interaction between the ammonium iodides and the perovskite rather than physisorption. These results complement theoretical calculations and measured device performances.[21] We believe that by using newly developed surface science techniques (such as NAP-XPS in this work), a better understanding of the degradation mechanisms of halide perovskite materials can be uncovered.[8, 23] By this approach, passivation strategies can be developed, contributing to opportunities to commercialise PSCs.

Acknowledgments

The authors thank the University of Manchester and EPSRC (UK) (grant EP/K009710) for funding. Chun-Ren Ke thanks the University of Manchester for the award of a President's Doctoral Scholarship.

References

1. M. A. Green, A. Ho-Baillie and H. J. Snaith, *Nature Photonics*, 2014, *8*, 506-514.
2. A. Kojima, K. Teshima, Y. Shirai and T. Miyasaka, *Journal of the American Chemical Society*, 2009, **131**, 6050-6051.
3. D. P. McMeekin, G. Sadoughi, W. Rehman, G. E. Eperon, M. Saliba, M. T. Hörantner, A. Haghighirad, N. Sakai, L. Korte and B. Rech, *Science*, 2016, **351**, 151-155.
4. T. A. Berhe, W.-N. Su, C.-H. Chen, C.-J. Pan, J.-H. Cheng, H.-M. Chen, M.-C. Tsai, L.-Y. Chen, A. A. Dubale and B.-J. Hwang, *Energy & Environmental Science*, 2016, **9**, 323-356.
5. H. Tsai, W. Nie, J.-C. Blancon, C. C. Stoumpos, R. Asadpour, B. Harutyunyan, A. J. Neukirch, R. Verduzco, J. J. Crochet, S. Tretiak, M. G. Kanatzidis and A. D. Mohite, *Nature*, 2016, **536**, 312-316.
6. J.-W. Lee, Z. Dai, T.-H. Han, C. Choi, S.-Y. Chang, S.-J. Lee, N. De Marco, H. Zhao, P. Sun and Y. Huang, *Nature communications*, 2018, **9**, 3021.
7. B. Lee, A. Krenselewski, S. I. Baik, D. Seidman and R. P. Chang, *Sustainable Energy & Fuels*, 2017, **1**, 710-724.
8. J. C.-R. Ke, D. J. Lewis, A. S. Walton, B. F. Spencer, P. O'Brien, A. G. Thomas and W. R. Flavell, *Journal of Materials Chemistry A*, 2018, **6**, 11205-11214.
9. F. Igbari, R. Wang, Z.-K. Wang, X.-J. Ma, Q. Wang, K.-L. Wang, Y. Zhang, L.-S. Liao and Y. Yang, *Nano letters*, 2019, **19**, 2066-2073.
10. J.-H. Im, I.-H. Jang, N. Pellet, M. Grätzel and N.-G. Park, *Nature nanotechnology*, 2014, **9**, 927-932.
11. M. Jung, T. J. Shin, J. Seo, G. Kim and S. I. Seok, *Energy & Environmental Science*, 2018, **11**, 2188-2197.
12. B. Hailegnaw, S. Kirmayer, E. Edri, G. Hodes and D. Cahen, *The journal of physical chemistry letters*, 2015, **6**, 1543-1547.
13. J. Yang, B. D. Siempelkamp, D. Liu and T. L. Kelly, ACS Nano, 2015, 9, 1955-1963.
14. Q. Tai, P. You, H. Sang, Z. Liu, C. Hu, H. L. Chan and F. Yan, *Nature communications*, 2016, **7**, 11105.
15. F. Yang, G. Kapil, P. Zhang, Z. Hu, M. A. Kamarudin, T. Ma and S. Hayase, *ACS Applied Materials & Interfaces*, 2018, **10**, 16482-16489.
16. Q. Chen, M. Z. Mokhtar, J. C.-R. Ke, A. G. Thomas, A. Hadi, E. Whittaker, M. Curioni and Z. Liu, *Sustainable Energy & Fuels*, 2018, **2**, 1216-1224.
17. G. Grancini, C. Roldán-Carmona, I. Zimmermann, E. Mosconi, X. Lee, D. Martineau, S. Narbey, F. Oswald, F. De Angelis and M. Graetzel, *Nature Communications*, 2017, **8**,

15684.
18. C.-R. Ke, D. J. Lewis, A. S. Walton, Q. Chen, B. F. Spencer, M. Mokhtar, C. L. Compean-Gonzalez, P. O'Brien, A. G. Thomas and W. R. Flavell, *ACS Applied Energy Materials*, 2019, **2**, 6012-6022.
19. F. Palazon, D. Pérez-del-Rey, S. Marras, M. Prato, M. Sessolo, H. J. Bolink and L. Manna, *ACS Energy Letters*, 2018, **3**, 835-839.
20. Z. Wu, S. R. Raga, E. J. Juarez-Perez, X. Yao, Y. Jiang, L. K. Ono, Z. Ning, H. Tian and Y. Qi, *Advanced Materials*, 2018, **30**, 1703670.
21. S. Yang, Y. Wang, P. Liu, Y.-B. Cheng, H. J. Zhao and H. G. Yang, *Nature Energy*, 2016, **1**, 15016.
22. S. Bai, P. Da, C. Li, Z. Wang, Z. Yuan, F. Fu, M. Kawecki, X. Liu, N. Sakai and J. T.-W. Wang, *Nature*, 2019, **571**, 245.
23. J. C.-R. Ke, A. S. Walton, D. J. Lewis, A. Tedstone, P. O'Brien, A. G. Thomas and W. R. Flavell, *Chemical Communications*, 2017, **53**, 5231-5234.
24. W. Huang, J. S. Manser, P. V. Kamat and S. Ptasinska, *Chemistry of Materials*, 2015, **28**, 303-311.
25. L. Liu, J. A. McLeod, R. Wang, P. Shen and S. Duhm, *Applied Physics Letters*, 2015, **107**, 061904.
26. D. A. Shirley, *Physical Review B*, 1972, **5**, 4709.
27. N. Fairley, *CasaXPS manual 2.3. 15*, Acolyte Science, 2009.
28. Q. Sun, P. Fassl, D. Becker-Koch, A. Bausch, B. Rivkin, S. Bai, P. E. Hopkinson, H. J. Snaith and Y. Vaynzof, *Advanced Energy Materials*, 2017, **7**, 1700977.
29. R. Lindblad, N. K. Jena, B. Philippe, J. Oscarsson, D. Bi, A. Lindblad, S. Mandal, B. Pal, D. D. Sarma and O. Karis, *The Journal of Physical Chemistry C*, 2015, **119**, 1818-1825.
30. W. Zhang, S. Pathak, N. Sakai, T. Stergiopoulos, P. K. Nayak, N. K. Noel, A. A. Haghighirad, V. M. Burlakov, A. Sadhanala and W. Li, *Nature communications*, 2015, **6**, 10030.
31. R. Lindblad, D. Bi, B.-w. Park, J. Oscarsson, M. Gorgoi, H. Siegbahn, M. Odelius, E. M. Johansson and H. k. Rensmo, *The Journal of Physical Chemistry Letters*, 2014, **5**, 648-653.
32. T.-W. Ng, C.-Y. Chan, M.-F. Lo, Z. Q. Guan and C.-S. Lee, *Journal of Materials Chemistry A*, 2015, **3**, 9081-9085.
33. H. Zhang, X. Ren, X. Chen, J. Mao, J. Cheng, Y. Zhao, Y. Liu, J. Milić, W. Yin and M. Grätzel, *Energy & Environmental Science*, 2018, **11**, 2253-2262.
34. D. Bi, C. Yi, J. Luo, J.-D. Décoppet, F. Zhang, S. M. Zakeeruddin, X. Li, A. Hagfeldt and M. Grätzel, *Nature Energy*, 2016, **1**, 16142.

35. D. H. Aue, H. M. Webb and M. T. Bowers, *Journal of the American Chemical Society*, 1976, **98**, 318-329.
36. A.-A. Guilbault and C. Y. Legault, *ACS Catalysis*, 2012, **2**, 219-222.
37. B. Philippe, B.-W. Park, R. Lindblad, J. Oscarsson, S. Ahmadi, E. M. Johansson and H. k. Rensmo, *Chemistry of Materials*, 2015, **27**, 1720-1731.
38. Y. Li, X. Xu, C. Wang, C. Wang, F. Xie, J. Yang and Y. Gao, *The Journal of Physical Chemistry C*, 2015, **119**, 23996-24002.
39. S. J. Park, S. Jeon, I. K. Lee, J. Zhang, H. Jeong, J.-Y. Park, J. Bang, T. K. Ahn, H.-W. Shin and B.-G. Kim, *Journal of Materials Chemistry A*, 2017, **5**, 13220-13227.

6.2.2 Supporting Information

Electronic Supplementary Information (ESI) †

Investigation of degradation at halide perovskite surfaces passivated by ammonium iodides using *in situ* X-ray photoelectron spectroscopy in a humid environment†

Jack Chun-Ren Ke,[abcf] Jacob Tse-Wei Wang,[d] Alex S. Walton,[bce] Andrew G. Thomas,*[bcf] and Wendy R. Flavell*[abc]

a. Department of Physics and Astronomy, The University of Manchester, Oxford Road, Manchester, M13 9PL, United Kingdom

b. Photon Science Institute, The University of Manchester, Oxford Road, Manchester, M13 9PL, United Kingdom

c. Henry Royce Institute, The University of Manchester, Oxford Road, Manchester, M13 9PL, United Kingdom

d. CSIRO Energy, Mayfield West, NSW, 2304, Australia

e. Department of Chemistry, The University of Manchester, Oxford Road, Manchester, M13 9PL, United Kingdom

f. Department of Materials, The University of Manchester, Oxford Road, Manchester, M13 9PL, United Kingdom

Corresponding authors (emails)

Prof W.R. Flavell: wendy.flavell@manchester.ac.uk

Dr A.G. Thomas: andrew.g.thomas@manchester.ac.uk

Scanning Electron Microscopy (SEM)

The morphology of the pristine MAPI films without surface functionalisation was examined using SEM (Zeiss Sigma) by taking secondary electron images. A typical example is shown in Figure S1.

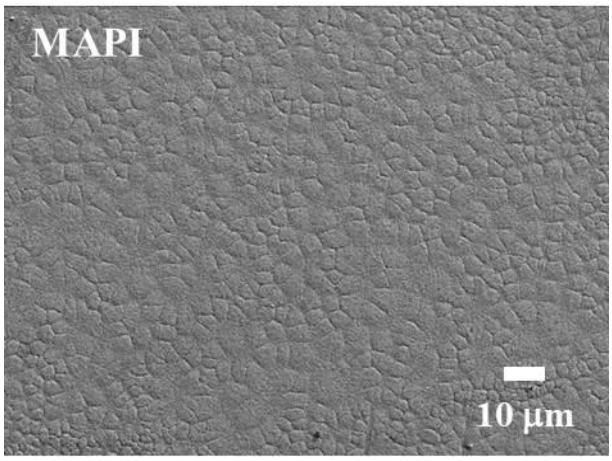

Figure S1 SEM image of a spin-coated MAPI film composed of micrometre-sized grains.

Estimation of the thickness of the deposited ammonium iodides

The estimated thicknesses of the ammonium iodides (TEAI and TMAI) can be obtained by considering the attenuation of Pb signals after deposition, since no additional lead was deposited, whilst extra nitrogen, iodine, and carbon signals are produced by TEAI or TMAI. For both cases, the Pb 4f peaks of the functionalised MAPI surfaces retained *ca.* 85% of their original peak intensity/area recorded from the pristine MAPI films at the same focus points. By using the NIST electron mean free path database,[1] we obtain estimated thicknesses of 0.6 ± 0.2 nm for TEAI and TMAI that is expected to produce *ca.* 15% attenuation in the Pb 4f

signals. A single overlayer of TEAI and TMAI molecules is expected to be *ca.* 0.6 and 0.5 nm thick, respectively.[2] As a result, it is believed that only a single layer of each ammonium iodide attaches on the outermost surface of the MAPI films following vacuum deposition.

C 1s spectra before and after ammonium iodide (TEAI or TMAI) deposition

According to Table S1, the concentrations of C—C/C—H and C—N/C—OH relative to Pb increase following ammonium iodide deposition, which can be ascribed to the iodide adsorption and to contamination. TEAI is expected to contribute new C—C/C—H and C—N/C—OH signals, with a stoichiometry with respect to Pb = 1.0 of 0.8 and 0.8, respectively, based on the increases in the I/Pb and N/Pb ratios (Table 1). TMAI molecules are expected to only give a new C—N/C—OH signal as there is no extra C—C bond in the chemical structure of TMAI. This is should have a stoichiometry of 0.8 relative to Pb=1.0. In addition, some carbon contamination is inevitable in the thermal evaporation process,[3] and a trace of COOH is often observed at the surface of materials containing carbon.[4]

Table S1 Stoichiometries of the MAPI films determined using XPS at different stages, both before and after depositing ammonium iodide molecules. These values are normalised to the Pb^{2+} concentration (*i.e.* to Pb=1.0), as in Table 1 in the main text. The corresponding C 1s spectra can be seen in Figure S2.

Sample ID	C—C/C—H	C—N/C—OH
MAPI (1)	4.0 ± 0.2	1.2 ± 0.2
TEAI-MAPI	5.2 ± 0.2	2.4 ± 0.2
MAPI (2)	2.8 ± 0.2	2.0 ± 0.2
TMAI-MAPI	3.2 ± 0.2	3.6 ± 0.2

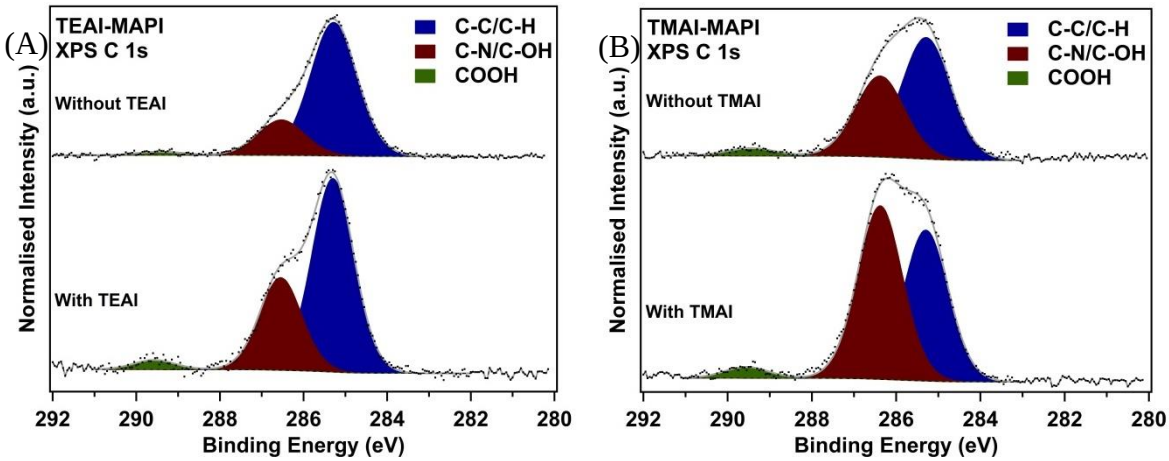

Figure S2 XPS spectra of C 1s core levels probed from the MAPI films before and after (A) TEAI or (B) TMAI deposition. All the spectra are normalised to the total Pb $4f_{7/2}$ peak area for comparison.

References

1. C. Powell and A. Jablonski, *Journal of Surface Analysis*, 2002, **9**, 322-325
2. D. H. Aue, H. M. Webb and M. T. Bowers, *Journal of the American Chemical Society*, 1976, **98**, 318-329.
3. J. C.-R. Ke, A. S. Walton, D. J. Lewis, A. Tedstone, P. O'Brien, A. G. Thomas and W. R. Flavell, *Chemical Communications*, 2017, **53**, 5231-5234.
4. E. Desimoni, G. Casella, A. Morone and A. Salvi, *Surface and Interface Analysis*, 1990, **15**, 627-634.

Chapter 7 Heat- and Moisture-Induced Degradation of Mixed-Cation Perovskite Surfaces

7.1 Introduction

This paper involves an external collaboration initiated by Dr Jacob Tse-Wei Wang (CSIRO Energy) and the author. Unlike the previous results chapters, this work focuses on mixed-cation mixed-halide perovskites since these perovskites offer better PCEs. Although photovoltaic devices containing such perovskites have also shown better operational stability, there are a limited number of studies that report the surface stability of these perovskite films. In this work, two types of commonly used mixed-cation lead perovskites ($(FA_{0.83}Cs_{0.17})Pb(I_{0.83}Br_{0.17})_3$ and $(FA_{0.83}MA_{0.17})_{0.95}Cs_{0.05}Pb(I_{0.83}Br_{0.17})_3$) are investigated using NAP-XPS. The surface stability of the films against moisture and/or thermal stress (up to 150 ^{o}C) is probed *in situ*. The degradation mechanisms are proposed based on the results obtained in this research. This chapter will be combined with other results (from CSIRO Energy) prior to publication.

Contribution

The high-quality mixed-cation lead perovskite films were fabricated by Dr Jacob Tse-Wei Wang (CSIRO Energy). The NAP-XPS experiment was conducted by the author, with the assistance of Dr Alex Walton. The SEM images were also taken by the author and more characterisation data including device performance will be provided by Dr Jacob Tse-Wei Wang (under Dr Gregory Wilson's supervision) before future publication. The author analysed the data shown in this chapter and wrote the manuscript with Dr Andrew Thomas and Prof Wendy Flavell, with suggestions from the co-authors.

7.2 Paper 4

7.2.1 Main Text

Thermal Degradation Behaviour of Mixed-Cation Perovskite Surfaces Probed by *In Situ* X-Ray Photoelectron Spectroscopy under Humid Conditions

Jack Chun-Ren Ke,[a,b,c,d], Jacob Tse-Wei Wang,[f] Alex S. Walton,[b,c,d] Gregory J. Wilson,[f] Andrew G. Thomas,[b,c,d] and Wendy R. Flavell[a,b,c]

a. Department of Physics and Astronomy, The University of Manchester, Oxford Road, Manchester M13 9PL, United Kingdom

b. Photon Science Institute, The University of Manchester, Oxford Road, Manchester M13 9PL, United Kingdom

c. Henry Royce Institute, The University of Manchester, Oxford Road, Manchester, M13 9PL, United Kingdom

d. Department of Materials, The University of Manchester, Oxford Road, Manchester M13 9PL, United Kingdom

e. Department of Chemistry, The University of Manchester, Oxford Road, Manchester M13 9PL, United Kingdom

f. CSIRO Energy, Mayfield West, NSW 2304, Australia

Abstract

The heat and water resistance of halide perovskite materials for use in perovskite solar cells (PSCs) are crucial for the future deployment of PSCs around the world. The surface stability of halide perovskites is one clear indicator for predicting the lifetime of the resultant photovoltaic devices. Here, we use X-ray photoelectron spectroscopy (XPS) to investigate the effect of heat on the dual- $((FA_{0.83}Cs_{0.17})Pb(I_{0.83}Br_{0.17})_3$ perovskite, where FA is formamidinium) and the triple-mixed-cation $((FA_{0.83}MA_{0.17})_{0.95}Cs_{0.05}Pb(I_{0.83}Br_{0.17})_3$ perovskite, where MA is methylammonium). Under ultra-high vacuum conditions we find that FA and Br are lost together from both films following heating at 100 and 150 ^{o}C. The amount of Cs is also reduced as a result of thermal stress, probably leaving from the films in the form of metallic Cs vapour in vacuum. Near-ambient pressure XPS (NAP-XPS) is also used to study the thermal degradation of the perovskite films in a more realistic environment, with the presence of water vapour (pressure of 9 mbar, equivalent to a relative humidity of 30% at room temperature). It is found that, compared to bromine, more iodine is lost at the perovskite surfaces in moist conditions. Moreover, upon exposure to water vapour, conversion of FA to MA is demonstrated, through loss of a nitrogen atom, most probably in the form of ammonia gas. We find an insulating species formed upon H_2O vapour exposure, which can be removed by heating to temperatures over 100 ^{o}C.

Introduction

The perovskite solar cell (PSC) has rapidly emerged as one of the game changing technologies in the field of photovoltaics (PVs), with a certified power conversion efficiency (PCE) over 25%.[1] Their high PCEs and relatively low production cost compared to other PV cells enables PSC devices to be extremely competitive to substitute for,[2] or be in tandem with mainstream silicon solar cells;[3] the latter have achieved PCEs as high as 28%.[1] The perovskite structure is shown in Figure 1. The perovskite light absorbers have the general formula ABX_3 (where A is organic and/or inorganic cations, B can be Pb^{2+} and/or Sn^{2+}, and X can be I^-, Br^-, and/or Cl^- anions).[4] A major advantage of these materials is that the A and X ions can be substituted, resulting in mixed cations or anions, allowing the physical properties of the absorbers to be precisely tuned *via* chemical composition engineering.[5] The most widely used cations for the A site of ABX_3 used in PSCs are Cs,[6] formamidinium ($CH(NH_2)_2^+$, FA)[7], and the prototype, methylammonium ($CH_3NH_3^+$, MA) ions[8]. It has been found that FA-based PSCs can deliver better PCEs due to the smaller optical energy bandgap of $FAPbI_3$ (*ca.* 1.48 eV) compared to $MAPbI_3$ (*ca.* 1.55 eV) and hence the higher current density.[9] However, pure $FAPbI_3$ films have intrinsic phase instability issues as a result of inherent thermodynamics; *i.e.*, it preferentially produces a non-photoactive yellow phase rather than the desired black phase at room temperature.[10] Amongst these, mixed-cation perovskites containing FA have been found to not only improve the stability of PSC devices but also to give superior electrical power output.[3, 11]

Recently, triple-mixed-cation perovskites containing FA, MA, and Cs have been used to produce outstanding PCEs higher than 21%, with satisfactory operational stability.[11] However, the presence of MA in the structure is still a concern since it may lead to thermal instability,[12, 13] and thereby potentially reduce durability. Dual-mixed-cation perovskites

(Cs and FA) without MA are expected to have better thermal stability.[3] To date, there have been a limited number of fundamental studies of the stability of these two types (dual and triple) of mixed-cation perovskites. Improving the stability of PSCs is an essential task in order to boost the future real-world deployment of PSCs. X-ray photoelectron spectroscopy (XPS) is well known as a powerful technique to investigate the (surface) stability of halide perovskites.[13, 14] Whilst MAPI has been well studied using XPS,[13, 14] the stability of mixed-cation perovskite surfaces, particularly their water resistance, remains barely explored. This is important since it is well known that MA-containing perovskites decompose on exposure to even small amounts of water vapour, by loss of nitrogen and iodine.[13] The combined effect of heat- and moisture-induced degradation at mixed-cation perovskite surfaces is of particular interest and importance since in a realistic environment thermal stress and moisture can be present simultaneously.

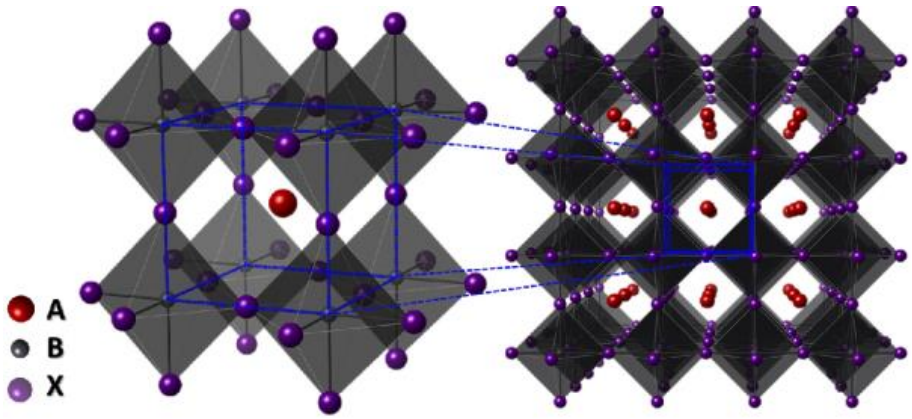

Figure 1 The typical 3D perovskite crystal structure in the cubic phase, showing a 4x4x4 supercell (right) and the unit cell outlined in blue (expanded on the left). The unit call has a general chemical formula of ABX_3, where A (MA^+, FA^+, Cs^+) and B (Pb^{2+}) are cations, and X (I^-, Br^-) are anions.

Here we carry out a study of the stability of the mixed-cation perovskites, $(FA_{0.83}Cs_{0.17})Pb(I_{0.83}Br_{0.17})_3$ and $(FA_{0.83}MA_{0.17})_{0.95}Cs_{0.05}Pb(I_{0.83}Br_{0.17})_3$ (denoted hereafter as FACs and FAMACs, respectively), using XPS under ultra-high vacuum (UHV) and near-ambient pressure (NAP-XPS) conditions. The NAP-XPS technique enables XPS to be used in more realistic environments during measurements, *e.g.* 9 mbar H_2O vapour, equivalent to a relative humidity (RH) of 30%. The moisture-induced degradation processes of MAPI and Cs_2SnI_6, under water vapour alone, using NAP-XPS have been reported.[13, 15, 16] In this work, we compare the thermal stability, water resistance, and their combined effect of the mixed-cation perovskite surfaces. The differences between the degradation in response to heat without and with the presence of water are also discussed. We believe, these results and discussion can lead to insights which will feed into the future development to improve stability with regard to heat and moisture for halide perovskites and in turn pave the way towards highly efficient and stable PSC devices.

Experimental Section

Materials

All chemicals were purchased from Sigma Aldrich, Tokyo Chemical Industry (TCI), or Greatcell Solar and used as received unless stated otherwise.

Substrate preparation

Samples were fabricated on fluorine-doped tin oxide (FTO) coated glass substrates (Pilkington). Substrates were cleaned sequentially with 2% Hellmanex, deionized water, acetone, and isopropanol in an ultrasonic bath for 15 minutes with substrates immersed in

each solution. After sonication, the substrates were rinsing with isopropanol and blow-dried with a nitrogen gun. Finally the substrates were treated with air plasma for 15 minutes.

Preparation of mixed-cation perovskite films

The perovskite films were deposited onto cleaned FTO substrates in a nitrogen-filled glovebox using pre-mixed precursor solutions that were also prepared in the glovebox. For the $(FA_{0.83}MA_{0.17})_{0.95}Cs_{0.05}Pb(I_{0.83}Br_{0.17})_3$ perovskite (denoted as FAMACs hereinafter), the precursor solution consisted of formamidinium iodide (FAI, Dyesol, 1 M), lead iodide (PbI_2, TCI, 1.05 M), methylammonium bromide (MABr, Dyesol, 0.2 M), caesium iodide (CsI, Alfa Aesar, 0.06 M), and lead bromide ($PbBr_2$, TCI, 0.22 M) in a mixture of anhydrous *N*,*N*-dimethylformamide (DMF): dimethylsulfoxide (DMSO) 4:1 (v:v). Pre-dissolved caesium iodide (CsI, Alfa Aesar, 0.06 M) from a 1.5 M stock solution in DMSO, was added to the perovskite precursor solution to achieve the desired triple mixed cation stoichiometry.[11]

For the $(FA_{0.83}Cs_{0.17})Pb(I_{0.83}Br_{0.17})_3$ perovskite (denoted as FACs hereinafter), the precursor consists of formamidinium iodide (FAI, Dyesol, 1.05 M), lead iodide (PbI_2, TCI, 0.94 M), caesium iodide (CsI, Alfa, 0.22 M), and lead bromide ($PbBr_2$, TCI, 0.32 M) in a mixture of anhydrous DMF:DMSO 4:1 (v:v). Both of the perovskite solutions were spin coated using a two-step program at 1000 rpm and 6000 rpm for 10 s and 20 s with 200 $rpms^{-1}$ and 1000 $rpms^{-1}$ acceleration, respectively, in a nitrogen-filled glovebox. During the second step, 300 μL of chlorobenzene was pipetted onto the spinning substrate 5 s prior to the end of the program. The substrates were then annealed at 100 ℃ for 30 min.

(NAP-)XPS measurements

In order to prevent degradation by reaction with ambient air the following protocol was adopted for both samples. Following the formation of the perovskite films, all samples were placed in a tightly-sealed nitrogen-filled box covered with Al foil and placed in a plastic vacuum-sealed bag. Sample mounting on the XPS sample plate was conducted in a nitrogen-filled glovebox and the sample plate placed inside a vacuum desiccator and evacuated. The vacuum desiccator containing the sample plate was put into a glove bag attached to the fast-entry load lock of the NAP-XPS system (SPECS). The glove bag was filled with pure Ar and the desiccator was opened and sample transferred to the load-lock. The load lock was then evacuated and the sample transferred to the NAP-XPS system. The NAP XPS instrument is a custom built system equipped with a SPECS Focus 500 monochromated Al Kα X-ray source ($h\nu$ = 1486.6 eV and SPECS 150 mm Phoibos 150 hemispherical analyser with a three-stage, differentially-pumped electrostatic lens. XPS spectral acquisition can be carried out either under conventional UHV conditions or in a near-ambient pressure (NAP) cell backfilled with 9 mbar water vapour, which is approximately equivalent to a relative humidity (RH) of 30%, at a standard atmospheric temperature of 25 ^{o}C. The samples without heating are denoted as RT (room temperature, at *ca.* 25 ^{o}C) hereinafter. Sample heating was carried out by radiative heating of the sample plate from a filament placed behind the sample. The temperature was measured by a thermocouple sandwiched between the sample plate and the FTO substrate. XPS acquisition was begun when the temperature had been allowed to stabilise for five minutes. The filament heating remained on throughout the whole measurement at the chosen temperature conditions (100 ^{o}C or 150 ^{o}C). The binding energy (BE) scale in the measurements is calibrated to the hydrocarbon-derived on the MAPI surfaces C 1s peak at a

binding energy (BE) of 285.3 eV.[13, 16, 17] This results in a BE for the metallic lead Pb $4f_{7/2}$ peak of the fresh perovskites films of *ca.* 137.0 eV, in agreement with the literature.[13, 17, 18] BE values are quoted to an accuracy of ±0.1 eV. A Shirley background and Gaussian/Lorentzian curves were used to fit the XPS core level spectra using CasaXPS software.[19, 20] The built-in CasaXPS sensitivity factors (Kratos) were used to calculate the chemical stoichiometry of the samples. The spectra and concentrations are normalised to the corresponding Pb $4f_{7/2}$ Pb^{2+} peak without calculating metallic lead.

Morphology

The morphology of the films was measured using scanning electron microscopy (SEM - Zeiss Sigma VP FEG-SEM). The SEM sample was exposed to ambient air for one minute, which is not expected to produce significant impact on the morphology.

Results and Discussion

The XPS results for the FACs and FAMACs materials are divided into four sections to investigate the thermal- and moisture-induced degradation of these perovskites: (1) FACs perovskite in UHV conditions, (2) FAMACs perovskite in UHV, (3) FACs perovskite + 9 mbar water vapour, (4) FAMACs perovskite + 9 mbar water vapour. Prior to XPS measurements, the morphology of FACs and FAMACs perovskite samples were examined using SEM, as shown in Figures S1A&B (see Supporting Information), in order to determine the quality of the films. Both films are pinhole-free and composed of densely packed, well-defined grains. There is no significant difference between the morphologies of the films prepared in the presence of MA (yielding the FAMACs perovskite) and in its absence (yielding FACs).

(1) FACs perovskite in UHV conditions

XPS spectra of a spin-coated FACs perovskite film recorded from different core levels at various temperatures in UHV conditions are shown in Figure 2. Two components are fitted to the Pb 4f spectra (Figure 2A), giving rise to two sets of Pb $4f_{7/2,5/2}$ doublets, under all conditions and corresponding to two distinct chemical states. The Pb $4f_{7/2}$ components recorded from the fresh FACs film at binding energies (BEs) of 138.6 ± 0.1 and 137.0 ± 0.1 eV BE can be assigned to the Pb^{2+} in the FACs perovskite and metallic lead (Pb^0), respectively.[13, 21] The BE value of the perovskite peak of the FACs perovskite (*ca.* 138.6 eV) is similar to that of MAPI films without Br doping.[13, 14] This suggests that the presence of Br at the surface (Figure 2D) of the FACs perovskite does not significantly change the Pb chemical environment in the halide perovskite framework. Following heating in UHV at 100 ^oC and 150 ^oC, the Pb $4f_{7/2}$ BE shifts to 138.9 ± 0.1 eV (*ca.* 0.3 BE shift), suggesting the formation of PbI_2 at the FACs perovskite surfaces under thermal stress.[13, 14] The amount of metallic lead (Pb^0) dramatically increases after raising the temperature of the sample.

The I 3d XPS spectra (I $3d_{5/2,3/2}$ doublets with a single component), in Figure 2B, of the FACs sample reveal a similar BE shift (*ca.* 0.3 eV) after heating at both 100 and 150 ^oC in UHV, from 619.5 ± 0.1 to 619.8 ± 0.1 eV BE for the I $3d_{5/2}$ peak. This suggests also thermal-induced chemical transition from the FACs perovskite into lead iodide,[13, 14] consistent with the observation in the Pb 4f XPS spectra. The surface stoichiometry information depicts this change in elemental chemical composition more completely, as summarised in Table 1. It can be seen that the I/Pb ratio of the as-deposited film is 2.4 ± 0.1, consistent with the expected stoichiometric ratio of 2.5, based on the halide ratio of the precursor solution.

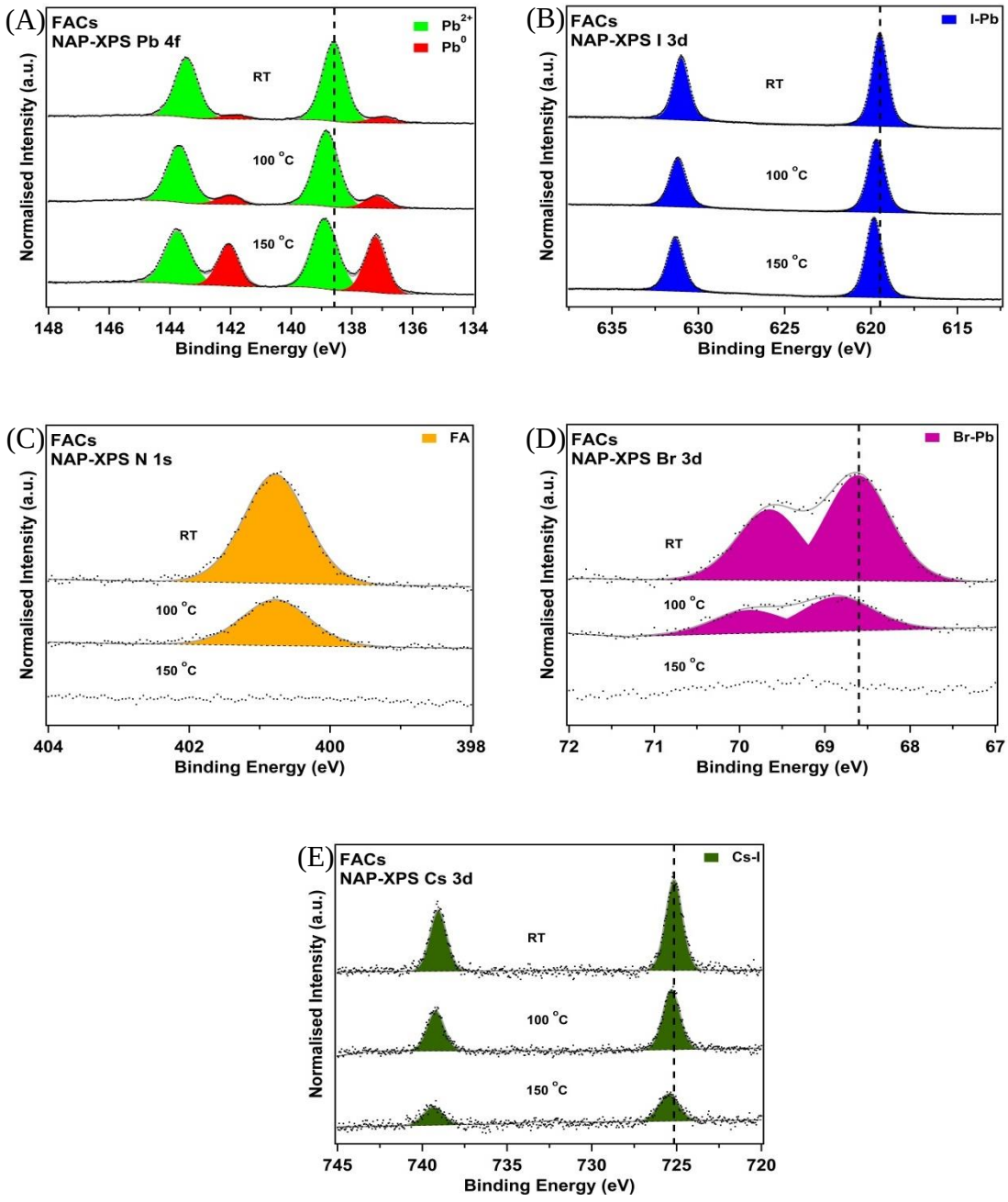

Figure 2 High-resolution XPS (A) Pb 4f, (B) I 3d, (C) N 1s, (D) Br 3d, and (F) Cs 3d core-level spectra of a spin-coated FACs perovskite film recorded in UHV conditions at room temperature (RT), 100 ^{o}C, and 150 ^{o}C. All spectra are normalised to the Pb $4f_{7/2}$ peak areas (for Pb^{2+}) for comparison.

Following heating to 100 and 150 ^{o}C, the values drop to approximately 2.0, clearly suggesting that the decomposition product at the surface is PbI_2. The N 1s XPS spectra shown in Figure 2C can be fitted with a single component at a BE of 400.8 ± 0.1 eV. This can be assigned to N in the FA cation in FA-containing perovskites.[21] Upon heating, the nitrogen signal is attenuated upon heating to 100 ^{o}C, and completely lost following heating at 150 ^{o}C in UHV. This is in agreement with previous work on MAPI which suggests formation of PbI_2 is accompanied by the loss of iodine and nitrogen from the perovskite.

Figure 2D shows the XPS core-level spectra of the minor halide element, Br, showing that the Br $3d_{5/2}$ peaks sit at a BE of ~68.6 eV, attributed to Br in the FACs perovskite.[22] Table 1 shows that the Br/Pb ratio decreases after heating in UHV. The decrease in signal from Br is similar to that of N (FA) relative to Pb (both around half), when heated at 100 ^{o}C in UHV. This suggests that there may be a correlation between Br and FA in the thermal-induced degradation processes. This finding is in agreement with literature reports that reveal the synchronous loss of FA and Br, probably in the form of FABr vapour under thermal stress.[23] Here, owing to the fact that more FA is present at the surface of the fresh film, FA is lost more quickly compared to Br as a result of heating. Since the N signal is lost completely following heating to 150 ℃, the nitrogen must also be lost in another form, possibly formamidine, FAI or NH_3. NH_3 gas has been found to be lost during degradation of MAPI films induced by moisture.[13, 24] In moisture-induced degradation of MAPI this results in the formation of a hydrocarbon film at the surface. Following heating of the FACs film at 100 and 150 ^{o}C, however, the concentration of C—H bonding relative to Pb reduces from *ca.* 2.4 to 1.9 and 1.5 (Table S1), respectively. This indicates the hydrocarbon moiety of the perovskite films is also lost from the material surface upon heating. Therefore, it is more likely that the nitrogen escapes in the form of FAI and/or FA plus HI.

Table 1 Atomic concentrations of different components in spin-coated FACs perovskite films determined from (NAP-)XPS recorded under RT and thermal stress (100 or 150 °C) in UHV and under with 9 mbar H_2O vapour exposure. Note the stoichiometries with H_2O vapour exposures are calculated from the data "after" H_2O vapour exposure rather than "during". All elements are normalised to $[Pb^{2+}] = 1.0$. RT(1) and RT(2) represent room temperature data from the different fresh films.

Condition	Pb (Pb $4f_{7/2}$)	Cs (Cs $3d_{5/2}$)	FA (N 1s)	MA (N 1s)	High BE component (N 1s)	Total cation	Pb^0	I (I $3d_{5/2}$)	Br (Br $3d_{5/2}$)	Total Halide
Ideal	1.0±0.1	0.17±0.02	0.8±0.1	0.0±0.1	-	1.0±0.2	0±2%	2.5±0.1	0.5±0.1	3.0±0.2
RT (1)	1.0±0.1	0.10±0.02	0.7±0.1	0.0±0.1	-	0.8±0.2	8±2%	2.4±0.1	0.4±0.1	2.8±0.2
100 °C	1.0±0.1	0.07±0.02	0.3±0.1	0.0±0.1	-	0.4±0.2	16±2%	2.0±0.1	0.2±0.1	2.2±0.2
150 °C	1.0±0.1	0.04±0.02	0.0±0.1	0.0±0.1	-	0.0±0.2	73±2%	2.0±0.1	0.0±0.1	2.0±0.2
RT (2)	1.0±0.1	0.12±0.02	0.7±0.1	0.0±0.1	-	0.8±0.2	6±2%	2.4±0.1	0.4±0.1	2.8±0.2
RT H_2O	1.0±0.1	0.03±0.02	0.3±0.1	0.2±0.1	0.3±0.1	0.8±0.2	2±2%	2.0±0.1	0.4±0.1	2.4±0.2
100 °C H_2O	1.0±0.1	0.05±0.02	0.3±0.1	0.1±0.1	0.3±0.1	0.7±0.2	3±2%	1.6±0.1	0.4±0.1	2.1±0.2
150 °C H_2O	1.0±0.1	0.08±0.02	0.3±0.1	0.0±0.1	-	0.3±0.2	2±2%	1.6±0.1	0.4±0.1	2.0±0.2

The Cs 3d core-level XPS spectra are shown in Figure 2E, and show a single Cs chemical environment with spin-orbit split Cs $3d_{5/2}$ and $3d_{3/2}$ peaks at BEs of 725.1 ± 0.1 eV and 739.0 ± 0.1 eV, respectively. These binding energies are consistent with Cs—I/Cr—Br bonding.[15] Table 1 shows that the concentration of Cs is reduced after heating accompanied by a BE shift to 725.5 ± 0.1 eV at 150 ^{o}C (*ca.* 0.4 eV BE shift). The increase in BE is consistent with the formation of CsI and CsBr at the surface. It has been previously observed that the BE of CsI is higher than that of the Cs in a Cs_2SnI_6 double perovskite,[25] most likely due to the stronger ionic character of Cs in the halide compared to the perovskite. With regard to the loss of Cs upon heating, it is unlikely that CsI and/or CsBr vapours will be formed due to the high melting and vapourisation temperatures of alkali metal halides. It is tentatively proposed therefore that loss of Cs with increasing temperatures may be due to evaporation of metallic Cs from the surface. The low melting point of Cs metal of 28 ^{o}C means that sublimation of elemental Cs may occur under ultra-high vacuum conditions even 100 – 150 ℃. Based on the data presented above, we propose the thermal decomposition route under the stress up to 150 ^{o}C in UHV for FACs perovskites as below:

$$(FA_{1-x}Cs_x)Pb(I_{1-x}Br_x)_3(s) \xrightarrow{heat} Pb\ (s) + Cs\ (g) + CsI\ (s) + HI\ (g) + HBr\ (g) + FAI\ (g) + FABr\ (g) + FA\ (g) + PbI_2\ (s) + I_2\ (g) + Br_2\ (g), \quad \text{(Eq.1)}$$

where x is 0.17 in this work. Note this equation only refers to the degradation process in vacuo. The degradation route induced by heat in humid conditions will be discussed later. In addition, this degradation reaction simply exhibits the potential by-products produced by thermal degradation since we are not able to analyse the products leaving the material upon heating in vacuum, only the material left at the surface.

(2) FAMACs perovskite in UHV conditions

FAMACs, exhibits similar XPS core-level spectra, before and after heating in UHV, as shown in Figure 3. With the exception of the MA cation ($CH_3NH_3^+$) derived N 1s peak in Figure 3C, all BEs of the fresh FAMACs film are similar to those detected from the FACs sample, suggesting MA at the concentration studied (0.2 relative to Pb) does not greatly affect the binding energy and chemical state of the other elements. The BE of the MA constituent (N－C) in lead perovskites is higher than that of FA, located at a BE of around 402.5 eV.[13] Upon heating the MA at the FAMACs perovskite surface is completely removed from the surface of the film by heating at 100 ^oC in UHV. This indicates that the MA is less stable and more volatile under thermal stress in UHV compared to the FA in mixed-cation perovskites.[3] The chemical composition changes of the FAMACs film under heating are summarised in Table 2. The results show that the fresh FAMACs sample possesses an ideally stoichiometric surface. However, the Pb^0 concentration of the fresh FAMACs surface (Figure 3A) relative to Pb^{2+} is much higher than that of the fresh FACs perovskite. After heating in UHV, the MA-containing perovskites produce more metallic lead. We note that the increasing levels of metallic lead at the surfaces of both the perovskites with and without MA are almost identical regardless of the different initial values. By comparing the thermal stability of the perovskites with and without MA following heating in UHV, the loss of I, Br (Figure 3D), and FA, are also quite similar. Nonetheless, MA itself is thermally unstable at only 100 oC (Figure 3C),[3] and therefore synthesising novel halide perovskites which do not contain MA is important in improving stability.

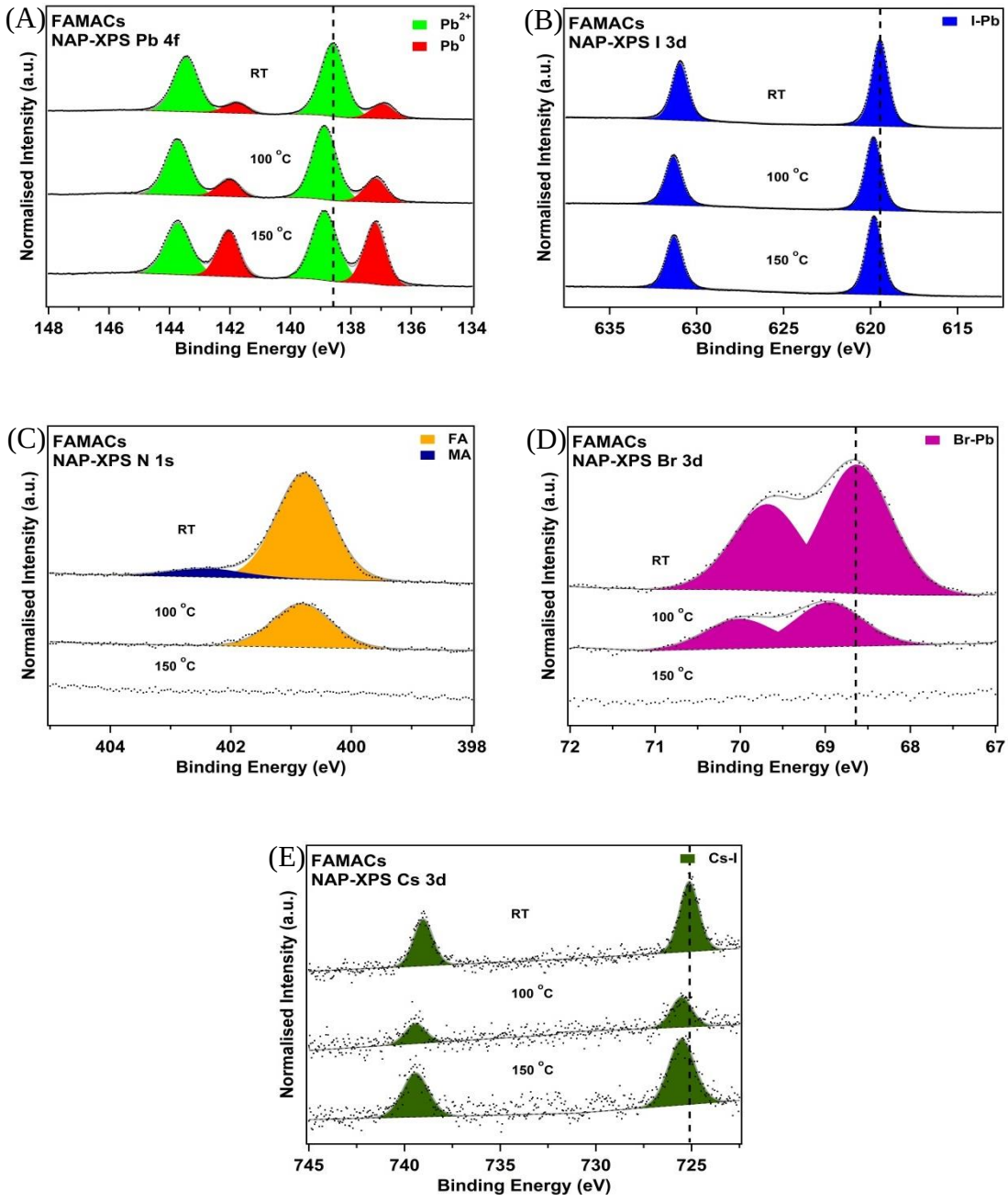

Figure 3 High resolution XPS (A) Pb 4f, (B) I 3d, (C) N 1s, (D) Br 3d, and (F) Cs 3d core-level spectra of a spin-coated FAMACs perovskite film recorded in UHV conditions at room temperature (RT), 100 ^{o}C, and 150 ^{o}C. All spectra are normalised to the Pb $4f_{7/2}$ peak areas (Pb^{2+}) for comparison.

Under UHV heating, the amount of Cs remains similar for the FAMACs sample (Figure 3E) fluctuating between 0.01 and 0.03 within error relative to Pb (Table 2). This may be due to the fact that much smaller amount of Cs is present in the FAMACs perovskite structure. Following heating, the BEs of the Cs $3d_{5/2}$ peak shift towards higher BE, as shown in Figure 3E, suggesting again the conversion from caesium halide bonds in the FAMACs film to CsI and CsBr,[15] consistent with the observation for the FACs perovskite (Figure 2E).

In Table 2, we can see that the reduction in the concentration of the total halide is similar to the decrease in that of the total organic cation. It is known that FA can be lost from the surface in the form of FABr and FAI vapours.[23] Similarly, the amount of hydrocarbon species (Table S2) decreases following heating in UHV. Similarly, the amount of hydrocarbon species (Table S2) decreases following heating in UHV. This suggests that the carbon moieties from either FA or MA escape with the nitrogen rather than staying at the surface of the films when heated in UHV as is observed for water induced degradation of MAPI. The degradation process of the FAMACs perovskite under thermal stress can be expressed as Eq.2 as below:

$$(FA_{1-x}MA_x)_{1-y}Cs_yPb(I_{1-x}Br_x)_3\ (s) \xrightarrow{heat} Pb\ (s) + Cs\ (g) + CsI\ (s) + HI\ (g) + HBr\ (g) + FAI\ (g) + FABr\ (g) + FA\ (g) + MAI\ (g) + MABr\ (g) + MA\ (g) + PbI_2\ (s) + I_2\ (g) + Br_2\ (g), \quad \text{(Eq.2)}$$

Where *x* equals to 0.17 and *y* is 0.05 in this work for the FAMACs perovskites and noting this equation again only applies to an environment without the presence of moisture. As for the FACs material the products are somewhat speculative since we are only able to determine what is left on the surface, and do not measure the species lost to the vacuum

system. The data above show the effect of temperature under UHV conditions, however in a realistic environment, water is always likely to be present. Hence, the thermal degradation of the mixed-cation perovskite films in an environment containing moisture is of significant interest.

(3) FACs perovskite + 9 mbar water vapour

Figure 4 shows the NAP-XPS spectra of a FACs perovskite film recorded from the strongest core levels with and without the presence of 9 mbar H_2O vapour. The main peak of the Pb 4f spectra (Figure 4A) moves to a higher BE (ca. 0.2 eV shift) of *ca.* 138.8 eV after exposure to 9 mbar H_2O vapour at room temperature, suggesting the formation of PbI_2.[13] When heated to 100 and 150 ^oC in moisture, the peak shifts again towards higher BE at approximately 138.9 eV, consistent with the reaction of lead perovskites with water to form PbI_2.[13] Interestingly, the amount of metallic Pb (Figure 4A) remains at a similar level following heating in a humid environment, contrary to the heating of the FACs sample in UHV. This indicates that H_2O vapour suppresses the formation of metallic lead at the lead perovskite induced by thermal stress. In addition, in our previous study of water-induced degradation of MAPI, the metallic lead concentration of MAPI was still found to substantially increase following exposure to an identical partial pressure of water.[13] It is therefore more likely that the lead in the perovskite and PbI_2 reacts with water vapour to form $Pb(OH)_2$.[18, 26] The BE of $Pb(OH)_2$ is known to be similar to that of PbI_2,[18, 26] making it difficult to be resolve the Pb^{2+} peak of PbI_2 from $Pb(OH)_2$.

Table 2 Atomic concentrations of different components in spin-coated FAMACs perovskite films determined from (NAP-)XPS recorded under RT and thermal stress (100 or 150 °C) in UHV and under 9 mbar H_2O vapour exposure. Note the stoichiometries with H_2O vapour exposures are calculated from the data "after" H_2O vapour exposure rather than "during". All elements are normalised to $[Pb^{2+}] = 1.0$. RT(1) and RT(2) represent room temperature data from the different fresh films.

Condition	Pb (Pb $4f_{7/2}$)	Cs (Cs $3d_{5/2}$)	FA (N 1s)	MA (N 1s)	High BE component (N 1s)	Total cation	Pb^0	I (I $3d_{5/2}$)	Br (Br $3d_{5/2}$)	Total halide
Ideal	1.0±0.1	0.05±0.02	0.8±0.1	0.2±0.1	-	1.0±0.2	0±2%	2.5±0.1	0.5±0.1	3.0±0.2
RT (1)	1.0±0.1	0.02±0.02	0.7±0.1	0.2±0.1	-	0.9±0.2	20±2%	2.5±0.1	0.5±0.1	3.0±0.2
100 °C	1.0±0.1	0.01±0.02	0.3±0.1	0.0±0.1	-	0.3±0.2	31±2%	2.1±0.1	0.2±0.1	2.3±0.2
150 °C	1.0±0.1	0.03±0.02	0.0±0.1	0.0±0.1	-	0.0±0.2	83±2%	2.1±0.1	0.0±0.1	2.1±0.2
RT (2)	1.0±0.1	0.03±0.02	0.7±0.1	0.2±0.1	-	0.9±0.2	18±2%	2.3±0.1	0.5±0.1	2.8±0.2
RT H_2O	1.0±0.1	0.01±0.02	0.3±0.1	0.3±0.1	0.3±0.1	0.9±0.2	2±2%	1.8±0.1	0.4±0.1	2.2±0.2
100 °C H_2O	1.0±0.1	0.02±0.02	0.3±0.1	0.1±0.1	0.3±0.1	0.7±0.2	2±2%	1.8±0.1	0.4±0.1	2.2±0.2
150 °C H_2O	1.0±0.1	0.03±0.02	0.1±0.1	0.0±0.1	-	0.2±0.2	4±2%	2.1±0.1	0.1±0.1	2.2±0.2

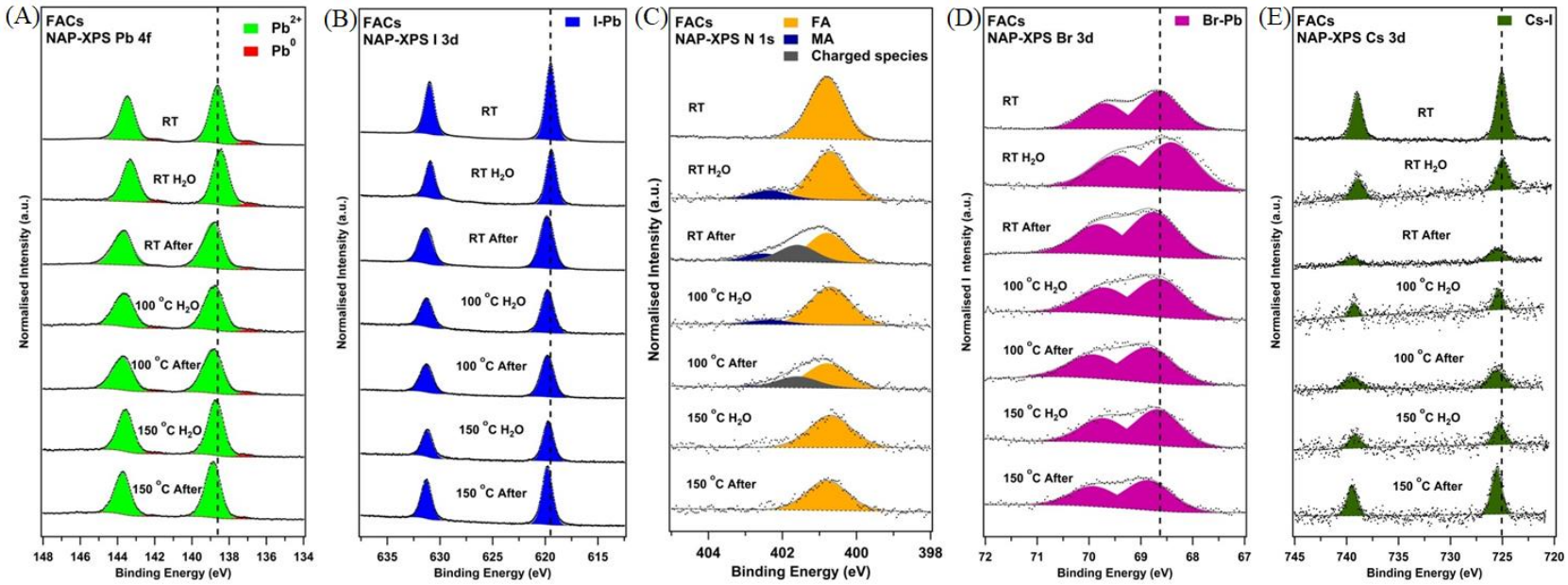

Figure 4 NAP-XPS (A) Pb 4f, (B) I 3d, (C) N 1s, (D) Br 3d, and (F) Cs 3d core-level spectra of a spin-coated FACs perovskite film recorded before, during, and after exposure to 9 mbar H_2O exposure at room temperature (RT), 100 °C, and 150 °C. All spectra are normalised to the Pb $4f_{7/2}$ peak areas (Pb^{2+}) for comparison.

There is an identical BE shift observed in the I 3d NAP-XPS spectra (Figure 4B). The chemical composition of the FACs film after exposure to water and heating is summarised in Table 1 (denoted "with H_2O"). Upon H_2O exposure at RT, the concentration of FA drops to around half its original concentration (also see Figure 4C), in contrast to the reaction of MAPI with water vapour where the MA is lost completely after exposure to 9 mbar water vapour.[13] Figure 4C also shows that upon exposure to water the N 1s spectrum can be fitted with an additional peak at a BE of 402.5 ± 0.1 eV. This feature can be assigned to formation of the MA (N—C) cation ($CH_3NH_3^+$) and/or the formation of NH_3^+ species at the surface.[13, 16] This suggests the loss of nitrogen may occur *via* the loss of ammonia gas (NH_3), triggered by reaction of the FA ion with H_2O vapour,[13] as expressed below:

$$CH_5N_2^+ (s) + 4H^+(g) \xrightarrow{H_2O} CH_3NH_3^+(s) + NH_3 (g), \quad \text{(Eq.3)}$$

where H^+ comes from H_2O vapour. After H_2O exposure at RT and 100 ^oC, and then allowing the NAP cell to return to UHV leads to broadening of the N 1s peaks. Since one would not expect a large change in the full-width-half-maximum (FWHM) of the peak, it is fitted with a second peak with fixed FWHM. This additional component, at a binding energy of 401.6 ± 0.1 eV, however, does not appear during H_2O exposure. One possible explanation is that as the surface undergoes degradation by reaction with water, the surface products are insulating and lead to charging at the surface. Upon exposure to water the H_2O gas can extract accumulated holes generated by the photoemission process, reducing the charging effect. We previously found that charged constituents are produced at MAPI surfaces degraded in ambient air.[16] Contrary to this though, no such charged species are observed in any of the other core-level spectra, and after exposure of the film to H_2O vapour at 150 ^oC, this higher energy component is lost. This suggests that the additional species is

lost as a result higher temperature, along with the MA and NH_3^+ species. The origin of this peak is therefore unclear. It may be an intermediate which remains adsorbed below 150 ℃ but this does not explain why it is only present after the system is returned to UHV.

The evolution of the Br 3d (Figure 4D) and Cs 3d (Figure 4E) core-level peaks of the FACs sample under thermal stress in humid conditions show a similar trend for the sample heated in dry vacuum. In addition, it can be seen that during H_2O vapour exposure at various temperatures for all core-level XPS spectra, the BE generally shifts towards lower values owing to the fact that H_2O molecules remove the surface charge (holes) which arise from the photoemission process. The halide concentrations relative to Pb of the FACs sample under various conditions are shown in Table 1. The concentration of the total halide (I + Br) decreases from *ca.* 2.8 to 2.5 following H_2O vapour exposure at RT. The reduction is mainly due to the loss of iodine (Figure 4B), whilst the bromine stays at similar levels (Figure 4D). For the I/Pb concentrations (Figure 4B and Table 1), the decrease in the values for the sample heated in moisture is higher than those heated without H_2O vapour. This suggests that H_2O vapour facilitates the removal of I, and appears to confirm previous findings suggesting formation of HI upon reaction of MAPI with water.[13] On the other hand, Br remains at similar levels at the surface of the film in the presence of moisture, again a significantly different result compared to the films heated in UHV. Similarly, the degradation of FA is less severe as a result of heating under H_2O compared to the films heated in UHV. The variations in the elemental concentration of FA are again similar to those of Br. This suggests that these two elements may be lost in the form of FABr from the surface of the FACs perovskite films, as proposed for the samples heated in UHV.

In addition, the Cs/Pb value (Figure 4E) drops following exposure at RT, consistent with the observation for the FACs film under thermal stress in dry condition. On the other

hand, when the film is heated in a humid environment, the Cs/Pb value increases with temperature following an initial drop as a result of H_2O vapour at RT (Figure 4E). The reason for the initial drop in Cs concentration upon exposure to water is not clear. One possibility is that the reaction products formed upon exposure to water remain adsorbed on the surface, as seems to be the case with the additional nitrogen species. This leads to the Cs being buried below the layer of degradation products. Upon heating to 100 ℃ some of these products are lost from the surface leading to the observed rise in Cs/Pb ratio, and a corresponding decrease in the intensity of the N 1s peak at *ca.* 401.6 eV. Heating to 150 ℃ leads to further removal of the decomposition and increase again in the Cs/Pb ratio and loss of the higher N 1s binding energy.

(4) FAMACs perovskite + 9 mbar water vapour

The surface chemical compositions of a FAMACs film exposed to 9 mbar H_2O vapour without (RT) and with heating (100 or 150 ^oC) are summarised in Table 2 and the corresponding XPS spectra are shown in Figure 5. Compared to the FACs sample, the decrease in the FA (Figure 5C) and Br (Figure 5D) concentrations relative to Pb for the FAMACs sample is much higher, particularly at 150 ^oC. This suggests that the presence of MA in the perovskite film leads FA and Br ions to be more likely to leave from the surface of the film under hot, humid, low pressure conditions. In other words, MA is not only inherently vulnerable to heat and moisture itself but also influences the thermal stability of other elements in the perovskite films when water vapour is present. It is worth noting that the amount of MA increases following H_2O vapour exposure at RT. This suggests again that under humid environment, FA converts into MA first in the perovskite structure in agreement with the FACs film. The MA of MAPI appears to be vulnerable to moisture, resulting in reduced amount.[13] Therefore, the amount of MA in the FAMACs film is

supposed to reduce under moist condition if FA cannot convert to it. Again we observe an additional feature in the N 1s spectrum after exposure to water, but not during exposure which seems to further suggest this may be an intermediate species of the water/FAMACs material.

The total cation concentration of the FAMACs sample at 150 ^{o}C is apparently lower than that obtained from the FACs perovskite due to the presence of thermally unstable MA. For the iodine concentrations (Table 2 and Figure 5B), the degradation trend with heating temperature is roughly the same regardless of the presence of MA. Heating the sample in moisture leads to relatively severe reduction in iodine concentrations compared to the film heated in UHV. It was suggested that water vapour facilitates the formation of iodine vacancies, probably through the loss of hydrogen iodide gas.[13] Last but not least, the amount of Cs relative to Pb remains similar within error. There is a small apparent decrease in Cs upon exposure to water, consistent with the FACs film, but the low initial concentration makes it difficult to draw any conclusions from this. We note however, that the BE shifts towards higher values following heating the FAMACs sample in water vapour consistent with the formation of Cs halides.

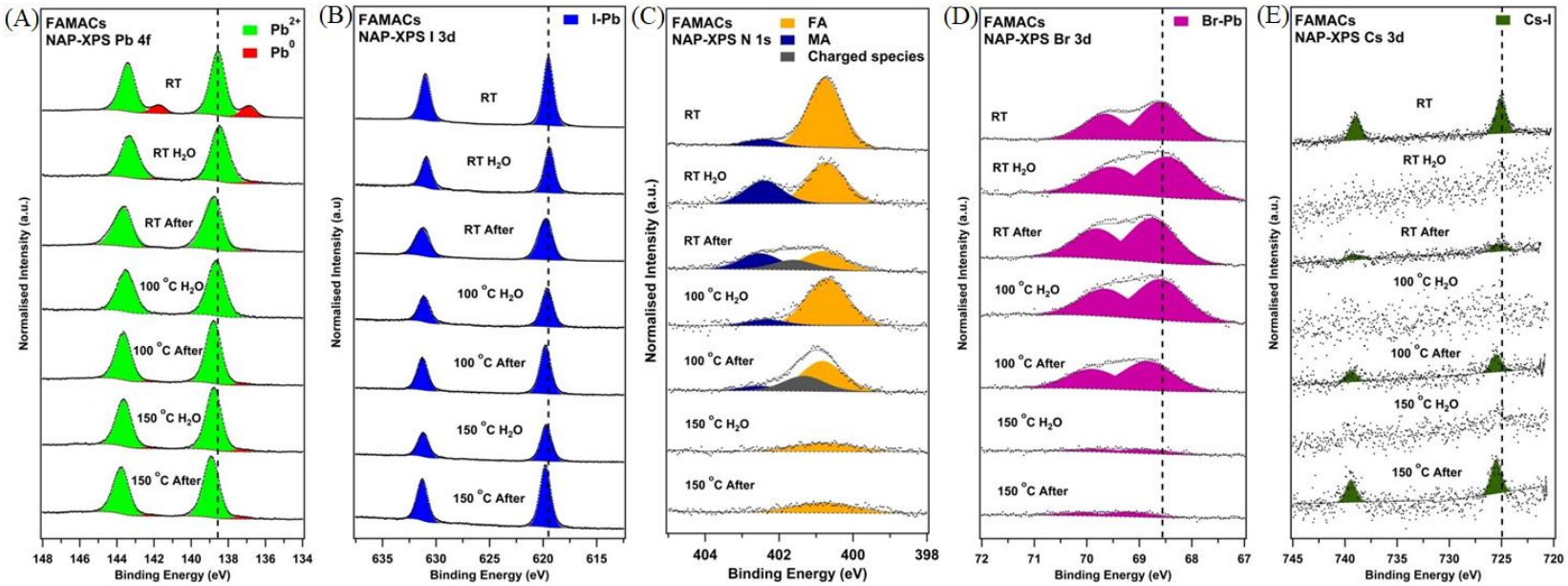

Figure 5 NAP-XPS (A) Pb 4f, (B) I 3d, (C) N 1s, (D) Br 3d, and (E) Cs 3d core-level spectra of a spin-coated FAMACs perovskite film recorded before, during, and after exposure to 9 mbar H_2O exposure at room temperature (RT), 100 °C, and 150 °C. All spectra are normalised to the Pb $4f_{7/2}$ peak areas (Pb^{2+}) for comparison.

Conclusions

In conclusion, here, we present a comprehensive study of thermal effect on the surface of the mixed-cation (FAMACs and FACs) mixed-halide perovskites with and without MA, respectively, under conditions with and without the presence of moisture. The results clearly demonstrate the thermal-induced degradation pathways of FACs and FAMACs perovskite films in UHV and in near-ambient-pressure conditions with a RH of 30% using NAP-XPS. MA is relatively vulnerable to heat under both conditions regardless of the presence of H_2O vapour compared to the FA and Cs in the perovskite structure. Interestingly, if H_2O vapour is present, the FA cation appears to convert into MA cation by losing nitrogen, probably in the form of ammonia gas Furthermore, under humid environments, bromine appears to be more stable than iodine in the perovskite structures studied. This suggests that partially replacing iodine with bromine may be a relevant strategy to improve the stability of halide perovskites against moisture. Moreover, both with and without H_2O vapour, it is clearly observed that FA and Br show synchronous loss, consistent with previous literature.[23] Overall, the FAMACs is less thermally stable since not only is MA unstable but also appears to make other ions, such as FA and Br, become less stable in humid conditions.

Acknowledgments

The authors thank the University of Manchester and EPSRC (UK) (grant EP/K009710) for funding. Chun-Ren Ke thanks the University of Manchester for the award of a President's Doctoral Scholarship.

References

1 N. R. E. Laboratory, Best research-cell efficiency chart, https://www.nrel.gov/pv/assets/pdfs/best-research-cell-efficiencies.20190802.pdf, Accessed 20.August.2019.

2 G. E. Eperon, T. Leijtens, K. A. Bush, R. Prasanna, T. Green, J. T.-W. Wang, D. P. McMeekin, G. Volonakis, R. L. Milot and R. May, *Science*, 2016, **354**, 861-865.

3 D. P. McMeekin, G. Sadoughi, W. Rehman, G. E. Eperon, M. Saliba, M. T. Hörantner, A. Haghighirad, N. Sakai, L. Korte and B. Rech, *Science*, 2016, **351**, 151-155.

4 A. Kojima, K. Teshima, Y. Shirai and T. Miyasaka, *Journal of the American Chemical Society*, **2009**, 131, 6050-6051.

5 N. J. Jeon, J. H. Noh, W. S. Yang, Y. C. Kim, S. Ryu, J. Seo and S. I. Seok, *Nature*, 2015,**517** , 476-480.

6 E. M. Sanehira, A. R. Marshall, J. A. Christians, S. P. Harvey, P. N. Ciesielski, L. M. Wheeler, P. Schulz, L. Y. Lin, M. C. Beard and J. M. Luther, *Science advances*, 2017, **3**, eaao4204.

7 W. S. Yang, J. H. Noh, N. J. Jeon, Y. C. Kim, S. Ryu, J. Seo and S. I. Seok, *Science*, 2015, **348**, 1234-1237.

8 M. Liu, M. B. Johnston and H. J. Snaith, *Nature*, 2013, **501**, 395-398.

9 G. E. Eperon, S. D. Stranks, C. Menelaou, M. B. Johnston, L. M. Herz and H. J. Snaith, *Energy & Environmental Science*, 2014, **7**, 982-988.

10 Y. Fu, T. Wu, J. Wang, J. Zhai, M. J. Shearer, Y. Zhao, R. J. Hamers, E. Kan, K. Deng and X.-Y. Zhu, *Nano letters*, 2017, **17**, 4405-4414.

11 M. Saliba, T. Matsui, J.-Y. Seo, K. Domanski, J.-P. Correa-Baena, M. K. Nazeeruddin, S. M. Zakeeruddin, W. Tress, A. Abate, A. Hagfeldt and M. Graetzel, *Energy & environmental science*, 2016, **9**, 1989-1997.

12 N.-K. Kim, Y. H. Min, S. Noh, E. Cho, G. Jeong, M. Joo, S.-W. Ahn, J. S. Lee, S. Kim and K. Ihm, *Scientific Reports*, 2017, **7**, 4645.

13 J. C.-R. Ke, A. S. Walton, D. J. Lewis, A. Tedstone, P. O'Brien, A. G. Thomas and W. R. Flavell, *Chemical Communications*, 2017, **53**, 5231-5234.
14 B. Philippe, B.-W. Park, R. Lindblad, J. Oscarsson, S. Ahmadi, E. M. Johansson and H. k. Rensmo, *Chemistry of Materials*, 2015, **27**, 1720-1731.
15 J. C.-R. Ke, D. J. Lewis, A. S. Walton, B. F. Spencer, P. O'Brien, A. G. Thomas and W. R. Flavell, *Journal of Materials Chemistry A*, 2018, **6**, 11205-11214.
16 C.-R. Ke, D. J. Lewis, A. S. Walton, Q. Chen, B. F. Spencer, M. Mokhtar, C. L. Compean-Gonzalez, P. O'Brien, A. G. Thomas and W. R. Flavell, *ACS Applied Energy Materials*, 2019, **2**, 6012-6022.
17 L. Liu, J. A. McLeod, R. Wang, P. Shen and S. Duhm, *Applied Physics Letters*, 2015, **107**, 061904.
18 W. Huang, J. S. Manser, P. V. Kamat and S. Ptasinska, *Chemistry of Materials*, 2015, **28**, 303-311.
19 D. A. Shirley, *Physical Review B*, 1972, **5**, 4709.
20 N. Fairley, *CasaXPS manual 2.3. 15*, Acolyte Science, 2009.
21 B. Philippe, M. Saliba, J.-P. Correa-Baena, U. B. Cappel, S.-H. Turren-Cruz, M. Grätzel, A. Hagfeldt and H. Rensmo, *Chemistry of Materials*, 2017, **29**, 3589-3596.
22 B. Philippe, T. J. Jacobsson, J.-P. Correa-Baena, N. K. Jena, A. Banerjee, S. Chakraborty, U. B. Cappel, R. Ahuja, A. Hagfeldt and M. Odelius, *The Journal of Physical Chemistry C*, 2017, **121**, 26655-26666.
23 M. Long, T. Zhang, M. Liu, Z. Chen, C. Wang, W. Xie, F. Xie, J. Chen, G. Li and J. Xu, *Advanced Materials*, 2018, **30**, 1801562.
24 Y. Li, X. Xu, C. Wang, C. Wang, F. Xie, J. Yang and Y. Gao, *The Journal of Physical Chemistry C*, 2015, **119**, 23996-24002.
25 N. Krishnan, W. Delgass and W. Robertson, *Journal of Physics F: Metal Physics*, 1977, **7**, 2623.
26 D. J. Cant, K. L. Syres, P. J. Lunt, H. Radtke, J. Treacy, P. J. Thomas, E. A. Lewis, S. J. Haigh, P. O'Brien and K. Schulte, *Langmuir*, 2015, **31**, 1445-1453.
27 S. Booth, A. Tripathi, I. Strashnov, R. Dryfe and A. Walton, *Journal of Physics: Condensed Matter*, 2017, **29**, 454001.

7.2.2 Supporting Information

Supporting Information (SI)

Thermal Degradation Behaviour of Mixed-Cation Perovskite Surfaces Probed by *In Situ* X-Ray Photoelectron Spectroscopy under Humid Conditions

Jack Chun-Ren Ke,[a,b,c,d], Jacob Tse-Wei Wang,[f] Alex S. Walton,[b,c,d] Gregory J. Wilson,[f] Andrew G. Thomas,[b,c,d] and Wendy R. Flavell[a,b,c]

g. Department of Physics and Astronomy, The University of Manchester, Oxford Road, Manchester M13 9PL, United Kingdom

h. Photon Science Institute, The University of Manchester, Oxford Road, Manchester M13 9PL, United Kingdom

i. Henry Royce Institute, The University of Manchester, Oxford Road, Manchester, M13 9PL, United Kingdom

j. Department of Materials, The University of Manchester, Oxford Road, Manchester M13 9PL, United Kingdom

k. Department of Chemistry, The University of Manchester, Oxford Road, Manchester M13 9PL, United Kingdom

l. CSIRO Energy, Mayfield West, NSW 2304, Australia

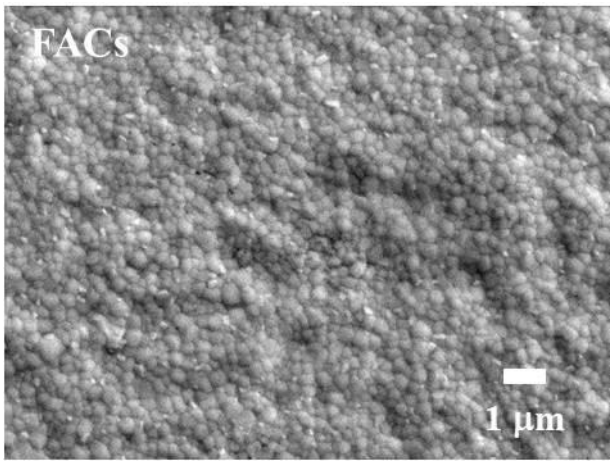

(A)

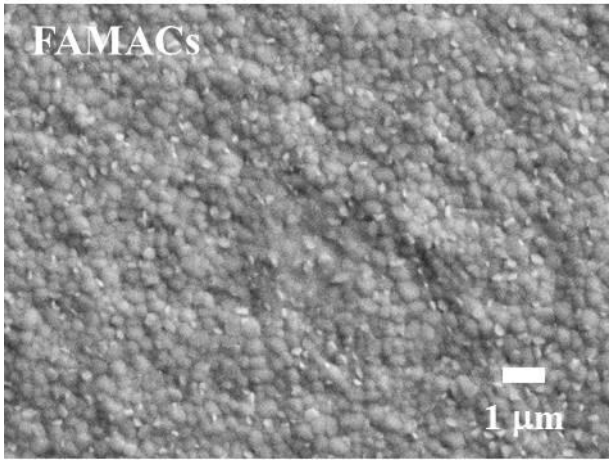

(B)

Figure S1 High-resolution SEM images of the (A) FACs and (B) FAMACs perovskite films after storage in a vacuum-sealed bag.

Table S1 Atomic concentrations of different components in spin-coated FACs perovskite films determined from (NAP-)XPS recorded under RT and thermal stress (100 or 150 ^{o}C) under UHV and with 9 mbar H_2O vapour exposure. Note the stoichiometries with H_2O vapour exposures are calculated from the data "after" H_2O vapour exposure rather than "during". All elements are normalised to $[Pb^{2+}] = 1.0$.

Condition	Pb (Pb $4f_{7/2}$)	C—C/C—H	C—N(MA)/C—OH	N—C—N(FA)/C=O
RT (1)	1.0±0.1	2.4±0.1	0.3±0.1	0.8±0.1
100 ^{o}C	1.0±0.1	1.9±0.1	0.3±0.1	0.4±0.1
150 ^{o}C	1.0±0.1	1.5±0.1	0.6±0.1	0.0±0.1
RT (2)	1.0±0.1	3.7±0.1	0.3±0.1	1.0±0.1
RT H_2O	1.0±0.1	6.8±0.1	3.8±0.1	1.5±0.1
100 ^{o}C H_2O	1.0±0.1	14.9±0.1	7.3±0.1	1.5±0.1
150 ^{o}C H_2O	1.0±0.1	24.9±0.1	3.8±0.1	0.0±0.1

The change in the concentrations of MA and FA peaks obtained from the C 1s spectra is supposed to match the change in those acquired from the N 1s spectra. However, C—OH, C=O, and C—C/C—H can increase due to the contamination introduced into the NAP cell particularly with the presence of H_2O vapour, as the increased pressure in the cell tends to displace gas, such as CO, CO_2, and small organics from the chamber walls.[1] The heating at 150 ^{o}C with the presence of H_2O vapour can reduce the surface contaminations of the film as observed in the C—OH and C=O concentrations. The increase in hydrocarbon could be partially attributed to the conversion from the organic part of the perovskite as a result of H_2O vapour.[2]

Table S2 Atomic concentrations of different components in spin-coated FAMACs perovskite films determined from (NAP-)XPS recorded under RT and thermal stress (100 or 150 ^{o}C) under UHV and with 9 mbar H_2O vapour exposure. Note the stoichiometries with H_2O vapour exposures are calculated from the data "after" H_2O vapour exposure rather than "during". All elements are normalised to $[Pb^{2+}] = 1.0$.

Condition	Pb (Pb $4f_{7/2}$)	C—C/C—H	C—N(MA)/C—OH	N—C—N(FA)/C=O
RT (1)	1.0±0.1	3.3±0.1	0.3±0.1	1.0±0.1
100 ^{o}C	1.0±0.1	1.0±0.1	0.1±0.1	0.3±0.1
150 ^{o}C	1.0±0.1	0.5±0.1	0.3±0.1	0.0±0.1
RT (2)	1.0±0.1	4.7±0.1	0.9±0.1	1.2±0.1
RT H_2O	1.0±0.1	8.1±0.1	7.9±0.1	2.6±0.1
100 ^{o}C H_2O	1.0±0.1	11.5±0.1	7.6±0.1	2.6±0.1
150 ^{o}C H_2O	1.0±0.1	18.9±0.1	2.9±0.1	0.0±0.1

The explanation for the changes in the concentrations of these carbon-containing components generally follows the discussion presented for the aforementioned table (Table S1).

References

1 S. Booth, A. Tripathi, I. Strashnov, R. Dryfe and A. Walton, *Journal of Physics: Condensed Matter*, 2017, **29**, 454001.

2 J. C.-R. Ke, A. S. Walton, D. J. Lewis, A. Tedstone, P. O'Brien, A. G. Thomas and W. R. Flavell, *Chemical Communications*, 2017, **53**, 5231-5234.

Chapter 8 Inorganic Cs_2SnI_6 double perovskite thin films *via* AACVD

This paper has been first published in Journal of Materials Chemistry A on 10/05/2018

Cite this: *J. Mater. Chem. A,* 2018, **6**, 11205

8.1 Introduction

This chapter contains a paper that has been published in *Journal of Materials Chemistry A*.[9] The work (Paper 5) extends halide perovskite research from organic lead perovskites (Chapter 4 to 7) to an inorganic lead-free tin perovskite. This paper compares the bulk and surface stability of Cs_2SnI_6 double perovskite films fabricated by spin coating and AACVD. The reasons why choose this material as the lead-free candidate to reduce toxicity are the low optical bandgap of ~1.3 eV and air-stable property of this material. The latter is partially due to the inorganic nature and Sn^{4+} in the Cs_2SnI_6 chemical structure, which cannot be further oxidised. We found that AACVD-grown samples have better stability than spin-coated counterparts, probably due to larger grain sizes, which have less surface-to-volume ratios to react with atmospheres, consistent with the results in Chapter 5. Furthermore, the addition of HI in the precursor solution plays an important role in phase purity and defect chemistry. XPS results show that excess I and Sn are present at the film surface, which can be attributed to the presence of tin iodide. For NAP-XPS experiment, in addition to water vapour exposure, we also investigated the oxygen-induced degradation of Cs_2SnI_6. The outcome for both exposures shows some changes in Sn and I concentrations relative to Cs whilst the amount of CsI remains similar. The results

suggest that tin iodide may passivate the Cs_2SnI_6 surface/grain boundaries, protecting the films from degradation caused by moisture or oxygen.

Contribution

The author designed and performed most of the experiments, including sample preparation and characterisation. NAP-XPS and XPS measurements were greatly supported by Dr Alex Walton and Dr Ben Spencer, respectively. The AACVD instruments used are the facilities built by the group of Dr David Lewis and Prof Paul O'Brien (deceased). I obtained advice from Dr David Lewis for fine-tuning the AACVD process to make perovskites. The author analysed all the data acquired and wrote this paper with Prof Wendy Flavell and Dr Andrew Thomas, with suggestions from the co-authors.

8.2 Paper 5

8.2.1 Main Text

Journal of Materials Chemistry A

PAPER

View Article Online
View Journal | View Issue

Cite this: J. Mater. Chem. A, 2018, 6, 11205

Ambient-air-stable inorganic Cs_2SnI_6 double perovskite thin films *via* aerosol-assisted chemical vapour deposition†

Jack Chun-Ren Ke,[ab] David J. Lewis,[c] Alex S. Walton,[bd] Ben F. Spencer,[c] Paul O'Brien,[cd] Andrew G. Thomas[*bc] and Wendy R. Flavell[*ab]

Air-stable caesium tin iodide double perovskite (Cs_2SnI_6) thin films have been fabricated *via* aerosol-assisted chemical vapour deposition (AACVD). We compare the properties of the double perovskite films made using AACVD with those made by the widely used spin-coating method. Films with purer crystalline phase (less CsI impurity) and far better stability in ambient air can be obtained by AACVD compared with spin coating. The AACVD-grown Cs_2SnI_6 films retain high phase purity for at least ~100 days aging in air with negligible CsI impurities detected over this time, as determined by X-ray diffraction. The films exhibit an optical band gap energy (E_g) of *ca.* 1.3 eV and a homogeneous morphology with the expected nominal stoichiometry within error, as probed by energy-dispersive X-ray spectroscopy. Overall, the characteristics of the Cs_2SnI_6 films are highly process-dependent, *e.g.* they are influenced by the presence of hydroiodic acid (HI) in the precursor solution. Without HI addition, an iodine-deficient film with more CsI is produced, which also exhibits a larger E_g of *ca.* 1.6 eV. In addition to bulk properties, we utilise X-ray photoelectron spectroscopy (XPS) to scrutinise the surface characteristics in detail. We find excess Sn and I located at the surfaces. This can be attributed to the presence of SnI_4 from the deposition precursor vapour. Furthermore, following aging in air, an increase in CsI impurity for the AACVD (+HI)-grown film is observed, along with a reduction in SnI_4 at the surfaces. Near-ambient pressure XPS (NAP-XPS) is used to examine the surface stability of AACVD (+HI)-grown films on exposure to O_2 and H_2O. No enhancement in the amount of CsI impurity is observed after both H_2O vapour (9 mbar) and O_2 (5 mbar) exposure. Nevertheless, the concentrations of tin and iodine change after exposure, suggesting that SnI_4 protects Cs_2SnI_6 from degradation. This passivation effect of SnI_4 on Cs_2SnI_6 surfaces is proposed to explain the additional stability of Cs_2SnI_6 fabricated *via* AACVD.

Received 5th April 2018
Accepted 9th May 2018

DOI: 10.1039/c8ta03133a

rsc.li/materials-a

1 Introduction

In recent years, perovskite solar cells (PSCs) have attracted tremendous attention,[1–8] since the first description by Kojima *et al.* in 2009.[9] Within a decade, this type of photovoltaic technology has undergone unprecedented advances in certificated power conversion efficiency (PCE), which has reached more than 20%.[4–7] As a result, the PSCs are considered to be highly promising candidates for reduction in the cost per watt of commercial solar-energy-conversion devices. Nevertheless, there are two dominant concerns still constraining the development of PSC commercialisation: toxicity and stability. To date, all of the most efficient PSCs have been composed of lead-containing light absorbers, potentially resulting in serious human-body and environmental damage. Consequently, developing lead-free perovskite materials for use in PSCs is preferable to reduce the toxicity of photovoltaic devices. In addition, the instability/degradation of typical perovskite materials, particularly when placed in a humid environment is extremely problematic;[10] upon exposure to moisture, the most widely used organolead perovskite, methylammonium lead (tri-)iodide (MAPI), degrades into lead iodide with a complete loss of the nitrogen moiety.[11] Many attempts to improve the stability of halide perovskites have been investigated by a variety of approaches, including the use of alternative lead precursors,[12] mixed cations,[13,14] and fabrication of two-dimensional perovskites.[15] Nonetheless, the stability still lags behind industrial photovoltaic standards which typically require a <10% loss in power generation after utilisation of 20 years.[16] Therefore, the synthesis of stable halide perovskite films for use in photovoltaics is essential for the future development of PSCs.

[a]School of Physics and Astronomy, The University of Manchester, Manchester M13 9PL, UK. E-mail: wendy.flavell@manchester.ac.uk
[b]Photon Science Institute, The University of Manchester, Manchester M13 9PL, UK. E-mail: andrew.g.thomas@manchester.ac.uk
[c]School of Materials, The University of Manchester, Manchester M13 9PL, UK
[d]School of Chemistry, The University of Manchester, Manchester M13 9PL, UK

† Electronic supplementary information (ESI) available. See DOI: 10.1039/c8ta03133a

Among lead-free halide perovskite materials, tin-based perovskites are widely investigated as tin is a group IV metal and can be isoelectronic with lead. The first pure organo-Sn PSC was reported in 2014 with an initial PCE of approximately 6%.[17] However, compared to organo-Pb PSCs, organo-Sn PSCs show not only lower PCEs but even poorer atmospheric stability (typically showing degradation within an hour).[17] To stabilise Sn perovskites, it is possible to replace the unstable organic cation (*e.g.* methylammonium, MA) with inorganic metal ions such as caesium (Cs). However, the PCEs of $CsSnI_3$ PSCs are typically below 4%,[18–20] with a current champion PCE of 4.8% reported recently.[21] The stability with respect to oxidation is poor owing to the fact that Sn^{2+} in $CsSnI_3$ (or $MASnI_3$ *etc.*) is readily oxidised to Sn^{4+}.[20] Therefore, the Sn-deficient derivative perovskite, Cs_2SnI_6, has been investigated as one of the most promising Pb-free light absorbers in very recent years. This is due to the tetravalent Sn in the Cs_2SnI_6 structure, which cannot be further oxidised. As a result, the Cs_2SnI_6 double perovskite can offer far better stability under atmospheric conditions containing oxygen and water vapour.[22–30]

The Cs_2SnI_6 double perovskite which is ambipolar (*i.e.* it can be doped as n-type or p-type) exhibits excellent carrier mobility when doped as an n-type semiconducting material. In addition, it has a relatively low optimised energy band gap (E_g) of *ca.* 1.3 eV and high absorption coefficient (of over 10^5 cm^{-1} for energies above 1.7 eV), which shows great potential for use as a light absorber in photovoltaic devices.[22–24] Very recently, using a special architecture, Cs_2SnI_6-based solar cells with PCEs of *ca.* 2.0% and acceptable stability in air have been reported.[23] By doping Br into the structure, a higher PCE of *ca.* 5.2% has been reported for $Cs_2SnBr_xI_{6-x}$ ($x = \sim 2$).[31] Nevertheless, many discrepancies in the properties of Cs_2SnI_6 have arisen, such as variations in E_g between 1.3 eV and 1.6 eV and carrier mobility (varying over the range 1–310 cm^2 V^{-1} s^{-1}), which are both found to be highly process-dependent.[22–25] Lee *et al.* demonstrated that different CsI-impurity levels lead to variations in the band gap energies, carrier concentrations and mobilities, which can be controlled by preparation methods.[23] Given the improvement in Pb-based perovskites, one may envisage the potential to obtain high quality Cs_2SnI_6 thin films with favourable characteristics for use in photovoltaics using novel preparation approaches.

Aerosol-assisted chemical vapour deposition (AACVD) is a promising process for fabrication of perovskite thin films (one-step[32–34] and two-step processes[35,36]), since it merges the advantages from solution-based methods (low cost) and chemical vapour deposition (high quality, controlled thickness).[37–40] Nonetheless, until now, AACVD studies of halide perovskites are still limited since Lewis *et al.* first introduced AACVD-grown organo-Pb perovskite thin films.[32–35] A detailed study of AACVD-grown Sn-based perovskites, which includes characterisation of their bulk and surface properties and surface stability/degradation has not been reported thus far. In this work, we utilise a one-step AACVD process to fabricate high quality Cs_2SnI_6 thin films for the first time. A thorough study of the fabrication and characterisation of Cs_2SnI_6 material is also provided. By applying this facile, scalable process, films with high purity and uniformity can be obtained. The growth of films at a relatively low temperature of 150 °C is well adapted to flexible device applications,[41–45] when compared to vacuum deposition (190 °C).[25] We also demonstrate the importance of addition of hydroiodic (HI) acid to the precursor solution to afford Cs_2SnI_6 films with a reduced number of macroscopic defects such as pinholes. Iodine vacancies (V_I) are easily formed as well as tin interstitials (Sn_i) in this material.[29] HI is selected for two reasons: firstly, it is an ideal iodine source to afford I-rich Cs_2SnI_6 material. Secondly, using excess SnI_4 to supply iodine could potentially lead to deleterious formation of Sn_i. We also employ near-ambient pressure X-ray photoelectron spectroscopy (NAP-XPS) to measure the *in situ* degradation of the AACVD-grown films prepared with the addition of HI. By combining XPS data from a number of experiments, we show that surface passivation through a layer containing excess Sn and I is one factor imparting stability of the Cs_2SnI_6 films. These insights will help the future development to Pb-free halide perovskites for use in photovoltaic devices.

2 Experimental

2.1 Sample preparation

Firstly, 0.5196 g of caesium iodide (CsI, 99.9%, Aldrich) was added into 10 mL of warm (~70 °C) anhydrous *N*,*N*-dimethylformamide (DMF, 99.8%, Sigma-Aldrich) solvent with gentle stirring to generate a clear pale-yellow solution (0.2 M). A stoichiometric amount (0.6263 g, 0.1 M) of tin(IV) iodide (SnI_4, 99.999%, Aldrich) was poured into the solution. The colour of the precursor solution immediately became dark brown and then black after a few minutes. A small amount (300 μL, 0.2 M) of hydroiodic acid (HI, 57 wt%, Aldrich) was added to produce an I-rich solution (denoted as +HI). Another precursor solution was prepared without the addition of HI (denoted as −HI) for comparison. The resulting solutions were used for the AACVD process or spin-coating.

The prepared solution was directly used as the feed for AACVD without further procedures. The apparatus used for AACVD has been previously described in detail by Ramasamy *et al.*[46] Firstly, 10 mL of the DMF solution was poured into a two-necked 100 mL round-bottom flask with a gas inlet. This allows Ar carrier gas (flow rate ~300 sccm) to pass into the solution to support the transport of aerosol generated by a humidifier. This flask was connected to a tube in a furnace where the temperature during deposition was set to 130 °C. Indium tin oxide (ITO)-coated glass (Ossila) with a size of 2.0 × 1.5 cm or gold-coated silicon (Au–Si) were utilised as substrates. The deposition rate was approximately 20 nm per minute as measured by a Veeco Dektak 8 Surface Profilometer and the deposition time was set for an hour. As a result, we obtained films with a thickness of around 1.2 μm on the substrates. Following the deposition, the samples were annealed at 150 °C in ambient air to remove residual solvent from the samples and tube for 30 minutes. The sample was then allowed to cool to below 100 °C before removal from the AACVD tube. The prepared samples were placed into (sample) tubes filled with Ar and then stored in a small desiccator. For the aging study, the films were aged in ambient air at

an average relative humidity (RH) of >70% for periods up to ~100 days. All fresh samples were exposed to ambient air for less than 10 minutes when transferring from the growth tubes to a characterisation chamber.

A small volume (100 μL) of the same precursor solutions (+HI) was also used to prepare spin-coated films of similar (~1.2 μm) thickness for comparison. The films were deposited at 4000 rpm for 30 seconds and subsequently transferred to a hot plate for annealing at 150 °C in air for 30 minutes. The resultant samples were stored or aged in the same way as the AACVD-processed samples.

2.2 Instrumentation

X-ray diffraction (XRD) patterns were recorded using a Bruker D8 Advance. A grazing incidence (GI) angle of 3° was used to detect the signals from the thin films without the substrates. The scanning range (2θ) was recorded from 5° to 80° with a step size of 0.05° and dwell time of 4.5 s.

The morphology of the films was measured using scanning electron microscopy (SEM) and bulk elemental analysis was carried out using an energy-dispersive X-ray spectroscopy (EDX, Philips XL30 equipped with a DX4 EDX spectrometer). EDX was conducted in the SEM chamber and the error in bulk stoichiometry measurements was ±2%.

Optical diffuse reflectance measurements were performed using an ultra-violet-visible-near-infra-red (UV-VIS-NIR) spectrometer (PerkinElmer Lambda-1050) with an integrated sphere (IS) module to collect the scattered light. Spectra were recorded over a wavelength range of 300 to 1500 nm from samples deposited on soda-lime glass substrates. Reflectance (R) was automatically converted to absorption (α) data in accordance with the Kubelka–Munk equation. The optical energy band gap (E_g) was acquired using a Tauc plot to find the onset point of the absorption spectra.

X-ray photoelectron spectroscopy (XPS) measurements were performed with either a Kratos Axis Ultra or SPECS XPS instrument. Both facilities are equipped with monochromated Al Kα X-ray sources with a photon energy of 1486.6 eV. Emitted photoelectrons were collected using either a 165 mm hemispherical energy analyser (Kratos) or a 150 mm hemispherical energy analyser (Phoibos 150 SPECS), respectively. All measurements conducted in this section were carried out in ultra-high vacuum (UHV) conditions. Binding energies (BEs) were calibrated to C 1s from adventitious carbon at 284.8 eV for ITO-glass substrates or Au $4f_{7/2}$ at 84.0 eV for Au–Si substrates.

The SPECS instrument also allows for NAP-XPS measurements to be carried out and the details can be found elsewhere.[11] The NAP cell is equipped with differential pumping to enable gas pressures up to ~15 mbar to be applied during measurement. In this work, 9 mbar water vapour (RH = ~30%) and 5 mbar oxygen were separately applied. All XPS data were analysed using CasaXPS software, in which a Shirley background and pseudo-Voigt peaks (30% Lorentzian and 70% Gaussian) were fitted to the photoelectron peaks acquired.[47]

BE values are quoted to an accuracy of ±0.1 and ±0.05 eV for typical and *in situ* XPS study, respectively, due to instrumental precision. To obtain quantified surface compositional information, the built-in CasaXPS sensitivity factors (Kratos, relative to F 1s as 1.0) are utilised for calculating the available stoichiometry. Note that this does not allow the quantitative analysis of spectra acquired at near-ambient pressure (NAP) conditions due to the absence of adapted transmission-function data. All surface elemental concentrations are normalised to Cs (Cs $3d_{5/2}$ spectra) as 2 in an ideal stoichiometric Cs_2SnI_6 film. Excess concentrations of Sn and I above 1 and 6, respectively are likely to indicate the presence of non-Cs_2SnI_6 species.

3 Results and discussion

Following annealing under ambient air in the AACVD reactor, highly uniform and black AACVD (+HI)-processed Cs_2SnI_6 films were formed, as shown in Fig. 1A. This indicates strong visible-light absorption by the as-prepared AACVD (+HI)-grown Cs_2SnI_6 film as the part of the logo covered by the film is barely visible. Following ~100 days storage under ambient air (average RH > 70%), the appearance of the film (Fig. 1B) is similar to the fresh sample (Fig. 1A). This suggests that there is no significant change in the visible light absorption of the film after being aged in a humid environment. Peeling and scratching tests suggest that the AACVD films produced here show significantly better adhesion to the substrates than the spin-coated films prepared under similar conditions (see ESI, Fig. S1†).

In order to determine the crystalline phase, grazing incidence X-ray diffraction (GIXRD) patterns of various films (Fig. 2) were examined. Fig. 2A shows XRD reflections of a typical AACVD (+HI)-grown film as a function of aging time (up to ~100 days). For the pristine sample, the XRD peaks indicate that the crystal structure is in excellent agreement with the Cs_2SnI_6 double perovskite structure (JCPDS no. 51-0466, cubic, space group $Fm3m$, a = 11.65 Å).[26] The dominant (strongest) diffraction peak from the (222) crystal plane at 26.55° and other primary peaks such as (400) are also annotated in the figure. The face-centred-cubic double perovskite structure (with Sn deficiency at the centre) increases the intensity of the (222)

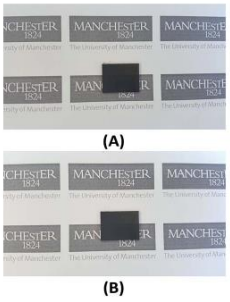

Fig. 1 Photographs of an AACVD (+HI)-grown Cs_2SnI_6 film on ITO-glass substrates: (A) as-deposited (B) after aging in ambient air for ~100 days. The thicknesses of the films are around 1.2 μm.

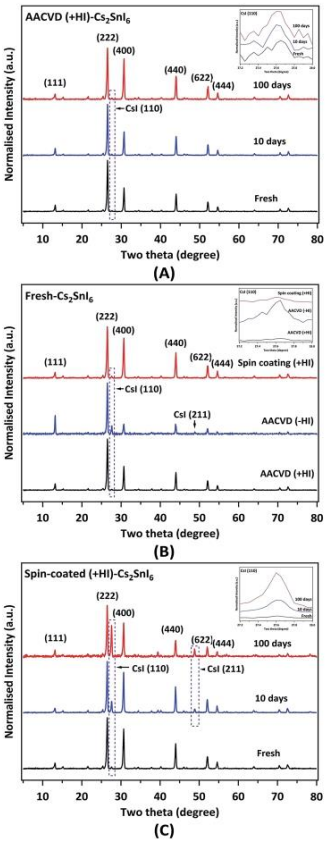

Fig. 2 XRD patterns of Cs_2SnI_6 films on ITO-glass substrates recorded with a grazing incidence (GI) angle of 3° showing: (A) the effect of aging in air (RH > 70%) on AACVD (+HI)-processed film, (B) samples obtained from different precursor solutions and deposition processes (as annotated), and (C) the effect of aging on a spin-coated sample. The primary peaks for both Cs_2SnI_6 and CsI are indicated; the purple dashed squares highlight the 2θ range for the dominant (strongest) reflection of the CsI impurity. The top-right inset in each figure shows the expansion of the CsI (110) region.

reflection relative to the (111) reflection.[22] A more detailed examination reveals a diffraction peak due to the (110) reflection from a trace amount of the cubic CsI impurity at 27.60° (JCPDS no. 89-4257).[48] The amount of this contaminant is very low in fresh samples (Fig. 2A), suggesting that the AACVD process allows formation of highly pure Cs_2SnI_6 crystalline films. In addition, we observe that the AACVD (+HI)-processed film appears to be highly stable following ~10 and ~100 days exposure to air (Fig. 2A). The amount of CsI impurity remains low and there are no other new crystalline phases generated. The ratios of the intensity of the CsI (110) reflection to that of the Cs_2SnI_6 (220) reflection are summarised in Table 1. This highlights the relatively small change in the amount of CsI impurity when aged in ambient air. As shown, the ratio is in the vicinity of ~0.020 after 100 days' aging, showing that AACVD (+HI)-processed Cs_2SnI_6 is significantly more stable than the widely used methylammonium lead iodide perovskite. MAPI is easily transformed to lead iodide (PbI_2) under ambient air within a week due to reaction with moisture in the environment.[49]

Fig. 2B shows the effect on crystal structure produced by the addition of HI in the precursor solution. In the absence of HI, a noticeable amount of CsI impurity is present ($I_{CsI(110)}/I_{Cs_2SnI_6(222)} = \sim 0.160$, 10 times more than that observed in the AACVD (+HI)-grown films, as shown in Table 1). This indicates that the synthesis process (+HI or −HI) can significantly influence the crystalline phase composition. In the relatively I-poor environment (−HI), iodine vacancies (V_I) can form more easily.[29] A density functional theory (DFT) study suggests V_I and interstitial tin (Sn_i) are the dominant defect types in Cs_2SnI_6.[29] The optimised molar concentration of HI in the precursor solution to minimise the CsI impurity phase was found to be 0.2 M, as described in the Experimental section. The concentration is roughly equivalent to twice the SnI_4 precursor molar concentration, in good agreement with the following reaction for formation of $[SnI_6]^{2-}$ octahedra in Cs_2SnI_6:[50]

$$SnI_4 + 2I^- \rightarrow [SnI_6]^{2-} \quad (1)$$

Thus it appears that excess iodine (in an I-rich environment) facilitates the formation of the $[SnI_6]^{2-}$ sub-lattice of the Cs_2SnI_6 double perovskite material. Not only do the different preparation methods lead to distinct phase compositions but the stability can also be affected by the thin film deposition method. The preparation route used to synthesise Cs_2SnI_6 has been shown to be a critical factor governing its stability.[25] Samples prepared by spin coating were found to contain a significant CsI impurity phase after only 5 days under ambient air.[22,25] Fig. 2C shows the effect of aging in ambient air on samples prepared by spin coating. There is a significant increase in CsI content with aging compared to the AACVD (+HI)-processed sample. The $I_{CsI(110)}/I_{Cs_2SnI_6(222)}$ ratio of the pristine spin-coated (+HI) film is attributed to a slightly higher initial impurity level (~0.034) relative to that of the pristine AACVD (+HI)-grown film. After 100 days, a substantial amount (~0.600) of CsI is observed in the spin-coated film. As described, the precursor solution (+HI) and the annealing process are identical between the AACVD and spin-coating processes. Therefore, the difference in stability can be attributed to the method used to prepare the thin films. The amount of CsI appearing with time in the AACVD (+HI)-processed samples is compared with the results of Saparov *et al.* for films deposited by vacuum deposition in Fig. S2 (ESI†).[25] This suggests that the stability of the Cs_2SnI_6 films fabricated by AACVD is comparable to or even better than that of films made *via* vacuum vapour deposition.[25] We note that the AACVD (+HI)-grown films were

Table 1 Summary of the results from characterisation of the different samples: $I_{CsI(110)}/I_{Cs_2SnI_6(222)}$ indicates the ratios of the intensity of CsI (110) to Cs_2SnI_6 (222) reflections from the XRD patterns. Elemental bulk stoichiometries (atomic) Cs/Sn and I/Sn are obtained from EDX. The optical energy bandgaps (E_g) are acquired from Tauc plots of the absorption spectra. The ratios of CsI to Cs_2SnI_6 at the surface, acquired from XPS of the Cs 3d signal (Kratos) are also shown. Note '—' means no data available

Sample ID	$I_{CsI(110)}/I_{Cs_2SnI6(222)}$ (XRD)	Cs/Sn (EDX)	I/Sn (EDX)	E_g	CsI/Cs_2SnI_6 (XPS)
AACVD (+HI) fresh	0.016 ± 0.002	2.0 ± 0.1	6.0 ± 0.2	1.30	0.14 ± 0.01
AACVD (+HI) 10 days	0.021 ± 0.002	2.0 ± 0.1	5.9 ± 0.2	—	—
AACVD (+HI) 100 days	0.024 ± 0.002	2.0 ± 0.1	5.8 ± 0.2	1.35	0.20 ± 0.02
AACVD (−HI) fresh	0.160 ± 0.020	1.9 ± 0.1	5.6 ± 0.2	1.60	0.34 ± 0.03
Spin-coated (+HI) fresh	0.034 ± 0.003	2.0 ± 0.1	5.8 ± 0.2	1.35	0.21 ± 0.02
Spin-coated (+HI) 10 days	0.218 ± 0.020	1.9 ± 0.1	5.4 ± 0.2	—	0.35 ± 0.04
Spin-coated (+HI) 100 days	0.600 ± 0.060	1.9 ± 0.1	4.9 ± 0.2	1.60	—

placed in an ambient environment with higher relative humidity (R.H. > 70%) when compared to the environment in the work of Saparov and others.[25] These results suggest that AACVD (+HI) can produce Cs_2SnI_6 double perovskite films that are stable in humid air.

Nevertheless, films prepared by both AACVD and spin-coating were degraded (to a lesser or greater extent) producing CsI when aged in ambient air. This may imply a bulk decomposition mechanism:

$$Cs_2SnI_6 \rightarrow 2CsI + SnI_4. \quad (2)$$

Clearly, to generate CsI by decomposition of Cs_2SnI_6, SnI_4 should be formed in accordance with this reaction. However, no peaks which can be assigned to SnI_4 are observed in the XRD patterns. This may be because SnI_4 is somehow absent, which we discuss in later sections. In order to determine whether the film quality could be influencing the stability of the films, the morphology of the as-prepared films was examined using SEM, as shown in Fig. 3. The crystal structures at high magnification for samples produced by AACVD (+HI), AACVD (−HI), and spin-coating (+HI) are shown in Fig. 3A, C, and E, respectively. All of the samples show micrometre-sized octahedral grains; however, the average size of the grains is larger for the AACVD (+HI)-Cs_2SnI_6 film. The shape of the crystals in films made without HI is less well-defined, with what appears to be melted material at the surface.

SEM shows that the different processing techniques lead to differences in grain sizes. Larger grain sizes for the AACVD (+HI)-Cs_2SnI_6 film have a lower overall surface-to-volume ratio, and are thus more resilient to atmospheric degradation partially contributing to an enhanced stability. By measuring grain sizes for the different films, we estimate that the surface area of the AACVD (+HI)-grown film (Fig. 3A) is approximately 16× that of the film prepared by spin coating (Fig. 3E). However, the rate of degradation of the spin-coated film is *ca.* 70× that of the AACVD (+HI)-prepared film, as estimated from XRD (Fig. S2†). This suggests that additional factors are important in determining the stability of the AACVD-prepared films.

At a lower magnification, the homogeneity of the films is shown in Fig. 3B, D, and F. The AACVD (+HI)-processed film (Fig. 3B) is very smooth, uniform, and (relatively) pin-hole free, which is important to its application as a light absorber in photovoltaic devices.[51] The other two samples (Fig. 3D and F, AACVD (−HI) and spin-coated (+HI) respectively) show higher roughness, less homogeneity, and more pinholes. This could also contribute to differences in the stability between AACVD and spin-coated samples. Degradation sources such as water vapour or oxygen are able to enter the bulk *via* pinholes or pores more easily. This is consistent with the rapid and more obvious degradation of the spin-coated film as measured by XRD compared to the AACVD-grown films.

The bulk stoichiometries of the films, as determined by energy-dispersive X-ray (EDX) spectroscopy, are also shown in Table 1. The AACVD (+HI)-prepared sample has the expected elemental stoichiometry of ideal Cs_2SnI_6 within experimental error. The Cs : Sn ratios for all samples are very similar, and lie in the range 1.9–2.0. This suggests that if Cs_2SnI_6 is converted

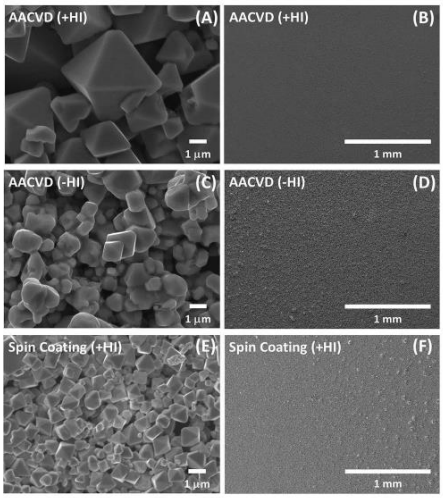

Fig. 3 SEM images of fresh Cs_2SnI_6 films on ITO-glass substrates (A & B) AACVD (+HI)-processed film, (C & D) AACVD (−HI)-grown film, and (E & F) spin-coated (+HI) film at higher (A, C & E) and lower (B, D & F) magnifications.

into CsI, the CsI impurity and Sn degradation products remain in the film since it is unlikely that both are lost at the same rate. Nevertheless, the ratios of iodine to tin do show some variations, indicating a clear loss of iodine with aging for the spin-coated sample. Moreover, the slight lack of iodine in the fresh AACVD (−HI)-grown sample indicates that in an I-poor environment, V_I defects tend to be generated.

The optical band gap energies (E_g) of the films were determined using ultraviolet-visible-near-infrared (UV-VIS-NIR) spectroscopy. The Tauc plots (Fig. 4) were obtained from the absorption spectra transformed from the diffuse reflection spectra *via* the Kubelka–Munk function. Cs_2SnI_6 is typically referred to as a direct bandgap material, which has been confirmed by photo-luminescence results.[22,23,52] By determining the onset of the plots, the value of E_g was obtained for the different samples. In Fig. 4A, we observe that the AACVD (+HI)-grown Cs_2SnI_6 film has a bandgap of *ca.* 1.30 eV, which is consistent with the smallest value in the range previously reported (1.3–1.6 eV).[22–25,52,53] Following aging for ~100 days, the band gap energy increases slightly to *ca.* 1.35 eV. More significant differences are observed in comparing films prepared with and without the addition of HI. Fig. 4B shows that the AACVD (−HI)-prepared sample has a relatively high E_g of *ca.* 1.60 eV. This again suggests that iodine deficiency or the presence of CsI impurities can significantly influence the properties of the Cs_2SnI_6 thin films. It can be observed in Table 1 that an increase in CsI impurity level leads to higher E_g, in good agreement with a recent finding.[23] Lee *et al.* found that, by using spin-coating with different parameters, varying levels of CsI impurity were formed in Cs_2SnI_6 films.[23] This results in a range of E_g values from 1.3 to 1.4 eV as well as differences in carrier concentration and mobility.[23] Our study further demonstrates that the characteristics of Cs_2SnI_6 films are highly process and defect dependent. Therefore, innovation in the preparation of Cs_2SnI_6 films is of importance in optimising these characteristics.

These results illustrate the effects of degradation and the intrinsic differences between the bulk properties of the films prepared by various methods. The surface characteristics are equally important since degradation occurs at the solid–vapour interfaces first, where the surfaces are in contact with degradation-inducing reactants. The X-ray photoelectron spectra (XPS) shown in Fig. 5 depict the surface compositions of various fresh and aged films obtained by recording the Cs 3d core levels. Two components, giving rise to two $3d_{5/2,3/2}$ doublets, are observed for all of the double perovskite samples, both fresh and aged. The higher and lower binding energy (BE) Cs $3d_{5/2}$ components, located at 725.1 ± 0.1 eV and 724.2 ± 0.1 eV, can be attributed to CsI and Cs_2SnI_6, respectively.[54] The assignment of the CsI features is also confirmed by comparison with spectra of a spin-coated pristine CsI film, also shown in Fig. 5. Moreover, we observed that each sample showed different surface CsI-impurity levels; spectra of films with a significant amount of CsI show pronounced high-binding-energy shoulders in the Cs 3d peaks ($3d_{5/2}$ and $3d_{3/2}$). In order to easily compare, the area ratios of the CsI to Cs_2SnI_6 Cs $3d_{5/2}$ components fitted are summarised in Table 1. The amount of CsI surface impurity in the AACVD (+HI)-prepared sample increases only slightly after aging for ~100 days (CsI : Cs_2SnI_6 increases from 0.14 ± 0.01 to 0.20 ± 0.02). By contrast, that of the spin-coated film significantly increases (corresponding ratios 0.21 ± 0.02 to 0.35 ± 0.04) as a result of aging for a much shorter period (10 days).

This indicates the surface stability of the AACVD (+HI)-grown film is better than the spin-coated one, and this is consistent with the findings from the bulk properties. Interestingly, we observe that the CsI : Cs_2SnI_6 ratio in the fresh sample fabricated without HI (0.34 ± 0.03) is similar to that of the aged spin-coated sample. These observations suggest that the presence of CsI impurity at the surfaces is strongly influenced by the preparation process. Table 1 shows that the variations between films in the relative amount of CsI impurity found at the surface are similar to the trends observed in the bulk. While we cannot directly compare the concentrations determined from XPS with

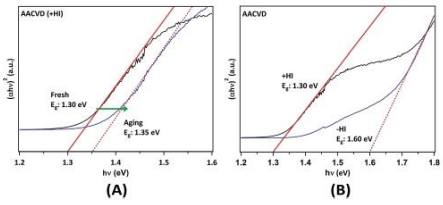

Fig. 4 Tauc plots from the UV-VIS-NIR spectra of AACVD-grown Cs_2SnI_6 thin films obtained *via* the Kubelka–Munk equation by taking Cs_2SnI_6 as a direct band gap semiconductor: (A) the fresh and aged AACVD-prepared film and (B) with (+HI) and without (−HI) HI addition in the precursor solutions.

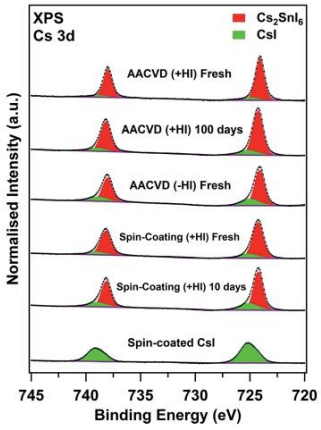

Fig. 5 XPS spectra of the Cs 3d region for various Cs_2SnI_6 samples and a spin-coated CsI film for reference. All spectra are normalised to the integrated area of the overall Cs $3d_{5/2}$ peaks (Cs_2SnI_6 + CsI).

the ratio $I_{CsI(110)}/I_{Cs_2SnI_6(222)}$ obtained from XRD, we note that for the AACVD (+HI)-grown films, the surface CsI : Cs_2SnI_6 ratio is approximately ten times that of $I_{CsI(110)}/I_{Cs_2SnI_6(222)}$, whereas for the more degraded films this factor is lower (approximately 2–5). This suggests that in the initial stages of degradation, CsI is localised at the film surfaces.

In addition to the amounts of CsI impurity, the stoichiometry of the other elements is of importance in understanding the surface compositions of the various films, and is shown in Table S1.† In order to easily observe deviations from stoichiometry at the surface of the films, we normalise the calculated ratios of the elements to [Cs] = 2.0 (*i.e.* $Cs_2Sn_xI_y$), as for an ideal stoichiometric Cs_2SnI_6 film. We found that all samples, whether fresh or aged, and regardless of preparation method contain excess Sn ([Sn] > 1). These Sn atoms could originate from the SnI_4 precursor as we also observe excess I at the surface in all samples. For the fresh AACVD (+HI)-grown sample, the excess I is close to 4 times the excess Sn. This suggests the presence of SnI_4 in significant excess, as the excess values for I and Sn are high. In addition, the amount of SnI_4 is far more than that of CsI, suggesting that the majority of the SnI_4 does not originate from the decomposition process in eqn (2). As fresh AACVD-grown films have a larger excess of I and Sn, we speculate that the residual SnI_4 vapour in the AACVD tube attaches to the outermost surfaces of the film. This may occur particularly during the cooling process at temperatures of ~100-150 °C, when the reaction between SnI_4 and CsI cannot happen. The more volatile component, SnI_4,[50] continues to be transported along the tube and condenses on the surface of the film during the cooling cycle. The relative changes in Sn concentration can also be observed in Fig. S3† by comparing the intensities of the Cs $3d_{5/2}$ and Sn $3p_{3/2}$ peaks.

After aging the AACVD-grown film in ambient air, the excess Sn decreases somewhat while the concentration of excess I is very significantly reduced. This suggests the SnI_4 at the surfaces undergoes decomposition (loss of iodine) with I_2 or HI release from the film by some mechanism. SnI_4 is known to be easily hydrolysed in the presence of water, so the SnI_4 at the surfaces is expected to react with moisture, forming hydrated SnO_2 ($SnO_2 \cdot nH_2O$).[55–58] By comparison, the changes in the surface composition of the spin-coated film on aging are much smaller, starting from a smaller initial excess of Sn and I. This reinforces the suggestion that the excess SnI_4 on the surfaces of the AACVD-prepared samples is due to the nature of the process. Interestingly, the fresh AACVD (−HI)-grown sample contains a very significant amount of excess Sn but a lower excess of I compared to the fresh AACVD (+HI)-prepared film, consistent with the EDX finding. The large excess of Sn could be due to a significant amount of I-deficient tin iodide, and I-deficient Sn sites within the perovskite phase. This also suggests again that without addition of HI, the formation of Cs_2SnI_6 cannot be facilitated as per eqn (1).

It is clear that changes in surface composition of the films are observed after aging in air even for the relatively stable AACVD (+HI)-grown sample. It is therefore of interest to identify which gases in air (*e.g.* H_2O vapour or O_2) are responsible for the surface degradation. NAP-XPS is a novel technique which allows investigation of the surface stability and degradation mechanisms of halide perovskite materials.[11] This is because this technique enables the surface composition of the films to be measured under near-ambient pressure (NAP) conditions in a chamber filled with specific gases, and changes during gas exposure can be determined. In this study, the effects of water vapour and oxygen were explored. The Cs 3d NAP-XPS spectra recorded from fresh AACVD (+HI)-grown Cs_2SnI_6 films during and after exposure to O_2 (5 mbar) and water vapour (9 mbar, corresponding to ~30% RH at 25 °C) are shown in Fig. 6. The two samples were prepared from the same initial sample by cutting it into two pieces. Following water vapour exposure (Fig. 6A), we observe that the CsI component does not increase relative to Cs_2SnI_6. Similarly, no obvious change was found in the Cs 3d spectra before and after the film was exposed to O_2. These results suggest under those environments, the films do not degrade significantly *via* the mechanism in eqn (2), which should form CsI and SnI_4.

This is possibly as a result of insufficient exposure time as well as the limited gas pressure in the chamber. However, as compared to similar studies of MAPI, it is clear that Cs_2SnI_6 shows higher resistance to moisture when both films are exposed to environments with a RH of ~30%.[11] Cs remains at the surfaces of the Cs_2SnI_6 film, whereas the equivalent 'A' cation in the ABX_3 perovskite structure of MAPI, the methylammonium ion ($CH_3NH_3^+$), decomposes and nitrogen is lost from the surfaces of the film in the form of ammonia gas. Other

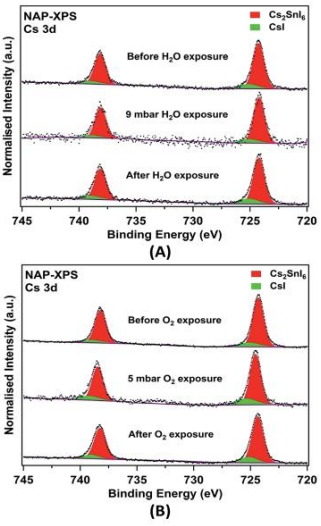

Fig. 6 NAP-XPS Cs 3d core-level spectra of AACVD (+HI)-grown films before, during, and after exposure to (A) 9 mbar H_2O vapour and (B) 5 mbar O_2. All spectra are normalised to the Cs $3d_{5/2}$ peak areas for comparison.

Table 2 Ratios of the concentrations of different components in a fresh AACVD (+HI)-prepared film determined from NAP-XPS before and after exposure to 9 mbar H_2O or 5 mbar O_2. All elements are normalised to [Cs] = 2.0, consistent with Table 1. Excess Sn (excess I) refers to the amount of SnI that cannot be accounted for in the Cs_2SnI_6 (Cs_2SnI_6 + CsI) phase(s)

Fresh AACVD (+HI)	CsI/Cs_2SnI_6	Total Cs	Cs in CsI	Cs in Cs_2SnI_6	Sn	I	Excess Sn	Excess I
Ideal stoichiometry	—	—	—	2	1	6	0	0
UHV before H_2O exposure	0.19 ± 0.02	2.4 ± 0.2	0.4 ± 0.1	2.0 ± 0.2	3.8 ± 0.4	14.2 ± 1.0	2.8 ± 0.3	7.8 ± 1.0
UHV after H_2O exposure	0.17 ± 0.02	2.3 ± 0.2	0.3 ± 0.1	2.0 ± 0.2	4.5 ± 0.5	17.4 ± 2.0	3.5 ± 0.4	11.1 ± 1.1
UHV before O_2 exposure	0.15 ± 0.02	2.4 ± 0.2	0.3 ± 0.1	2.0 ± 0.2	1.8 ± 0.2	9.6 ± 1.0	0.8 ± 0.1	3.3 ± 0.3
UHV after O_2 exposure	0.18 ± 0.02	2.3 ± 0.2	0.4 ± 0.1	2.0 ± 0.2	2.3 ± 0.2	9.2 ± 1.0	1.3 ± 0.1	2.8 ± 0.3

core level spectra (I 3d, Sn 3d, C 1s, and O 1s) recorded from the films are shown in Fig. S4† for H_2O vapour and Fig. S5† for O_2 exposure, respectively. In both I and Sn 3d spectra, we do not observe BE changes or new components after exposure. We note, however, that the chemical shifts between Cs_2SnI_6, SnI_4 and CsI cannot be resolved in either I 3d or Sn 3d spectra.[59] In addition, the potential by-product formed by hydrolysis ($SnO_2 \cdot nH_2O$), also has a similar Sn 3d BE to SnI_4 (Sn $3d_{5/2}$ at BEs of ~487.0 eV),[60–63] and therefore cannot be directly observed by XPS. Nevertheless, we can observe relative changes in quantified atomic concentrations after exposure, which are summarised in Table 2. Again, we observe excess Sn and I in both fresh films although the initial stoichiometries are different. This suggests that the amount of SnI_4 attaching on the film surfaces is inhomogeneous and difficult to control in the AACVD process. Nevertheless, the presence of excess Sn and I at the film surfaces is clearly revealed. For both exposure cases, the amount of Sn at the film surface increases during exposure (relative to the amount of Cs). The I concentration increases after the film is exposed to moisture, by an amount consistent with an increase in the concentration of SnI_4 at the surface, whereas I is lost from the surface after exposure to O_2. There are no significant changes in the amount of CsI relative to Cs_2SnI_6 during exposure to H_2O or O_2 (Table 2). Changes are observed in the O content of the surfaces, as shown in Fig. S4, S5 and Table S2;† however, simultaneous accumulation of the C 1s spectra shows that these are largely associated with surface contamination, in particular with hydroxide attached to carbon. We found high levels of hydrocarbon contamination in the fresh films (Table S2†), which can be attributed to ex situ preparation and utilisation of an organic solvent (DMF). We note that it is possible for trace carbon-containing and water contaminants to be introduced during exposure to even very pure gases in NAP-XPS,[64] as is suggested by Table S2.† Thus we cannot rule out the introduction of some H_2O during the O_2-exposure experiment.

The picture that emerges is therefore a complex one, but it is clear that the surface is unstable with respect to Sn and I content during exposure to air. All the fresh AACVD (+HI)-grown films contain an amount of CsI at the surface in excess of that observed in the bulk; however the amount of SnI_4 is considerably in excess of that expected by the simple decomposition reaction in eqn (2). We therefore suggest that the initial 'fresh' surface concentrations are determined by some decomposition, beginning at grain boundaries, to give CsI and SnI_4, supplemented by an excess of Sn and I (largely as SnI_4) from residual precursor attaching during the AACVD growth. In our experiments on surface exposure and aging, we take the results from NAP-XPS to indicate the initial stages of degradation, and those from XPS after 100 days to give information on longer-term effects. The NAP-XPS data suggest that the next stages of degradation involve an increase in surface Sn content, with some indication of further SnI_4 formation or migration from the bulk, while the longer term aging experiments suggest this is followed by hydrolysis of this SnI_4 over the longer term, accompanied by loss of I from the surface. We believe that the large excess of SnI_4 at the surface of the AACVD (+HI)-prepared films provides a passivation functionality that protects Cs_2SnI_6 from degradation when exposed to air. This is reinforced by the absence of any increase (within error) in CsI concentration at the surfaces after exposure to H_2O or O_2 in NAP-XPS, and by the rather small increase in surface and bulk concentrations after 100 days aging in air. This suggests why AACVD-grown films have better stability when they are placed in ambient air compared to those fabricated through spin coating.

To summarise, we propose the decomposition of Cs_2SnI_6 occurs by the following steps: (1) initial decomposition at grain boundaries *via* eqn (2) to produce CsI and SnI_4; (2) some further migration of Sn, possibly as SnI_4 to the outermost surfaces; (3) SnI_4 is consumed by hydrolysis with loss of I_2 or HI; (4) Cs_2SnI_6 is re-exposed due to removal of SnI_4 and therefore decomposed to CsI and SnI_4 in air; (5) excess SnI_4 is consumed again *via* (3).

4 Conclusions

To conclude, we have successfully fabricated ambient-air-stable Cs_2SnI_6 double perovskite films resistive to decomposition in ambient air *via* a novel deposition method, AACVD. Compared to spin-coating, a reduction in the amounts of CsI impurity phase in the films made by AACVD has been demonstrated. We also find that addition of HI to the precursor solution reduces not only the amount of CsI in the film but the overall iodine deficiency. Moreover, the AACVD (HI+)-grown films show superior stability in humid ambient air. No further CsI is formed at the film surface on exposure to up to 9 mbar of H_2O vapour or 5 mbar O_2. We find that excess SnI_4 present at the surfaces of AACVD (+HI)-grown films (most probably from precursor adsorption) may act as a protective layer to prevent Cs_2SnI_6 from degradation. We propose the degradation proceeds by decomposition into CsI and SnI_4, followed by hydrolysis and loss of the latter. Ultimately, this study provides

an insight into novel stable-halide-perovskite fabrication and an understanding of the enhanced stability of Cs_2SnI_6 films made by AACVD.

Conflicts of interest

There are no conflicts to declare.

Acknowledgements

The authors thank the University of Manchester and EPSRC (UK) (grant number EP/K009710) for funding. C. R. Ke thanks the University of Manchester for the award of a President's Doctoral Scholarship. The data associated with this paper are openly available from DOI: 10.17632/77hhc87fnk.1.

Notes and references

1 M. Liu, M. B. Johnston and H. J. Snaith, *Nature*, 2013, **501**, 395–398.
2 H. Chen, F. Ye, W. Tang, J. He, M. Yin, Y. Wang, F. Xie, E. Bi, X. Yang, M. Grätzel and L. Han, *Nature*, 2017, **550**, 92–95.
3 A. Ummadisingu, L. Steier, J.-Y. Seo, T. Matsui, A. Abate, W. Tress and M. Grätzel, *Nature*, 2017, **545**, 208–212.
4 W. S. Yang, B.-W. Park, E. H. Jung, N. J. Jeon, Y. C. Kim, D. U. Lee, S. S. Shin, J. Seo, E. K. Kim, J. H. Noh and S. I. Seok, *Science*, 2017, **356**, 1376–1379.
5 Y. Hou, X. Du, S. Scheiner, D. P. McMeekin, Z. Wang, N. Li, M. S. Killian, H. Chen, M. Richter, I. Levchuk, H. J. Snaith and C. J. Brabec, *Science*, 2017, **358**, 1192–1197.
6 N. Arora, M. I. Dar, A. Hinderhofer, N. Pellet, F. Schreiber, S. M. Zakeeruddin and M. Grätzel, *Science*, 2017, **358**, 768–771.
7 H. Tan, A. Jain, O. Voznyy, X. Lan, F. P. G. de Arquer, J. Z. Fan, R. Quintero-Bermudez, M. Yuan, B. Zhang, Y. Zhao and E. H. Sargent, *Science*, 2017, **355**, 722–726.
8 Z. Wang, Q. Lin, F. P. Chmiel, N. Sakai, L. M. Herz and H. J. Snaith, *Nat. Energy*, 2017, **2**, 17135.
9 A. Kojima, K. Teshima, Y. Shirai and T. Miyasaka, *J. Am. Chem. Soc.*, 2009, **131**, 6050–6051.
10 P. D. Matthews, D. J. Lewis and P. O'Brien, *J. Mater. Chem. A*, 2017, **5**, 17135–17150.
11 J. Chun-Ren Ke, A. S. Walton, D. J. Lewis, A. Tedstone, P. O'Brien, A. G. Thomas and W. R. Flavell, *Chem. Commun.*, 2017, **53**, 5231–5234.
12 Q. Tai, P. You, H. Sang, Z. Liu, C. Hu, H. L. Chan and F. Yan, *Nat. Commun.*, 2016, **7**, 11105.
13 M. Saliba, T. Matsui, J.-Y. Seo, K. Domanski, J.-P. Correa-Baena, M. K. Nazeeruddin, S. M. Zakeeruddin, W. Tress, A. Abate, A. Hagfeldt and M. Graetzel, *Energy Environ. Sci.*, 2016, **9**, 1989–1997.
14 J. W. Lee, D. H. Kim, H. S. Kim, S. W. Seo, S. M. Cho and N. G. Park, *Adv. Energy Mater.*, 2015, **5**, 1501310.
15 H. Tsai, W. Nie, J.-C. Blancon, C. C. Stoumpos, R. Asadpour, B. Harutyunyan, A. J. Neukirch, R. Verduzco, J. J. Crochet, S. Tretiak, M. G. Kanatzidis and A. D. Mohite, *Nature*, 2016, **536**, 312–316.
16 G. Grancini, C. Roldán-Carmona, I. Zimmermann, E. Mosconi, X. Lee, D. Martineau, S. Narbey, F. Oswald, F. De Angelis and M. Graetzel, *Nat. Commun.*, 2017, **8**, 15684.
17 F. Hao, C. C. Stoumpos, D. H. Cao, R. P. Chang and M. G. Kanatzidis, *Nat. Photonics*, 2014, **8**, 489–494.
18 K. P. Marshall, R. I. Walton and R. A. Hatton, *J. Mater. Chem. A*, 2015, **3**, 11631–11640.
19 K. Marshall, M. Walker, R. I. Walton and R. A. Hatton, *Nat. Energy*, 2016, **1**, 16178.
20 M. H. Kumar, S. Dharani, W. L. Leong, P. P. Boix, R. R. Prabhakar, T. Baikie, C. Shi, H. Ding, R. Ramesh and M. Asta, *Adv. Mater.*, 2014, **26**, 7122–7127.
21 T.-B. Song, T. Yokoyama, S. Aramaki and M. G. Kanatzidis, *ACS Energy Lett.*, 2017, **2**, 897–903.
22 B. Lee, C. C. Stoumpos, N. Zhou, F. Hao, C. Malliakas, C.-Y. Yeh, T. J. Marks, M. G. Kanatzidis and R. P. Chang, *J. Am. Chem. Soc.*, 2014, **136**, 15379–15385.
23 B. Lee, A. Krenselewski, S. I. Baik, D. Seidman and R. P. Chang, *Sustainable Energy Fuels*, 2017, **1**, 710–724.
24 X. Qiu, B. Cao, S. Yuan, X. Chen, Z. Qiu, Y. Jiang, Q. Ye, H. Wang, H. Zeng, J. Liu and M. G. Kanatzidis, *Sol. Energy Mater. Sol. Cells*, 2017, **159**, 227–234.
25 B. Saparov, J.-P. Sun, W. Meng, Z. Xiao, H.-S. Duan, O. Gunawan, D. Shin, I. G. Hill, Y. Yan and D. B. Mitzi, *Chem. Mater.*, 2016, **28**, 2315–2322.
26 A. Wang, X. Yan, M. Zhang, S. Sun, M. Yang, W. Shen, X. Pan, P. Wang and Z. Deng, *Chem. Mater.*, 2016, **28**, 8132–8140.
27 A. E. Maughan, A. M. Ganose, M. M. Bordelon, E. M. Miller, D. O. Scanlon and J. R. Neilson, *J. Am. Chem. Soc.*, 2016, **138**, 8453–8464.
28 M. J. Ashley, M. N. O'Brien, K. R. Hedderick, J. A. Mason, M. B. Ross and C. A. Mirkin, *J. Am. Chem. Soc.*, 2016, **138**, 10096–10099.
29 Z. Xiao, Y. Zhou, H. Hosono and T. Kamiya, *Phys. Chem. Chem. Phys.*, 2015, **17**, 18900–18903.
30 F. Giustino and H. J. Snaith, *ACS Energy Lett.*, 2016, **1**, 1233–1240.
31 M. G. Kanatzidis, R. P. H. Chang, K. Stoumpos and B. Lee, *US Pat.*, US 20160211083 A1, Northwestern University, 2016.
32 D. J. Lewis and P. O'Brien, *Chem. Commun.*, 2014, **50**, 6319–6321.
33 D. Bhachu, D. Scanlon, E. Saban, H. Bronstein, I. Parkin, C. Carmalt and R. Palgrave, *J. Mater. Chem. A*, 2015, **3**, 9071–9073.
34 M. Aamir, M. Sher, M. D. Khan, M. A. Malik, J. Akhtar and N. Revaprasadu, *Mater. Lett.*, 2017, **190**, 244–247.
35 S. Chen, J. Briscoe, Y. Shi, K. Chen, R. M. Wilson, S. Dunn and R. Binions, *CrystEngComm*, 2015, **17**, 7486–7489.
36 M. Afzaal, B. Salhi, A. Al-Ahmed, H. Yates and A. Hakeem, *J. Mater. Chem. C*, 2017, **5**, 8366–8370.
37 P. Marchand, I. A. Hassan, I. P. Parkin and C. J. Carmalt, *Dalton Trans.*, 2013, **42**, 9406–9422.
38 C. E. Knapp and C. J. Carmalt, *Chem. Soc. Rev.*, 2016, **45**, 1036–1064.
39 D. J. Lewis, A. A. Tedstone, X. L. Zhong, E. A. Lewis, A. Rooney, N. Savjani, J. R. Brent, S. J. Haigh, M. G. Burke and C. A. Muryn, *Chem. Mater.*, 2015, **27**, 1367–1374.

40 S. Ashraf, C. S. Blackman, R. G. Palgrave, S. C. Naisbitt and I. P. Parkin, *J. Mater. Chem.*, 2007, **17**, 3708–3713.
41 J. T.-W. Wang, J. M. Ball, E. M. Barea, A. Abate, J. A. Alexander-Webber, J. Huang, M. Saliba, I. Mora-Sero, J. Bisquert and H. J. Snaith, *Nano Lett.*, 2013, **14**, 724–730.
42 M. Z. Mokhtar, M. Chen, E. Whittaker, B. Hamilton, N. Aristidou, S. Ramadan, A. Gholinia, S. A. Haque, P. O'Brien and B. R. Saunders, *Phys. Chem. Chem. Phys.*, 2017, **19**, 7204–7214.
43 M. Chen, M. Z. Mokhtar, E. Whittaker, Q. Lian, B. Hamilton, P. O'Brien, M. Zhu, Z. Cui, S. A. Haque and B. R. Saunders, *Nanoscale*, 2017, **9**, 10126–10137.
44 C.-R. Ke and J.-M. Ting, *J. Power Sources*, 2012, **208**, 316–321.
45 C.-R. Ke, C.-C. Chang and J.-M. Ting, *J. Power Sources*, 2015, **284**, 489–496.
46 K. Ramasamy, V. L. Kuznetsov, K. Gopal, M. A. Malik, J. Raftery, P. P. Edwards and P. O'Brien, *Chem. Mater.*, 2013, **25**, 266–276.
47 N. Fairley, *CasaXPS manual 2.3. 15*, Acolyte Science, 2009.
48 S.-C. Lim, H.-P. Lin, W.-L. Tsai, H.-W. Lin, Y.-T. Hsu and H.-Y. Tuan, *Nanoscale*, 2017, **9**, 3747–3751.
49 J. A. Christians, P. A. Miranda Herrera and P. V. Kamat, *J. Am. Chem. Soc.*, 2015, **137**, 1530–1538.
50 T. Moeller, D. C. Edwards, R. L. Brandt and J. Kleinberg, in *Inorganic Syntheses*, John Wiley & Sons, Inc., 2007, vol. 4, ch. 40, pp. 119–121.
51 W. Qiu, T. Merckx, M. Jaysankar, C. M. de la Huerta, L. Rakocevic, W. Zhang, U. Paetzold, R. Gehlhaar, L. Froyen and J. Poortmans, *Energy Environ. Sci.*, 2016, **9**, 484–489.
52 X. Qiu, Y. Jiang, H. Zhang, Z. Qiu, S. Yuan, P. Wang and B. Cao, *Phys. Status Solidi RRL*, 2016, **10**, 587–591.
53 J. Zhang, C. Yu, L. Wang, Y. Li, Y. Ren and K. Shum, *Sci. Rep.*, 2014, **4**, 6954.
54 E. Il'inchik, V. Volkov and L. Mazalov, *J. Struct. Chem.*, 2005, **46**, 523–534.
55 J. J. Zuckerman and A. P. Hagen, in *Inorganic Reactions and Methods*, John Wiley & Sons, Inc., 1986, vol. 1, ch. 1.3.4.4, p. 94.
56 W. S. Cardoso, M. S. P. Francisco, A. M. Lucho and Y. Gushikem, *Solid State Ionics*, 2004, **167**, 165–173.
57 Z. Wang, D. Luan, F. Y. C. Boey and X. W. Lou, *J. Am. Chem. Soc.*, 2011, **133**, 4738–4741.
58 I. Kiricsi, I. Pálinkó, G. Tasi and I. Hannus, *Mol. Cryst. Liq. Cryst. Sci. Technol., Sect. A*, 1994, **244**, 149–154.
59 A. Babayigit, D. D. Thanh, A. Ethirajan, J. Manca, M. Muller, H.-G. Boyen and B. Conings, *Sci. Rep.*, 2016, **6**, 18721.
60 C.-l. Ma and X.-d. Sun, *Nanotechnology*, 2002, **13**, 565–569.
61 A. Cabot, J. Arbiol, J. R. Morante, U. Weimar, N. Barsan and W. Göpel, *Sens. Actuators, B*, 2000, **70**, 87–100.
62 Y.-D. Wang, C.-L. Ma, X.-H. Wu and X.-D. Sun, *Talanta*, 2002, **57**, 875–882.
63 A. Tselesh, *Thin Solid Films*, 2008, **516**, 6253–6260.
64 S. Booth, A. Tripathi, I. Strashnov, R. Dryfe and A. Walton, *J. Phys.: Condens. Matter*, 2017, **29**, 454001.

8.2.2 Supporting Information

Electronic Supplementary Material (ESI) for Journal of Materials Chemistry A.

Ambient-Air-Stable Inorganic Cs_2SnI_6 Double Perovskite Thin Films via Aerosol-Assisted Chemical Vapour Deposition

Jack Chun-Ren Ke, David J. Lewis, Alex S. Walton, Ben F. Spencer, Paul O'Brien

Andrew G. Thomas* and Wendy R. Flavell*

Electronic Supplementary Information†

Peeling and scratching tests for adhesion to the substrate.

In order to evaluate adherence between Cs_2SnI_6 film and ITO-glass substrate, we conducted sticking and scratching tests for films fabricated by AACVD and spin coating. The sticking test was carried out using adhesive tape of width of 1 cm. This was fastened to the films and then peeled off rapidly. For the scratching test, a needle was used to scratch the films by moderate force.

(A)

(B)

(C)

(D)

Figure S1 Photographs of Cs_2SnI_6 films fabricated *via* AACVD (A&B) and spin coating (C&D). A shows the as fabricated AACVD film and B following the peel and scratch tests. C and D are equivalent tests

for the spin-coated film. It is clear that the AACVD-grown film shows very little change following the scratch and peel tests. The tape remains clear of black powder and no line can be seen on the substrate following scratching. The spin coated film, on the other hand, shows significant removal by both the tape and scratching.

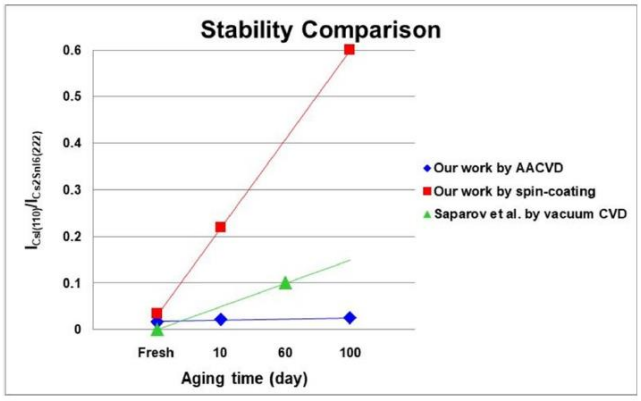

Figure S2 CsI-impurity-level comparison between the work reported by Saparov *et al.* through vacuum CVD and this work *via* AACVD and spin-coating showing the values of $I_{CsI(110)}/I_{Cs2SnI6(222)}$ determined from the XRD results as a function of aging up to around 100 days, as shown in Table 1. Note the data points obtained from the work of Saparov and the co-workers are estimated through measurement of the height of the corresponding reflections.

Table S1 Quantified atomic concentrations of various elements from the XPS spectra of Cs 3d (Figure 5), Sn $3p_{3/2}$ (Figure S3), and I 3d core levels. All elemental concentrations are normalised to [Cs] = 2.0 as in the ideal stoichiometry Cs_2SnI_6. Excess Sn (excess I) refers to the amount of Sn (I) that cannot be accounted for in the Cs_2SnI_6 (Cs_2SnI_6+CsI) phase(s).

Sample ID	Total Cs	Cs in CsI	Cs in Cs_2SnI_6	Sn	I	Excess Sn	Excess I
Ideal stoichiometry	**-**	**-**	**2.0**	**1.0**	**6.0**	**0.0**	**0.0**
AACVD (+HI) fresh	2.3 ± 0.2	0.3 ± 0.1	2.0 ± 0.2	4.1 ± 0.4	18.2 ± 1.8	3.1 ± 0.3	11.9 ± 1.2
AACVD (+HI) 100 days	2.4 ± 0.2	0.4 ± 0.1	2.0 ± 0.2	2.3 ± 0.2	6.8 ± 0.7	1.3 ± 0.1	0.4 ± 0.1
AACVD (-HI) fresh	2.7 ± 0.3	0.7 ± 0.1	2.0 ± 0.2	8.9 ± 0.9	9.2 ± 0.9	7.9 ± 0.8	2.5 ± 0.3
Spin-coated (+HI) fresh	2.4 ± 0.2	0.4 ± 0.1	2.0 ± 0.2	3.4 ± 0.3	7.2 ± 0.7	2.4 ± 0.2	0.8 ± 0.1
Spin-coated (+HI) 10 days	2.7 ± 0.3	0.7 ± 0.1	2.0 ± 0.2	2.8 ± 0.3	7.2 ± 0.7	1.8 ± 0.2	0.5 ± 0.1

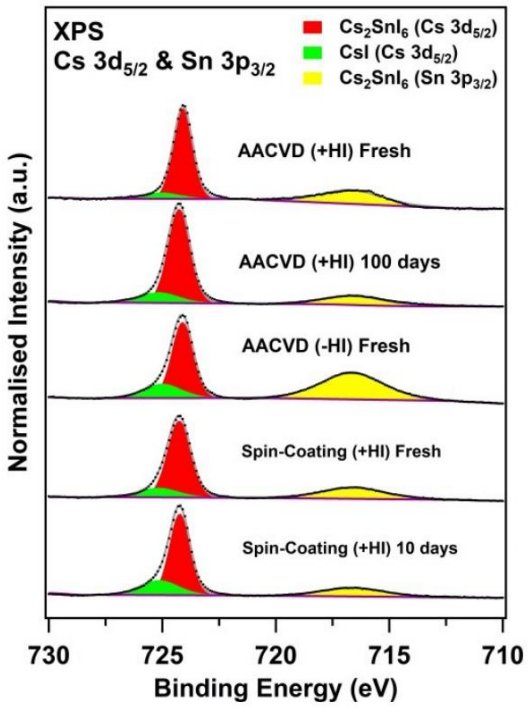

Figure S3 Sn $3p_{3/2}$ with Cs $3d_{5/2}$ core-level XPS spectra of various films prepared by AACVD or spin-coating. All spectra are normalised to the Cs $3d_{5/2}$ area for comparison of the relative concentrations of atomic Sn.

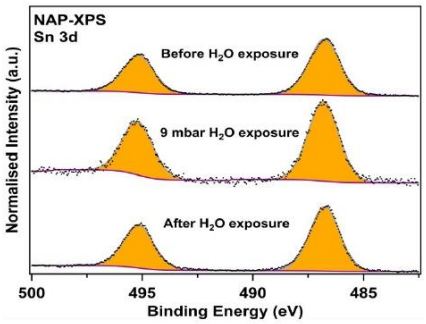
NAP-XPS
Sn 3d
Before H_2O exposure
9 mbar H_2O exposure
After H_2O exposure
Normalised Intensity (a.u.)
500
495
490
485
Binding Energy (eV)

(A)

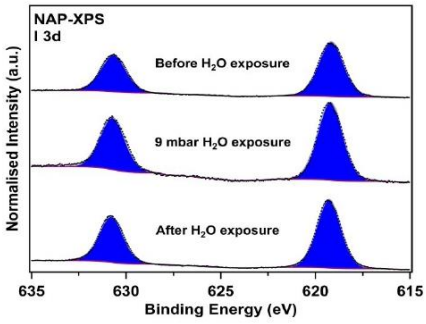
NAP-XPS
I 3d
Before H_2O exposure
9 mbar H_2O exposure
After H_2O exposure
Normalised Intensity (a.u.)
635
630
625
620
615
Binding Energy (eV)

(B)

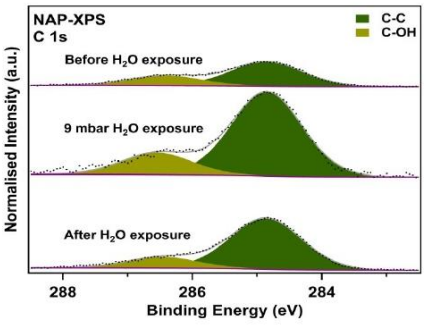
NAP-XPS
C 1s
C-C
C-OH
Before H_2O exposure
9 mbar H_2O exposure
After H_2O exposure
Normalised Intensity (a.u.)
288
286
284
Binding Energy (eV)

(C)

6

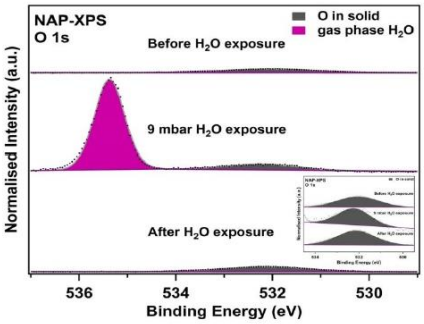

(D)

Figure S4(A) Sn 3d, (B) I 3d, (C) C 1s, and (D) O 1s core-level NAP-XPS spectra of AACVD (+HI)-grown film, recorded before, during, and after exposure to 9 mbar H_2O vapour. All spectra are normalised to the relevant Cs $3d_{5/2}$ area for comparison.

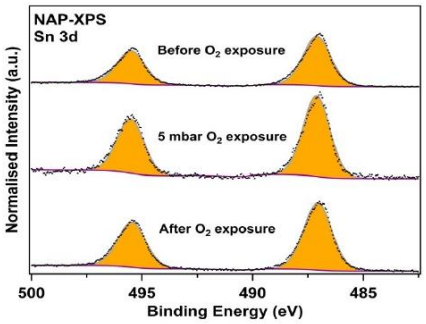
NAP-XPS
Sn 3d
Before O_2 exposure
5 mbar O_2 exposure
After O_2 exposure
Normalised Intensity (a.u.)
500
495
490
485
Binding Energy (eV)

(A)

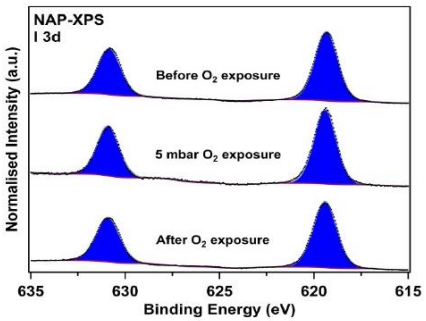
NAP-XPS
I 3d
Before O_2 exposure
5 mbar O_2 exposure
After O_2 exposure
Normalised Intensity (a.u.)
635
630
625
620
615
Binding Energy (eV)

(B)

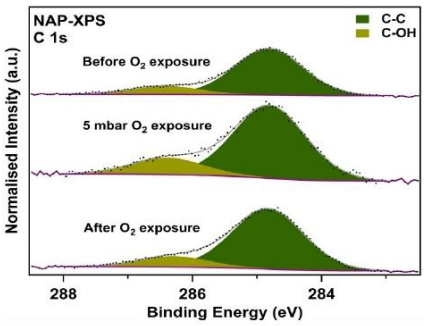
NAP-XPS
C 1s
C-C
C-OH
Before O_2 exposure
5 mbar O_2 exposure
After O_2 exposure
Normalised Intensity (a.u.)
288
286
284
Binding Energy (eV)

(C)

8

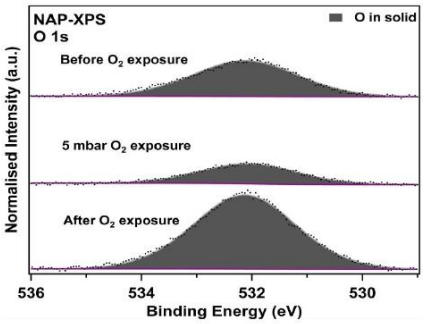

(D)

Figure S5 (A) Sn 3d, (B) I 3d, (C) C 1s, and (D) O 1s core-level NAP-XPS spectra of AACVD (+HI)-grown film, recorded before, during, and after exposure to 5 mbar O_2. All spectra are normalised to the relevant Cs $3d_{5/2}$ area for comparison.

Table S2 Quantified atomic concentrations of C–O (BE: 286.3 ± 0.1 eV) from the C 1s NAP-XPS spectra and O–C (BE: 532.1 ± 0.1 eV) from the O 1s NAP-XPS spectra of AACVD (+HI)-grown films. All elements are normalised to Cs (using [Cs] = 2.0), consistent with Tables 1&2. Spectra were measured under UHV conditions before and after exposure to water or O_2.

Fresh AACVD (+HI)	C–O	O–C
UHV before H_2O exposure	15.8 ± 1.6	12.0 ± 1.2
UHV after H_2O exposure	26.5 ± 2.7	16.1 ± 1.6
UHV before O_2 exposure	5.4 ± 0.5	4.7 ± 0.5
UHV after O_2 exposure	9.2 ± 0.9	9.2 ± 0.9

Chapter 9 Conclusions and Outlook

9.1 Conclusions

With immense concern about climate change, developing alternative renewable energy is of paramount importance. PSC is one of the brightest PV technologies of the future due to potentially low cost and high flexibility compared to mainstream silicon solar cells. The major deficiencies of PSCs are the instability and short lifetime issues under operating conditions, which are key factors for the future deployment of PSC panels. The main reason for the reduced performance of PSCs with time is the decomposition of perovskite light absorbers. Many sources can degrade halide perovskite films, including moisture and oxygen in ambient air, thermal stress and even light. We have taken the advantages of NAP-XPS to investigate the atmospheric degradation reactions of halide perovskites (in particular water vapour). Three key factors (processing, materials and understanding degradation mechanism) are all studied and included in this thesis with an emphasis on understanding the degradation mechanism. Investigation of moisture-induced degradation behaviour at perovskite surfaces using NAP-XPS is the fundamental part of these works, which are all built on the study in Chapter 4.

In Chapter 4, we report a significant breakthrough in the introduction of NAP-XPS to investigate the moisture-induced degradation behaviour of halide perovskites for the first time. We measured *in situ* deposited MAPI films using NAP-XPS in the presence of 3 and 9 mbar water vapour (equivalent to relative humidity (RH) of ~30%). It has been demonstrated that an ultrathin MAPI film can be deposited using a simple UHV-compatible thermal evaporator ($PbCl_2$ and MAI as precursors). The film was never

exposed to ambient air, eliminating other factors which could influence the results of degradation study. In the paper, we unambiguously show the decomposition route, where hydrogen iodide and ammonia gases are released from the film as a result of water vapour. Interestingly, we found carbon was not lost from the film surface upon water vapour exposure, whereas the nitrogen moiety completely degraded at RH ~30%. This suggests the vulnerability of the organic component of MAPI mainly originates from nitrogen rather than the carbon part.

Chapter 5 confirms AACVD can give MAPI films better stability in ambient air than spin-coated counterparts. This is probably due to larger grain sizes produced as well as slightly better surface coverage. The lead precursor applied in this work is $Pb(SCN)_2$, which could enable humid air processing. Without antisolvent treatment in the spin-coating method, the MAPI film obtained is very transparent, whereas AACVD can afford a dark and opaque MAPI film without additional treatment. The use of excess MAI leads to the reduced amount of PbI_2 impurity and defects and the formation of CH_3NH_2 at the surface, where the latter was determined using XPS. The CH_3NH_2 may act as a passivating agent to stabilise the MAPI surface. Furthermore, the MAPI films using $Pb(SCN)_2$ in this work are more stable than those made from $PbCl_2$ under the identical condition (Chapter 4). The surface passivation effect of MAPI films is further discussed in Chapter 6. In this work, we used thermal evaporation to deposit bulky ammonium iodides onto the MAPI surface. It was found that the metallic lead defects were healed by ammonium iodides, as determined by XPS. Ammonium iodides with longer carbon chains give the MAPI surface better water resistance. The degradation process induced by H_2O still follows the reaction proposed in Chapter 4: nitrogen and iodine have synchrotron loss in the form of ammonia and hydrogen iodide gases.

Chapter 7 not only focuses on the water resistance of mixed-cation perovskites but also the thermal stability since in the real world solar panels could experience both hot and humid environments. Mixed-cation mixed-halide perovskites containing FA have become mainstream lead perovskites due to better electricity output and lifetime. We found the perovskite containing MA has worse thermal stability as the MA component tends to escape from the film surface at 100 ^{o}C. It is worth noting that upon water vapour exposure the FA in the perovskites could lose one nitrogen atom first to form MA cation, prior to complete escape. Furthermore, NAP-XPS reveals that on exposure to moisture and/or heat FA and Br have synchronous loss, possibly in the form of FABr gas.

In Chapter 8, we focus on lead-free tin perovskites. The unstable nature of Sn^{2+} in typical tin perovskites makes them easily degraded. In this paper, a potential lead-free candidate, Cs_2SnI_6 double perovskite, has been studied. The material has optimised optical bandgap for single-junction solar cells and is relatively air stable. Cs_2SnI_6 have appeared to be highly process-dependent in accordance with numerous pieces of literature and this research. We found that the addition of HI in the precursor solution can lower the optical bandgap energy. Furthermore, AACVD-grown samples can produce larger grain sizes than spin-coated counterparts, which could impart better stability to the surfaces against moisture. XPS results reveal the presence of excess tin and iodine at the surface of Cs_2SnI_6. Following exposure to H_2O or O_2, the concentrations of tin and iodine changes, whereas the amount of CsI impurity remains similar. This suggests tin iodide may passivate the surface, preventing Cs_2SnI_6 from degradation induced by atmospheres.

In summary, this thesis provides a better understanding of the degradation behaviour of halide perovskite surfaces and provides directions for the improved stability. We believe the insights obtained in this thesis can pave the way towards stable PSC devices.

9.2 Outlook

Here we discuss the outlook by three viewpoints for stability: processing, materials, and understanding the degradation mechanisms. For processing, we have demonstrated a scalable process, AACVD, to deposit perovskite films. However, during the experimental period, it was found that AACVD needs thicker films to obtain good surface coverage, but too thick films are not preferred for use in PSCs. Therefore, further process modification is required to bring AACVD into the fabrication of PSCs. For materials, Cs_2SnI_6 has appeared to have strong metallic behaviour, preventing the devices from high PCEs.[226] Its Ti-based derivative, Cs_2TiBr_6, has shown a promising first PCE of 3.3% with excellent optical and electronic properties, which may merit further investigation.[227] Lead-free perovskites should be continuously studied to reduce the environmental impact of applying PSCs.

In this thesis, surface passivation has been demonstrated as an effective way to improve the stability of halide perovskites. Since it only modifies the surface rather than bulk, XPS would be very useful to investigate the effect of surface passivation. Many agents could passivate surface defects. Amongst them, ionic liquids could play an important role in surface passivation to improve device performance and lifetime.[228, 229] In future research, it would be of great interest to use surface characterisation techniques such as XPS to study the interaction between ionic liquids and halide perovskites. In addition to the moisture-induced degradation mechanism, more degradation processes caused by other factors (*e.g.* light and heat) or their combined effects should also be investigated. Better connection between device outcome and analytical results can significantly contribute to highly stable and efficient PSCs. Moreover, the evolution of

the surface degradation of halide perovskites has not been systematically investigated. Well-designed time-resolved studies are required to gain understanding in the degradation kinetics. Furthermore, some of the degradation reactions proposed have not been completely supported by direct evidence, such as reduction of metallic lead upon exposure to water vapour in some cases. Further elucidation of the underlying surface redox chemistry would gain insight into accurate degradation mechanisms.

Appendix

This chapter aims to present some selected important results obtained during PhD research, which are not included in the previous result sections. A few PSC device performance data from side projects are presented here as fabricating some photovoltaic devices can help the author gain knowledge about PSCs and in turn facilitate understanding of film deposition. Two types of planar devices are introduced here: MAPI and FAPI-based PSCs.

Experimental Section

Device Fabrication

To make planar PSC devices, patterned ITO-glass substrates (Ossila) with a size of 2.0 x 1.5 cm were used. Before any deposition, these substrates were carefully cleaned by immersing them in solutions in an ultrasonic bath, respectively containing 3 vt% Hellmanex III detergent in DI water, DI water, acetone, and ethanol in succession for 10 minutes in each step. The cleaned substrates were then dried immediately by an air blower prior to UV-O_3 treatment. Just before depositing compact TiO_2 layers, the cleaned substrates were treated by UV-O_3 for 15 minutes to remove organic residuals.

Next, we used a two-step spin-coating process to deposit compact TiO_2 layers (c-TiO_2) on an ITO-glass substrate in order to minimise the number of voids and pinholes formed. The compact TiO_2 solutions are composed of titanium diisopropoxide bis(acetylacetonate) (Sigma-Aldrich, 75 wt% in isopropanol) in 1-butanol (Sigma-Aldrich, ≥99%) with molar concentrations of 0.1 M and 0.3 M for the first and second steps, respectively. The solutions were stirred rigorously at room temperature for 30 minutes. Then, 100 μl of the

0.1 M solution was dropped onto an ITO-glass and the substrate was spun by a spin coater at 2000 rpm for 40 seconds. Subsequently, the coated substrate was placed on a hot plate at 120 ^{o}C for 10 minutes to dry the solvent. The above procedures were then repeated for the 0.3 M solution before annealing. Following drying, the substrates coated with c-TiO_2 layers were placed in a furnace and heated at 500 ^{o}C for 30 minutes.

Both perovskite solutions (MAPI and FAPI) were prepared under ambient air. For MAPI, first, lead acetate trihydrate (Sigma-Aldrich, 99.999%) was dissolved in a mixed solution (1.0 M) of anhydrous *N*,*N*-dimethylformamide (DMF, Sigma-Aldrich, 99.8%) and dimethyl sulfoxide (DMSO, Sigma-Aldrich, ≥99.7%) at a volume ratio of 4:1. Then the solution was stirred for an hour at 70 ^{o}C. Next, methylamine iodide (MAI, Ossila, 98%) was added into the lead-containing solution (3.0 M) and the resulting solution was stirred at room temperature for another 30 minutes to form a translucent yellow solution.

Before depositing the MAPI solution, substrates were heated at 70 ^{o}C for 5 minutes and then immediately transferred to the spin coater. 100 μl of the MAPI solution was subsequently dropped onto a warm substrate and the coated substrate was spun at 4000 rpm for 30 seconds. At 8 seconds after starting spinning, an antisolvent, 200 μl of anhydrous ethyl acetate (Sigma-Aldrich, 99.8%) was dripped onto the spinning substrate for a second. The films were then annealed at a hot plate at 100 ^{o}C for 10 minutes.

For FAPI, the solution preparation and deposition process are similar to MAPI. First, lead iodide (Alfa Aesar, 99.9985%) were dissolved in a warm DMF/DMSO (v:v of 4:1) mixed solution (1.0 M, 70 ^{o}C). The solution was stirred at 70 ^{o}C for 30 minutes until a clear solution was produced. After cooling down, formamidinium iodide (FAI, Ossila, 98%) was added into the solution (1.0 M) and the resulting solution was stirred for another

30 minutes. Then, the spin-coating process follows the procedures used for MAPI. The only difference is that FAPI films require annealing at 150 ^{o}C for 10 minutes on a hot plate.

To prepare solutions for HTM deposition, we prepared a bis(trifluoromethane)sulfonimide lithium salt (LiTFSI, Sigma-Aldrich, 99.95%) stock solution using acetonitrile as the solvent (520 mg in 1 mL) and a solution containing 43 mg of Spiro-MeOTAD in 0.5 mL of chlorobenzene. Subsequently, 10 μl of the LiTFSI solution and 15 μl of 4-*tert*-butylpyridine were poured into the Spiro-MeOTAD solution in succession to form the final HTM solution. The solution was then stirred for 10 minutes and used immediately for spin coating. 100 μl of the HTM solution was dripping onto the spinning substrate at 4000 rpm for 30 seconds. Finally, 80 nm of gold was thermally deposited on the top of HTM to produce a complete PSC device.

J-V Curve Measurement

The measurements generally follow the setup mentioned in Section 3.4.4.3. A metallic mask was used to define an active area. There are 8 subcells with an active area of 0.024 cm^2 in a single PSC. The *J-V* curve of each subcell was recorded under reverse scan (applied voltage from 1.2 to -0.2 V) and forward scan (from -0.2 to 1.2 V).

Results and Discussion

As shown in Figure A1, the PSCs (both MAPI and FAPI) fabricated under ambient air have PCEs of over 14%. We developed PSCs with PCEs from 0%, to near 9%,[218] then to almost 15% as shown here and to approaching 20% (will be published elsewhere), which are top PCEs in ambient-air-processed PSCs. It is worth noting that the PCE (14.15%) of the FAPI-based PSC is higher than that of a PSC (10.86%) with a similar structure fabricated in a nitrogen-filled glovebox (published in Science).[53]

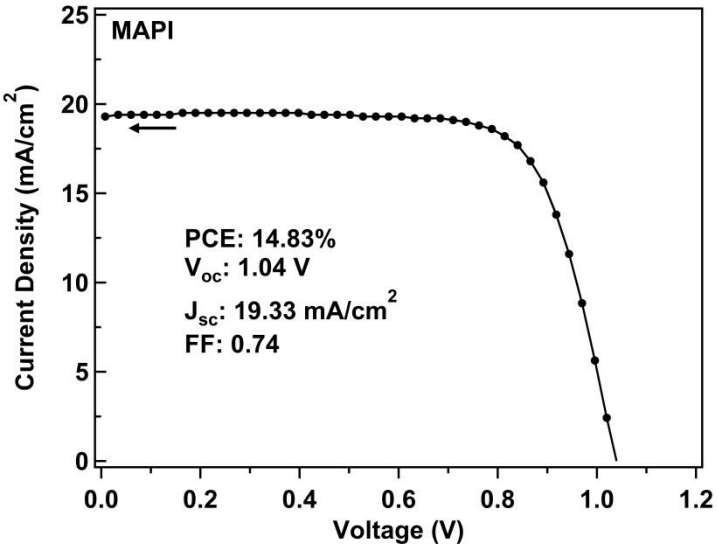

(A)

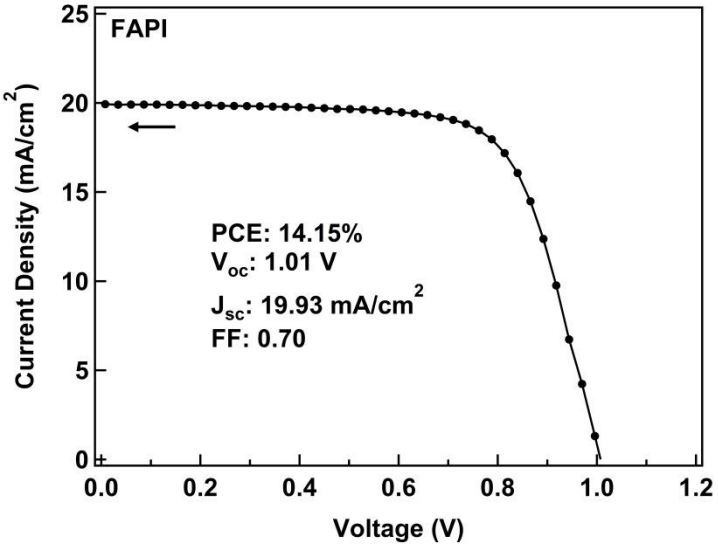

(B)

Figure A1 *J*−*V* curves of the champion (sub)cells in (A) MAPI and (B) FAPI-based PSCs *via* reverse scans under 1 sun illumination and the corresponding photovoltaic parameters are also shown in the figures.

Bibliography

[1] Gian-Reto Walther, Eric Post, Peter Convey, Annette Menzel, Camille Parmesan, Trevor JC Beebee, *et al.*, Ecological responses to recent climate change. *Nature* **2002,** *416*, p. 389.

[2] International Energy Agency, Key world energy statistics 2017. https://www.iea.org/publications/freepublications/publication/KeyWorld2017.pdf (14.July.2019).

[3] Oliver Morton, Solar energy: Silicon Valley sunrise. *Nature* **2006,** *443*, p. 19.

[4] National Renewable Energy Laboratory, Best research-cell efficiency chart. https://www.nrel.gov/pv/assets/pdfs/best-research-cell-efficiencies.20190802.pdf (20.August.2019).

[5] Arnulf Jäger-Waldau, PV status report 2018. http://publications.jrc.ec.europa.eu/repository/bitstream/JRC113626/pv_status_report_2018_online.pdf (14.July.2019).

[6] Akihiro Kojima, Kenjiro Teshima, Yasuo Shirai, Tsutomu Miyasaka, Organometal halide perovskites as visible-light sensitizers for photovoltaic cells. *Journal of the American Chemical Society* **2009,** *131*, p. 6050.

[7] Henry J Snaith, Present status and future prospects of perovskite photovoltaics. *Nature materials* **2018,** *17*, p. 372.

[8] Jack Chun-Ren Ke, Alex S. Walton, David J. Lewis, Aleksander Tedstone, Paul O'Brien, Andrew G. Thomas, *et al.*, In situ investigation of degradation at organometal halide perovskite surfaces by X-ray photoelectron spectroscopy at realistic water vapour pressure. *Chemical Communications* **2017,** *53*, p. 5231.

[9] Jack Chun-Ren Ke, David J Lewis, Alex S Walton, Ben F Spencer, Paul O'Brien, Andrew G Thomas, *et al.*, Ambient-air-stable inorganic Cs2SnI6 double perovskite thin films via aerosol-assisted chemical vapour deposition. *Journal of Materials Chemistry A* **2018,** *6*, p. 11205.

[10] Simon M Sze, Kwok K Ng, Physics of semiconductor devices, John Wiley & Sons, 2006.

[11] Charles Kittel, Paul McEuen, Introduction to solid state physics, John Wiley & Sons,

2005.

[12] E Becquerel, On electric effects under the influence of solar radiation. *Comptes Rendus Chimie* **1839,** *9*, p. 561.

[13] Valerio D'innocenzo, Giulia Grancini, Marcelo JP Alcocer, Ajay Ram Srimath Kandada, Samuel D Stranks, Michael M Lee, *et al.*, Excitons versus free charges in organo-lead tri-halide perovskites. *Nature communications* **2014,** *5*, p. 3586.

[14] Peter Würfel, Uli Würfel, Physics of solar cells: from basic principles to advanced concepts, John Wiley & Sons, 2016.

[15] William Shockley, Hans J Queisser, Detailed balance limit of efficiency of p-n junction solar cells. *Journal of Applied Physics* **1961,** *32*, p. 510.

[16] Luis M Pazos-Outón, Monika Szumilo, Robin Lamboll, Johannes M Richter, Micaela Crespo-Quesada, Mojtaba Abdi-Jalebi, *et al.*, Photon recycling in lead iodide perovskite solar cells. *Science* **2016,** *351*, p. 1430.

[17] William Shockley, WT Read Jr, Statistics of the recombinations of holes and electrons. *Physical review* **1952,** *87*, p. 835.

[18] David P McMeekin, Golnaz Sadoughi, Waqaas Rehman, Giles E Eperon, Michael Saliba, Maximilian T Hörantner, *et al.*, A mixed-cation lead mixed-halide perovskite absorber for tandem solar cells. *Science* **2016,** *351*, p. 151.

[19] Lei Meng, Jingbi You, Yang Yang, Addressing the stability issue of perovskite solar cells for commercial applications. *Nature communications* **2018,** *9*, p. 5265.

[20] Xiong Li, Dongqin Bi, Chenyi Yi, Jean-David Décoppet, Jingshan Luo, Shaik Mohammed Zakeeruddin, *et al.*, A vacuum flash–assisted solution process for high-efficiency large-area perovskite solar cells. *Science* **2016,** *353*, p. 58.

[21] Jeong-Hyeok Im, Chang-Ryul Lee, Jin-Wook Lee, Sang-Won Park, Nam-Gyu Park, 6.5% efficient perovskite quantum-dot-sensitized solar cell. *Nanoscale* **2011,** *3*, p. 4088.

[22] Hui-Seon Kim, Chang-Ryul Lee, Jeong-Hyeok Im, Ki-Beom Lee, Thomas Moehl, Arianna Marchioro, *et al.*, Lead iodide perovskite sensitized all-solid-state submicron thin film mesoscopic solar cell with efficiency exceeding 9%. *Scientific reports* **2012,** *2*, p. 591.

[23] Lioz Etgar, Peng Gao, Zhaosheng Xue, Qin Peng, Aravind Kumar Chandiran, Bin Liu, *et al.*, Mesoscopic CH3NH3PbI3/TiO2 heterojunction solar cells. *Journal of the American Chemical Society* **2012,** *134*, p. 17396.

[24] Michael M Lee, Joël Teuscher, Tsutomu Miyasaka, Takurou N Murakami, Henry J Snaith, Efficient hybrid solar cells based on meso-superstructured organometal halide perovskites. *Science* **2012,** *338*, p. 643.

[25] James M Ball, Michael M Lee, Andrew Hey, Henry J Snaith, Low-temperature processed meso-superstructured to thin-film perovskite solar cells. *Energy & Environmental Science* **2013,** *6*, p. 1739.

[26] Jin Hyuck Heo, Sang Hyuk Im, Jun Hong Noh, Tarak N Mandal, Choong-Sun Lim, Jeong Ah Chang, *et al.*, Efficient inorganic–organic hybrid heterojunction solar cells containing perovskite compound and polymeric hole conductors. *Nature photonics* **2013,** *7*, p. 486.

[27] Julian Burschka, Norman Pellet, Soo-Jin Moon, Robin Humphry-Baker, Peng Gao, Mohammad K Nazeeruddin, *et al.*, Sequential deposition as a route to high-performance perovskite-sensitized solar cells. *Nature* **2013,** *499*, p. 316.

[28] Mingzhen Liu, Michael B Johnston, Henry J Snaith, Efficient planar heterojunction perovskite solar cells by vapour deposition. *Nature* **2013,** *501*, p. 395.

[29] Samuel D Stranks, Giles E Eperon, Giulia Grancini, Christopher Menelaou, Marcelo JP Alcocer, Tomas Leijtens, *et al.*, Electron-hole diffusion lengths exceeding 1 micrometer in an organometal trihalide perovskite absorber. *Science* **2013,** *342*, p. 341.

[30] Chien-Hung Chiang, Zong-Liang Tseng, Chun-Guey Wu, Planar heterojunction perovskite/PC71BM solar cells with enhanced open-circuit voltage via a (2/1)-step spin-coating process. *Journal of Materials Chemistry A* **2014,** *2*, p. 15897.

[31] Giles E Eperon, Samuel D Stranks, Christopher Menelaou, Michael B Johnston, Laura M Herz, Henry J Snaith, Formamidinium lead trihalide: a broadly tunable perovskite for efficient planar heterojunction solar cells. *Energy & Environmental Science* **2014,** *7*, p. 982.

[32] Huanping Zhou, Qi Chen, Gang Li, Song Luo, Tze-bing Song, Hsin-Sheng Duan, *et al.*, Interface engineering of highly efficient perovskite solar cells. *Science* **2014,** *345*, p. 542.

[33] Jeong-Hyeok Im, In-Hyuk Jang, Norman Pellet, Michael Grätzel, Nam-Gyu Park, Growth of CH3NH3PbI3 cuboids with controlled size for high-efficiency perovskite solar cells. *Nature Nanotechnology* **2014,** *9*, p. 927.

[34] Jin Hyuck Heo, Hye Ji Han, Dasom Kim, Tae Kyu Ahn, Sang Hyuk Im, Hysteresis-less inverted CH3NH3PbI3 planar perovskite hybrid solar cells with 18.1% power conversion efficiency. *Energy & Environmental Science* **2015,** *8*, p. 1602.

[35] Woon Seok Yang, Jun Hong Noh, Nam Joong Jeon, Young Chan Kim, Seungchan Ryu, Jangwon Seo, *et al.*, High-performance photovoltaic perovskite layers fabricated through intramolecular exchange. *Science* **2015,** *348*, p. 1234.

[36] Jay B Patel, Jennifer Wong-Leung, Stephan Van Reenen, Nobuya Sakai, Jacob Tse Wei Wang, Elizabeth S Parrott, *et al.*, Influence of interface morphology on hysteresis in vapor-deposited perovskite Solar cells. *Advanced Electronic Materials* **2017,** *3*, p. 1600470.

[37] Michael Saliba, Taisuke Matsui, Ji-Youn Seo, Konrad Domanski, Juan-Pablo Correa-Baena, Mohammad Khaja Nazeeruddin, *et al.*, Cesium-containing triple cation perovskite solar cells: improved stability, reproducibility and high efficiency. *Energy & Environmental Science* **2016,** *9*, p. 1989.

[38] Michael Saliba, Taisuke Matsui, Konrad Domanski, Ji-Youn Seo, Amita Ummadisingu, Shaik M Zakeeruddin, *et al.*, Incorporation of rubidium cations into perovskite solar cells improves photovoltaic performance. *Science* **2016,** *354*, p. 206.

[39] Woon Seok Yang, Byung-Wook Park, Eui Hyuk Jung, Nam Joong Jeon, Young Chan Kim, Dong Uk Lee, *et al.*, Iodide management in formamidinium-lead-halide–based perovskite layers for efficient solar cells. *Science* **2017,** *356*, p. 1376.

[40] Nam Joong Jeon, Hyejin Na, Eui Hyuk Jung, Tae-Youl Yang, Yong Guk Lee, Geunjin Kim, *et al.*, A fluorene-terminated hole-transporting material for highly efficient and stable perovskite solar cells. *Nature Energy* **2018,** *3*, p. 682.

[41] Giles E Eperon, Tomas Leijtens, Kevin A Bush, Rohit Prasanna, Thomas Green, Jacob Tse-Wei Wang, *et al.*, Perovskite-perovskite tandem photovoltaics with optimized band gaps. *Science* **2016,** *354*, p. 861.

[42] Kevin A Bush, Axel F Palmstrom, J Yu Zhengshan, Mathieu Boccard, Rongrong Cheacharoen, Jonathan P Mailoa, *et al.*, 23.6%-efficient monolithic perovskite/silicon tandem solar cells with improved stability. *Nature Energy* **2017,** *2*, p. 17009.

[43] Florent Sahli, Jérémie Werner, Brett A Kamino, Matthias Bräuninger, Raphaël Monnard, Bertrand Paviet-Salomon, *et al.*, Fully textured monolithic perovskite/silicon tandem solar cells with 25.2% power conversion efficiency. *Nature materials* **2018,** *17*, p. 820.

[44] César Omar Ramírez Quiroz, Yilei Shen, Michael Salvador, Karen Forberich, Nadine Schrenker, George D Spyropoulos, *et al.*, Balancing electrical and optical losses for efficient 4-terminal Si–perovskite solar cells with solution processed percolation electrodes. *Journal*

of Materials Chemistry A **2018,** *6*, p. 3583.

[45] Juan-Pablo Correa-Baena, Michael Saliba, Tonio Buonassisi, Michael Grätzel, Antonio Abate, Wolfgang Tress, *et al.*, Promises and challenges of perovskite solar cells. *Science* **2017,** *358*, p. 739.

[46] Victor Moritz Goldschmidt, Die gesetze der krystallochemie. *Naturwissenschaften* **1926,** *14*, p. 477.

[47] Christopher Eames, Jarvist M Frost, Piers RF Barnes, Brian C O'regan, Aron Walsh, M Saiful Islam, Ionic transport in hybrid lead iodide perovskite solar cells. *Nature communications* **2015,** *6*, p. 7497.

[48] Yucheng Liu, Zhou Yang, Dong Cui, Xiaodong Ren, Jiankun Sun, Xiaojing Liu, *et al.*, Two-inch-sized perovskite CH3NH3PbX3 (X= Cl, Br, I) crystals: growth and characterization. *Advanced Materials* **2015,** *27*, p. 5176.

[49] Ayan A Zhumekenov, Makhsud I Saidaminov, Md Azimul Haque, Erkki Alarousu, Smritakshi Phukan Sarmah, Banavoth Murali, *et al.*, Formamidinium lead halide perovskite crystals with unprecedented long carrier dynamics and diffusion length. *ACS Energy Letters* **2016,** *1*, p. 32.

[50] Jin-Wook Lee, Dong-Jin Seol, An-Na Cho, Nam-Gyu Park, High-efficiency perovskite solar cells based on the black polymorph of HC(NH2)2PbI3. *Advanced Materials* **2014,** *26*, p. 4991.

[51] Constantinos C Stoumpos, Christos D Malliakas, Mercouri G Kanatzidis, Semiconducting tin and lead iodide perovskites with organic cations: phase transitions, high mobilities, and near-infrared photoluminescent properties. *Inorganic chemistry* **2013,** *52*, p. 9019.

[52] Tongle Bu, Xueping Liu, Yuan Zhou, Jianpeng Yi, Xin Huang, Long Luo, *et al.*, A novel quadruple-cation absorber for universal hysteresis elimination for high efficiency and stable perovskite solar cells. *Energy & Environmental Science* **2017,** *10*, p. 2509.

[53] Silver-Hamill Turren-Cruz, Anders Hagfeldt, Michael Saliba, Methylammonium-free, high-performance, and stable perovskite solar cells on a planar architecture. *Science* **2018,** *362*, p. 449.

[54] Hsinhan Tsai, Wanyi Nie, Jean-Christophe Blancon, Constantinos C Stoumpos, Reza Asadpour, Boris Harutyunyan, *et al.*, High-efficiency two-dimensional Ruddlesden–Popper perovskite solar cells. *Nature* **2016,** *536*, p. 312.

[55] Bo Peng, Jian Li, Qi Li, Yue Li, Hai Zhu, Li Zhang, *et al.*, Bose–Einstein oscillators and the excitation mechanism of free excitons in 2D layered organic–inorganic perovskites. *RSC Advances* **2017,** *7*, p. 18366.

[56] J-C Blancon, Hsinhan Tsai, Wanyi Nie, Costas C Stoumpos, Laurent Pedesseau, Claudine Katan, *et al.*, Extremely efficient internal exciton dissociation through edge states in layered 2D perovskites. *Science* **2017,** *355*, p. eaal4211.

[57] Giles E Eperon, Giuseppe M Paternò, Rebecca J Sutton, Andrea Zampetti, Amir Abbas Haghighirad, Franco Cacialli, *et al.*, Inorganic caesium lead iodide perovskite solar cells. *Journal of Materials Chemistry A* **2015,** *3*, p. 19688.

[58] Erin M Sanehira, Ashley R Marshall, Jeffrey A Christians, Steven P Harvey, Peter N Ciesielski, Lance M Wheeler, *et al.*, Enhanced mobility CsPbI3 quantum dot arrays for record-efficiency, high-voltage photovoltaic cells. *Science advances* **2017,** *3*, p. eaao4204.

[59] Taiyang Zhang, M Ibrahim Dar, Ge Li, Feng Xu, Nanjie Guo, Michael Grätzel, *et al.*, Bication lead iodide 2D perovskite component to stabilize inorganic α-CsPbI3 perovskite phase for high-efficiency solar cells. *Science advances* **2017,** *3*, p. e1700841.

[60] Feng Hao, Constantinos C Stoumpos, Duyen Hanh Cao, Robert PH Chang, Mercouri G Kanatzidis, Lead-free solid-state organic-inorganic halide perovskite solar cells. *Nature photonics* **2014,** *8*, p. 489.

[61] Weiqiang Liao, Dewei Zhao, Yue Yu, Corey R Grice, Changlei Wang, Alexander J Cimaroli, *et al.*, Lead-free inverted planar formamidinium tin triiodide perovskite solar cells achieving power conversion efficiencies up to 6.22%. *Advanced Materials* **2016,** *28*, p. 9333.

[62] Efat Jokar, Cheng-Hsun Chien, Cheng-Min Tsai, Amir Fathi, Eric Wei-Guang Diau, Robust tin-based perovskite solar cells with hybrid organic cations to attain efficiency approaching 10%. *Advanced Materials* **2018,** *31*, p. 1804835.

[63] Shuyan Shao, Jian Liu, Giuseppe Portale, Hong-Hua Fang, Graeme R Blake, Gert H ten Brink, *et al.*, Highly reproducible Sn-based hybrid perovskite solar cells with 9% efficiency. *Advanced Energy Materials* **2018,** *8*, p. 1702019.

[64] Tze-Bin Song, Takamichi Yokoyama, Shinji Aramaki, Mercouri G Kanatzidis, Performance enhancement of lead-free tin-based perovskite solar cells with reducing atmosphere-assisted dispersible additive. *ACS Energy Letters* **2017,** *2*, p. 897.

[65] Byunghong Lee, Constantinos C Stoumpos, Nanjia Zhou, Feng Hao, Christos

Malliakas, Chen-Yu Yeh, *et al.*, Air-stable molecular semiconducting iodosalts for solar cell applications: Cs2SnI6 as a hole conductor. *Journal of the American Chemical Society* **2014,** *136*, p. 15379.

[66] Xiaofeng Qiu, Bingqiang Cao, Shuai Yuan, Xiangfeng Chen, Zhiwen Qiu, Yanan Jiang, *et al.*, From unstable CsSnI3 to air-stable Cs2SnI6: A lead-free perovskite solar cell light absorber with bandgap of 1.48 eV and high absorption coefficient. *Solar Energy Materials and Solar Cells* **2017,** *159*, p. 227.

[67] Bayrammurad Saparov, Jon-Paul Sun, Weiwei Meng, Zewen Xiao, Hsin-Sheng Duan, Oki Gunawan, *et al.*, Thin-film deposition and characterization of a Sn-deficient perovskite derivative Cs2SnI6. *Chemistry of Materials* **2016,** *28*, p. 2315.

[68] Byunghong Lee, Anthony Krenselewski, Sung Il Baik, David Seidman, Robert PH Chang, Solution processing of air-stable molecular semiconducting iodosalts, Cs2SnI6-xBrx, for potential solar cell application. *Sustainable Energy & Fuels* **2017,** *1*, p. 710.

[69] Mercouri G Kanatzidis, Robert P H Chang, Konstantinos Stoumpos, Byunghong Lee Solar cells with perovskite-based light sensitization layers. US9966198B2, 08.May, **2018**.

[70] Zewen Xiao, Yuanyuan Zhou, Hideo Hosono, Toshio Kamiya, Intrinsic defects in a photovoltaic perovskite variant Cs2SnI6. *Physical Chemistry Chemical Physics* **2015,** *17*, p. 18900.

[71] Adam H Slavney, Te Hu, Aaron M Lindenberg, Hemamala I Karunadasa, A bismuth-halide double perovskite with long carrier recombination lifetime for photovoltaic applications. *Journal of the American Chemical Society* **2016,** *138*, p. 2138.

[72] Anna J Lehner, Douglas H Fabini, Hayden A Evans, Claire-Alice Hébert, Sara R Smock, Jerry Hu, *et al.*, Crystal and electronic structures of complex bismuth iodides A3Bi2I9 (A= K, Rb, Cs) related to perovskite: aiding the rational design of photovoltaics. *Chem. Mater* **2015,** *27*, p. 7137.

[73] Martina Pantaler, Kyung Taek Cho, Valentin IE Queloz, Inés García Benito, Christian Fettkenhauer, Irina Anusca, *et al.*, Hysteresis-free lead-free double-perovskite solar cells by interface engineering. *ACS Energy Letters* **2018,** *3*, p. 1781.

[74] Bayrammurad Saparov, Feng Hong, Jon-Paul Sun, Hsin-Sheng Duan, Weiwei Meng, Samuel Cameron, *et al.*, Thin-film preparation and characterization of Cs3Sb2I9: A lead-free layered perovskite semiconductor. *Chemistry of Materials* **2015,** *27*, p. 5622.

[75] Karunakara Moorthy Boopathi, Priyadharsini Karuppuswamy, Anupriya Singh,

Chintam Hanmandlu, Lin Lin, Syed Ali Abbas, *et al.*, Solution-processable antimony-based light-absorbing materials beyond lead halide perovskites. *Journal of Materials Chemistry A* **2017,** *5*, p. 20843.

[76] Gordon Haxel, James Hedrick, Greta Orris, Abundance of the chemical elements in upper continental crust. https://pubs.usgs.gov/fs/2002/fs087-02/ (27.December.2018).

[77] Jin-Wook Lee, Do-Kyoung Lee, Dong-Nyuk Jeong, Nam-Gyu Park, Control of crystal growth toward scalable fabrication of perovskite solar cells. *Advanced Functional Materials* **2018,** *N/A*, p. 1807047.

[78] Qidong Tai, Peng You, Hongqian Sang, Zhike Liu, Chenglong Hu, Helen LW Chan, *et al.*, Efficient and stable perovskite solar cells prepared in ambient air irrespective of the humidity. *Nature communications* **2016,** *7*, p. 11105.

[79] Yu-Hsien Chiang, Hsin-Min Cheng, Ming-Hsien Li, Tzung-Fang Guo, Peter Chen, Low-pressure vapor-assisted solution process for thiocyanate-based pseudohalide perovskite solar cells. *ChemSusChem* **2016,** *9*, p. 2620.

[80] Taiyang Zhang, Mengjin Yang, Yixin Zhao, Kai Zhu, Controllable sequential deposition of planar CH3NH3PbI3 perovskite films via adjustable volume expansion. *Nano letters* **2015,** *15*, p. 3959.

[81] Yian Xie, Feng Shao, Yaoming Wang, Tao Xu, Deliang Wang, Fuqiang Huang, Enhanced Performance of Perovskite CH3NH3PbI3 Solar Cell by Using CH3NH3I as Additive in Sequential Deposition. *ACS applied materials & interfaces* **2015**, p. 12937.

[82] David E Starr, Golnaz Sadoughi, Evelyn Handick, Regan G Wilks, Jan H Alsmeier, Leonard Köhler, *et al.*, Direct observation of an inhomogeneous chlorine distribution in CH3NH3PbI3−xClx layers: surface depletion and interface enrichment. *Energy & Environmental Science* **2015,** *8*, p. 1609.

[83] Wei Zhang, Sandeep Pathak, Nobuya Sakai, Thomas Stergiopoulos, Pabitra K Nayak, Nakita K Noel, *et al.*, Enhanced optoelectronic quality of perovskite thin films with hypophosphorous acid for planar heterojunction solar cells. *Nature communications* **2015,** *6*, p. 10030.

[84] Nam Joong Jeon, Jun Hong Noh, Young Chan Kim, Woon Seok Yang, Seungchan Ryu, Sang Il Seok, Solvent engineering for high-performance inorganic–organic hybrid perovskite solar cells. *Nature materials* **2014,** *13*, p. 897.

[85] Manda Xiao, Fuzhi Huang, Wenchao Huang, Yasmina Dkhissi, Ye Zhu, Joanne

Etheridge, *et al.*, A fast deposition-crystallization procedure for highly efficient lead iodide perovskite thin-film solar cells. *Angewandte Chemie International Edition* **2014,** *53*, p. 9898.

[86] Fu Yang, Gaurav Kapil, Putao Zhang, Zhaosheng Hu, Muhammad Akmal Kamarudin, Tingli Ma, *et al.*, Dependence of acetate-based antisolvents for high humidity fabrication of CH3NH3PbI3 perovskite devices in ambient atmosphere. *ACS applied materials & interfaces* **2018,** *10*, p. 16482.

[87] Joel Troughton, Katherine Hooper, Trystan M Watson, Humidity resistant fabrication of CH3NH3PbI3 perovskite solar cells and modules. *Nano Energy* **2017,** *39*, p. 60.

[88] Peng Cui, Dong Wei, Jun Ji, Hao Huang, Endong Jia, Shangyi Dou, *et al.*, Planar p–n homojunction perovskite solar cells with efficiency exceeding 21.3%. *Nature Energy* **2019,** *4*, p. 150.

[89] Olga Malinkiewicz, Aswani Yella, Yong Hui Lee, Guillermo Mínguez Espallargas, Michael Graetzel, Mohammad K Nazeeruddin, *et al.*, Perovskite solar cells employing organic charge-transport layers. *Nature photonics* **2014,** *8*, p. 128.

[90] Olga Malinkiewicz, Cristina Roldán-Carmona, Alejandra Soriano, Enrico Bandiello, Luis Camacho, Mohammad Khaja Nazeeruddin, *et al.*, Metal-oxide-free methylammonium lead iodide perovskite-based solar cells: the influence of organic charge transport layers. *Advanced Energy Materials* **2014,** *4*, p. 1400345.

[91] Luis K Ono, Matthew R Leyden, Shenghao Wang, Yabing Qi, Organometal halide perovskite thin films and solar cells by vapor deposition. *Journal of Materials Chemistry A* **2016,** *4*, p. 6693.

[92] Qi Chen, Huanping Zhou, Ziruo Hong, Song Luo, Hsin-Sheng Duan, Hsin-Hua Wang, *et al.*, Planar heterojunction perovskite solar cells via vapor-assisted solution process. *Journal of the American Chemical Society* **2013,** *136*, p. 622.

[93] Jun Yin, Hui Qu, Jing Cao, Huiling Tai, Jing Li, Nanfeng Zheng, Vapor-assisted crystallization control toward high performance perovskite photovoltaics with over 18% efficiency in the ambient atmosphere. *Journal of Materials Chemistry A* **2016,** *4*, p. 13203.

[94] David J Lewis, Paul O'Brien, Ambient pressure aerosol-assisted chemical vapour deposition of (CH 3 NH 3) PbBr 3, an inorganic–organic perovskite important in photovoltaics. *Chemical Communications* **2014,** *50*, p. 6319.

[95] DS Bhachu, DO Scanlon, EJ Saban, H Bronstein, IP Parkin, CJ Carmalt, *et al.*,

Scalable route to CH3NH3PbI3 perovskite thin films by aerosol assisted chemical vapour deposition. *Journal of Materials Chemistry A* **2015,** *3,* p. 9071.

[96] Mohammad Afzaal, Heather M Yates, Growth patterns and properties of aerosol-assisted chemical vapor deposition of CH3NH3PbI3 films in a single step. *Surface and Coatings Technology* **2017,** *321,* p. 336.

[97] Shreya Basak, Mohammad Afzaal, Heather M Yates, Optically tuned and large-grained bromine doped CH3NH3PbI3 perovskite thin films via aerosol-assisted chemical vapour deposition. *Materials chemistry and physics* **2019,** *223,* p. 157.

[98] Muhammad Aamir, Muhammad Sher, Malik Dilshad Khan, Mohammad Azad Malik, Javeed Akhtar, Neerish Revaprasadu, Controlled synthesis of all inorganic CsPbBr2I perovskite by non-template and aerosol assisted chemical vapour deposition. *Materials Letters* **2017,** *190,* p. 244.

[99] M Afzaal, B Salhi, A Al-Ahmed, HM Yates, AS Hakeem, Surface-related properties of perovskite CH3NH3PbI3 thin films by aerosol-assisted chemical vapour deposition. *Journal of Materials Chemistry C* **2017,** *5,* p. 8366.

[100] Shuqun Chen, Joe Briscoe, Yi Shi, Kan Chen, Rory M Wilson, Steve Dunn, *et al.*, A simple, low-cost CVD route to high-quality CH3NH3PbI3 perovskite thin films. *CrystEngComm* **2015,** *17,* p. 7486.

[101] Peter Marchand, Iman A Hassan, Ivan P Parkin, Claire J Carmalt, Aerosol-assisted delivery of precursors for chemical vapour deposition: expanding the scope of CVD for materials fabrication. *Dalton Transactions* **2013,** *42,* p. 9406.

[102] G Grancini, C Roldán-Carmona, I Zimmermann, E Mosconi, X Lee, D Martineau, *et al.*, One-Year stable perovskite solar cells by 2D/3D interface engineering. *Nature communications* **2017,** *8,* p. 15684.

[103] Neha Arora, M Ibrahim Dar, Alexander Hinderhofer, Norman Pellet, Frank Schreiber, Shaik Mohammed Zakeeruddin, *et al.*, Perovskite solar cells with CuSCN hole extraction layers yield stabilized efficiencies greater than 20%. *Science* **2017,** *358,* p. 768.

[104] Nicholas Aristidou, Irene Sanchez-Molina, Thana Chotchuangchutchaval, Michael Brown, Luis Martinez, Thomas Rath, *et al.*, The role of oxygen in the degradation of methylammonium lead trihalide perovskite photoactive layers. *Angewandte Chemie* **2015,** *127,* p. 8326.

[105] Nicholas Aristidou, Christopher Eames, Irene Sanchez-Molina, Xiangnan Bu, Jan

Kosco, M Saiful Islam, *et al.*, Fast oxygen diffusion and iodide defects mediate oxygen-induced degradation of perovskite solar cells. *Nature communications* **2017,** *8*, p. 15218.

[106] Weiguang Kong, Arash Rahimi-Iman, Gang Bi, Xusheng Dai, Huizhen Wu, Oxygen intercalation induced by photocatalysis on the surface of hybrid lead halide perovskites. **2016,** *120*, p. 7606.

[107] Qing Sun, Paul Fassl, David Becker-Koch, Alexandra Bausch, Boris Rivkin, Sai Bai, *et al.*, Role of microstructure in oxygen induced photodegradation of methylammonium lead triiodide perovskite films. *Advanced Energy Materials* **2017,** *7*, p. 1700977.

[108] Qi Wang, Bo Chen, Ye Liu, Yehao Deng, Yang Bai, Qingfeng Dong, *et al.*, Scaling behavior of moisture-induced grain degradation in polycrystalline hybrid perovskite thin films. *Energy & Environmental Science* **2017,** *10*, p. 516.

[109] Giles E Eperon, Severin N Habisreutinger, Tomas Leijtens, Bardo J Bruijnaers, Jacobus J van Franeker, Dane W deQuilettes, *et al.*, The importance of moisture in hybrid lead halide perovskite thin film fabrication. *ACS nano* **2015,** *9*, p. 9380.

[110] Jingbi You, Yang Yang, Ziruo Hong, Tze-Bin Song, Lei Meng, Yongsheng Liu, *et al.*, Moisture assisted perovskite film growth for high performance solar cells. *Applied physics letters* **2014,** *105*, p. 183902.

[111] Jinli Yang, Braden D Siempelkamp, Dianyi Liu, Timothy L Kelly, Investigation of CH3NH3PbI3 degradation rates and mechanisms in controlled humidity environments using in situ techniques. *ACS nano* **2015,** *9*, p. 1955.

[112] Guangda Niu, Wenzhe Li, Fanqi Meng, Liduo Wang, Haopeng Dong, Yong Qiu, Study on the stability of CH3NH3PbI3 films and the effect of post-modification by aluminum oxide in all-solid-state hybrid solar cells. *Journal of Materials Chemistry A* **2014,** *2*, p. 705.

[113] Aurélien MA Leguy, Yinghong Hu, Mariano Campoy-Quiles, M Isabel Alonso, Oliver J Weber, Pooya Azarhoosh, *et al.*, Reversible hydration of CH3NH3PbI3 in films, single crystals, and solar cells. *Chemistry of Materials* **2015,** *27*, p. 3397.

[114] Bekele Hailegnaw, Saar Kirmayer, Eran Edri, Gary Hodes, David Cahen, Rain on methylammonium lead iodide based perovskites: possible environmental effects of perovskite solar cells. *The journal of physical chemistry letters* **2015,** *6*, p. 1543.

[115] Jarvist M Frost, Keith T Butler, Federico Brivio, Christopher H Hendon, Mark Van

Schilfgaarde, Aron Walsh, Atomistic origins of high-performance in hybrid halide perovskite solar cells. *Nano letters* **2014,** *14*, p. 2584.

[116] Youzhen Li, Xuemei Xu, Chenggong Wang, Congcong Wang, Fangyan Xie, Junliang Yang, *et al.*, Degradation by exposure of coevaporated CH3NH3PbI3 thin films. *The Journal of Physical Chemistry C* **2015,** *119*, p. 23996.

[117] Paul Pistor, Thomas Burwig, Carlo Brzuska, Björn Weber, Wolfgang Fränzel, Thermal stability and miscibility of co-evaporated methyl ammonium lead halide (MAPbX 3, X= I, Br, Cl) thin films analysed by in situ X-ray diffraction. *Journal of Materials Chemistry A* **2018,** *6*, p. 11496.

[118] Tae Woong Kim, Naoyuki Shibayama, Ludmila Cojocaru, Satoshi Uchida, Takashi Kondo, Hiroshi Segawa, Real-Time In Situ Observation of Microstructural Change in Organometal Halide Perovskite Induced by Thermal Degradation. *Advanced Functional Materials* **2018,** *28*, p. 1804039.

[119] Jacobus J van Franeker, Koen H Hendriks, Bardo J Bruijnaers, Martinus WGM Verhoeven, Martijn M Wienk, René AJ Janssen, Monitoring thermal annealing of Perovskite solar cells with in situ photoluminescence. *Advanced Energy Materials* **2017,** *7*, p. 1601822.

[120] Tom Baikie, Yanan Fang, Jeannette M Kadro, Martin Schreyer, Fengxia Wei, Subodh G Mhaisalkar, *et al.*, Synthesis and crystal chemistry of the hybrid perovskite (CH3NH3)PbI3 for solid-state sensitised solar cell applications. *Journal of Materials Chemistry A* **2013,** *1*, p. 5628.

[121] Bert Conings, Jeroen Drijkoningen, Nicolas Gauquelin, Aslihan Babayigit, Jan D'Haen, Lien D'Olieslaeger, *et al.*, Intrinsic thermal instability of methylammonium lead trihalide perovskite. *Advanced Energy Materials* **2015,** *5*, p. 1500477.

[122] Yuanhang Cheng, Qing-Dan Yang, Jingyang Xiao, Qifan Xue, Ho-Wa Li, Zhiqiang Guan, *et al.*, Decomposition of organometal halide perovskite films on zinc oxide nanoparticles. *ACS applied materials & interfaces* **2015,** *7*, p. 19986.

[123] S Kumar, A Dhar, Accelerated thermal-aging-induced degradation of organometal triiodide perovskite on ZnO nanostructures and its effect on hybrid photovoltaic devices. *ACS applied materials & interfaces* **2016,** *8*, p. 18309.

[124] Mingzhu Long, Tiankai Zhang, Mingzhen Liu, Zefeng Chen, Chen Wang, Weiguang Xie, *et al.*, Abnormal synergetic effect of organic and halide ions on the stability and optoelectronic properties of a mixed perovskite via in situ characterizations. *Advanced*

Materials **2018,** *30*, p. 1801562.

[125] Zhaobing Zeng, Jing Zhang, Xinlei Gan, Hongrui Sun, Minghui Shang, Dagang Hou, *et al.*, In situ grain boundary functionalization for stable and efficient inorganic CsPbI2Br perovskite solar cells. *Advanced Energy Materials* **2018,** *8*, p. 1801050.

[126] Xiaofeng Tang, Marco Brandl, Benjamin May, Ievgen Levchuk, Yi Hou, Moses Richter, *et al.*, Photoinduced degradation of methylammonium lead triiodide perovskite semiconductors. *Journal of Materials Chemistry A* **2016,** *4*, p. 15896.

[127] Jianming Yang, Qiuming Hong, Zhongcheng Yuan, Ruipeng Xu, Xuewen Guo, Shaobing Xiong, *et al.*, Unraveling photostability of mixed cation perovskite films in extreme environment. *Advanced Optical Materials* **2018,** *6*, p. 1800262.

[128] Tomas Leijtens, Giles E Eperon, Sandeep Pathak, Antonio Abate, Michael M Lee, Henry J Snaith, Overcoming ultraviolet light instability of sensitized TiO 2 with meso-superstructured organometal tri-halide perovskite solar cells. *Nature communications* **2013,** *4*, p. 2885.

[129] Guangquan Lu, Amy Linsebigler, John T Yates Jr, The adsorption and photodesorption of oxygen on the TiO2 (110) surface. *The Journal of chemical physics* **1995,** *102*, p. 4657.

[130] Tjalling Koopmans, Ü ber die zuordnung von wellenfunktionen und eigenwerten zu den einzelnen elektronen eines atoms. *Physica* **1934,** *1*, p. 104.

[131] LS Cederbaum, G Hohlneicher, W Von Niessen, On the breakdown of the Koopmans' theorem for nitrogen. *Chemical Physics Letters* **1973,** *18*, p. 503.

[132] Peter J Feibelman, DE Eastman, Photoemission spectroscopy—correspondence between quantum theory and experimental phenomenology. *Physical Review B* **1974,** *10*, p. 4932.

[133] Bertrand Philippe, Byung-Wook Park, Rebecka Lindblad, Johan Oscarsson, Sareh Ahmadi, Erik MJ Johansson, *et al.*, Chemical and electronic structure characterization of lead halide perovskites and stability behavior under different exposures A photoelectron spectroscopy investigation. *Chemistry of Materials* **2015,** *27*, p. 1720.

[134] M Brun, A Berthet, JC Bertolini, XPS, AES and Auger parameter of Pd and PdO. *Journal of Electron Spectroscopy and Related Phenomena* **1999,** *104*, p. 55.

[135] J Wayne Rabalais, Principles of ultraviolet photoelectron spectroscopy, John Wiley

& Sons, 1976.

[136] John C Vickerman, Ian S Gilmore, Surface analysis: the principal techniques, John Wiley & Sons, 2011.

[137] Ch D Wagner, GE Muilenberg, Handbook of x-ray photoelectron spectroscopy, Perkin-Elmer, 1979.

[138] James D Ingle Jr, Stanley R Crouch, Spectrochemical analysis, 1988.

[139] Shigeo Tanuma, Cedric J Powell, David R Penn, Calculations of electron inelastic mean free paths. V. Data for 14 organic compounds over the 50–2000 eV range. *Surface and interface analysis* **1994,** *21*, p. 165.

[140] Werner H Gries, A universal predictive equation for the inelastic mean free pathlengths of X-ray photoelectrons and auger electrons. *Surface and interface analysis* **1996,** *24*, p. 38.

[141] Neal Fairley, CasaXPS manual 2.3. 15, Acolyte Science, 2009.

[142] David Briggs, MP Seah, Practical surface analysis: by Auger and X-ray photoelectron spectroscopy, John Wiley & Sons, 2003.

[143] S Yamamoto, H Bluhm, K Andersson, G Ketteler, H Ogasawara, M Salmeron, *et al.*, In situ x-ray photoelectron spectroscopy studies of water on metals and oxides at ambient conditions. *Journal of Physics: Condensed Matter* **2008,** *20*, p. 184025.

[144] Mark J Jackman, Andrew G Thomas, Chris Muryn, Photoelectron spectroscopy study of stoichiometric and reduced anatase TiO2 (101) surfaces: the effect of subsurface defects on water adsorption at near-ambient pressures. *The Journal of Physical Chemistry C* **2015,** *119*, p. 13682.

[145] Jan Haubrich, Ryan G Quiller, Lauren Benz, Zhi Liu, Cynthia M Friend, In situ ambient pressure studies of the chemistry of NO2 and water on rutile TiO2 (110). *Langmuir* **2010,** *26*, p. 2445.

[146] Reza Vakili, Emma K Gibson, Sarayute Chansai, Shaojun Xu, Nadeen Al-Janabi, Peter P Wells, *et al.*, Understanding the CO oxidation on Pt nanoparticles supported on MOFs by operando XPS. *ChemCatChem* **2018,** *10*, p. 4238.

[147] Kwangjin An, Selim Alayoglu, Nathan Musselwhite, Sheba Plamthottam, Gérôme Melaet, Avery E Lindeman, *et al.*, Enhanced CO oxidation rates at the interface of mesoporous oxides and Pt nanoparticles. *Journal of the American Chemical Society* **2013,**

135, p. 16689.

[148] Hendrik Bluhm, Michael Hävecker, Axel Knop-Gericke, Evgueni Kleimenov, Robert Schlögl, Detre Teschner, *et al.*, Methanol oxidation on a copper catalyst investigated using in situ X-ray photoelectron spectroscopy. *The Journal of Physical Chemistry B* **2004,** *108*, p. 14340.

[149] Rebecka Lindblad, Dongqin Bi, Byung-wook Park, Johan Oscarsson, Mihaela Gorgoi, Hans Siegbahn, *et al.*, Electronic structure of TiO2/CH3NH3PbI3 perovskite solar cell interfaces. *The journal of physical chemistry letters* **2014,** *5*, p. 648.

[150] Yu Kwon Kim, Byungwook Jeon, Hui Joon Park, Interfacial electronic structure of methylammonium lead iodide grown on a mesoporous TiO2 layer on F-doped tin oxide substrate. *The Journal of Physical Chemistry C* **2016,** *120*, p. 22460.

[151] R Clayton Shallcross, Yilong Zheng, S Scott Saavedra, Neal R Armstrong, Determining band-edge energies and morphology-dependent stability of formamidinium lead perovskite films using spectroelectrochemistry and photoelectron spectroscopy. *Journal of the American Chemical Society* **2017,** *139*, p. 4866.

[152] Bert Conings, Linny Baeten, Christopher De Dobbelaere, Jan D'Haen, Jean Manca, Hans-Gerd Boyen, Perovskite-based hybrid solar cells exceeding 10% efficiency with high reproducibility using a thin film sandwich approach. *Advanced Materials* **2014,** *26*, p. 2041.

[153] Farzaneh Arabpour Roghabadi, Vahid Ahmadi, Karim Oniy Aghmiuni, Organic-inorganic halide perovskite formation: in situ dissociation of cation halide and metal halide complexes during crystal formation. *The Journal of Physical Chemistry C* **2017,** *121*, p. 13532.

[154] Wan-Jian Yin, Tingting Shi, Yanfa Yan, Unusual defect physics in CH3NH3PbI3 perovskite solar cell absorber. *Applied physics letters* **2014,** *104*, p. 063903.

[155] Elisa M Miller, Yixin Zhao, Candy C Mercado, Sudip K Saha, Joseph M Luther, Kai Zhu, *et al.*, Substrate-controlled band positions in CH3NH3PbI3 perovskite films. *Physical Chemistry Chemical Physics* **2014,** *16*, p. 22122.

[156] Ye Zou, Qing Meng, Hongying Mao, Daoben Zhu, Substrate effect on the interfacial electronic structure of thermally-evaporated CH3NH3PbI3 perovskite layer. *Organic Electronics* **2017,** *41*, p. 307.

[157] Rebecka Lindblad, Naresh K Jena, Bertrand Philippe, Johan Oscarsson, Dongqin Bi, Andreas Lindblad, *et al.*, Electronic structure of CH3NH3PbX3 perovskites: dependence on

the halide moiety. *The Journal of Physical Chemistry C* **2015,** *119*, p. 1818.

[158] Takashi Komesu, Xin Huang, Tula R Paudel, Yaroslav B Losovyj, Xin Zhang, Eike F Schwier, *et al.*, Surface electronic structure of hybrid organo lead bromide perovskite single crystals. *The Journal of Physical Chemistry C* **2016,** *120*, p. 21710.

[159] Bertrand Philippe, T Jesper Jacobsson, Juan-Pablo Correa-Baena, Naresh K Jena, Amitava Banerjee, Sudip Chakraborty, *et al.*, Valence level character in a mixed perovskite material and determination of the valence band maximum from photoelectron spectroscopy: variation with photon energy. *The Journal of Physical Chemistry C* **2017,** *121*, p. 26655.

[160] Xianzhong Zhou, Wang Ye, Xiaoli Li, Wei Zheng, Richeng Lin, Feng Huang, *et al.*, Band alignment of MAPb(I1–xBrx)3 thin films by vacuum deposition. *Applied physics letters* **2016,** *109*, p. 233906.

[161] Byung-wook Park, Bertrand Philippe, Sagar M Jain, Xiaoliang Zhang, Tomas Edvinsson, Håkan Rensmo, *et al.*, Chemical engineering of methylammonium lead iodide/bromide perovskites: tuning of opto-electronic properties and photovoltaic performance. *Journal of Materials Chemistry A* **2015,** *3*, p. 21760.

[162] Chi Li, Jian Wei, Mikio Sato, Harunobu Koike, Zhong-Zhi Xie, Yan-Qing Li, *et al.*, Halide-substituted electronic properties of organometal halide perovskite films: direct and inverse photoemission studies. *ACS applied materials & interfaces* **2016,** *8*, p. 11526.

[163] Chenggong Wang, Congcong Wang, Xiaoliang Liu, John Kauppi, Yuchuan Shao, Zhengguo Xiao, *et al.*, Electronic structure evolution of fullerene on CH3NH3PbI3. *Applied physics letters* **2015,** *106*, p. 111603.

[164] Maryline Ralaiarisoa, Yan Busby, Johannes Frisch, Ingo Salzmann, Jean-Jacques Pireaux, Norbert Koch, Correlation of annealing time with crystal structure, composition, and electronic properties of CH3NH3PbI3−xClx mixed-halide perovskite films. *Physical Chemistry Chemical Physics* **2017,** *19*, p. 828.

[165] Hao-Chung Chia, Hwo-Shuenn Sheu, Yu-Yun Hsiao, Shao-Sian Li, Yi-Kang Lan, Chung-Yao Lin, *et al.*, A critical intermediate structure that directs the crystalline texture and surface morphology of organo-lead trihalide perovskite. *ACS applied materials & interfaces* **2017,** *9*, p. 36897.

[166] Jennifer Emara, Tobias Schnier, Neda Pourdavoud, Thomas Riedl, Klaus Meerholz, Selina Olthof, Impact of Film Stoichiometry on the Ionization Energy and Electronic Structure of CH3NH3PbI3 Perovskites. *Advanced Materials* **2016,** *28*, p. 553.

[167] Tsz-Wai Ng, Hrisheekesh Thachoth Chandran, Chiu-Yee Chan, Ming-Fai Lo, Chun-Sing Lee, Ionic charge transfer complex induced visible light harvesting and photocharge generation in perovskite. *ACS applied materials & interfaces* **2015,** *7*, p. 20280.

[168] Benjamin J Foley, Daniel L Marlowe, Keye Sun, Wissam A Saidi, Louis Scudiero, Mool C Gupta, *et al.*, Temperature dependent energy levels of methylammonium lead iodide perovskite. *Applied physics letters* **2015,** *106*, p. 243904.

[169] Philip Schulz, Eran Edri, Saar Kirmayer, Gary Hodes, David Cahen, Antoine Kahn, Interface energetics in organo-metal halide perovskite-based photovoltaic cells. *Energy & Environmental Science* **2014,** *7*, p. 1377.

[170] Xiaoliang Liu, Chenggong Wang, Lu Lyu, Congcong Wang, Zhengguo Xiao, Cheng Bi, *et al.*, Electronic structures at the interface between Au and CH 3 NH 3 PbI 3. *Physical Chemistry Chemical Physics* **2015,** *17*, p. 896.

[171] Nilushi Wijeyasinghe, Anna Regoutz, Flurin Eisner, Tian Du, Leonidas Tsetseris, Yen-Hung Lin, *et al.*, Copper (I) thiocyanate (CuSCN) hole-transport layers processed from aqueous precursor solutions and their application in thin-film transistors and highly efficient organic and organometal halide perovskite solar cells. *Advanced Functional Materials* **2017,** *27*, p. 1701818.

[172] Tao Ding, Ruifeng Li, Weiguang Kong, Bingpo Zhang, Huizhen Wu, Band alignments at interface of ZnO/FAPbI 3 heterojunction by X-ray photoelectron spectroscopy. *Applied Surface Science* **2015,** *357*, p. 1743.

[173] Muhammad Naufal Lintangpradipto, Nikolai Tsevtkov, Byeong Cheul Moon, Jeung Ku Kang, Size-controlled CdSe quantum dots to boost light harvesting capability and stability of perovskite photovoltaic cells. *Nanoscale* **2017,** *9*, p. 10075.

[174] Satyajit Gupta, Tatyana Bendikov, Gary Hodes, David Cahen, CsSnBr3, a lead-free halide perovskite for long-term solar cell application: insights on SnF2 addition. *ACS Energy Letters* **2016,** *1*, p. 1028.

[175] Shan-Ting Zhang, Hervé Roussel, Odette Chaix-Pluchery, Michel Langlet, David Muñoz-Rojas, Daniel Bellet, *et al.*, Polymorphism of the blocking TiO2 layer deposited on F: SnO2 and its influence on the interfacial energetic alignment. *The Journal of Physical Chemistry C* **2017,** *121*, p. 17305.

[176] Weiming Qiu, Ulrich W Paetzold, Robert Gehlhaar, Vladimir Smirnov, Hans-Gerd Boyen, Jeffrey G Tait, *et al.*, An electron beam evaporated TiO2 layer for high efficiency

planar perovskite solar cells on flexible polyethylene terephthalate substrates. *Journal of Materials Chemistry A* **2015,** *3*, p. 22824.

[177] Muhammad Talha Masood, Christian Weinberger, Jawad Sarfraz, Emil Rosqvist, Simon Sandén, Oskar J Sandberg, *et al.*, Impact of film thickness of ultrathin dip-coated compact TiO2 layers on the performance of mesoscopic perovskite solar cells. *ACS applied materials & interfaces* **2017,** *9*, p. 17906.

[178] Shanglei Feng, Yingguo Yang, Meng Li, Jinmiao Wang, Zhendong Cheng, Jihao Li, *et al.*, High-performance perovskite solar cells engineered by an ammonia modified graphene oxide interfacial layer. *ACS applied materials & interfaces* **2016,** *8*, p. 14503.

[179] Wenzhe Li, Haopeng Dong, Xudong Guo, Nan Li, Jiangwei Li, Guangda Niu, *et al.*, Graphene oxide as dual functional interface modifier for improving wettability and retarding recombination in hybrid perovskite solar cells. *Journal of Materials Chemistry A* **2014,** *2*, p. 20105.

[180] Tsz-Wai Ng, Chiu-Yee Chan, Ming-Fai Lo, Zhi Qiang Guan, Chun-Sing Lee, Formation chemistry of perovskites with mixed iodide/chloride content and the implications on charge transport properties. *Journal of Materials Chemistry A* **2015,** *3*, p. 9081.

[181] Claudia Hartmann, Golnaz Sadoughi, Roberto Félix, Evelyn Handick, Hagen W Klemm, Gina Peschel, *et al.*, Spatially resolved insight into the chemical and electronic structure of solution-processed perovskites—why to (not) worry about pinholes. *Advanced Materials Interfaces* **2018,** *5*, p. 1701420.

[182] Hui Yu, Feng Wang, Fangyan Xie, Wenwu Li, Jian Chen, Ni Zhao, The role of chlorine in the formation process of "CH3NH3PbI3-xClx" perovskite. *Advanced Functional Materials* **2014,** *24*, p. 7102.

[183] Silvia Colella, Edoardo Mosconi, Giovanna Pellegrino, Alessandra Alberti, Valentino LP Guerra, Sofia Masi, *et al.*, Elusive presence of chloride in mixed halide perovskite solar cells. *The journal of physical chemistry letters* **2014,** *5*, p. 3532.

[184] Giovanna Pellegrino, Silvia Colella, Ioannis Deretzis, Guglielmo G Condorelli, Emanuele Smecca, Giuseppe Gigli, *et al.*, Texture of MAPbI3 layers assisted by chloride on flat TiO2 substrates. *The Journal of Physical Chemistry C* **2015,** *119*, p. 19808.

[185] Alberto Calloni, Antonio Abate, Gianlorenzo Bussetti, Giulia Berti, Rossella Yivlialin, Franco Ciccacci, *et al.*, Stability of organic cations in solution-processed CH3NH3PbI3 perovskites: formation of modified surface layers. *The Journal of Physical*

Chemistry C **2015,** *119*, p. 21329.

[186] Min-Cherl Jung, Young Mi Lee, Han-Koo Lee, Jinwoo Park, Sonia R Raga, Luis K Ono, *et al.*, The presence of CH3NH2 neutral species in organometal halide perovskite films. *Applied physics letters* **2016,** *108*, p. 073901.

[187] Philip Schulz, Jan O Tiepelt, Jeffrey A Christians, Igal Levine, Eran Edri, Erin M Sanehira, *et al.*, High-work-function molybdenum oxide hole extraction contacts in hybrid organic–inorganic perovskite solar cells. *ACS applied materials & interfaces* **2016,** *8*, p. 31491.

[188] Bertrand Philippe, Michael Saliba, Juan-Pablo Correa-Baena, Ute B Cappel, Silver-Hamill Turren-Cruz, Michael Grätzel, *et al.*, Chemical distribution of multiple cation (Rb+, Cs+, MA+, and FA+) perovskite materials by photoelectron spectroscopy. *Chemistry of Materials* **2017,** *29*, p. 3589.

[189] Benjia Dou, Elisa M Miller, Jeffrey A Christians, Erin M Sanehira, Talysa R Klein, Frank S Barnes, *et al.*, High-performance flexible perovskite solar cells on ultrathin glass: implications of the TCO. *The journal of physical chemistry letters* **2017,** *8*, p. 4960.

[190] Lijia Liu, John A McLeod, Rongbin Wang, Pengfei Shen, Steffen Duhm, Tracking the formation of methylammonium lead triiodide perovskite. *Applied physics letters* **2015,** *107*, p. 061904.

[191] Sagar Motilal Jain, Bertrand Philippe, Erik MJ Johansson, Byung-wook Park, Håkan Rensmo, Tomas Edvinsson, *et al.*, Vapor phase conversion of PbI2 to CH3NH3PbI3: spectroscopic evidence for formation of an intermediate phase. *Journal of Materials Chemistry A* **2016,** *4*, p. 2630.

[192] Youzhen Li, Xuemei Xu, Chenggong Wang, Congcong Wang, Fangyan Xie, Junliang Yang, *et al.*, Investigation on thermal evaporated CH3NH3PbI3 thin films. *AIP Advances* **2015,** *5*, p. 097111.

[193] Xianzhong Zhou, Xiaoli Li, Yuan Liu, Feng Huang, Dingyong Zhong, Interface electronic properties of co-evaporated MAPbI3 on ZnO (0001): In situ X-ray photoelectron spectroscopy and ultraviolet photoelectron spectroscopy study. *Applied physics letters* **2016,** *108*, p. 121601.

[194] M Pl Seah, WA Dench, Quantitative electron spectroscopy of surfaces: A standard data base for electron inelastic mean free paths in solids. *Surface and interface analysis* **1979,** *1*, p. 2.

[195] Haitao Xu, Yanglin Wu, Jian Cui, Chaowei Ni, Fuzong Xu, Jiang Cai, *et al.*, Formation and evolution of the unexpected PbI2 phase at the interface during the growth of evaporated perovskite films. *Physical Chemistry Chemical Physics* **2016,** *18*, p. 18607.

[196] Haipeng Xie, Xiaoliang Liu, Lu Lyu, Dongmei Niu, Qi Wang, Jinsong Huang, *et al.*, Effects of precursor ratios and annealing on electronic structure and surface composition of CH3NH3PbI3 perovskite films. *The Journal of Physical Chemistry C* **2015,** *120*, p. 215.

[197] Melepurath Deepa, Manuel Salado, Laura Calio, Samrana Kazim, SM Shivaprasad, Shahzada Ahmad, Cesium power: low Cs+ levels impart stability to perovskite solar cells. *Physical Chemistry Chemical Physics* **2017,** *19*, p. 4069.

[198] Fabio Matteocci, Yan Busby, Jean-Jacques Pireaux, Giorgio Divitini, Stefania Cacovich, Caterina Ducati, *et al.*, Interface and composition analysis on perovskite solar cells. *ACS applied materials & interfaces* **2015,** *7*, p. 26176.

[199] Weiming Qiu, Ulrich W Paetzold, Robert Gehlhaar, Vladimir Smirnov, Hans-Gerd Boyen, Jeffrey G Tait, *et al.*, An electron beam evaporated TiO 2 layer for high efficiency planar perovskite solar cells on flexible polyethylene terephthalate substrates. *Journal of Materials Chemistry A* **2015,** *3*, p. 22824.

[200] Xiaoming Li, Ye Wu, Shengli Zhang, Bo Cai, Yu Gu, Jizhong Song, *et al.*, CsPbX3 quantum dots for lighting and displays: room-temperature synthesis, photoluminescence superiorities, underlying origins and white light-emitting diodes. *Advanced Functional Materials* **2016,** *26*, p. 2435.

[201] Quyet Van Le, Minjoon Park, Woonbae Sohn, Ho Won Jang, Soo Young Kim, Investigation of energy levels and crystal structures of cesium lead halides and their application in full-color light-emitting diodes. *Advanced Electronic Materials* **2017,** *3*, p. 1600448.

[202] G Rajendra Kumar, Hee-Je Kim, Senthil Karupannan, Kandasamy Prabakar, Interplay between iodide and tin vacancies in CsSnI3 perovskite solar cells. *The Journal of Physical Chemistry C* **2017,** *121*, p. 16447.

[203] Weixin Huang, Subha Sadhu, Sylwia Ptasinska, Heat-and gas-induced transformation in CH3NH3PbI3 perovskites and its effect on the efficiency of solar cells. *Chemistry of Materials* **2017,** *29*, p. 8478.

[204] Golnaz Sadoughi, David E Starr, Evelyn Handick, Samuel D Stranks, Mihaela Gorgoi, Regan G Wilks, *et al.*, Observation and mediation of the presence of metallic lead in

organic–inorganic perovskite films. *ACS applied materials & interfaces* **2015,** *7*, p. 13440.

[205] Chunhua Wang, Chujun Zhang, Sichao Tong, Jianqiang Shen, Can Wang, Youzhen Li, *et al.*, Air-induced high-quality CH3NH3PbI3 thin film for efficient planar heterojunction perovskite solar cells. *The Journal of Physical Chemistry C* **2017,** *121*, p. 6575.

[206] Weixin Huang, Joseph S Manser, Prashant V Kamat, Sylwia Ptasinska, Evolution of chemical composition, morphology, and photovoltaic efficiency of CH3NH3PbI3 perovskite under ambient conditions. *Chemistry of Materials* **2015,** *28*, p. 303.

[207] Zafer Hawash, Luis K Ono, Sonia R Raga, Michael V Lee, Yabing Qi, Air-exposure induced dopant redistribution and energy level shifts in spin-coated spiro-MeOTAD films. *Chemistry of Materials* **2015,** *27*, p. 562.

[208] Congcong Wang, Youzhen Li, Xuemei Xu, Chenggong Wang, Fangyan Xie, Yongli Gao, Degradation of co-evaporated perovskite thin film in air. *Chemical Physics Letters* **2016,** *649*, p. 151.

[209] Zubair Ahmad, Mansoor Ani Najeeb, RA Shakoor, Abdulla Alashraf, Shaheen A Al-Muhtaseb, Ahmed Soliman, *et al.*, Instability in CH3NH3PbI3 perovskite solar cells due to elemental migration and chemical composition changes. *Scientific reports* **2017,** *7*, p. 15406.

[210] Maryline Ralaiarisoa, Ingo Salzmann, Feng-Shuo Zu, Norbert Koch, Effect of water, oxygen, and air exposure on CH3NH3PbI3–xClx perovskite surface electronic properties. *Advanced Electronic Materials* **2018,** *4*, p. 1800307.

[211] Youzhen Li, Xuemei Xu, Congcong Wang, Ben Ecker, Junliang Yang, Jinsong Huang, *et al.*, Light-induced degradation of CH3NH3PbI3 hybrid perovskite thin film. *The Journal of Physical Chemistry C* **2017,** *121*, p. 3904.

[212] Ute B Cappel, Sebastian Svanström, Valeria Lanzilotto, Fredrik OL Johansson, Kerttu Aitola, Bertrand Philippe, *et al.*, Partially reversible photoinduced chemical changes in a mixed-ion perovskite material for solar cells. *ACS applied materials & interfaces* **2017,** *9*, p. 34970.

[213] K Xerxes Steirer, Philip Schulz, Glenn Teeter, Vladan Stevanovic, Mengjin Yang, Kai Zhu, *et al.*, Defect tolerance in methylammonium lead triiodide perovskite. *ACS Energy Letters* **2016,** *1*, p. 360.

[214] Keisuke Motoki, Yu Miyazawa, Daisuke Kobayashi, Masashi Ikegami, Tsutomu

Miyasaka, Tomoyuki Yamamoto, *et al.*, Degradation of CH3NH3PbI3 perovskite due to soft x-ray irradiation as analyzed by an x-ray photoelectron spectroscopy time-dependent measurement method. *Journal of Applied Physics* **2017,** *121*, p. 085501.

[215] Aleksandar R Milosavljević, Weixin Huang, Subha Sadhu, Sylwia Ptasinska, Low-energy electron-induced transformations in organolead halide perovskite. *Angewandte Chemie International Edition* **2016,** *55*, p. 10083.

[216] Yuichi Kato, Luis K Ono, Michael V Lee, Shenghao Wang, Sonia R Raga, Yabing Qi, Silver iodide formation in methyl ammonium lead iodide perovskite solar cells with silver top electrodes. *Advanced Materials Interfaces* **2015,** *2*, p. 1500195.

[217] David B Hall, Patrick Underhill, John M Torkelson, Spin coating of thin and ultrathin polymer films. *Polymer Engineering & Science* **1998,** *38*, p. 2039.

[218] Qian Chen, Muhamad Z Mokhtar, Jack Chun-Ren Ke, Andrew G Thomas, Aseel Hadi, Eric Whittaker, *et al.*, A one-step laser process for rapid manufacture of mesoscopic perovskite solar cells prepared under high relative humidity. *Sustainable Energy & Fuels* **2018,** *2*, p. 1216.

[219] Nobuya Sakai, Sandeep Pathak, Hsin-Wei Chen, Amir A Haghighirad, Samuel D Stranks, Tsutomu Miyasaka, *et al.*, The mechanism of toluene-assisted crystallization of organic–inorganic perovskites for highly efficient solar cells. *Journal of Materials Chemistry A* **2016,** *4*, p. 4464.

[220] Ping Fan, Di Gu, Guang-Xing Liang, Jing-Ting Luo, Ju-Long Chen, Zhuang-Hao Zheng, *et al.*, High-performance perovskite CH3NH3PbI3 thin films for solar cells prepared by single-source physical vapour deposition. *Scientific reports* **2016,** *6*, p. 29910.

[221] William Henry Bragg, William Lawrence Bragg, The reflection of X-rays by crystals. *Proceedings of the Royal Society of London. Series A* **1913,** *88*, p. 428.

[222] Stefaan De Wolf, Jakub Holovsky, Soo-Jin Moon, Philipp Löper, Bjoern Niesen, Martin Ledinsky, *et al.*, Organometallic halide perovskites: sharp optical absorption edge and its relation to photovoltaic performance. *The journal of physical chemistry letters* **2014,** *5*, p. 1035.

[223] Paul Kubelka, Franz Munk, An article on optics of paint layers. *Z. Tech. Phys* **1931,** *12*, p. 1.

[224] Chun-Ren Ke, David J Lewis, Alex S Walton, Qian Chen, Ben Felix Spencer, Muhammad Mokhtar, *et al.*, Air-stable methylammonium lead iodide perovskite thin films

fabricated via aerosol-assisted chemical vapor deposition from a pseudohalide Pb(SCN)2 precursor. *ACS Applied Energy Materials* **2019,** *2*, p. 6012.

[225] Shuang Yang, Yun Wang, Porun Liu, Yi-Bing Cheng, Hui Jun Zhao, Hua Gui Yang, Functionalization of perovskite thin films with moisture-tolerant molecules. *Nature Energy* **2016,** *1*, p. 15016.

[226] Fawen Guo, Zonghuan Lu, Dibyajyoti Mohanty, Tianmeng Wang, Ishwara B Bhat, Shengbai Zhang, *et al.*, A two-step dry process for Cs2SnI6 perovskite thin film. *Materials Research Letters* **2017,** *5*, p. 540.

[227] Min Chen, Ming-Gang Ju, Alexander D Carl, Yingxia Zong, Ronald L Grimm, Jiajun Gu, *et al.*, Cesium titanium (IV) bromide thin films based stable lead-free perovskite solar cells. *Joule* **2018,** *2*, p. 558.

[228] Dong Yang, Xin Zhou, Ruixia Yang, Zhou Yang, Wei Yu, Xiuli Wang, *et al.*, Surface optimization to eliminate hysteresis for record efficiency planar perovskite solar cells. *Energy & Environmental Science* **2016,** *9*, p. 3071.

[229] Sai Bai, Peimei Da, Cheng Li, Zhiping Wang, Zhongcheng Yuan, Fan Fu, *et al.*, Planar perovskite solar cells with long-term stability using ionic liquid additives. *Nature* **2019,** *571*, p. 245.